Synthesis Lectures on
Materials and Optics

SYNTHESIS
COLLECTION OF TECHNOLOGY

John X. J. Zhang

Plasmonic MEMS

Springer

Synthesis Lectures on Materials and Optics

This series publishes concise books on topics that include advanced and state-of-the-art methods to understand and develop materials for optics. Leading experts on the subject present and discuss both classical and new wave theory, techniques, and interdisciplinary applications in the field. Optical materials play an integral role in the development of numerous advances in areas from communications to sensors to photonics and more, and this series discusses a broad range of topics and principles in condensed matter physics, materials science, chemistry, and electrical engineering.

John X. J. Zhang

Plasmonic MEMS

Springer

John X. J. Zhang
Dartmouth College
Hanover, NH, USA

ISSN 2691-1930 ISSN 2691-1949 (electronic)
Synthesis Lectures on Materials and Optics
ISBN 978-3-031-23136-0 ISBN 978-3-031-23137-7 (eBook)
https://doi.org/10.1007/978-3-031-23137-7

© The Editor(s) (if applicable) and The Author(s), under exclusive license to Springer Nature Switzerland AG 2023
This work is subject to copyright. All rights are solely and exclusively licensed by the Publisher, whether the whole or part of the material is concerned, specifically the rights of translation, reprinting, reuse of illustrations, recitation, broadcasting, reproduction on microfilms or in any other physical way, and transmission or information storage and retrieval, electronic adaptation, computer software, or by similar or dissimilar methodology now known or hereafter developed.
The use of general descriptive names, registered names, trademarks, service marks, etc. in this publication does not imply, even in the absence of a specific statement, that such names are exempt from the relevant protective laws and regulations and therefore free for general use.
The publisher, the authors, and the editors are safe to assume that the advice and information in this book are believed to be true and accurate at the date of publication. Neither the publisher nor the authors or the editors give a warranty, expressed or implied, with respect to the material contained herein or for any errors or omissions that may have been made. The publisher remains neutral with regard to jurisdictional claims in published maps and institutional affiliations.

This Springer imprint is published by the registered company Springer Nature Switzerland AG
The registered company address is: Gewerbestrasse 11, 6330 Cham, Switzerland

Preface

The ability to manipulate light beyond traditional diffraction limit at nanoscale physical dimensions is driving the rapid development of nanophotonics. Major developments in theoretical modeling, design, simulations, robust, and reliable nanofabrication techniques are responsible for the variety of emerging applications of nanophotonics from computing, communication to biomedical sensing and imaging. The rapidly growing field of plasmonics, as a subsection of nanophotonics, deals with confining optical energy into dimensions far below the diffraction limit. Surface plasmons, collective oscillations of the conduction electrons, as a building block of plasmonics have found large applications in label-free biosensing, molecular-specific imaging, and photothermal therapy of cancer.

Recent years have seen an exciting and gradually emerging field of "Plasmonic MEMS", which attempts to combine plasmonics with Microelectromechanical System (MEMS) technology towards achieving remarkably enhanced system performance. Progress and improvements in Optical MEMS in the past two decades have led to a variety of miniaturized movable and tunable mirrors, lenses, filters, and other optical structures. Plasmonic MEMS provides a new set of perspectives and design tools through in-depth coupling of physics and chemistry at surfaces and interfaces with multiscale engineering, which has great interdisciplinary appeal, attracting researchers from fields as diverse as electrical engineering, mechanical engineering, optics, biochemistry, biomedical engineering, and biology towards new system designs.

Our intention in creating this book is to cover the key topics in the emerging field of plasmonic MEMS, with the emphasis on the practical aspects of this area. Extended readings can be referred to many comprehensive and well-written textbooks on electromagnetic waves, nanophotonics, and plasmonics. However, most of these literatures are lengthy and lack the focus needed for thoroughly grasp on plasmonic micromachining and MEMS. This handbook is organized in six chapters that reflect the current status of the evolving scientific field. Chapter 1 introduces the main framework of plasmonic MEMS and overviews the introductory concepts in plasmonics and MEMS along with the status of the field and the existing challenges. Chapter 2 describes the basic foundations of plasmonic MEMS. An abbreviated overview of the basic physics and devices

related to electromagnetic waves and surface plasmons is also presented. It is a foundational and self-contained chapter, starting with Maxwell's equations and concluding with the derivation of the grating equation. Chapter 3 describes recent advances in the fabrication of sub-100-nm patterns on microscale devices and structures and reviews the emerging techniques in the fabrication of plasmonic systems. This chapter also includes a comprehensive and historical review of the current advances in the area of plasmonic nanofabrication. Chapter 4 focuses on an appealing and distinctive aspect of plasmonics as a tool for patterning and the fabrication of ultra-fine resolution structures. Chapter 5 reviews the recent developments in plasmonic MEMS and microsystems for biosensing applications, including refractive-index-based label-free biosensing, plasmonic integrated lab-on-chip systems, plasmonic for Near-Field Scanning Optical Microscopy (NSOM), and plasmonics on-chip system for cellular imaging. Chapter 6 presents our perspective on the current direction in plasmonic MEMS and micropatterning in conjunction with the final remarks. The advanced and sophisticated readers can read the book in any preferred order and can read only sections of personal interest.

We hope this concise book grows to be a valuable reference manual and a useful tool for both students, researchers, and industrial practitioners in the field of plasmonics and MEMS. We encourage readers to contribute their valuable comments/suggestions so that the book can be improved further.

Hanover, USA
January 2023

John X. J. Zhang

Contents

1 Introduction 1
- 1.1 MEMS and Optical MEMS 1
- 1.2 Plasmonic MEMS: A Frontier of Photonic Devices 6
- 1.3 Status of the Field 8
- 1.4 Existing Challenges 10
- References 11

2 Theoretical Foundations 15
- 2.1 Maxwell's Equations and Electromagnetic Wave Theory 15
- 2.2 Diffraction and Interference 22
- 2.3 Transmission Line Theory (TLT) 23
- 2.4 Plasmonic Nanograting Theory 26
- 2.5 Numerical Methods 29
- References 29

3 Fabrication Techniques 31
- 3.1 Nanofabrication Using Photons 32
  - 3.1.1 Photolithography 32
  - 3.1.2 Electron Beam Lithography 39
  - 3.1.3 Focused-Ion Beam Lithography 46
  - 3.1.4 Scanning Probe Lithography 53
- 3.2 Emerging Techniques 61
  - 3.2.1 Nanoimprint Lithography 62
  - 3.2.2 Soft Lithography 66
  - 3.2.3 Nanosphere Lithography 70
  - 3.2.4 Nanofabrication by Self-assembly 72
- References 83

4 Plasmonics as a Fabrication Tool 97
4.1 Prism-Coupled Plasmonic Nanolithography 97
4.2 Grating-Coupled Plasmonic Nanolithography 99
4.3 Focused Plasmonic Nanolithography 101
References 104

5 Plasmonic MEMS in Biosensing and Imaging 107
5.1 Refractive-Index Based Label-Free Biosensing 107
5.2 Plasmonic Near-Field Scanning Optical Microscopy 118
5.3 Plasmonic Nanosensors for Point-Of-Care (POC) Biomarker Screening 122
5.4 Signal Read-Out Method 126
5.4.1 Colorimetric 126
5.4.2 Fluorescence, Raman, and Handheld-Format Systems 131
5.5 Nanoparticle Based Designs 134
5.5.1 Sphere 134
5.5.2 Cube 141
5.5.3 Spike/Star 145
5.6 Sandwich-, Chip-, and Paper-Based Designs 146
5.6.1 Sandwich Structure 146
5.6.2 Microfluidic Chip 149
5.6.3 Paper Based Design 151
5.7 Meta-Surface Patterned Design 153
5.7.1 Lithographic Patterning 157
5.7.2 Nanoisland Films 158
5.7.3 Chemical Growth 160
5.8 Challenges and Perspectives 161
5.8.1 Covid-19 Testing 162
5.8.2 Machine Learning 163
5.8.3 Miniaturization 163
5.8.4 Gold Standard 164
References 165

Summary and Future Perspectives 183

Appendix 1 185

Introduction

1

1.1 MEMS and Optical MEMS

Micro-Electro-Mechanical Systems (MEMS) is the technology of integrated mechanical and electro-mechanical micro-elements on a single chip. The micro-scale moving components of MEMS devices can be readily and robustly fabricated using the well-developed micro/nano fabrication techniques (details are covered in Chap. 3). Mechanical displacement in MEMS devices can be obtained via external electrical actuation. MEMS technology aims to revolutionize nearly every product group by substituting sensors, actuators, detectors, and gears with micrometer-scale equivalents [1–3].

Since its early proposal and demonstration in late 1980s, major advancements have taken place motivated by urgent requirements for large scale production of miniaturized and compact sensors and actuators.

One of the main reasons for the development of MEMS technology in recent years, is the drastic reduction of the size of the device components along with the additional and complemented mechanical modulation functionality which can enable tunable on-chip sensors and actuators [4, 5]. MEMS can provide microstructures in a variety of desirable shapes and sizes with critical future size of micro or nano meter along with significant mechanical tunability as shown in Fig. 1.1.

MEMS devices have been realized using a variety of materials including semiconductors, polymers, glasses, ceramics, metals, and various other alloys. But Silicon, as a horse power in IC industry, and due to a very mature and well-developed fabrication processes, has found a distinctive place in MEMS [3].

The precision mechanics of MEMS technology and micromachining have ignited the possibility of using this technology for a wide variety of applications in high-speed digital

© The Author(s), under exclusive license to Springer Nature Switzerland AG 2023

J. X. J. Zhang, *Plasmonic MEMS*, Synthesis Lectures on Materials and Optics,
https://doi.org/10.1007/978-3-031-23137-7_1

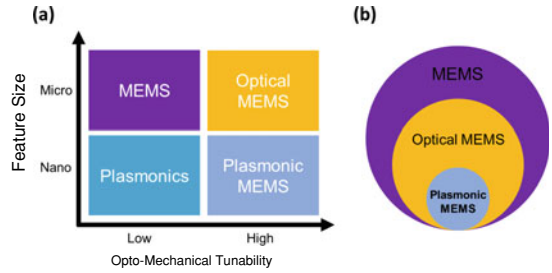

Fig. 1.1 The framework of MEMS, Optical MEMS, Plasmonics, and Plasmonic MEMS. **a** Comparison by the critical feature size and the optomechanical tunability. **b** Classified view of each field. Plasmonic MEMS can be considered as a subset of optical MEMS with plasmonic materials and components

circuits [6], radio frequency (RF) and Infrared (IR) devices [7, 8], wireless communications and nanosatellites [9], unmanned air vehicles (UAVs) [10], optical detectors [11], biomedical devices and imaging [12–14], to name a few.

Integration of MEMS with biomedical devices has opened up a new world of possibilities for medical applications. Healthcare industry such as pharmaceuticals, healthcare equipment, biotechnology and related life sciences possess a significant demand for biomedical MEMS (Bio-MEMS). Figure 1.2 shows a few representative BioMEMS apparatuses.

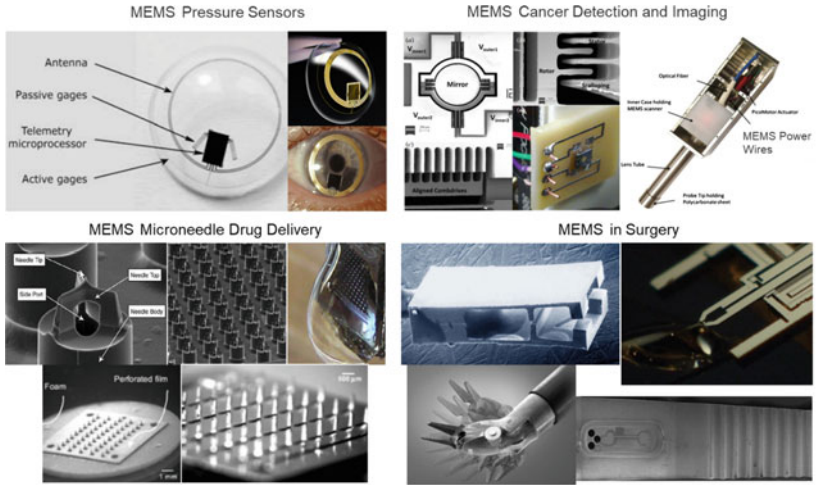

Fig. 1.2 A few BioMEMS representative applications including MEMS pressure sensors, MEMS cancer detection and imaging, MEMS microneedles drug delivery, and MEMS in surgery. Images are taken from top-left [15, 16], top-right [12, 17], bottom left [18, 19], bottom right [20–22]

One of the first MEMS devices to be utilized in the biomedical and bioengineering community were pressure sensors in the late 1980s [23]. In one of the pioneering works, Leonardi, et al. realized the first wireless contact lens for intraocular pressure (IOP) monitoring using a miniaturized MEMS biosensor integrated with biocompatible materials to detect deformations of the eyeball. The device can be used to treat very complex diseases such as Glaucoma. The wireless sensor was built using a microprocessor and an antenna integrated into the soft contact lens shown in Fig. 1.2. The MEMS pressure sensor consists of passive strain gages to determine corneal curvature alterations in response to IOP.

Cancer is among the leading causes of death worldwide. Among different types of cancer, the death rate for oral and oropharyngeal cancer is significantly higher [16]. Wang et al. realized a MEMS enabled handheld high resolution confocal imaging probe for portable oral cancer detection [17]. Record high field of view was achieved using a programmable MEMS micromirror as shown in Fig. 1.2. The MEMS device utilizes a voltage-controlled biaxial gimbal structure to rotate along the two perpendicular axes. The realized handheld scanner imaging device illustrates great promise as a prospective clinical tool for cancer risk assessment, evaluation and treatment.

MEMS can enable microneedles (needles orders of magnitude smaller than the conventional ones) for drug delivery, vaccine delivery and fluid sampling and analysis. These microneedles can be manufactured using a variety of materials including glass, ceramics, silicon, bio-compatible polymers and also water-soluble materials [19, 24]. Scanning electron microscope (SEM) photographs of e few microneedles are presented in Fig. 1.2. Authors in [25] carried out the first human study to show that microneedles are painless. 400 microneedles in an area of 3×3 mm used in this study. Each microneedle was approximately 150 μm tall with a base diameter of 80 μm and the tip radius curvature of 1 μm. Many commercialized microneedles have been developed for a variety of applications such as monitoring and controlling blood glucose levels, transdermal micro-projection delivery, and treating alopecia and skin restoration.

Minimally invasive surgery (MIS) is a type of procedure done to limit the size of incision (cut). Advantages of MIS are less scarring, less injury to tissue, shorter hospital stays and less pain. MEMS based microsurgical tools such as microtweezers, microsensors, and microgrippers have been ascertained as a central enabling technology for MIS. A pair of microgrippers and a temperature sensor embedded in robotic microgripper for surgical applications are shown in Fig. 1.2 [22]. One very important and revolutionary aspect of MEMS as a pressure sensor in MIS is to distinguish between different types of tissue during the surgery. This helps the surgeon to identify the proper tissue before making any incision. Menciassi et al. [26] reported a pioneering and an inventive MEMS device for the palpation of tissue using strain gauges. The realized microgripper apparatus was fabricated using an electroplated nickel covered with a thin gold layer, with an overall width of about 7.5 mm and a thickness of 0.4 mm. An overall displacement of 17 μm at the fingertips was achieved using flexure joints.

Photonics; the science of generating and harnessing light, are among the research fields touched by the MEMS technology. The pioneering paper of Petersen's on silicon scanner [27] galvanized the extensive interest in optical MEMS. Since then, optical MEMS have led to the development of MEMS tunable digital displays [28], deformable mirrors [29], tunable photonic crystal [30], adjustable lenses and apertures [31], endoscopic imaging devices [32], and optical telecommunication systems [33]. The application of optical MEMS scanning has resulted in miniaturized devices for biomedical applications such 3D imaging devices for in vivo diagnostics [34], MEMS based optical biopsy [35], and optical coherence tomography (OCT) systems [13, 32].

Figure 1.3 shows an optical MEMS enabled endoscopic OCT imaging system. Since its first demonstration by Pan et al. [37], MEMS based endoscopic devices have made significant progress and improvements and currently are being used a vast majority of endoscopic OCT imaging devices. Shown in Fig. 1.3b, is the first 3D endoscopic optical biopsy system. This device is capable of taking high-resolution, noninvasive in vivo clinical images. The integrated optical MEMS scanning micromirror exploits a 2D gimbal-less vertical comb and operates at resonant frequencies of 1.8 and 2.4 kHz in x and y directions respectively. Interested readers can refer to more comprehensive and dedicated textbooks and review papers for more in-depth discussion on fundamentals and recent advances in optical MEMS [3, 33, 38].

- Plasmonics (brief principle, physics and recent development)

Nanophotonics, the study of light at the nanoscale, has become a vibrant field of research, as the flow of light can be manipulated at length scales far below the optical wavelength, largely surpassing the classical limits imposed by diffraction. Driven by remarkable advances in micro/nanofabrication, atomic-resolution imaging, and ultrafast laser technologies, the interface between nanophotonics and MEMS has attested a tremendous progress in the past few years. Prime examples include compact systems for optical communication and interconnects [11, 39, 40], high resolution display [41], ultrafast cameras

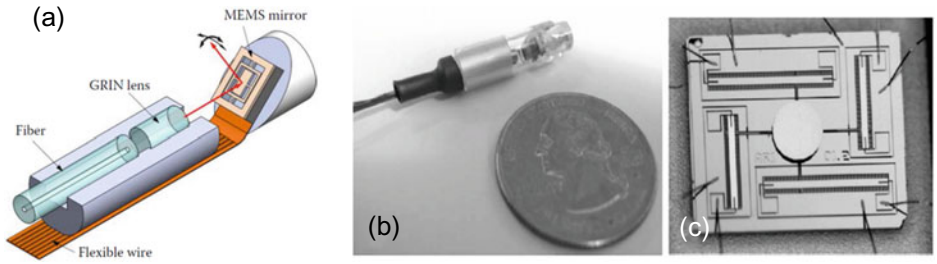

Fig. 1.3 **a** Schematic of a MEMS-tunable endoscopic OCT probe. **b** realized MEMS-based OCT probe. **c** Two-axis MEMS micromirror [36]

Fig. 1.4 Diffraction pattern appears as the distance between two optical emitters reduces and the radiation pattern of the two sources are indistinguishable

and photon detectors [42], and novel optical sensors for clinical and security concerns [43].

Conventional photonic devices are limited by diffraction. The diffraction limit is an optical effect which encumbers the progress toward the miniaturization of photonic devices by preventing localization of electromagnetic waves into nanoscale regions; scales much smaller than the wavelength. One important conclusion is that light will diffract when it propagates through a hole or a slit which is smaller than approximately half of its wavelength (Fig. 1.4).

The diffraction pattern follows a simple but intuitive formula. That is

$$d = \frac{\lambda}{2n\sin\theta} \triangleq \frac{\lambda}{2NA} \tag{1.1}$$

where n is the refractive index, θ is the angle of incidence, and NA is the numerical aperture of the lens.

Plasmonics, the study of the interaction between electromagnetic field and free electrons in a metal, provides a solution to this dilemma. In plasmonic devices, free electrons in the metal can be excited by the electric component of light to have collective oscillations. Using metallic and dielectric nanostructures precisely sculpted into two-dimensional (2D) and 3D nanoarchitectures, light can be scattered, refracted, confined, filtered, and processed in fascinating new ways that are impossible to achieve with natural materials and in conventional geometries. Strictly speaking, plasmonics; investigates plasmons; quanta of collective oscillations of the conduction electrons in a plasma. Plasmonics can squeeze light into dimensions far beyond the diffraction limit by coupling light with the surface collective oscillation of free electrons at the interface of a metal and a dielectric [44]. This control over light at the nanoscale has not only unveiled a plethora of new phenomena but has also led to a variety of relevant applications, including new venues for integrated circuitry, optical computing, solar, and medical technologies, setting high expectations for many novel discoveries in the years to come.

Four classical types of plasmons include, surface plasmon polaritons (SPPs), surface plasmon resonances (SPRs), localized surface plasmons (LSPs), and spoof plasmons.

SPPs result from the interaction of excited electrons with polarized light at the interface between a negative and positive permittivity materials. SPPs are propagating modes with well-defined frequency and wavevector and are evanescently confined in the direction

perpendicular to the propagation. This interaction gives rise to a new type of quasi-particle called polaritons. Polaritons originate from strong light-matter interaction (strong confinement) [45].

SPRs refers to resonances instigating from the collective oscillations of electrons in metals at the interface due to Coulombic interaction with positive background. To excite SPPs, polarized incident photons (light must be polarized to excite the longitudinal mode) and SPRs must have the same frequency and wave vector.

LSPs are generated when electromagnetic field interacts with conduction electrons on the surface of a conductive nanoparticle of size comparable to or smaller than the excitation wavelength. LSPs are non-propagating excitations.

Metals have negative permittivity in the Visible and Ultraviolet regimes of the electromagnetic spectrum, thus support surface plasmons. However, when the wavelength is increased to the Infrared (IR) and Terahertz (THz) regions metals act as perfect electric conductors (PEC). Spoof plasmons are guided leaky waves in the IR and THz regions which can be recognized in metal surfaces patterned with periodic subwavelength grooves, holes and nanowires [46]. A wide selection of materials can support surface plasmons. Please see [47–49] for comprehensive review on plasmonic materials.

Tunable functionality of plasmonic devices is of outmost importance for realizing active and reconfigurable optoelectronic devices. Several modulation techniques can be used to achieve tunable response from plasmonic devices including electrical, optical, and mechanical modulation [50]. Active manipulation of surface plasmons provides a course to tweak the optical functionalities of the plasmonic structure and could be used in light modulators, plasmonic switches and spectrometers to name a few.

1.2 Plasmonic MEMS: A Frontier of Photonic Devices

Plasmonic MEMS is a rising field, inspired by the concepts of optical metamaterials and the peculiar features of plasmonic nanopatterns. Low-profile patterned plasmonic surfaces are synergized with a broad class of silicon microstructures, to greatly enhance near-field nanoscale imaging, sensing and energy harvesting coupled with far-field free-space detection. The concept has demonstrated impact on several key areas from ultra-compact Microsystems for sensitive detection of small number of target molecules, and “surface” as devices for optical data storage to microimaging and displaying.

Plasmonic MEMS is evolving into a novel paradigm for the conception of optical plasmonic surfaces. Depending on the intrinsic material properties, different materials response distinctively to the applied voltage. This will allow a wide variety of plasmonic structure to be placed on electromechanically modulated substrate to control their optical spectrum. The idea is schematically shown in Fig. 1.5a. Another option, is to directly pattern a plasmonic grating or structure on the surface of a MEMS device as shown in Fig. 1.5b.

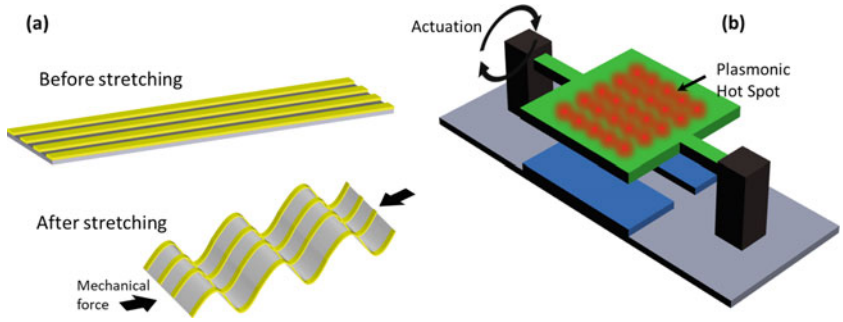

Fig. 1.5 Plasmonic MEMS. **a** Mechanical modulation of a plasmonics grating via stretchable substrate. **b** Integration of a plasmonic array with a MEMS device

The first experimental demonstration of electromechanically reconfigurable plasmonic structures was reported in 2013 by Ou and colleagues [51], in which they designed a reconfigurable plasmonic metamaterial operating in the near-infrared (NIR). Arrays of 50-nm-thick gold meander wires and near parallel gold wires was etched on a 50-nm-thick silicon nitride substrate by focused ion beam (FIB), (details of the fabrication method are explained in Chap. 3). To provide a flexible and robust platform to contain the gold pattern, the silicon nitride substrate is cut into 500 and 250 nm strings for the meander wires and parallel gold wires, respectively. The SEM of the structure with total dimensions of 12 mm $\times$ 35 mm is shown in Fig. 1.6a.

The major idea is to exploit the instigating electrostatic forces upon applying electric voltage to mechanically modulate the optical response of the patterned metamaterial. As it can be seen in Fig. 1.6c, applying a small voltage can decrease the gap between the meander wires and parallel wires. This dramatically affects the optical response of the transmitted wave.

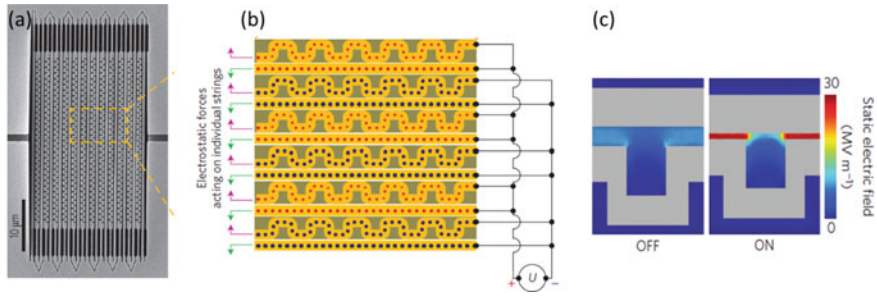

Fig. 1.6 First demonstration of an electrostatically actuated tunable plasmonic metamaterial. (**a**) SEM image (**b**) electrostatic forces acting on individual strings (**c**) static electric field simulations

The first thermomechanicaly tunable plasmonic MEMS device was reported in 2011 by the pioneering work of Ou et al. [52]. The device consists of gold plasmonic split-ring resonators (SRRs) supported by interchanging thermally tunable silicon nitride/gold bridges (silicon nitride and gold both have large thermal expansion coefficient). Their realized photonic metamaterial device operates three orders of magnitude faster than formerly reached modulation rate for the NIR spectrum. Potential applications of the device include tunable sensors, modulators, and spectral filters.

The first light-controlled plasmonic MEMS device was attained in the NIR regime via patterning asymmetrically spaced gold elements on silicon nitride strips [53]. The authors demonstrated that through pump-probe experiment with ultrafast laser diodes operating at 1550 and 1310 nm, large modulation of transmission can be achieved with milliwatt power levels. The photo-addressable capacitance can be cooled down in high-speed timescales on the order of 20 μs. Light modulated plasmonic devices can be used to realize reconfigurable nonlinear metadevices.

In summary, the paradigm of plasmonic MEMS enables low-profile conformal surfaces on microdevices, rather than a bulk material or coatings, which may provide clear advantages for the physical, chemical and biological-related sensing, imaging, light harvesting applications in addition to significantly easier realization, enhanced flexibility and tunability.

1.3 Status of the Field

In last few years, Plasmonic MEMS has developed tremendously. A summary of some landmark papers in the field are presented in Table 1.1. A more comprehensive table can be found in Appendix 1.

Despite recent advances in the field and the growing number of published works, many more ideas need to be explored. We believe that the tremendous obtainable opportunities in combining plasmonics with MEMS still remains largely underexploited and underexplored. Almost all current plasmonic MEMS devices and architectures exploit conventional metal plasmonics. We predict the field to branch out towards combining highly doped semiconductors as a plasmonic material for the Infrared and THz region. This indeed can instigate fields beyond plasmonics MEMS and give birth to fields such as epsilon-near zero (ENZ) MEMS.

Beside using metallic or highly doped semiconductor resonator, dielectric Mie resonators can also be integrated with MEMS technology to realized highly localized fields and tunable dielectric metamaterials and metasurfaces.

Table 1.1 Landmark papers in the field of plasmonic MEMS

Device	Control mechanism	Importance	Material	Fabrication method	Application	Year
Flexible plasmonics	Mechanical force	First demonstration of a flexible plasmonic device	PDMS substrate, gold nanorod	Electron beam lithography	Flexible, stretchable, nonplanar electronic and photonic systems	2010 [54]
Reconfigurable metamaterials	Thermomechanical	First demonstration of a thermomechanical plasmonic device	Silicon nitride membrane, gold	Focused ion beam	Reversible and large-range tunable metamaterials	2011 [52]
Reconfigurable metamaterials	Electromechanical	First demonstration of an electrostatic plasmonic device	Silicon nitride substrate, gold wires	Focused ion beam	Tunable spectral filters, switches, and modulators	2013 [51]
Tunable modulator	Optomechanical	First demonstration of an optomechanical plasmonic device	Gold on silicon nitride strips	Focused ion beam	Modulating light with light	2015 [53]

1.4 Existing Challenges

Emerging concepts, designs and applications of plasmonic MEMS have been demonstrated in the recent years, ranging from plasmonic gas and chemical sensors, microfilters for circulating tumor cells (CTC) capturing, DNA biosensing among many others. Fascinating new concepts explored in detail in the framework of this review, with the goal to devise new geometries on MEMS surfaces that may for example require no moving structures to tilt the radiated beam in the desired direction. We expect that the combination of design theory, modeling and experimental implementation may provide full degrees of freedom and enhanced performance for future plasmonic MEMS designs for specific applications.

Although many promising results have been reported, several challenges remain untouched. These challenges can be considered in three aspects.

1. Materials innovation are much needed to provide seamlessly integrated mechanical, optical, materials properties suitable for plasmonic MEMS; Emerging computational materials design approaches may be used to guide the development of new materials with unique properties for plasmonic operation under various physical and chemical conditions. In addition, just as the electronic devices, the performance of optical devices can be influenced by material stress and strain degradation. New materials to prevent large degradation of MEMS devices need to be realized. Also, Plasmonic MEMS for bioelectronic and bioengineering applications appear to be one of the most persuasive areas. The interface between devices and biology needs to be well considered, for example, for needed biocompatibility while maintaining core device functionalities.
2. New design strategies, through theoretical modeling and numerical simulations, enable fast, high throughput and flexible operations; high energy consumption of MEMS devices compared to the electronic counterparts hinder their path for large scale integration. Reducing the energy consumption of plasmonic MEMS devices demands urgent attention. While, megahertz modulation rates have been demonstrated and reported in the literature, faster modulation in the order of gigahertz is required. New design strategies might be able to push the field towards higher modulation rates.
3. Micro-nanofabrication advancement combined with smart geometric mechanics for compact implementation; patterning flexible plasmonic substrates with new design paradigms such as Origami and Kirigami needs to be explored. This can also open up new directions to realize high-contrast switching of plasmonic MEMS devices.

In this book, we discuss the theory, fabrication, and application of plasmonic MEMS and the recent progresses in the field for biosensing applications. We believe that the optical plasmonic surface on MEMS concept may constitute the much sought flexible and reliable bridge between near-field sensing, imaging at the nanoscale and far-field detection. In our

vision, these concepts may be combined to realize a fascinating paradigm to manipulate light at will with a clear impact on several key areas of interest for MEMS in the broad area of sensing, imaging, light harvesting applications in addition to significantly easier realization, enhanced flexibility and tunability.

References

1. M. Tanaka, "An industrial and applied review of new MEMS devices features," *Microelectronic Engineering,* vol. 84, pp. 1341–1344, 2007/05/01/ 2007.
2. S. Yang and Q. Xu, "A review on actuation and sensing techniques for MEMS-based microgrippers," *Journal of Micro-Bio Robotics,* vol. 13, pp. 1-14, October 01 2017.
3. O. Solgaard, *Photonic microsystems: Micro and nanotechnology applied to optical devices and systems*: Springer Science & Business Media, 2009.
4. H. T. Chorsi, M. T. Chorsi, and S. D. Gedney, "A Conceptual Study of Microelectromechanical Disk Resonators," *IEEE Journal on Multiscale and Multiphysics Computational Techniques,* vol. 2, pp. 29-37, 2017.
5. M. T. Chorsi and H. T. Chorsi, "Modeling and analysis of MEMS disk resonators," *Microsystem Technologies,* vol. 24, pp. 2517-2528, June 01 2018.
6. S. Tabatabaei and A. Partridge, "Silicon MEMS Oscillators for High-Speed Digital Systems," *IEEE Micro,* vol. 30, pp. 80-89, 2010.
7. C. A. Musca, J. Antoszewski, K. J. Winchester, A. J. Keating, T. Nguyen, K. K. M. B. D. Silva*, et al.*, "Monolithic integration of an infrared photon detector with a MEMS-based tunable filter," *IEEE Electron Device Letters,* vol. 26, pp. 888-890, 2005.
8. J. Sha, W. Chen, K. Yan, J. Luo, R. Xu, D. Yao*, et al.*, "Tunable Metamaterial IR Emitter by Using MEMS Microheater," in *2018 International Conference on Optical MEMS and Nanophotonics (OMN)*, 2018, pp. 1–2.
9. M. Mihailovic, T. V. Mathew, J. F. Creemer, B. T. C. Zandbergen, and P. M. Sarro, "MEMS silicon-based resistojet micro-thruster for attitude control of nano-satellites," in *2011 16th International Solid-State Sensors, Actuators and Microsystems Conference*, 2011, pp. 262–265.
10. J. Wendel, O. Meister, C. Schlaile, and G. F. Trommer, "An integrated GPS/MEMS-IMU navigation system for an autonomous helicopter," *Aerospace Science and Technology,* vol. 10, pp. 527–533, 2006/09/01/ 2006.
11. M. C. Wu, O. Solgaard, and J. E. Ford, "Optical MEMS for Lightwave Communication," *Journal of Lightwave Technology,* vol. 24, pp. 4433-4454, 2006.
12. Y. Wang, S. Bish, J. W. Tunnell, and X. J. Zhang, "MEMS scanner enabled real-time depth sensitive hyperspectral imaging of biological tissue," *Optics Express,* vol. 18, pp. 24101–24108, 2010/11/08 2010.
13. K. Karthik, C. C. Jonathan, M. Austin, J. K. Nate, H. Kazunori, E. M. Thomas*, et al.*, "Fast 3D in vivo swept-source optical coherence tomography using a two-axis MEMS scanning micromirror," *Journal of Optics A: Pure and Applied Optics,* vol. 10, p. 044013, 2008.
14. Y. Wang, S. Bish, J. W. Tunnell, and X. J. Zhang, "MEMS scanner based handheld fluorescence hyperspectral imaging system," *Sensors and Actuators A: Physical,* vol. 188, pp. 450–455, 2012/12/01/ 2012.
15. M. Leonardi, E. M. Pitchon, A. Bertsch, P. Renaud, and A. Mermoud, "Wireless contact lens sensor for intraocular pressure monitoring: assessment on enucleated pig eyes," *Acta Ophthalmologica,* vol. 87, pp. 433-437, 2009.

16. Available: https://www.sensimed.ch/
17. W. Youmin, R. Milan, H. S. McGuff, B. Gauri, Y. Bin, S. Ting, *et al.*, "Portable oral cancer detection using a miniature confocal imaging probe with a large field of view," *Journal of Micromechanics and Microengineering,* vol. 22, p. 065001, 2012.
18. P. Zhang, C. Dalton, and G. A. Jullien, "Design and fabrication of MEMS-based microneedle arrays for medical applications," *Microsystem Technologies,* vol. 15, pp. 1073-1082, July 01 2009.
19. E. Larrañeta, R. E. M. Lutton, A. D. Woolfson, and R. F. Donnelly, "Microneedle arrays as transdermal and intradermal drug delivery systems: Materials science, manufacture and commercial development," *Materials Science and Engineering: R: Reports,* vol. 104, pp. 1–32, 2016/06/01/ 2016.
20. A. P. Lee, D. R. Ciarlo, P. A. Krulevitch, S. Lehew, J. Trevino, and M. A. Northrup, "A practical microgripper by fine alignment, eutectic bonding and SMA actuation," *Sensors and Actuators A: Physical,* vol. 54, pp. 755–759, 1996/06/01/ 1996.
21. M. Kumemura, D. Collard, S. Yoshizawa, D. Fourmy, N. Lafitte, L. Jalabert, *et al.*, "Direct biomechanical sensing of enzymatic reaction On DNA by silicon nanotweezers," in *2010 IEEE 23rd International Conference on Micro Electro Mechanical Systems (MEMS)*, 2010, pp. 915–918.
22. R. K. J, "Applications of MEMS in surgery," *Proceedings of the IEEE,* vol. 92, pp. 43–55, 2004.
23. W. P. Eaton and J. H. Smith, "Micromachined pressure sensors: review and recent developments," *Smart Materials and Structures,* vol. 6, p. 530, 1997.
24. R. F. Donnelly, T. R. R. Singh, and A. D. Woolfson, "Microneedle-based drug delivery systems: Microfabrication, drug delivery, and safety," *Drug Delivery,* vol. 17, pp. 187–207, 2010/05/01 2010.
25. S. Kaushik, A. H. Hord, D. D. Denson, D. V. McAllister, S. Smitra, M. G. Allen, *et al.*, "Lack of Pain Associated with Microfabricated Microneedles," *Anesthesia & Analgesia,* vol. 92, pp. 502-504, 2001.
26. A. Menciassi, A. Eisinberg, G. Scalari, C. Anticoli, M. C. Carrozza, and P. Dario, "Force feedback-based microinstrument for measuring tissue properties and pulse in microsurgery," in *Proceedings 2001 ICRA. IEEE International Conference on Robotics and Automation (Cat. No.01CH37164)*, 2001, pp. 626–631 vol. 1.
27. K. E. Petersen, "Silicon Torsional Scanning Mirror," *IBM Journal of Research and Development,* vol. 24, pp. 631-637, 1980.
28. C. Liao and J. Tsai, "The Evolution of MEMS Displays," *IEEE Transactions on Industrial Electronics,* vol. 56, pp. 1057-1065, 2009.
29. T. Bifano, "MEMS deformable mirrors," *Nature Photonics,* vol. 5, p. 21, 01/01/online 2011.
30. Y. H. Cui, Q. Wu, W. Park, J. Jeon, M. J. Kim, and J. Lee, "Mems-based mechanically tunable flexible photonic crystal," in *TRANSDUCERS 2009 - 2009 International Solid-State Sensors, Actuators and Microsystems Conference*, 2009, pp. 509–512.
31. Y. Zou, W. Zhang, F. S. Chau, and G. Zhou, Miniature adjustable-focus endoscope using a MEMS Alvarez lens, in *2015 International Conference on Optical MEMS and Nanophotonics (OMN)*, 2015, pp. 1–2.
32. J. Sun and H. Xie, "MEMS-Based Endoscopic Optical Coherence Tomography," *International Journal of Optics,* vol. 2011, 2011.
33. O. Solgaard, A. A. Godil, R. T. Howe, L. P. Lee, Y. Peter, and H. Zappe, "Optical MEMS: From Micromirrors to Complex Systems," *Journal of Microelectromechanical Systems,* vol. 23, pp. 517-538, 2014.

34. W. Piyawattanametha, E. D. Cocker, L. D. Burns, R. P. J. Barretto, J. C. Jung, H. Ra*, et al.*, "In vivo brain imaging using a portable 2.9 g two-photon microscope based on a microelectromechanical systems scanning mirror," *Optics Letters,* vol. 34, pp. 2309–2311, 2009/08/01 2009.
35. D. T. McCormick, W. Jung, Y. Ahn, Z. Chen, and N. C. Tien, "A Three Dimensional Real-Time MEMS Based Optical Biopsy System for In-Vivo Clinical Imaging," in *TRANSDUCERS 2007 - 2007 International Solid-State Sensors, Actuators and Microsystems Conference*, 2007, pp. 203–208.
36. W. Jung, D. T. McCormick, Y.-C. Ahn, A. Sepehr, M. Brenner, B. Wong*, et al.*, "In vivo three-dimensional spectral domain endoscopic optical coherence tomography using a microelectromechanical system mirror," *Optics Letters,* vol. 32, pp. 3239–3241, 2007/11/15 2007.
37. Y. Pan, H. Xie, and G. K. Fedder, "Endoscopic optical coherence tomography based on a microelectromechanical mirror," *Optics Letters,* vol. 26, pp. 1966–1968, 2001/12/15 2001.
38. G. Zhou and C. Lee, *Optical MEMS, Nanophotonics, and Their Applications*: CRC Press, 2017.
39. J. E. Ford, V. A. Aksyuk, D. J. Bishop, and J. A. Walker, "Wavelength Add-Drop Switching Using Tilting Micromirrors," *Journal of Lightwave Technology,* vol. 17, p. 904, 1999/05/01 1999.
40. D. J. Bishop, C. R. Giles, and G. P. Austin, "The Lucent LambdaRouter: MEMS technology of the future here today," *IEEE Communications Magazine,* vol. 40, pp. 75-79, 2002.
41. J. Ma, "Advanced MEMS-based technologies and displays," *Displays,* vol. 37, pp. 2–10, 2015/04/01/ 2015.
42. F. Niklaus, C. Vieider, and H. Jakobsen, "MEMS-based uncooled infrared bolometer arrays: a review," in *Photonics Asia 2007*, 2008, p. 15.
43. X. J. Zhang, S. Zappe, R. W. Bernstein, O. Sahin, C. C. Chen, M. Fish*, et al.*, "Micromachined silicon force sensor based on diffractive optical encoders for characterization of microinjection," *Sensors and Actuators A: Physical,* vol. 114, pp. 197–203, 2004/09/01/ 2004.
44. J. A. Schuller, E. S. Barnard, W. Cai, Y. C. Jun, J. S. White, and M. L. Brongersma, "Plasmonics for extreme light concentration and manipulation, *Nat Mater,*" vol. 9, pp. 193–204, 03//print 2010.
45. D. N. Basov, M. M. Fogler, and F. J. García de Abajo, "Polaritons in van der Waals materials," *Science,* vol. 354, 2016.
46. R. Stanley, "Plasmonics in the mid-infrared," *Nature Photonics,* vol. 6, p. 409, 06/28/online 2012.
47. A. Boltasseva and H. A. Atwater, "Low-Loss Plasmonic Metamaterials," *Science,* vol. 331, pp. 290-291, 2011.
48. P. R. West, S. Ishii, G. V. Naik, N. K. Emani, V. M. Shalaev, and A. Boltasseva, "Searching for better plasmonic materials," *Laser & Photonics Reviews,* vol. 4, pp. 795-808, 2010.
49. G. V. Naik, V. M. Shalaev, and A. Boltasseva, "Alternative Plasmonic Materials: Beyond Gold and Silver," *Advanced Materials,* vol. 25, pp. 3264-3294, 2013.
50. N. I. Zheludev and E. Plum, "Reconfigurable nanomechanical photonic metamaterials," *Nature Nanotechnology,* vol. 11, p. 16, 01/07/online 2016.
51. J.-Y. Ou, E. Plum, J. Zhang, and N. I. Zheludev, "An electromechanically reconfigurable plasmonic metamaterial operating in the near-infrared," *Nature Nanotechnology,* vol. 8, p. 252, 03/17/online 2013.
52. J. Y. Ou, E. Plum, L. Jiang, and N. I. Zheludev, "Reconfigurable Photonic Metamaterials," *Nano Letters,* vol. 11, pp. 2142–2144, 2011/05/11 2011.
53. J.-Y. Ou, E. Plum, J. Zhang, and N. I. Zheludev, "Modulating light with light via giant nano-opto-mechanical nonlinearity of plasmonic metamaterial," *arXiv preprint* arXiv:1506.05852*,* 2015.

54. I. M. Pryce, K. Aydin, Y. A. Kelaita, R. M. Briggs, and H. A. Atwater, "Highly Strained Compliant Optical Metamaterials with Large Frequency Tunability," *Nano Letters,* vol. 10, pp. 4222–4227, 2010/10/13 2010.

Theoretical Foundations

2

This chapter provides the fundamentals of electromagnetic theory for the book in relation to plasmonic MEMS. First, a brief review of Maxwell's equations is provided. This is followed by a discussion of general surface waves, dielectric constant of metals, and plasmon dispersion. The next sections of the chapter focus on the intersection of memes and plasmonics and reviews the theories relevant to plasmonics MEMS in the literature.

2.1 Maxwell's Equations and Electromagnetic Wave Theory

Considering the classical and semi-classical wave nature of light, Maxwell's equations in a conventional macroscopic framework can be used to fully describe the electromagnetic wave interaction with metals. In differential form, Maxwell's equations can be written as

$$\nabla \times \vec{\mathrm{E}}(\mathbf{r}, t) = -\frac{\partial \vec{\mathrm{B}}(\mathbf{r}, t)}{\partial t}, \tag{2.1}$$

$$\nabla \times \vec{\mathrm{H}}(\mathbf{r}, t) = \frac{\partial \vec{\mathrm{D}}(\mathbf{r}, t)}{\partial t} + \vec{\mathrm{J}}(\mathbf{r}, t), \tag{2.2}$$

$$\nabla \cdot \vec{\mathrm{D}}(\mathbf{r}, t) = \rho(\mathbf{r}, t), \tag{2.3}$$

$$\nabla \cdot \vec{\mathrm{B}}(\mathbf{r}, t) = 0, \tag{2.4}$$

These equations couple the four macroscopic fields D (the electric flux density), E (the electric field), H (the magnetic field), and B (the magnetic flux density) with the charge density (ρ) and current densities ($\mathrm{J} = \mathrm{J_c}$ (conduction current density) + $\mathrm{J_i}$ (induction current density) + $\mathrm{J_d}$ (displacement current density)). In macroscopic frame, current density

© The Author(s), under exclusive license to Springer Nature Switzerland AG 2023

J. X. J. Zhang, *Plasmonic MEMS*, Synthesis Lectures on Materials and Optics,
https://doi.org/10.1007/978-3-031-23137-7_2

is expressed as the product of charge density and velocity for any location in space

$$\vec{\mathrm{J}}(\mathbf{r}, t) = \rho(\mathbf{r}, t)v \tag{2.5}$$

In time domain, fields can be related via the constitutive relations

$$\vec{\mathrm{D}}(\mathbf{r}, t) = \varepsilon_0 \vec{\mathrm{E}}(\mathbf{r}, t) + \vec{\mathrm{P}}(\mathbf{r}, t), \tag{2.6}$$

$$\vec{\mathrm{H}}(\mathbf{r}, t) = \mu_0^{-1} \vec{\mathrm{B}}(\mathbf{r}, t) - \vec{\mathrm{M}}(\mathbf{r}, t), \tag{2.7}$$

where ε_0 [Farads/meter] and μ_0 [Henries/meter] are the permittivity and the permeability of the vacuum, respectively. For an isotropic, linear, and nonmagnetic approximation, the constitutive relations can be written as:

$$\vec{\mathrm{D}}(\mathbf{r}, t) = \varepsilon_0 \varepsilon_r \vec{\mathrm{E}}(\mathbf{r}, t), \tag{2.8}$$

$$\vec{\mathrm{B}}(\mathbf{r}, t) = \mu_0 \mu_r \vec{\mathrm{H}}(\mathbf{r}, t), \tag{2.9}$$

where ε_r and μ_r are the relative permittivity and relative permeability, respectively. the electric polarization P and magnetization M consider the properties of the medium. The conduction current density $\mathrm{J_c}$ is related to the electric field using

$$J_c = \sigma E \tag{2.10}$$

where σ [siemens/meter] is the conductivity of the medium.

To derive the wave equation, we take the curl of Eq. (2.1). Using Eq. (2.2), for a source-free region, the wave equation can be written as

$$\nabla^2 \vec{\mathrm{E}}(\mathbf{r}, t) = \mu\varepsilon \frac{\partial^2 \vec{\mathrm{E}}(\mathbf{r}, t)}{\partial t^2}, \tag{2.11}$$

Here ε and μ are the electric permittivity (also called absolute permittivity, $\varepsilon = \varepsilon_0\varepsilon_r$) and magnetic permeability ($\mu = \mu_0\mu_r$). Equation (2.11) is actually three equations, which together comprise the x-, y- and z-vector components for the E field vector. The Laplacian in Cartesian coordinates is defined as

$$\nabla^2 \vec{\mathrm{E}} = \frac{\partial^2 \vec{\mathrm{E}}}{\partial x^2} + \frac{\partial^2 \vec{\mathrm{E}}}{\partial y^2} + \frac{\partial^2 \vec{\mathrm{E}}}{\partial z^2}, \tag{2.12}$$

The monochromatic solution (a set of complex-traveling wave solutions) to this wave equation has the following form

$$\vec{\mathrm{E}}(\mathbf{r}, t) = E_0 e^{j(\omega t - k.\vec{\mathrm{r}})}, \tag{2.13}$$

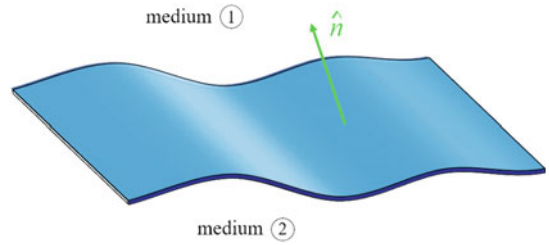

Fig. 2.1 Boundary surface of two media with tangential and normal components

$$\mathrm{Re}\{e^{j(\omega t - k.\vec{\mathrm{r}})}\} = e^{-\alpha.\vec{\mathrm{r}}}\cos(\omega t - \beta.\vec{\mathrm{r}}), \tag{2.14}$$

where α quantifies attenuation, β is the propagation constant, $\omega = kc$ with $c = 1/\sqrt{\varepsilon_0\mu_0}$ being the speed of light, and $\frac{\omega}{k} = v_{phase}$ is the phase velocity. The relation between the phase velocity and the frequency is known as the dispersion relation.

Boundary conditions state how the electromagnetic fields (E, D, H, B) change at the interface between two different materials (Fig. 2.1).

$$\hat{n} \times (\mathrm{E}_1 - \mathrm{E}_2) = 0 \tag{2.15}$$

$$\hat{n} \times (\mathrm{H}_1 - \mathrm{H}_2) = J_{im} \tag{2.16}$$

$$\hat{n} \cdot (\mu_1\mathrm{H}_1 - \mu_2 H_2) = 0 \tag{2.17}$$

$$\hat{n} \cdot (\mu_1\mathrm{E}_1 - \mu_2\mathrm{E}_2) = \rho_s \tag{2.18}$$

where J_{im} and ρ_s are the impressed electric current and surface charge density, respectively. The first two of these state that the tangential electric fields are continuous across the interface, though the tangential magnetic fields are discontinuous at the same location by an amount equal to the impressed electric current. Zenneck [1], more than a century ago, solved the Maxwell's equations for the planar interface of two different materials and initiated the concept of surface waves. A surface wave is an electromagnetic wave with parallel Poynting vector that propagates along a surface or an interface of two dissimilar media. The propagation of a surface wave is guided by the planar interface and decays exponentially in both media. Surface waves play a key role in studying properties of condensed matter at the interface. A more inclusive and mathematically rigorous derivation of surface waves was later done by Sommerfeld [2], and those surface waves have since become known as the Zenneck waves.

Equations (2.15) through (2.18) can be used to compute the fraction of a light wave reflected and transmitted by a flat interface between two media with different refractive indices (Fig. 2.2).

Applying the boundary conditions to a simple plane wave incident on a single planar interface leads to the Fresnel reflection and transmission coefficients. For TE case, tangential electric field is continuous at the boundary,

$$\mathrm{E}_i(y=0,t)+\mathrm{E}_r(y=0,t)=\mathrm{E}_t(y=0,t) \tag{2.19}$$

The tangential magnetic field is continuous

$$\mathrm{B}_i(y=0,t)\cos\theta_i+\mathrm{B}_r(y=0,t)\cos\theta_r=\mathrm{B}_t(y=0,t)\cos\theta_t \tag{2.20}$$

Using the constitutive relations and considering only the amplitude of the waves (E_0) at the boundary, the following relations can be derived for the reflection and transmission coefficient of TE and TM polarized waves

$$r_{TE}=r_\perp=\frac{\mathrm{E}_{0r}}{\mathrm{E}_{0i}}=\frac{n_i\cos\theta_i-n_t\cos\theta_t}{n_i\cos\theta_i+n_t\cos\theta_t} \tag{2.21}$$

$$t_{TE}=t_\perp=\frac{\mathrm{E}_{0t}}{\mathrm{E}_{0i}}=\frac{2n_i\cos\theta_i}{n_i\cos\theta_i+n_t\cos\theta_t} \tag{2.22}$$

$$r_{TM}=r_\parallel=\frac{\mathrm{E}_{0r}}{\mathrm{E}_{0i}}=\frac{n_t\cos\theta_i-n_i\cos\theta_t}{n_i\cos\theta_t+n_t\cos\theta_i} \tag{2.23}$$

$$t_{TM}=t_\parallel=\frac{\mathrm{E}_{0t}}{\mathrm{E}_{0i}}=\frac{2n_i\cos\theta_i}{n_i\cos\theta_t+n_t\cos\theta_i} \tag{2.24}$$

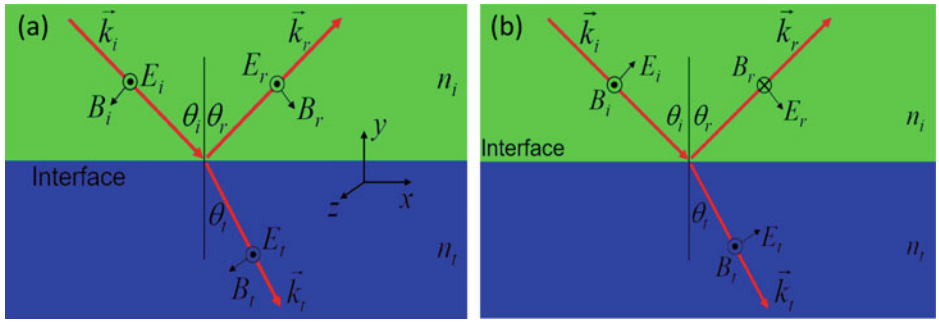

Fig. 2.2 Fresnel reflection and transmission coefficients. **a** TE, perpendicular, s-polarized. **b** TM, parallel, p-polarized, ("s" polarization (aka TE or horizontal) has an E field that is perpendicular to the plane of incidence, "p" polarization (aka TM or vertical) has an E field that is parallel to the plane of incidence), s and p stand for the German words senkrecht (perpendicular) and parallel (parallel)

where n_i and n_t are the refractive indices of the incident and reflected medium. A plot of Fresnel reflection and transmission coefficients for n = 1.5 is shown in Fig. 2.3.

At some angle, known as the critical angle, light traveling from a higher refractive index medium to a lower refractive index medium will be refracted at 90º. When the angle of incidence exceeds the critical angle, there is no refracted light. All the incident light is reflected back into the medium. The critical angle of incidence can be obtained for two media

$$\sin\theta_c = \frac{n_2}{n_1}, \quad n_1 > n_2 \tag{2.25}$$

Dielectric constant (relative permittivity) is a measure of the polarizability of a material and can be derived using the Lorentz model and the Drude model for dielectric and metallic materials, respectively. By solving the standard equation of motion for a harmonically bound classical electron, in analogy to the motion of a mass on a spring, we obtain the displacement $r(t) = r_0 e^{-i\omega t}$

$$m_e \frac{\partial^2 r}{\partial t^2} + m_e \gamma_d \frac{\partial r}{\partial t} = eE_0 e^{-i\omega t}, \tag{2.26}$$

where e and m_e are the charge and effective mass of the free electrons, and E_0 and ω are the amplitude and frequency of the applied electric field (actuation force). The damping term γ_d is proportional to $\gamma_d = v_F/l$, where v_F is the Fermi velocity and l is the electron mean free path between scattering events.

Applying Fourier transform, $F(r(t))$, we obtain $r(\omega)$. Using $r(\omega)$ and polarization vector, Lorentz equation can be derived as

$$\varepsilon_m(\omega) = \varepsilon_\infty + \frac{\omega_p^2}{\omega_0^2 - \omega^2 - j\gamma_d\omega}, \quad \omega_p = \sqrt{\frac{4\pi n_e e^2}{m_e}}, \tag{2.27}$$

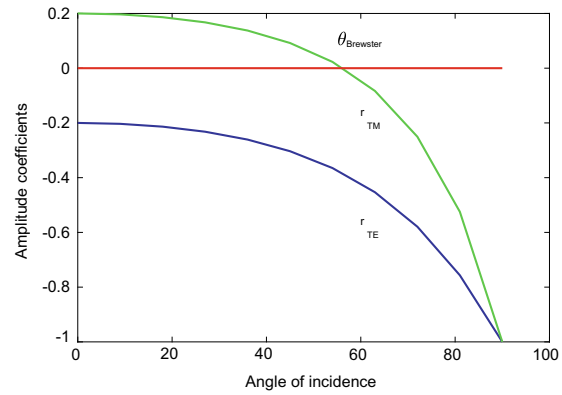

Fig. 2.3 Reflections of TE and TM modes for n = 1.5. Brewster's angle ($r_{TM} = 0$) is also plotted

here ω_p is the plasma frequency, ω_0 is the frequency of the restoring force, and ε_∞ describes the ionic background. Assuming the free electron model for metal ($\omega_0 = 0$), Drude model can be obtained using

$$\varepsilon_m(\omega) = \varepsilon_\infty - \frac{\omega_p^2}{\omega^2 + j\gamma_d\omega}, \tag{2.28}$$

If ω is larger than ω_p, corresponding refractive index is a real quantity, on the other hand if ω is smaller than ω_p, refractive index is imaginary since ε_m is negative.

The real and imaginary parts of the susceptibility are connected by the Kramers-Kroenig relations (KKR).

$$\varepsilon_r(\omega) = 1 + \frac{2}{\pi}\wp\int_0^\infty \frac{\omega'\varepsilon_i(\omega')d\omega'}{\omega'^2 - \omega^2}, \tag{2.29}$$

$$\varepsilon_i(\omega) = -\frac{2\omega}{\pi}\wp\int_0^\infty \frac{\varepsilon_r(\omega')d\omega'}{\omega'^2 - \omega^2}, \tag{2.30}$$

Here $\wp$ means the principal value of the integral.

Surface plasmons are surface waves that are the solution of Maxwell's equations. The simplest geometry supporting SPPs is a single, planar interface between a metal, with a negative dielectric constant ε_m, (metals at THz region have negative real permittivity as shown in Fig. 2.4) and a dielectric, with a positive dielectric constant as illustrated in Fig. 2.5. This is a critical criterion since in this situation wave can effectively penetrate inside the metal.

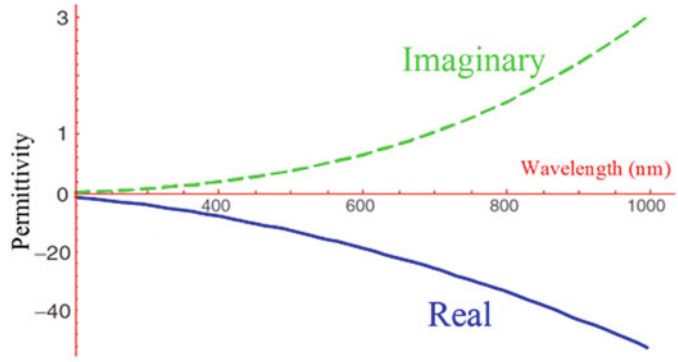

Fig. 2.4 Real and imaginary parts of the dielectric constant for gold in visible range of the wavelength according to the Drude model

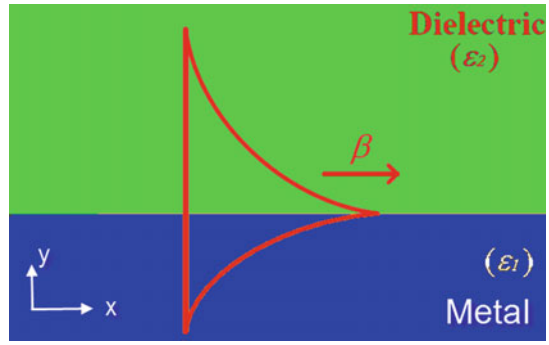

Fig. 2.5 Schematic view of surface wave propagating along a single metal–dielectric interface

Considering TM excitation (H_z, E_x, and E_y) and propagation along the x-direction, i.e. $\partial/\partial x = i\beta$,

$$E_x = i\frac{1}{\omega\varepsilon_0\varepsilon}\frac{\partial H_z}{\partial y} \tag{2.31}$$

$$E_y = \frac{\beta}{\omega\varepsilon_0\varepsilon}H_z \tag{2.32}$$

$$\frac{\partial^2 H_z}{\partial y^2} + (k_0^2\varepsilon - \beta^2)H_z = 0 \tag{2.33}$$

Equation (2.31) through (2.33) can be expanded separately for each region in Fig. 2.5. For the dielectric region, i.e. y > 0,

$$H_z(y) = A_2\, e^{i\beta x} e^{-k_2 y} \tag{2.34}$$

$$E_x(y) = -iA_2\frac{k_2}{\omega\varepsilon_0\varepsilon_2}\, e^{i\beta x} e^{-k_2 y} \tag{2.35}$$

$$E_y(y) = A_2\frac{\beta}{\omega\varepsilon_0\varepsilon_2}\, e^{i\beta x} e^{-k_2 y} \tag{2.36}$$

and for the metallic region, i.e. y > 0,

$$H_z(y) = A_1\, e^{i\beta x} e^{k_1 y} \tag{2.37}$$

$$E_x(y) = iA_1\frac{k_1}{\omega\varepsilon_0\varepsilon_1}\, e^{i\beta x} e^{k_1 y} \tag{2.38}$$

$$E_y(y) = A_1\frac{\beta}{\omega\varepsilon_0\varepsilon_1}\, e^{i\beta x} e^{k_1 y} \tag{2.39}$$

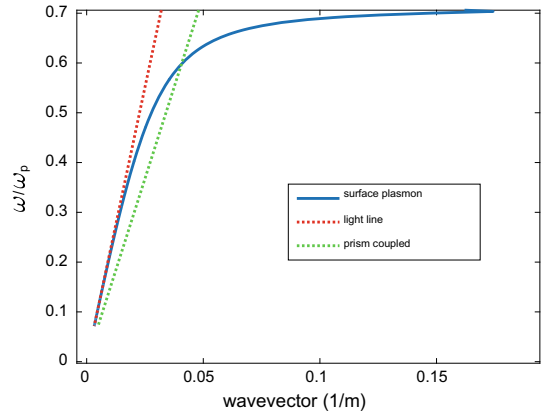

Fig. 2.6 Dispersion relation of SPPs

Applying the boundary condition equations from Eq. (2.15) to (2.18), we can obtain the relations in Eq. (2.40).

$$A_1 = A_2, \qquad \frac{k_2}{k_1} = -\frac{\varepsilon_2}{\varepsilon_1}, \qquad \begin{matrix} k_1^2 = \beta^2 - k_0^2\varepsilon_1 \\ k_2^2 = \beta^2 - k_0^2\varepsilon_2 \end{matrix} \tag{2.40}$$

Finally, the dispersion relation of SPPs propagating at the interface between the two half-spaces can be obtained as

$$\beta = k_0\sqrt{\frac{\varepsilon_1\varepsilon_2}{\varepsilon_1 + \varepsilon_2}} \tag{2.41}$$

Figure 2.6 shows plots of Eq. (2.41). As it can be seen from the figure, due to momentum matching, only the light coupled with a prism can excite SPPs.

2.2 Diffraction and Interference

As mention above, diffraction and interference are at the heart of plasmonics. We shall not discuss these effects at any length in this section, since they are included in all classical electromagnetic textbooks, but merely mention a few central results.

Diffraction refers to reshaping of light when it encounters a slit or an obstacle. Considering a planewave with wavelength λ incident on an aperture of width d, two distinct diffraction patterns can be attained depending on the slit width and the distance between the screen and the slit. The diffraction is said to be in the Fresnel or near-field limit if $L \leq d^2/\lambda$. On the other hand, when it is in the Fraunhofer region (Fig. 2.7).

The intensity of the diffraction pattern can be approximated using Eq. (2.42).

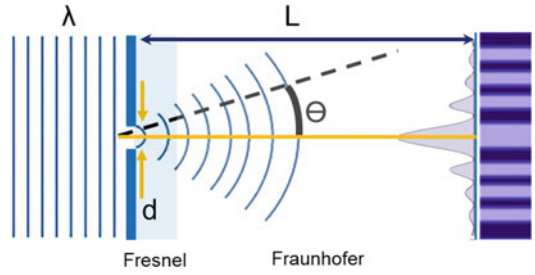

Fig. 2.7 The diffraction pattern created via a planewave incident at a slit

$$I(\theta) \propto \left(\frac{\sin(\mathrm{kd}\sin(\theta))}{\mathrm{kd}\sin(\theta)} \right)^2 \tag{2.42}$$

with $k = 2\pi/\lambda$ being the wave vector. Therefore, the maximum intensity (zero-order mode) pattern occurs at $\theta = 0$. Equation (2.42) can also be solved to calculate higher-order diffraction maxima.

2.3 Transmission Line Theory (TLT)

Transmission line theory (TLT) is a fully analytical, fast, and reliable methodology for analyzing wave propagation in metallic and dielectric structures. TLT bridges the gap between electromagnetics and basic circuit theory. The main concept is to use transmission line elements, i.e. a series resistance, a series inductance, a shunt capacitance, and a shunt conductance, to model and analyze electromagnetic field (in analogy to voltage (V) and current (I)) propagation in optical components such as waveguides, modulators, and gratings. TLT has been extensively exploited to investigate the wave propagation in plasmonic structures. In this section, we briefly review the literature on TLT concerning plasmonic MEMS. Inexperienced readers are encouraged to refer to electromagnetic textbooks for more elementary discussions (Fig. 2.8).

We start with a simple example, a metal-dielectric-metal (MDM) waveguide which consists of a dielectric layer of thickness h surrounded by two metallic layers. For h

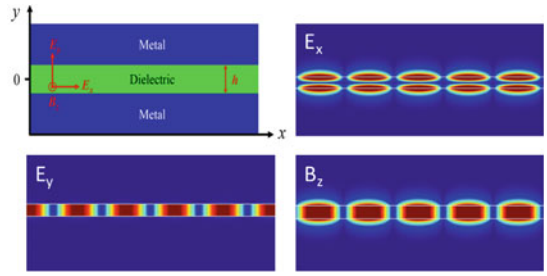

Fig. 2.8 Surface plasmon waveguide

much smaller than the wavelength, only the fundamental TM waveguide mode can propagate along the waveguide. The effective refractive index of an MDM waveguide can be calculated using

$$n_{eff} = \frac{\beta}{k} = \frac{\lambda}{\lambda_{MDM}} + i\frac{\lambda}{4\pi L_{SPP}} \tag{2.43}$$

The real part of Eq. (2.44) describes the guided wavelength (λ_{MDM}) and the imaginary part determines the propagation length (L_{SPP}). The characteristic impedance of the plasmonic waveguide can be calculated using $Z = V(x)/I(x) = V_0/I_0$.

$$V_0 = \frac{\beta}{\omega}\left(\frac{1}{\varepsilon_d k_d} + \frac{1}{\varepsilon_m k_m}\right) \tag{2.44}$$

$$I_0 = h\varepsilon_0\left(\frac{\varepsilon_m - \varepsilon_d}{\varepsilon_m \varepsilon_d}\right) \tag{2.45}$$

Using Eqs. (2.44) and (2.45)

$$Z = \frac{1}{\omega h}\left(\frac{\varepsilon_d + \varepsilon_m}{\varepsilon_0 \varepsilon_m}\right)\sqrt{\frac{-\varepsilon_m}{\varepsilon_d}} \tag{2.46}$$

Our first example considers a recent work by Li et al. [3] in which they have proposed a THz MDM waveguide sensor with an embedded microfluidic channel. The proposed structure is suitable for sensing the refractive index variations in liquid. The proposed THz waveguide with a two layer-stub structure is conceptually outlined in Fig. 2.9.

The transmission spectrum was analytically calculated using the TLT method. Obtained results was compared with the numerical results achieved using the finite-difference time domain (FDTD) method. Initially, the waveguide of width d is substituted by a

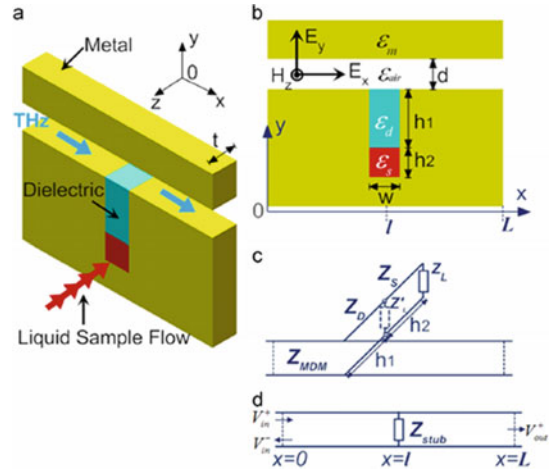

Fig. 2.9 The proposed microfluidic THz MDM waveguide with two stacked sensing stubs. **a** 3D schematic **b** 2D schematic and field components. **c**–**d** The equivalent transmission line representation, and its equivalent circuit model

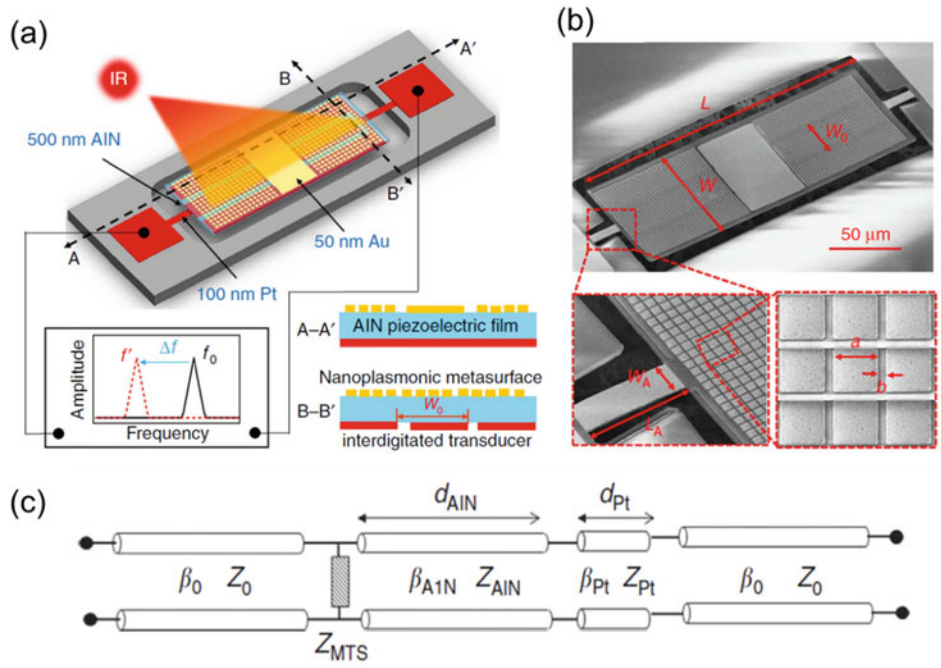

Fig. 2.9 **a** The proposed plasmonic piezoelectric MEMS device. **b** SEM images of the fabricated device. **c** Corresponding TLT circuit model. Z_{MTS}, is the surface impedance of the plasmonic metasurface

transmission line of characteristic impedance of

$$Z(d) = \frac{\beta(d) d \eta}{k_0 \varepsilon_d}, \quad \text{where,} \quad \beta(h) = k_0 \sqrt{\varepsilon_d - 2\varepsilon_d \frac{\sqrt{\varepsilon_d - \varepsilon_m}}{k_0 h \varepsilon_m}} \tag{2.47}$$

here ε_d and η are the relative permittivity of dielectric and wave impedance in the dielectric, respectively. The impedance of medium can be related to the impedance of free space η_0 using $\eta = \eta_0/n$ (inversely proportional to refractive index). The TLT equivalent network of the biosensor presentation is presented in Fig. 2.8c. The effective impedance corresponding to the dielectric and liquid sample of transmission can be derived by

$$Z_{stub} = Z_d \frac{Z'_L + j Z_d \tan(\beta_d h_1)}{Z_d + j Z'_L \tan(\beta_d h_1)} \tag{2.48}$$

in which β_d is the propagation constant of surface plasmons in the spacing dielectric, and Z'_L is the effective impedance of the liquid microfluidic sample which can be calculated via

$$Z'_L = Z_s \frac{Z_L + jZ_s \tan(\beta_s h_2)}{Z_s + jZ_L \tan(\beta_s h_2)} \tag{2.49}$$

here Z_d and Z_s are the characteristic impedances corresponding to dielectric ε_d and sample ε_s permittivity, respectively. β_s is the surface plasmon propagation constant in the microfluidic sample. Finally, the transmission properties of the MDM waveguide calculated using the following formula

$$T = \left|1 + \frac{Z_{stub}}{2Z_{air}}\right|^{-2} \exp\left(-\frac{L}{L_{SPP}}\right) \tag{2.50}$$

The second example includes a plasmonic piezoelectric nanomechanical resonant infrared detector analysis using the TLT method. The transmission properties of the plasmonic nanograting structures are usually coupled with sharp resonances over a narrow bandwidth. Theoretical analysis using the TLT method was used by the authors to analyze the scattering response of the device [4]. The proposed plasmonic piezoelectric MEMS device consists of a 500 nm aluminum nitride (AlN) film sandwiched between a 100 nm-thick platinum transducer and a 50 nm plasmonic gold grating. The resonator is anchored to the silicon base via two platinum contacts and can freely vibrate. The structure, dimensions, and the material are presented in Fig. 2.9a, b.

The surface impedance of the plasmonic array was modeled using the TLT as shown in Fig. 2.9c. The characteristic impedance and propagation constant of the different transmission line sections involved in the model are

$$\begin{aligned} Z_0 &= \sqrt{\frac{\mu_0}{\varepsilon_0}}, \quad Z_{AlN} = \sqrt{\frac{\mu_0}{\varepsilon_0 \varepsilon_{AlN}}}, \quad Z_{Pt} = \sqrt{\frac{\mu_0}{\varepsilon_0 \varepsilon_{Pt}}}, \\ \beta_0 &= \frac{\omega}{c}, \quad \beta_{AlN} = \frac{\omega}{c}\sqrt{\varepsilon_{AlN}}, \quad \beta_{Pt} = \frac{\omega}{c}\sqrt{\varepsilon_{Pt}}, \end{aligned} \tag{2.51}$$

The dielectric constant of AlN and platinum were obtained using the Drude model, i.e. Eq. 2.28. Finally, after applying the TLT and calculating the equivalent voltage and current, the surface impedance of the plasmonic metasurface can be obtained as

$$Z_{MTS} = \frac{a+b}{a\sigma_{Au}} - j\frac{\pi}{\omega\varepsilon_0(1+\varepsilon_{AlN})(a+b)\log(\csc(\frac{\pi b}{2a+b}))} \tag{2.52}$$

where σ_{Au} is the gold conductivity, and a and b are the dimensions and the periodicity of the grating, respectively as shown in Fig. 2.9b.

2.4 Plasmonic Nanograting Theory

Since the original report of diffraction grating by Hopkinson and Rittenhouse in 1786 [5], the interaction of light with periodic and grating structures have become a fascinating subject for understanding the nature of light-matter interaction.

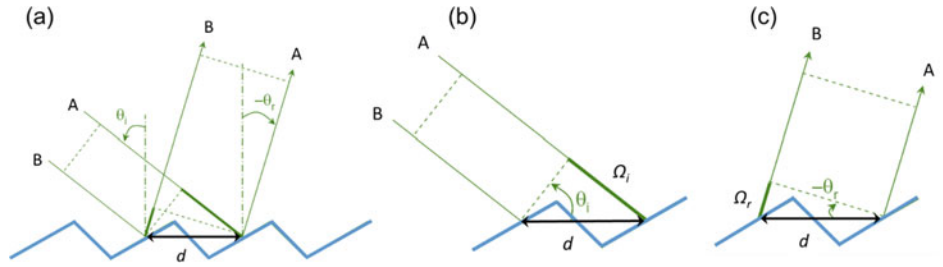

Fig. 2.10 Diagram presenting path difference between two incident rays A and B scattered from a grating's grooved surface

The grating equation can be used to calculate the diffraction angle of an array of incident beams. It can be obtained by calculating the path difference between two light rays as presented in Fig. 2.10.

$$\Omega_i = d\sin(\theta_i), \quad \Omega_r = -d\sin(\theta_r) \tag{2.53}$$

The total path length difference then can be calculated.

$$\Omega = d\sin(\theta_i) - (-d\sin(\theta_r)) = 2d(\sin(\theta_i) + \sin(\theta_r)), \tag{2.54}$$

When this path length difference is an integer (m) multiple of the wavelength, rays interfere constructively.

$$\Omega = m\lambda, \tag{2.55}$$

Substituting in Eq. (2.54).

$$m\lambda = 2d(\sin(\theta_i) + \sin(\theta_r)), \tag{2.56}$$

Which is the grating equation. here m is the order of diffraction, λ is the diffracted wavelength, and d is called the grating constant.

In one of the most recent works, diffracted beams from an array of sub-wavelength plasmonic nanogratings was exploited to design a metalens, which can focus the diffracted light beam. The proposed geometry contains arrays of subwavelength size gold cylinders with different radius and periodicity as shown in Fig. 2.11. When electrostatically actuated, the MEMS platform manipulates the angle of the metalens.

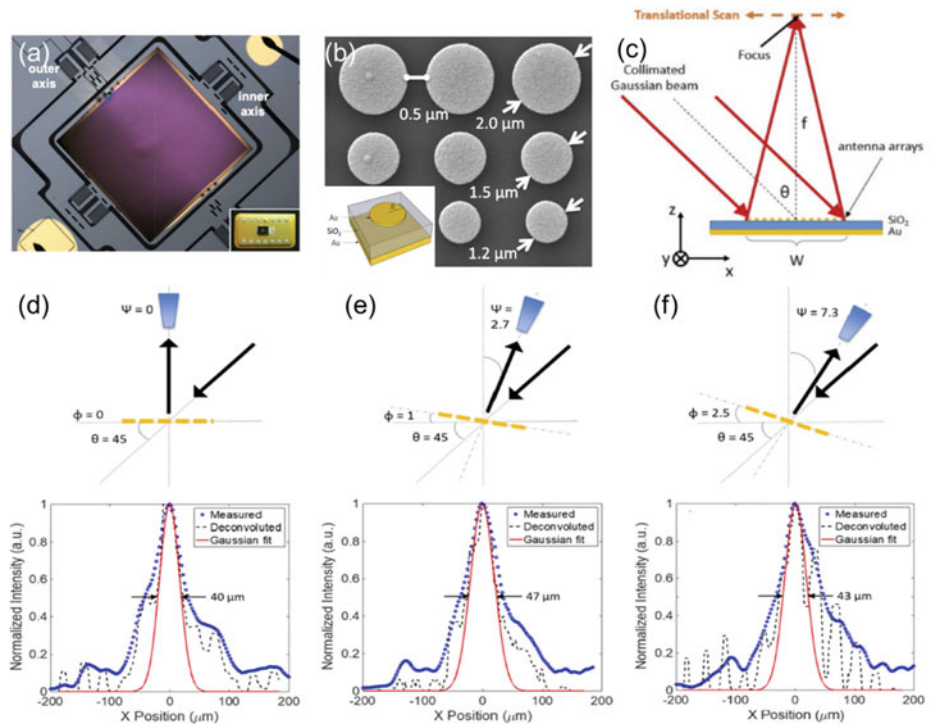

Fig. 2.11 **a** Optical microscope image of the proposed plasmonic MEMS flat lens. **b** SEM images of the fabricated nanograting. **c** Schematic representation of focusing characteristics using diffraction grating. **d**–**f** Schematic of the mechanical rotation of the MEMS device along with the optical profile at the focal line

The optical focusing performance of the realized plasmonic MEMS metalens is show in Fig. 2.11. The phase profile of the lens was obtained using the diffraction equation [6]. That is

$$\varphi(x) = \frac{2\pi}{\lambda}\left(f - \sqrt{x^2 + f^2} - x \cdot \sin(\theta)\right), \tag{2.57}$$

in which f is the focal length, x is the location of the element, and θ is incident angle.

2.5 Numerical Methods

Partial differential equations (PDEs) manifest in the quantitative modelling of various physical phenomena in electromagnetics. Usually, derived PDEs are so complex that finding their solutions by merely analytical means (e.g. by Laplace and Fourier transform methods, or Mie series) is either unfeasible or unpractical, and ones only recourse is to seek numerical approximations to the unknown analytical solution. Finite-Difference Time-Domain (FDTD) and Finite Element Method (FEM) are the most popular numerical methods to solve PDEs [7]. Both FDTD and FEM have been widely used in modeling plasmonic MEMS structures and devices [8–10].

References

1. J. Zenneck, "Über die Fortpflanzung ebener elektromagnetischer Wellen längs einer ebenen Leiterfläche und ihre Beziehung zur drahtlosen Telegraphie," *Annalen der Physik,* vol. 328, pp. 846-866, 1907.
2. A. Sommerfeld, "Über die Ausbreitung der Wellen in der drahtlosen Telegraphie," *Annalen der Physik,* vol. 333, pp. 665-736, 1909.
3. X. Li, J. Song, and X. J. Zhang, "Design of terahertz metal-dielectric-metal waveguide with microfluidic sensing stub," *Optics Communications,* vol. 361, pp. 130–137, 2016/02/15/ 2016.
4. Y. Hui, J. S. Gomez-Diaz, Z. Qian, A. Alù, and M. Rinaldi, "Plasmonic piezoelectric nanomechanical resonator for spectrally selective infrared sensing," *Nature Communications,* vol. 7, p. 11249, 04/15/online 2016.
5. F. Hopkinson and D. Rittenhouse, "An Optical Problem, Proposed by Mr. Hopkinson, and Solved by Mr. Rittenhouse," *Transactions of the American Philosophical Society,* vol. 2, pp. 201–206, 1786.
6. "Wideband plasmonic focusing metasurfaces," *Applied Physics Letters,* vol. 105, p. 053107, 2014.
7. S. D. Gedney, "Introduction to the finite-difference time-domain (FDTD) method for electromagnetics," *Synthesis Lectures on Computational Electromagnetics,* vol. 6, pp. 1-250, 2011.
8. Y. Yao, M. A. Kats, R. Shankar, Y. Song, J. Kong, M. Loncar*, et al.*, "Wide Wavelength Tuning of Optical Antennas on Graphene with Nanosecond Response Time," *Nano Letters,* vol. 14, pp. 214–219, 2014/01/08 2014.
9. Y. Gao, G. Ren, B. Zhu, H. Liu, and S. Jian, "Nanomechanical Plasmonic Switch Based on Multimode Interference," *IEEE Photonics Technology Letters,* vol. 28, pp. 2661-2664, 2016.
10. T. Stark, M. Imboden, S. Kaya, A. Mertiri, J. Chang, S. Erramilli*, et al.*, "MEMS Tunable Mid-Infrared Plasmonic Spectrometer," *ACS Photonics,* vol. 3, pp. 14–19, 2016/01/20 2016.

Fabrication Techniques

3

Nanotechnology deals with materials and structures at or around nanometer scale, with minimum dimensions currently defined (more-or-less arbitrarily) to be 100-nm. All the grand ambitions of nanotechnology are necessarily dependent upon practical and feasible fabrication methods. There are various nanofabrication techniques with different performances, choice of which depends upon the materials, applications, and geometries of the desired structure. These techniques can be roughly classified into either a "top-down" or "bottom-up" approach. Top-down fabrication refers to methods where one commences with macroscopically dimensioned material and carves the nanostructure out of the larger structure. On the other hand, in the bottom-up approach, assembly begins with smaller units: positions of atoms or molecules are manipulated to piece together the nanostructure. The top-down and bottom-up approaches are schematically shown in Fig. 3.1.

Because many materials below 100-nm can have properties and features considerably different from their bulk forms, the 100-nm dimensional scale has set the border between nanotechnology and conventional microscale technologies.

The topic of nanofabrication is far too vast to be covered in one review. The goal of this section of the paper is simply to introduce the method, review the substantial body of literature concerning sub-100-nm resolution fabrication, and mention recent advances in plasmonic, plasmonic MEMS, and plasmonic micromachining fabrication. For a more detailed discussion, we refer the readers to nanofabrication books [1–4].

Figure 3.2 classifies the fabrication techniques that are discussed in this paper under the conventional top-down and bottom-up approaches.

Here, however, a different perspective has been taken, and nanofabrication techniques are classified based on the fabrication tools (photons, charged particles, etc.). Various techniques of Nanofabrication that are currently under development in the laboratory and that require further improvements will be presented in the "Emerging Techniques" section.

© The Author(s), under exclusive license to Springer Nature Switzerland AG 2023

J. X. J. Zhang, *Plasmonic MEMS*, Synthesis Lectures on Materials and Optics,
https://doi.org/10.1007/978-3-031-23137-7_3

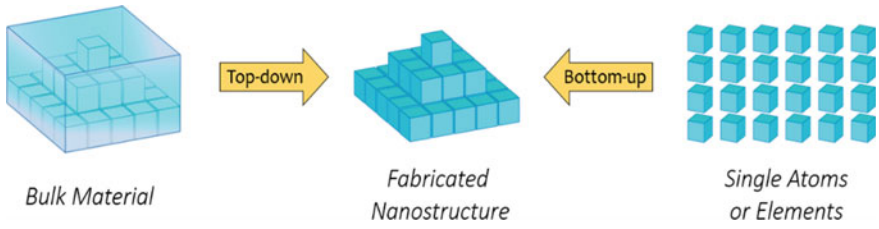

Fig. 3.1 Top-down and bottom-up nanofabrication approaches

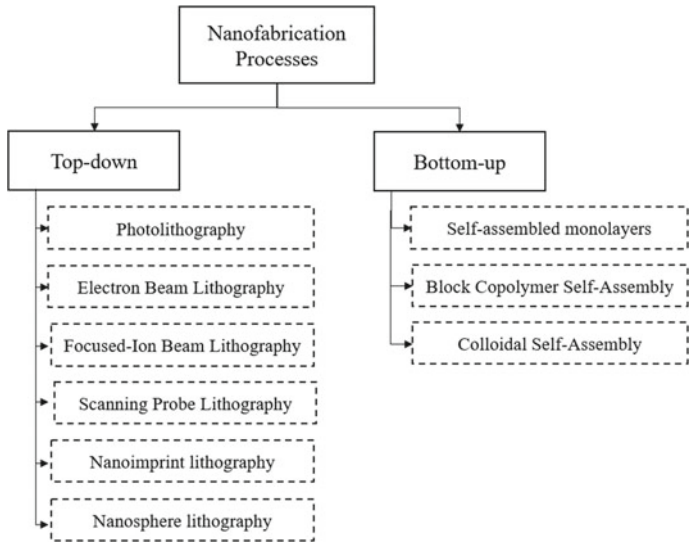

Fig. 3.2 Classification of the fabrication techniques that are discussed in this paper

3.1 Nanofabrication Using Photons

3.1.1 Photolithography

Photolithography is an optical tool used to engrave patterns onto a substrate. Initially invented for the microelectronics industry, photolithography, or "optical lithography", is the most reliable and economical lithography technology for industrial microfabrication.

In optical lithography, a mask or reticle is imaged onto a substrate which is painted with a thin layer of photoresist, a photosensitive polymer material. Focused photon energy causes chain-scission or cross-linking in the polymer. The mask pattern is then delineated into the photoresist after a development process. There are three primary exposure methods: contact, proximity, and projection, shown in Fig. 3.3.

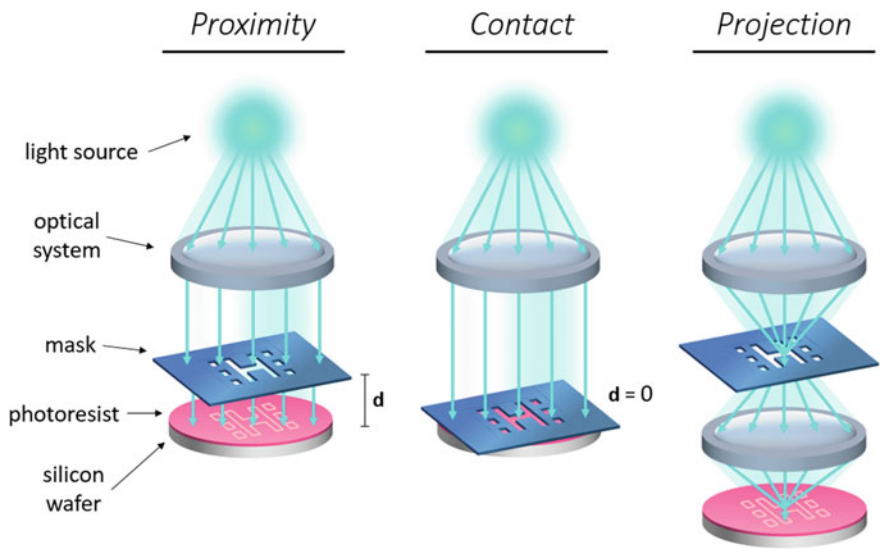

Fig. 3.3 Three primary exposure methods in photolithography

In contact lithography, the photomask is brought into physical contact with the wafer and then exposed to light. Contact lithography offers high resolution, but mask damage and a resultant low yield make this process impractical in most production environments. In proximity lithography, a gap is placed between mask and wafer in the range of 10–30 micro meters. Although proximity lithography does not suffer from mask damage as in contact printing, its low resolution makes it unsuitable for sub-100-nm fabrication. In projection lithography on the other hand, the image is projected onto the wafer with the help of a system of lenses. In this case, the mask can be used several times, substantially reducing the mask per wafer cost.

The early days of projection photolithography in the mid-1970's used visible light to fabricate structures at the micrometer scale. Unfortunately, conventional projection photolithography is incompetent for fabricating nanoscale structures. The resolution limit (minimum feature that can be printed, R) of a conventional projection photolithography system can be defined by the Rayleigh criterion [5], that is

$$R = k_1 \frac{\lambda}{NA} = \frac{\lambda}{n \sin\theta}, \tag{3.1}$$

where λ is the exposure wavelength, NA is the numerical aperture of the imaging optical system, k_1 is a factor related to the imaging process (not to be confused with the wavevector), n is the refractive index of the medium between the lens and the imaging plane, and θ is the half-angle of the maximum cone of light that can enter or exit the lens.

From Eq. 3.1, efforts to improve the resolution of conventional projection optical lithography for sub-100 nm lithography can be classified into three areas: photolithography at shorter wavelengths (λ), photolithography at high *NA*, and photolithography at reduced k_1.

Photolithography at shorter wavelengths

From Eq. 3.1, it is evident that reducing the illumination wavelength will enhance the resolution of an optical system. In the early days of optical lithography, mercury-rare gas discharge lamps with radiation between 365 nm (I-line) and 436 nm (G-line) were exploited. As the mask features shrank, the semiconductor industry employed the 248 or 193 nm illumination produced by krypton fluoride (KeF) or argon fluoride (ArF) excimer lasers (pulsed gas discharge lasers), respectively. Further demands in small mask features shifted the research to the 157 nm radiation produced by fluorine (F_2) laser. For this short wavelength, quartz optics was ineffective (such as not being transparent) so that new optical materials such as calcium fluorine (CaF_2) had to be utilized [6]. Another major issue with 157 nm radiation was designing consistent photoresist, since the designed photoresists for 248 or 193 nm were too absorptive at 157 nm. Considering the aforementioned problems and the fact that 157 nm technology would have been rapidly replaced in the next generation of integrated systems, the production industry decided to go directly to a much shorter wavelength, explicitly the 13 nm Extreme-Ultraviolet (EUV) technology, driving photolithography into the realm of EUV lithography. A schematic of EUV lithography is presented in Fig. 3.4.

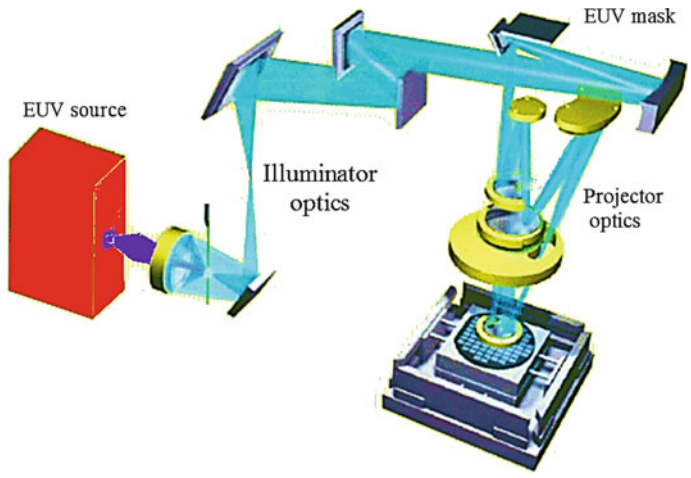

Fig. 3.4 Schematic of EUV system for 13 nm radiation. Four major components of EUV can be observed

The four main components of EUV lithography can be seen in Fig. 3.4. In order to generate the EUV source, laser-produced plasma (LPP) and discharge-produced plasma (DPP) are two frequent approaches. From a number of LPP-generating sources that can emit at 13.5 nm, three materials have garnered attention, namely, Sn [7], Xe [8], and Li [9]. Of these three, Sn has proven to be the most likely candidate, as it has the highest conversion efficiency [10, 11]. Another important component of EUV lithography is "EUV optics". The main components for EUV optics are mirrors coated with distributed Bragg reflectors (DBRs) in order to reach a high reflectivity. Typical DBRs consist of quarter wavelength-thick multiple layers of alternating materials that have different refractive indices [12]. New types of DBRs with different materials and geometries have been developed at different frequencies [13, 14]. EUV mask technology is considered to be one of the most critical issues for the successful implementation of nanofabrication processes. First a blank mask is designed, then, since EUV light is extremely absorptive by most materials at this frequency, the patterning of the refractive material is applied. The EUV mask should be free of defects in both substrate and refractive material. Recently several defect removal techniques have been devised for EUV masks; for an in-depth discussion, the reader can refer to the following papers [15–21]. Developing photoresists for EUV is one of the main challenges for the cost-effectiveness and the introduction of EUV lithography into high-volume manufacturing. In order for EUV lithography to be a competent technique for the next generation lithography (i.e., 100 wafers per hour), high-sensitivity resist (greater than 20 mJ cm^{-2}) is needed to compensate for the low power level of the EUV source. Higher sensitivity means lower line edge roughness (LER), which is not appropriate for EUV resists. LER has been a decisive issue for sub-100 nm lithography. Critical challenges for EUV resist materials are discussed in [22].

Recent innovations have addressed the challenges associated with the resist performance of EUV. For example, by introducing metals to the resists, Inpria© has shown excellent resolution with their hafnium oxide based resist [23]. More work on this has been mostly done by Cornell university in which they have achieved higher sensitivity [24, 25]. Molecular organometallic resists have been also exploited [26, 27]. A sensitivity of 50 mJ cm^{-2} has been obtained using platinum and palladium mononuclear complexes in [28].

Photolithography at high NA

The second parameter which affects the resolution of optical lithography, in addition to the wavelength as seen in Eq. 3.1, is the numerical aperture (NA). When light passes through a slit (mask), it diffracts, so a lens is needed to gather the diffracted rays. Lenses with larger diameters (higher NA) are more suitable for optical lithography since they can accumulate more diffracted light rays to focus onto the image plane, as can be seen from Fig. 3.5.

The higher the NA, the more complex, big, heavy, and expensive the lens has become. In the 1980s, a G-line stepper lens at 0.35 NA weighed only 14 kg. By the mid-1990s, an

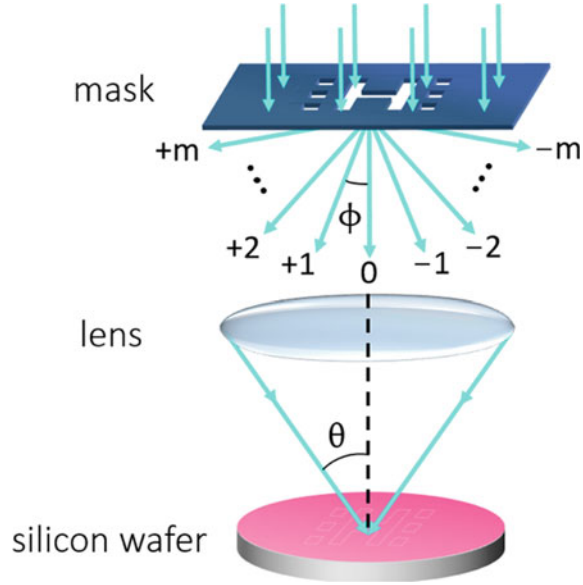

Fig. 3.5 Conceptual view of optical projection imaging

I-line stepper lens at 0.63 NA weighed over 500 kg [29]. Resolution has been improved by creating exposure tools with greater NAs for each wavelength. For 193 nm dry imaging, the lenses have progressively increased from 0.6 to 0.75 NA, 0.85 NA, and 0.93 NA. Typically, the projection optics and the wafer stage occur in air or in a vacuum, dictating that the numerical aperture, therefore, cannot be bigger than 1. Recently, immersion lithography has provided an alternative method of increasing the NA: by increasing *n*. In this case, the NA can be greater than 1. The gap between the last lens element and the resist can be filled with a liquid, as shown in Fig. 3.6, which will have a much higher refractive index *n* than air.

Photolithography at reduced k_1

In addition to the wavelength reduction and the increase of NA, the resolution of optical projection lithography can also be improved by the optimization of the process parameters, including illumination settings, mask, and photoresist process. These contributions can be included in the k_1 factor in Eq. 3.1, called the process factor. Improvements in imaging optics and photoresist processes have continuously driven down the k_1 factor. Figure 3.7 shows this reduction of k_1 from 1982 through 2000 [1]. Usually, a k_1 factor above 0.30 is needed for production, and k_1 cannot typically go below 0.25. A lithographic process in which $0.25 < k_1 < 0.30$ is difficult and requires very aggressive resolution enhancement techniques. This kind of low-k_1 process is useful during early technique development. For example, a 193 nm exposure tool with 0.85 NA used for production at the 90 nm half-pitch node ($k_1 = 0.396$) could also be used for advanced development of 65 nm

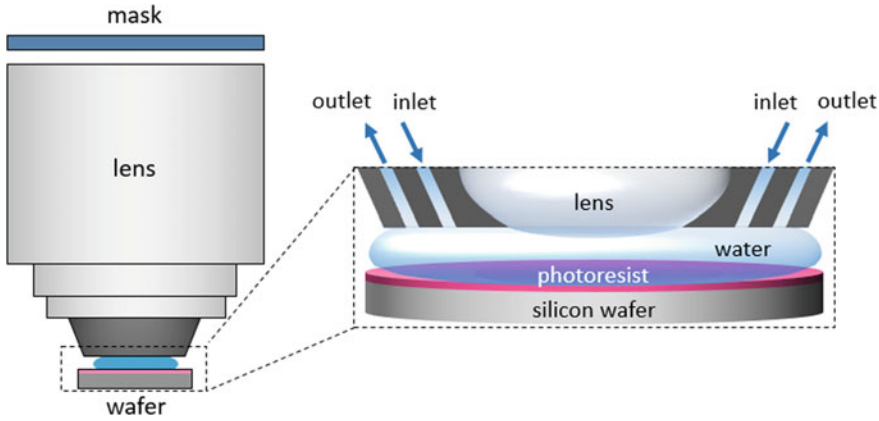

Fig. 3.6 Immersion lithography using water

half-pitch processes ($k_1 = 0.286$). Once the 0.93 NA tool became available, the 65 nm process could be transferred to this new tool.

Table 3.1 summarizes the recent advances towards reduction of the process factor. A brief review of the advancement of photolithography from its earliest days until 2002 can be found in [30]. More details about EUV lithography can also be found in [31, 32].

Photolithography is a robust approach for the fabrication of sub-100 nm structures. Fabrication of 100 nm line and space patterns and 70 nm isolated lines has been demonstrated by using an intermediate hard mask material such as silicon oxide or silicon oxynitride [34]. Sub-100-nm patterning using a single layer of deep-UV photoresist,

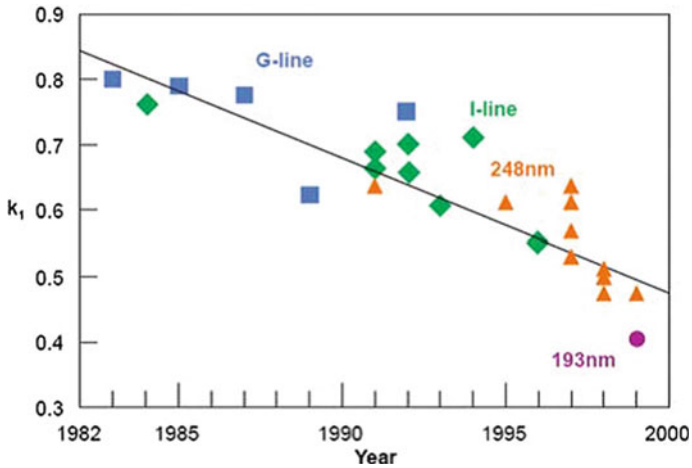

Fig. 3.7 Reduction of k_1 factor down to 193 nm optical lithography

Table 3.1 Summary of resolution enhancement techniques in photolithography. Table adapted from [33]

Components of optical lithography	Innovations to reduce k_1 factor
Photoresist layer	Top surface imaging (TSI), antireflective coating (ARC), double exposure or double patterning
Photomask	Phase-shifting masks (PSMs), optical proximity correction (OPC)
Illumination optics	Off-axis illumination (OAI): annular, quadrupole, or programmable

175 nm thick, with Sandia's 10x-Microstepper EUV imaging system has also been demonstrated [35]. Going to even shorter wavelength (X-ray), 50 nm and sub-30 nm structures have been fabricated using photolithography [36–38]. Researchers at ENEA Frascati Research Center in 2008 were able to use EUV (at 14.4 nm) to fabricate structures less than 90 nm (Fig. 3.8) [39, 40].

In 2015 [41], patterns with less than 20 nm have been fabricated with photolithography (Fig. 3.9).

In the previous sections, the flexibility and applicability of photolithography for the fabrication of sub-100 nm structures have been demonstrated and recent advances were summarized. Photolithography has also been widely applied in the fabrication of metamaterials that operate at THz frequency. Yen et al. [42] created an array of nonmagnetic and conducting split-ring resonators (SRRs), as shown in Fig. 3.10. They fabricated the metamaterial structure using a special photolithographic technique termed "photo-proliferated process" (PPP).

Plasmonic Waveguide Ring Resonators with a 4 nm Air Gap has also been constructed using photolithography in [43, 44]. Martin et al. have used photolithography to fabricate sub-10 nm gap sizes for plasmonic applications [45]. In their proposed method, EUV is exploited to provide a 1D line array on the substrate, which is typically float glass or silicon. Next, a coherent beam with 13.5 nm wavelength is incident on a mask comprising two identical gratings. Beams diffracted by the gratings interfere to form high resolution patterns with dimensions below 10 nm half pitch (Fig. 3.11).

To summarize this subsection, while mask-assisted photolithography has been widely used in microelectronics and semiconductor industry, it may not be considered as fully appropriate for plasmonics. Standard equipment is diffraction limited, leading to low-resolution nanostructures. Furthermore, the cost of deep UV and EUV equipment combined with immersion lithography prevents their use at academic level.

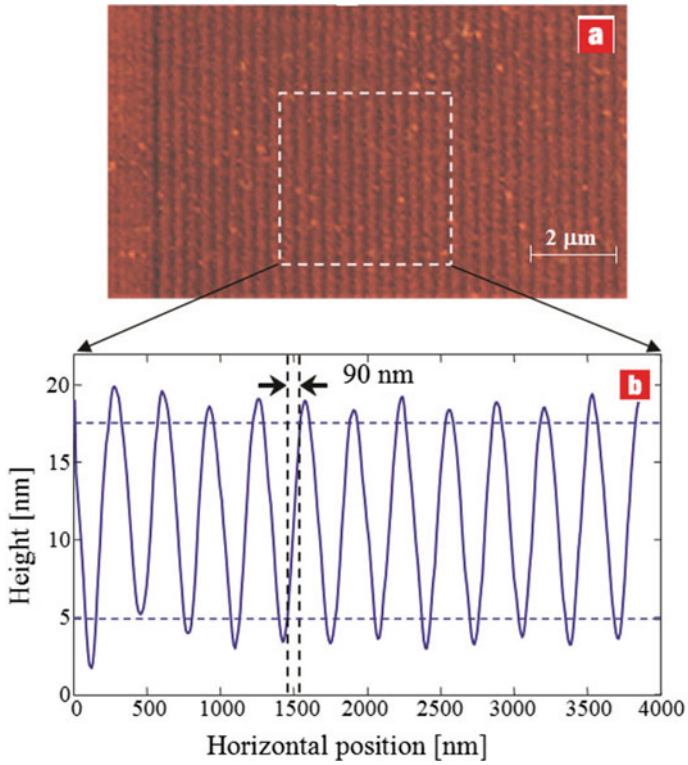

Fig. 3.8 Line-space printing on PMMA: **a** 160 nm and 110 nm pattern on PMMA examined using atomic force microscope (AFM); **b** Line profile integrated on the dashed portion of panel. Horizontal dashed lines are the 10 and 90% modulation levels. Vertical dashed lines display the corresponding edge response equal to 90 nm. Reproduced with permission from [39]

3.1.2 Electron Beam Lithography

Nanofabrication by charged beams, including electron beam lithography (EBL) and focused ion beam lithography (FIB), is based on carrying and shooting energy into a substrate material in order to perform structuring either by exposure of energy-sensitive polymer materials or by removing material directly. The advantages of using charged beams is that they can be focused into extremely small regions. The main advantages of charged beams lithography over the photolithography techniques include very high resolution and versatile pattern formation [46]. The basics of e-beam lithography technology have been introduced in this book [47]. This section goes beyond the basics and focuses on those issues associated with patterning at sub-100 nm scale and plasmonic structures when e-beam lithography and FIB are exploited.

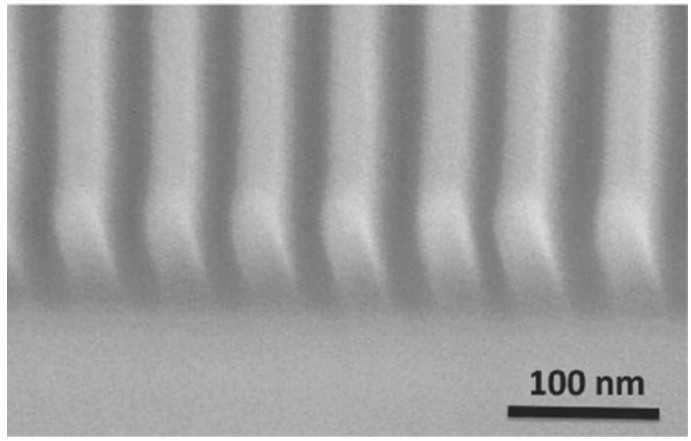

Fig. 3.9 Creation of under 20 nm half-pitch features with a 5:1 aspect ratio via photolithography. Reproduced with permission from [41]

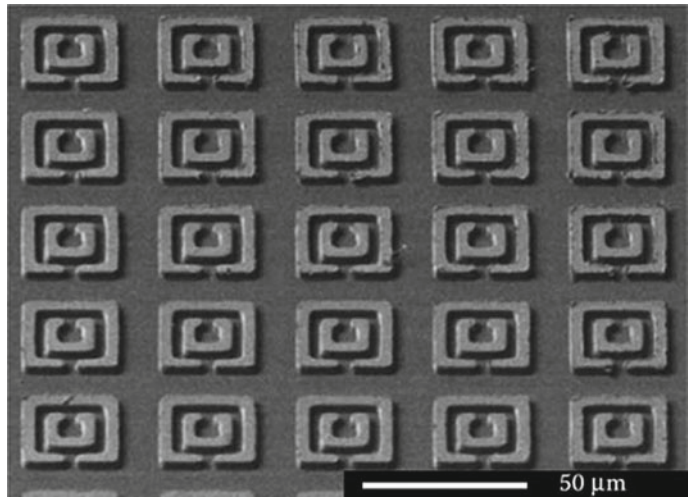

Fig. 3.10 Fabricated magnetic metamaterial structure using photolithography. Reproduced with permission from [42]

Electron beam lithography (EBL) has evolved from scanning electron microscope (SEM) in early 1960s by the introduction of an electron-sensitive polymer material, called polymethylmethacrylate (PMMA). Figure 3.12 shows the diagram of an EBL instrument.

An electron gun is a device that generates and projects a beam of electrons onto a substrate. Electrons are first generated by cathodes or electron emitters. They are then

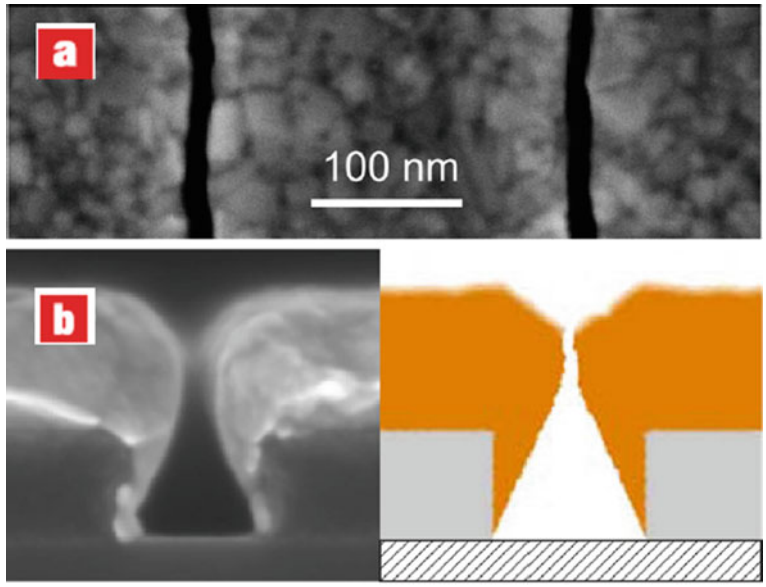

Fig. 3.11 **a** SEM top view and **b** side view of a gold nanogap array matched with ballistic simulation results. The 100-nm thick thin film was evaporated at 60° from the surface normal. The resulting gap size is ~13 nm. Reproduced with permission from [45]

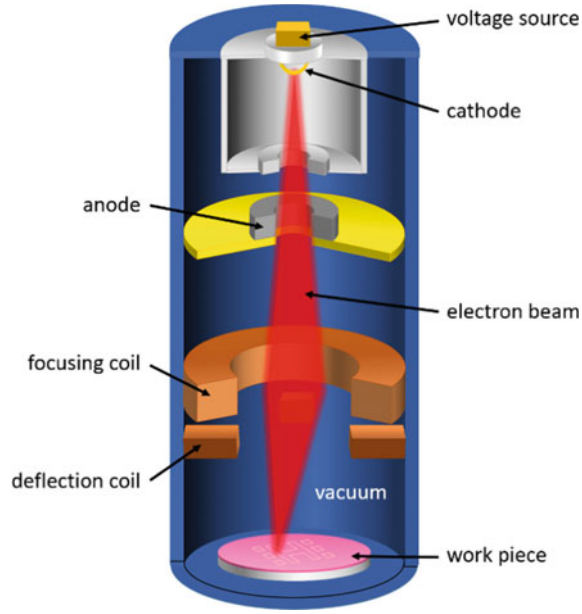

Fig. 3.12 Diagram of an EBL instrument

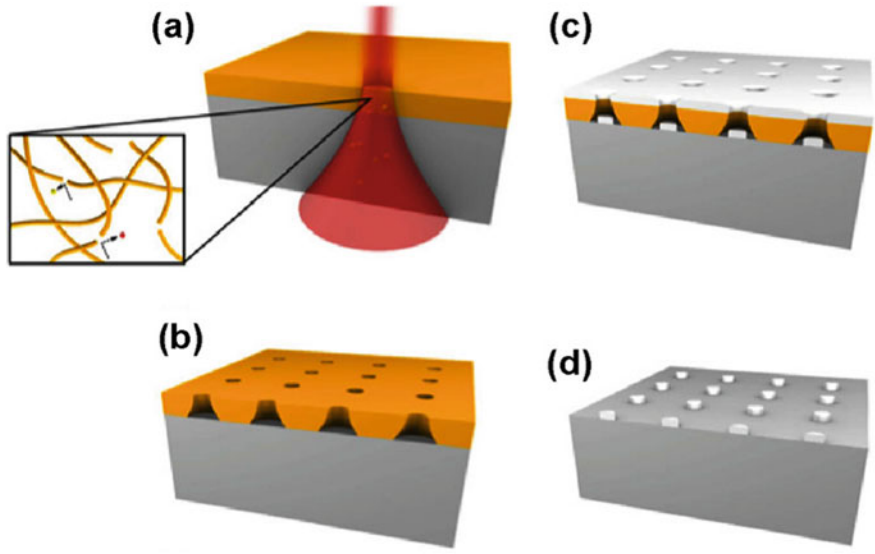

Fig. 3.13 EBL steps for metal deposition. **a** Energized electron-beam (red color) exposure of the resist (orange color) leading to polymeric chain breaking (inset). **b** Side view of the resist after development. The curved cup-shape is due to overexposure at the resist-substrate interface. **c** Metal coating and **d** Plasmonic pattern after removing the resist in a solvent. Reproduced with permission from [48]

accelerated and focused by electrostatic fields to obtain higher kinetic energy and shaped into an energetic beam. Finally, the guidance system, consisting of the electric and magnetic focusing coils and deflecting system, transmits the beam to a work point on the substrate. Outline of EBL process steps to form a nanoscale pattern in a positive-tone resist layer is shown in Fig. 3.13 [48].

First, the sample is coated with a thin layer of PMMA, then the desired structure or pattern is exposed with a certain dose of electrons. The exposed PMMA changes its solubility towards certain chemicals. This can be used to produce a trench in the thin layer. If one wants to produce a metallic structure, a metal film is evaporated onto the sample and after dissolving the unexposed PMMA with its cover (lift-off) the desired metallic nanostructure remains on the substrate.

In the early 1970s, e-beam lithography was already able to pattern features as small as 60 nm. In 1984, a functioning Aharonov-Bohm interference device was fabricated with EBL [49]. Figure 3.14 shows a group of sub-10 nm lines obtained by exposure at 80-keV and 5-nA beam current on 58-nm thick Hydrogen silsesquioxane (HSQ) resist (a liquid e-sensitive form of silicon dioxide) [50].

Muray et al. reported 1–2 nm features in metal halide resists [51]. El-Sayed et al. by using EBL fabricated pairs of gold nanoparticles with varying interparticle separation

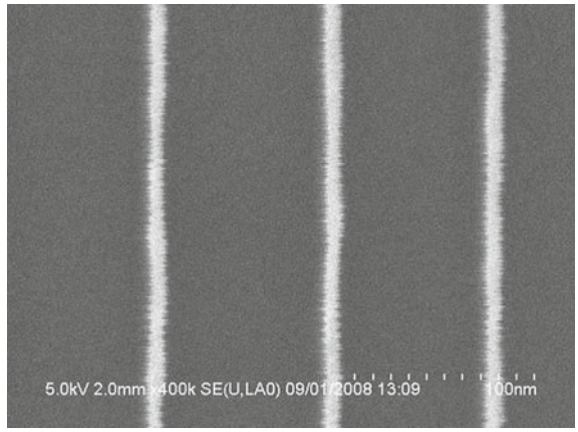

Fig. 3.14 Sub-10 nm resolution lines obtained by EBL. Reproduced with permission from [49]

in order to study the effect of plasmon field on the phonon oscillation [52]. The gold nanoparticle pairs were prepared on quartz slides using a JEOL JBX-9300FS 100 kV EBL system. The cleaned quartz slide was spin-coated with 65 nm PMMA 950 k electron-sensitive resist and cured at 180 °C for 3 min. The slide was mounted in a thermal evaporator and coated with 10 nm of gold to make the substrate conductive. The structure is shown in Fig. 3.15.

In 2009, Giessen's group in Universität Stuttgart reported the metamaterial structure that consists of an array of a stack of two identical SRRs [53]. Three gold alignment marks (size 4×100 μm) with a gold thickness of 250 nm were fabricated using a lift-off process on a quartz substrate. The substrate was covered with another 50 nm gold film using electron-beam evaporation, and then gold SRR structures were fabricated using

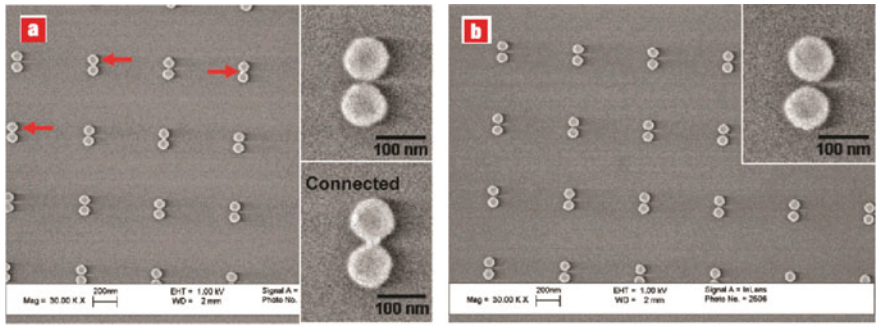

Fig. 3.15 SEM images of the different nanodisc pairs having gaps of **a** 2 nm, **b** 7 nm, the insets are enlarged images of a representative nanodisc pair. Reproduced with permission from [52]

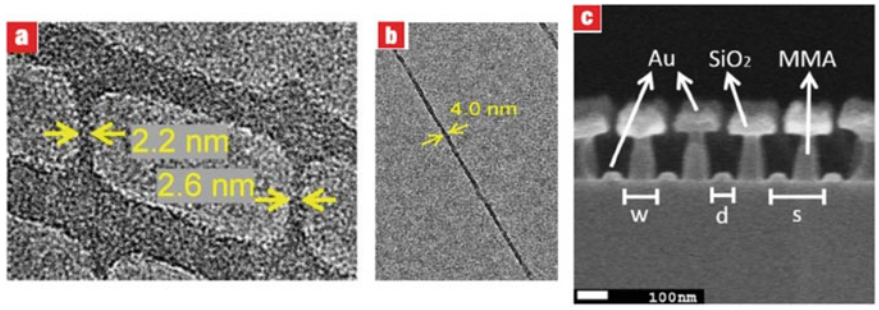

Fig. 3.16 **a** Gap sizes bout 3 nm size obtained by EBL in [55], **b** A solitary feature with average line width of 4 ± 0.8 nm [55], SEM cross-sectional micrograph of a tri-layer lift-off process after Au evaporation. Reproduced with permission from [54]

electron-beam lithography. Subsequently, a second SRR structure was fabricated on the sample using gold film evaporation and electron-beam lithography. The total area of the fabricated structures was 200×200 μm.

In addition to bi-layer structures, recently multilayer structures have been also fabricated [54]. Some modification of EBL like scanning transmission electron microscope (STEM) are capable of 2 nm [55] and even 0.7 nm patterning using electron beam-induced deposition (EBID) (Fig. 3.16) [56].

Electron-beam lithography is a very strong technique for the fabrication of plasmonic structures and has been widely used in this area. In this part we will review a few of these structures.

Plasmonic waveguides have attracted substantial attention during the past years, primarily due to their ability to support extremely confined modes. Plasmonic waveguiding in linear nanoparticle chains made by EBL has been reported in 2005 [57, 58]. EBL has the advantage of producing arrays of nanoparticles that all have the same size, shape, and interparticle distance, allowing quantitative measurements to be carried out even with ensemble techniques [59]. Schider et al. have studied surface plasmon modes on silver and gold nanowires of a fixed cross-section and different lengths, produced by EBL [60]. Plasmon waveguiding has been observed in metal stripes fabricated by electron-beam lithography [61]. One of the simplest nanoparticle geometries investigated for LSPR sensing is a planar seven-member "heptamer" cluster with one nanoparticle in the center of a six nanoparticle ring [62]. Heptamers have been predicted to have extremely large spectral shifts of their Fano resonance induced by changes in the surrounding refractive index (Fig. 3.17) [63].

Unlike silver and gold, aluminum has material properties that enable strong plasmon resonances spanning much of the visible region of the spectrum and into the ultraviolet [65]. E-beam lithography has been exploited in order to fabricate aluminum nanodisks with less than 35 nm radius.

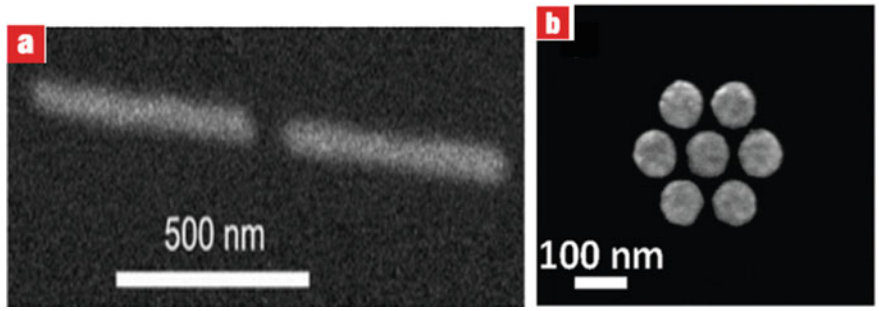

Fig. 3.17 **a** SEM micrograph of two nanowires in an array with 60 nm end-to-end distance constructed by EBL on ZnS [64], **b** 85 nm diameter constituent particles of a Heptamer. Reproduced with permission from [63]

Nanopatterned metallic surface over which tunable directional optical radiation is realized using a subwavelength slit has reported in [66]. Authors in [66, 67] have experimentally demonstrated tunable radiation from a periodic array of plasmonic nanoscatterers, tailored to convert surface plasmon polaritons into directive leaky modes. Schematic of a tunable directional optical antenna in shown in Fig. 3.18.

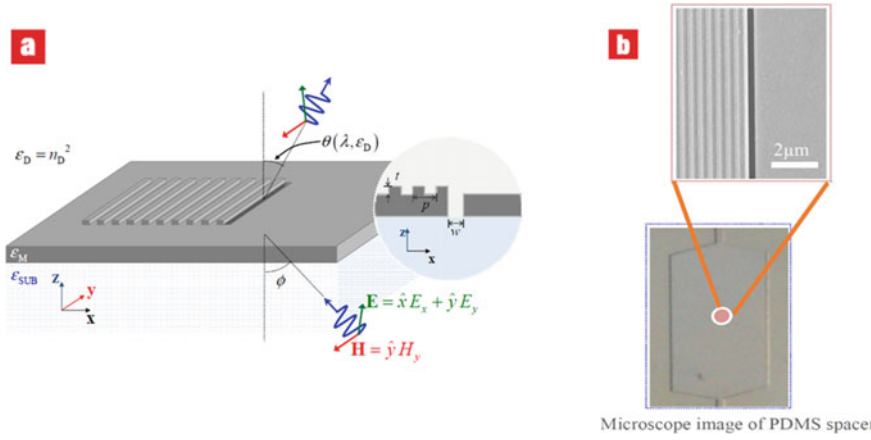

Fig. 3.18 **a** Schematic of a tunable directional nano-optical antenna: a subwavelength slit with a left-side array of periodic gratings, consisting of corrugations in a plasmonic screen. ε_D, ε_M, and ε_{SUM} indicate the relative permittivity of surrounding medium, metal, and supporting BK7 glass substrate, respectively. Focused radiation can be obtained at a specific angle θ by an appropriate choice of surrounding medium and wavelength λ of operation; and its directivity can be further enhanced by optimizing illumination angle φ. **b** SEM of the fabricated device

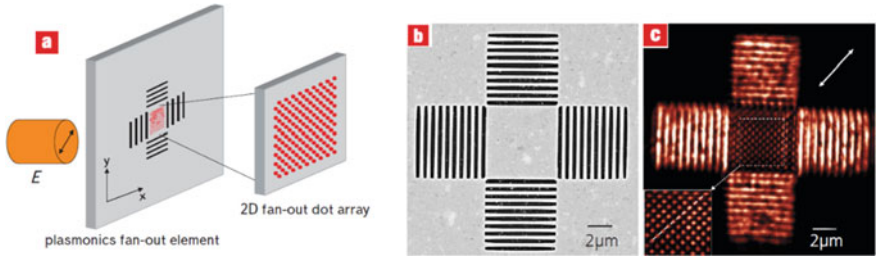

Fig. 3.19 **a** Vertical and horizontal subwavelength plasmonic apertures producing counter-propagating surface plasmons to form the plasmonic dots array. **b** SEM image of subwavelength slit arrays structure. **c** Near field image of electrical field distribution for diagonal polarization direction. The white arrow indicates the incident polarization direction with the excitation laser wavelength of 633 nm. Reproduced with permission from [68]

A traditional fan-out element splits a single beam into quasi plane waves by using phase gratings and lenses to generate an array of light spots. The authors in [68] demonstrated a two-dimensional plasmonic fan-out spot array by using subwavelength sized slit arrays. The plasmonic fan-out structure is presented in Fig. 3.19.

Generation of plasmonic Moiré fringes using a phase engineered optical vortex (OV) beam is experimentally demonstrated using EBL and reported in [69]. More recent papers have reported the applicability and versatility of EBL for the fabrication of plasmonic nanoparticles including nanostar arrays [70] and three-dimensional chiral nanostructures [71].

3.1.3 Focused-Ion Beam Lithography

A technique related to electron lithography is the focused ion-beam lithography or commonly called FIB. The FIB is based on the use of accelerated ions instead of electrons. If the wavelength of accelerated ions can be similar to that of accelerated electrons, therefore an atomic resolution is expected in the ideal case. The major difference lies in the mass of the ions that allows very efficient momentum transfer and therefore physical etching of a material (almost any kind of material).

FIB lithography is similar to EBL, but provides more functionalities. Not only focused ion can create a pattern on a resist, similar to EBL, but it is capable of locally removing away some parts of the structure by sputtering (subtractive lithography, a hydrogen ion is 1840 times heavier than an electron). FIB is capable of accurately depositing atoms with sub-10 nm resolution (additive lithography).

Probe-based nanoantennas are the key technical units of near-field scanning optical microscopy (NSOM). By focused ion (Ga+) beam milling authors in [72] have created a

well-defined elongated antenna (50 nm width, 20 nm radius of curvature) on a flat end-face next to a circular aperture (100 nm diameter). Figure 3.20 shows scanning electron microscopy (SEM) images of a resulting probe-based antenna [72, 73].

Figure 3.21 shows a bowtie antenna at the apex of a Si_3N_4 atomic force microscopy tip fabricated by focused ion beam milling [74].

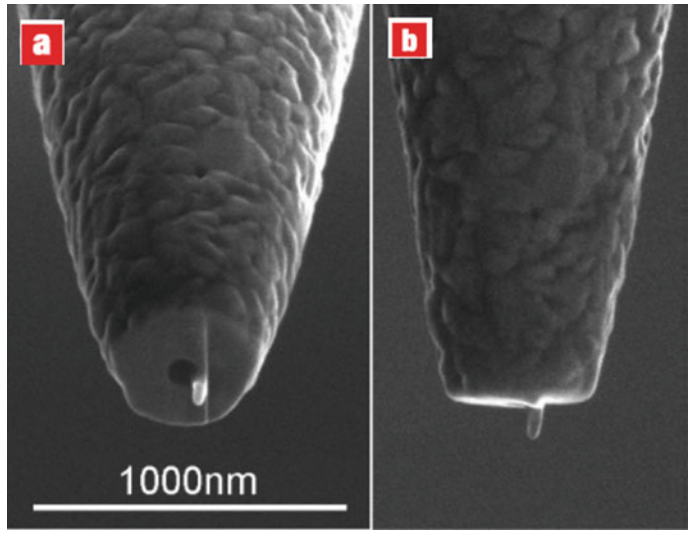

Fig. 3.20 A probe-based nanoantenna (SEM images): **a** viewed from a 52° angle and **b** side view

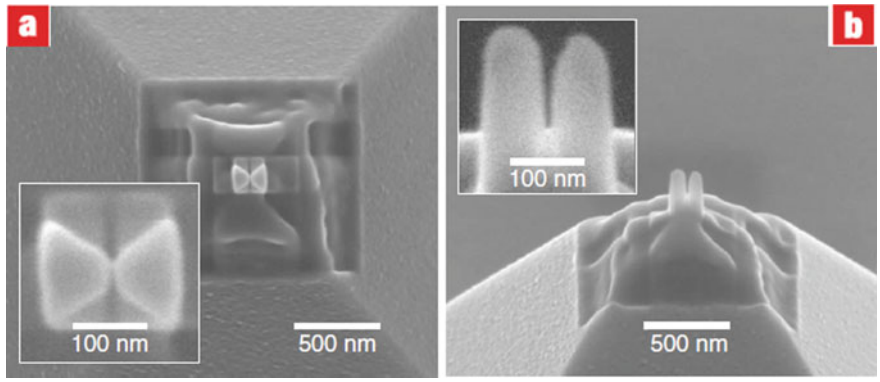

Fig. 3.21 An optical antenna at the apex of an AFM tip. **a** Top, **b** side view. Dimensions: aluminum thickness 40 nm; antenna overall length, 170 nm; flare angle, 40° and feed gap width, about 50 nm; radius of curvature at the feed gap, 30 nm

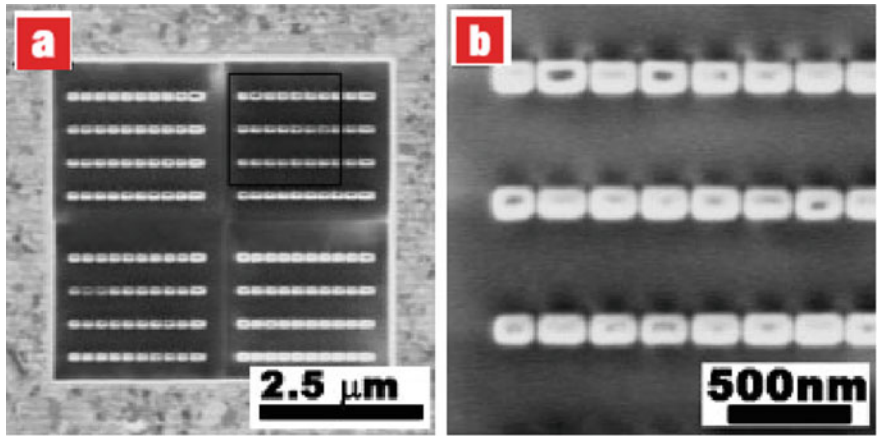

Fig. 3.22 **a** Low magnification SEM micrograph of the FIB milled gold nanopillars fabricated on a silica substrate. **b** SE micrograph showing FIB fabricated gold nanopillars on a planar silica substrate patterned as arrays of elliptical gold nanopillars separated by a ~ 15 nm gap. Reproduced with permission from [75]

Focused ion has been commonly used in order to fabricate photonic and plasmonic structures. The size of the smallest features can reach few tens of nanometers. In [75] the authors have employed FIB in order to fabricate metallic Au nanopillars and linear arrays of Au-containing nanodots for plasmonic waveguides. To carry out nano-scale fabrication of the metallic nanopillars using FIB, planar substrates were first coated with a 40–100 nm thick layer of gold using PVD 75 electron beam evaporator (Fig. 3.22).

For plasmonic applications, smooth surfaces are of utmost importance. Unfortunately, metal films deposited by evaporation are inherently rough due to polycrystallinity. In order to overcome this drawback, Oh research group from the University of Minnesota, combined template stripping with precisely patterned silicon substrates to obtain ultra-smooth pure metal films with grooves.

Figure 3.23 shows a silicon substrate with circular concentric grooves defined by FIB. A 275 nm thick silver layer is thermally evaporated on the substrate, epoxy is then added, and peeled off the bilayer [76].

Focused ion was used to define a series of parallel grooves, which serve as a Bragg grating to reflect SPP waves (Fig. 3.24) [77].

The nanocone geometry is an effective structure in providing a large enhancement of spontaneous emission while keeping a fairly high quantum efficiency of up to 80%. This property makes gold nanocones suitable candidates for probes in tip-enhanced Raman spectroscopy [78]. Fabrication of nanocones with base diameters and heights in the range of 100 nm using FIB of sputtered nanocrystalline gold layers have been considered in

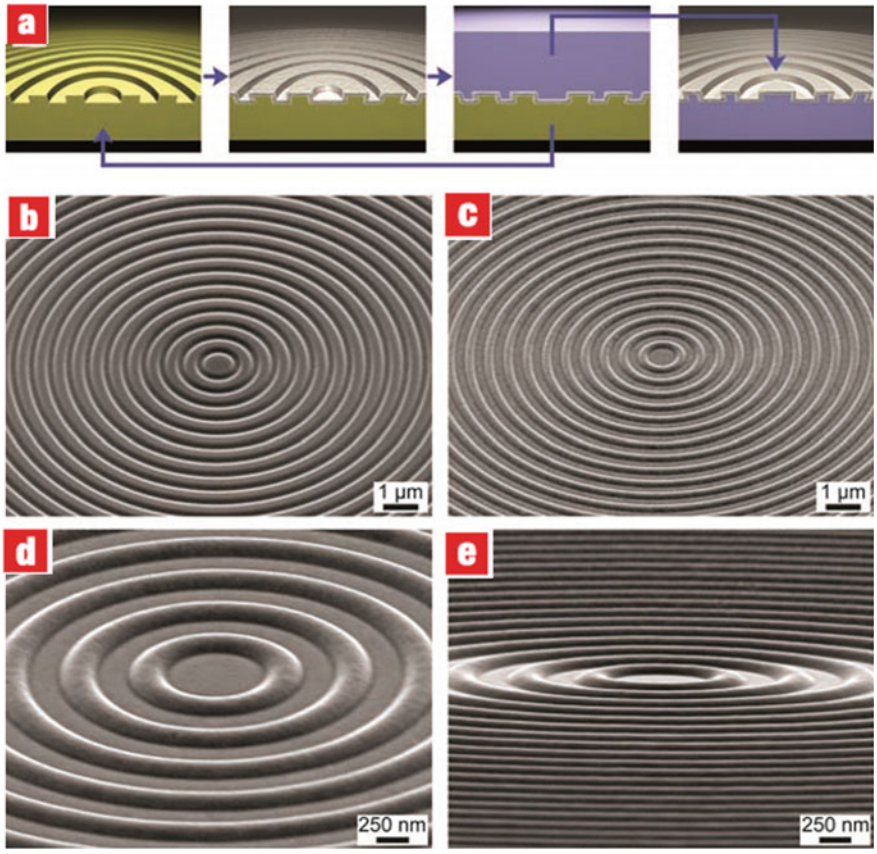

Fig. 3.23 Ultrasmooth plasmonic patterning: **a** Schematic for fabricating process. A thin film metal is deposited and then coated with epoxy shown in blue. The combined film can be peeled off of the substrate to reveal a smooth patterned surface. The structure can be reused as a mold to form identical structures. **b** SEM of a silicon wafer patterned with circular grooves (bull's eye) by FIB. The grooves were 285 nm wide and spaced every 570 nm. **c**–**e** Silver bull's eye that was template stripped off of the silicon substrate in **b** using epoxy. Reproduced with permission from [76]

[79]. The controlled fabrication process in Fig. 3.25 allows the realized cones with tailored plasmon resonances.

LSPs excited in gaps between metal surfaces generate trapping force. Authors in [80] proposed the radial gap-array consisting of plasmonic dot arrays which traps objects on the plasmonic dot array (plasmonic clipping). Silver dot array structures were fabricated by means of the FIB sculpturing for the thin silver film, which is evaporated on a slide glass substrate. The FIB (FB-2100, HITACHI) was based on Ga ion sputtering and had the material removal resolution of around 10 nm.

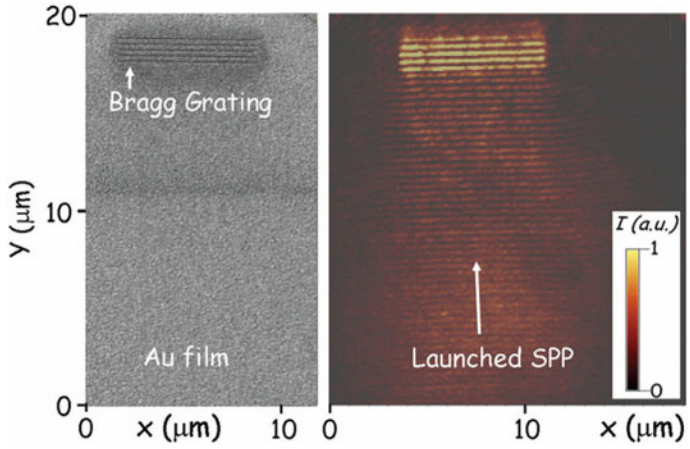

Fig. 3.24 (Left) SEM image of a gold film into which a Bragg grating has been defined using FIB. (Right) Photon scanning tunneling microscope image of a surface plasmon wave introduced along the metal film toward the grating. The reflection of the surface plasmon from the nanograting develops a standing wave interference pattern. Reproduced with permission from [77]

For realization of highly-integrated optical circuit, the combination of the Si and gap plasmonic waveguides is important. A typical optical junction between Si and the plasmonic waveguide with enough height for supporting the second plasmon mode is presented in [81]. The structure is fabricated using FIB. The metal–insulator-semiconductor (MIS) plasmonic tunnel junction for Si-based photonic circuitry has been fabricated on p-Si wafer and grating structures have been added on top metal (Ag) by focused-ion-beam milling [82].

It is known that a new class of metamaterials called metasurfaces emit terahertz (THz) waves by irradiation of a pulsed laser. This is a promising technique for new functional THz wave sources. Silver (Ag) films with pinwheel-like structures-plasmonic chiral metasurfaces- have been recently fabricated using a FIB milling technique [83]. Ag films 300 nm in thickness were deposited on fused quartz substrates by magnetron sputtering. Chiral metasurfaces were prepared on the Ag films using the FIB (FB-2200AN, Hitachi) milling technique. The metasurfaces consist of pinwheel-like structures with rectangular pits 1.2 μm in length and 0.3 μm in width (Fig. 3.26).

Recently, plasmonic color filters have drawn considerable attention [84, 85], thanks to their great potential for ultrahigh resolution display technology. Coaxial apertures are highly symmetrical structures in the 2D plane, thus, polarization insensitive [86]. This independency is extremely desirable for designing elegant plasmonic color filters with both high efficiency and simple architectures. Jiang et al. in 2016, have exploited the FIB for the fabrication of coaxial-aperture based plasmonic nanostructures in optically thick metal films. Metal films (both Ag and Au) with various thicknesses and an adhesion (5 nm

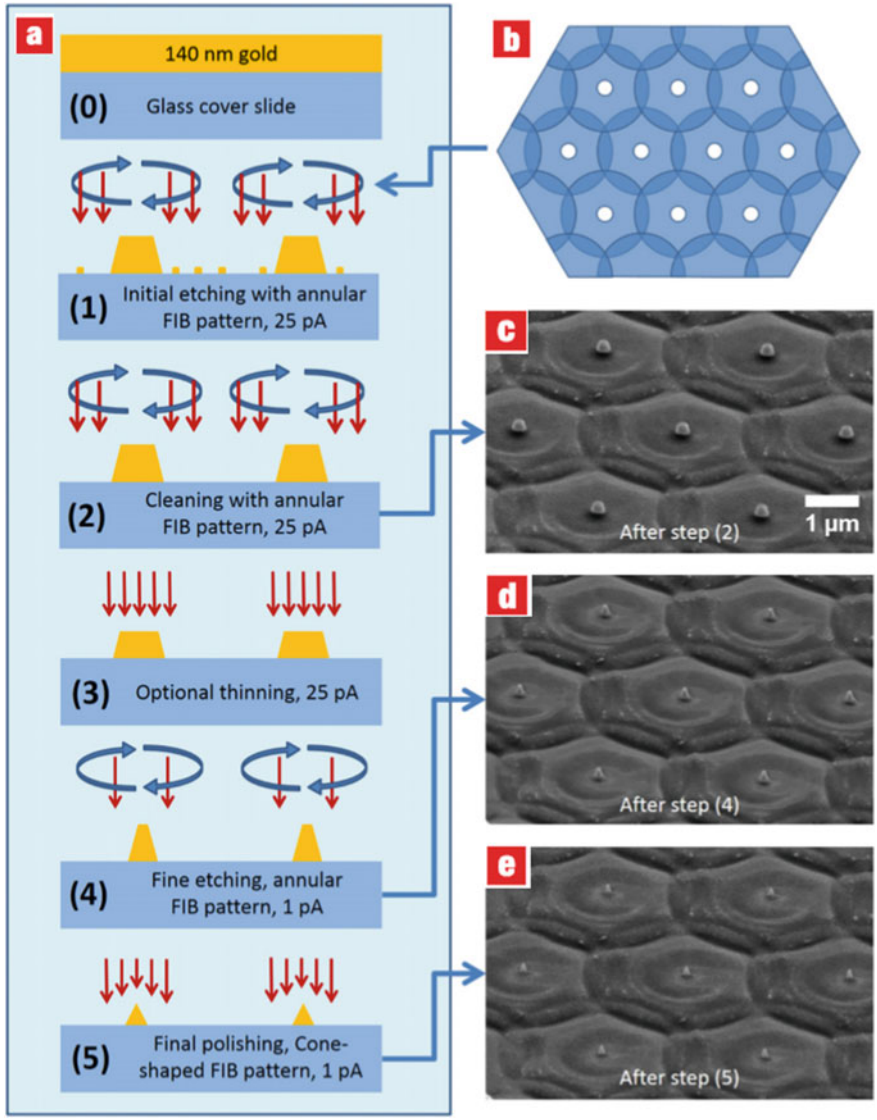

Fig. 3.25 **a** Sketch of the fabrication procedure which is divided into the five steps rough etching, cleaning, optional thinning, fine etching and final polishing. **b** FIB etching pattern for steps 1 and 2. **c**–**e** SEM images of a cone array after steps 2, 4 and 5, respectively

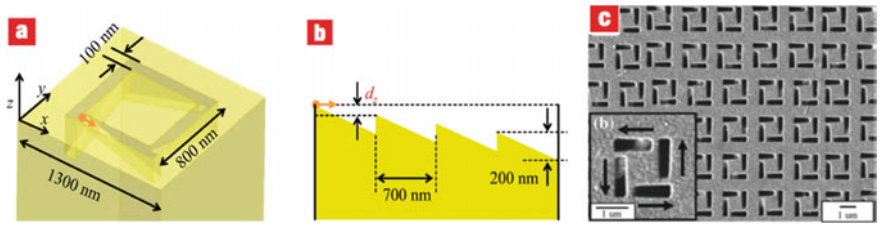

Fig. 3.26 **a** Top view of the unit cell **b** Side view of the developed unit cell **c** SEM image of CCW chiral metasurface on Ag film

Ti) layer were deposited on quartz substrates using electron beam evaporation (Edwards Auto 306 E-Beam Evaporator) at 4×10^{-7} mbar with a deposition rate of 0.07 nm/s. Afterwards, direct FIB milling was carried out to define patterns with varying etching depths. A single-beam (only the ion source) setup (FIB 200, FEI Corporation) was used and the milling current was set to be 70 pA. The structure is shown in Fig. 3.27.

In summary, although both e-beam and ion beam can form a fine probe and are able to pattern ultrahigh resolution whether by exposure or by high energy ion beam micromachining, they are fundamentally handicapped when applied to mass manufacturing of integrated circuits (ICs) because of their low throughput. The serial scanning manner of

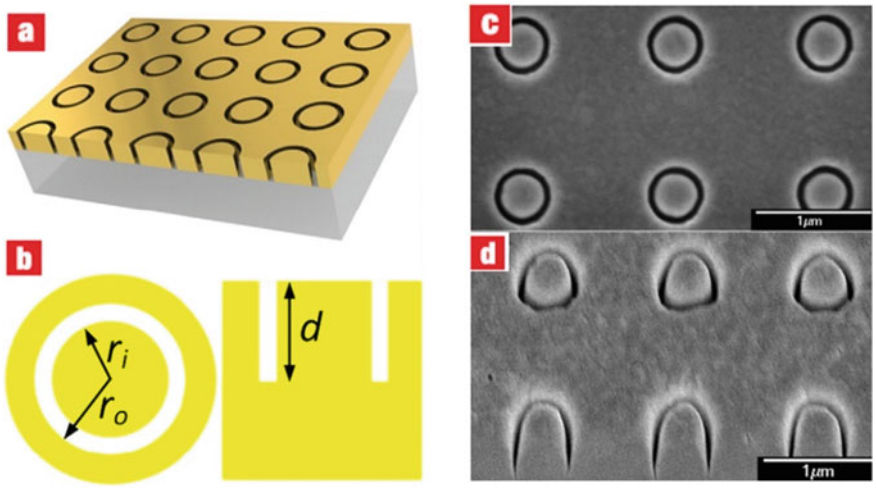

Fig. 3.27 **a** Schematic of gold coaxial apertures on a quartz substrate. **b** Top- and side-view sketches showing critical parameters for a coaxial aperture. **c** Top- and **d** side view SEM images of coaxial apertures fabricated via FIB milling

e-beam or FIB cannot compete with the parallel projection of photons in optical lithography. And it's mainly used in research laboratories or fabricating mask or mold for other fabrication techniques such as nanoimprint lithography (NIL).

3.1.4 Scanning Probe Lithography

Up to this point, we have reviewed photons and charged beams (electrons and ions) based-sub-100-nm and photonic/plasmonic nanofabrication. To be able to fabricate sub-100-nm scale structures using photolithography many tricks apart from short wavelength and high NA have to be used in photon-based lithography, on the other hand, very complicated charged beam systems are required in charged particle-based lithography. For low-cost nanoscale patterning technologies, scanning probe lithography (SPL) is definitely an alternative to expensive photon or charged beam techniques. Another problem with lithography using either photons or charged beams is that they always rely on a polymer material (photo-resist or electron-resist) as an imaging layer.

SPL, however, can be implemented with diverse mechanisms, such as a direct-write approach. SPL uses a scanning probe microscope device (a sharp tip) in close proximity to a sample to pattern nanometer-scale features on the sample. A scanning probe microscope (SPM) is an instrument that monitors the local interaction between a sharp tip (less than 100 nm in radius) and a sample to acquire physical, electrical, or chemical information about the surface with high spatial resolution. Today there are many different types of SPMs used for diverse applications ranging from biological probing to material science to semiconductor metrology [87].

Three major technologies within the SPM family are scanning tunneling microscopy (STM) [88], atomic force microscopy (AFM) [89], and near-field scanning optical microscopy (NSOM) [90]. The first SPM was the STM invented in 1981 by Binnig and Rohrer [88]. As shown in Fig. 3.28a, STM uses a sharpened conducting tip with a bias voltage applied between the tip and the target sample. When the tip is within the atomic range (about 1 nm) of the sample, electrons from the sample begin to tunnel through the gap to the tip or vice versa, depending on the sign of the bias voltage. The exponential dependence of the distance between the tip and the target gives STM its remarkable sensitivity with subangstrom precision vertically and sub-nanometer resolution laterally.

The primary limitation of STM is that it can only be used to image conducting substrates. The AFM was developed to assuage this constraint. The AFM based techniques are less restrictive than that of STM because AFM can be conducted in a normal room environment and can be used to image any kind of materials.

In AFM lithography, the interaction potential between the atoms of the end of the tip and the atoms of the target surface causes a localized force. This force is measured by the deflection of a laser beam which is focused on top the mechanical cantilever on which the tip is attached [91].

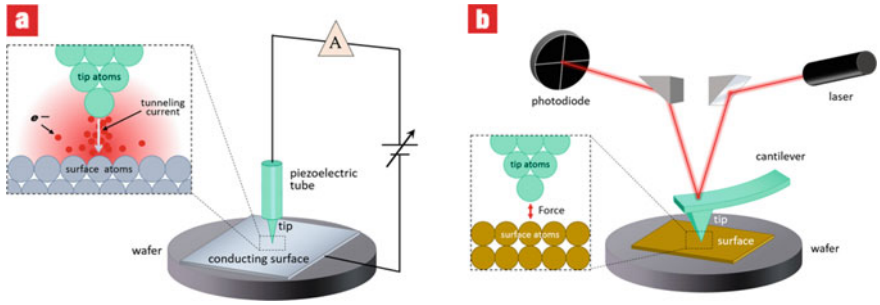

Fig. 3.28 **a** Scanning probe microscope (SPM) **b** atomic force microscopy (AFM)

The third major SPM, in addition to STM and AFM, is the near-field scanning optical microscope (NSOM). The main idea here is to utilize the perturbations of the evanescent waves in the near-field of the sample due to the interaction between the tip and the sample surface, and convert it into propagating light that can be detected via photodetectors (Fig. 3.29).

Two main types of NSOM probes are aperture type NSOM and apertureless techniques. In the first case, a subwavelength size aperture on a scanning tip is used as an optical probe. This is usually an opening in a metal coating of either an optical fiber tip or of a cantilever. Spatial resolution in the aperture type SNOM is, in general, determined by the

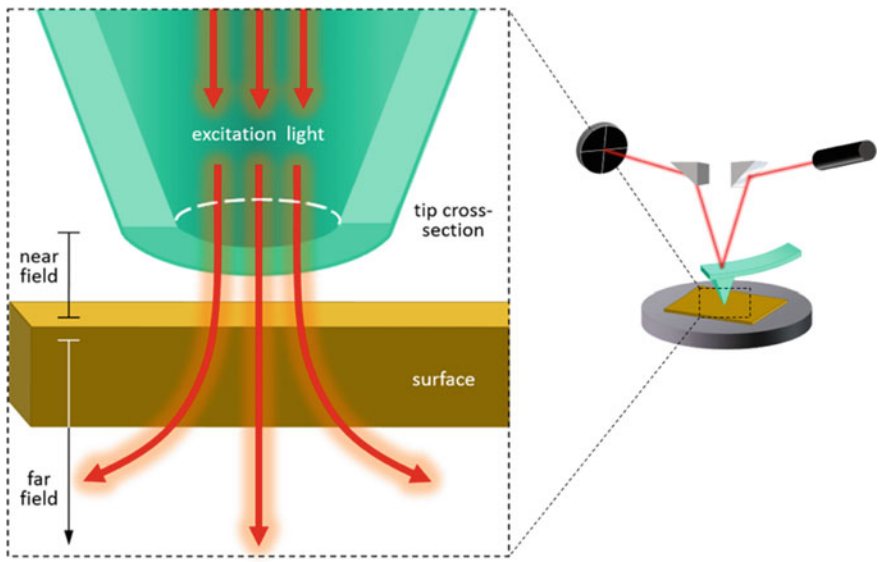

Fig. 3.29 Near-field scanning optical microscope (NSOM) tip and operation

aperture diameter. Apertureless techniques are based on the near-field optical phenomena as well, but do not require passing the light through an aperture. For SPL, the quality of the tip is defined by its crystallinity, surface roughness, and radius of curvature. High-resolution lithographic tools such as focused ion and electron beam have been used to mill, sculpt, and grow sharp tips for high-resolution imaging purposes [72, 92, 93].

For the rest of this section we will concentrate on sub-100-nm and plasmonic structures. Readers for more details about the SPL can refer to the following textbooks [87, 94].

The potential for atomic-level manipulation of matter with the STM has inspired substantial interest in the use of STM as a nanofabrication tool [95]. McCord and Pease, in 1986 [96, 97], for the first time used an STM device to pattern a 20 nm thick polymethylmethacrylate (PMMA) film that acts as a mask for the subsequent deposition or etching process. Later, in 1996, Adams et al. patterned nanoscale futures on silicon exploiting the Hydrogen desorption from Si(001) surface as an ideal probe of electron current density distributions at the sample surface [98]. Even before 1997, the SPL was capable of sub-100-nm patterning, but like e-beam and ion-beam, SPL also suffers from low-throughput because of its serial-patterning process. In order to sooth this problem, fabrication of probe arrays had been widely investigated [99]. SPL containing up to thousand tips have been recently reported [100, 101].

Magno and Bennett used an atomic force microscope to pattern nanometer-scale features in III–V semiconductors by cutting through a thin surface layer of a semiconductor, which is then used as an etch mask. Cuts up to 10 nm deep, which pass through 2–5 nm thick epilayers of both GaSb and InSb, have been formed [102]. Three cuts made in a GaSb/InAs heterostructure are illustrated in Fig. 3.30. Each cut was formed by drawing a silicon nitride AFM tip (spring constant of 0.37 N/m) along the surface for five cycles with a scan rate of 0.1 Hz for a writing rate of 0.02 mm/s.

The applicability of SPL to fabricate metal–semiconductor nanoelectronic devices is more recently investigated in [105]. Molecular resists (MRs), organic small molecules with a monodisperse, low molecular weight and exactly defined spatial extent, are a paradigm shift from traditional polymeric resists sue to its small and uniform pixel size over conventional polymeric resist systems [103]. Efforts in order to achieve sub-20 nm dense and sub-10 nm isolated patterning using conventional photolithography, EUV, and EBL were fruitless. Recently sub-10 nm resolution on bio-compatible and molecular resists using STM and AFM has achieved, which is of a great importance for biomedical and biosensing applications [103, 104].

Three dimensional (3D) nano-printing has attracted great interest recently due to its capability to produce 3D nano-scale objects. Efforts in this area include, direct deposition of small amounts of fluidic materials using a microsyringe [105] and focused laser beam-directed photopolymerization [106]. Although these technologies are capable of printing a wide range of materials into 3D patterns, but miniaturization is difficult due to the diffraction limit. More recently, in 2016, SPL has been used to fabricate 3D nanostructures

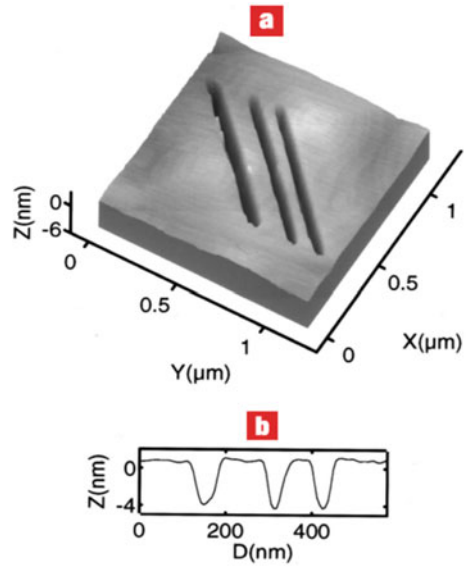

Fig. 3.30 **a** Three 0.5 μm long lines scribed in 5 nm GaSb/20 nm InAs, and **b** profile of the lines showing that they penetrate through the GaSb into the InAs. Reproduced with permission from [102]

[107]. Using AFM and polyelectrolyte (PE) complexes, authors have developed protocols to enable layer-by-layer deposition of PE complexes with nanometer precision in all three dimensions (Fig. 3.31).

In NSOM, patterning of nanostructures is done through a direct writing process which is performed by the produced optical near-field at the tip of a fiber probe. Therefore, the fabrication of nanostructures in a size below the diffraction limit of the light source is attainable. Both contact mode [108] and non-contact mode [109] NSOM has been used in order to fabricate sub-100-nm elements. Non-contact NSOM has been exploited to fabricate 2D photonic structures in [110].

In [111] authors have combined a femtosecond laser and NSOM to fabricate ~20 nm patterns on a spin-coated thin film of UV photoresist (ma-P 1205). The photoresist is sensitive to light radiation from 300 to 440 nm. The patterns are about one-half of the tip aperture size and 1/20 of the wavelength. Fabricated structures are shown in Fig. 3.32.

As mentioned before, NSOM is a direct writing lithography which is a promising plasmonic nanofabrication technique due to its sub-diffraction resolution limit. Zhang's group from UC Berkeley, for the first time, demonstrated a practical plasmonic NSOM system experimentally for near-field lithography [112]. The conic plasmonic lens demonstrated by them consists of a subwavelength aperture at the apex of the cone surrounded by concentric through rings in an Al thin film deposited on a tapered fiber tip, as shown in Fig. 3.33a. By using this method, tight focus of approximately a 100-nm beam spot was obtained which can be seen in Fig. 3.33b, c.

A conventional single aperture NSOM probe features spatial scanning resolution around 100 nm, which is largely determined by the aperture size, rather than by the

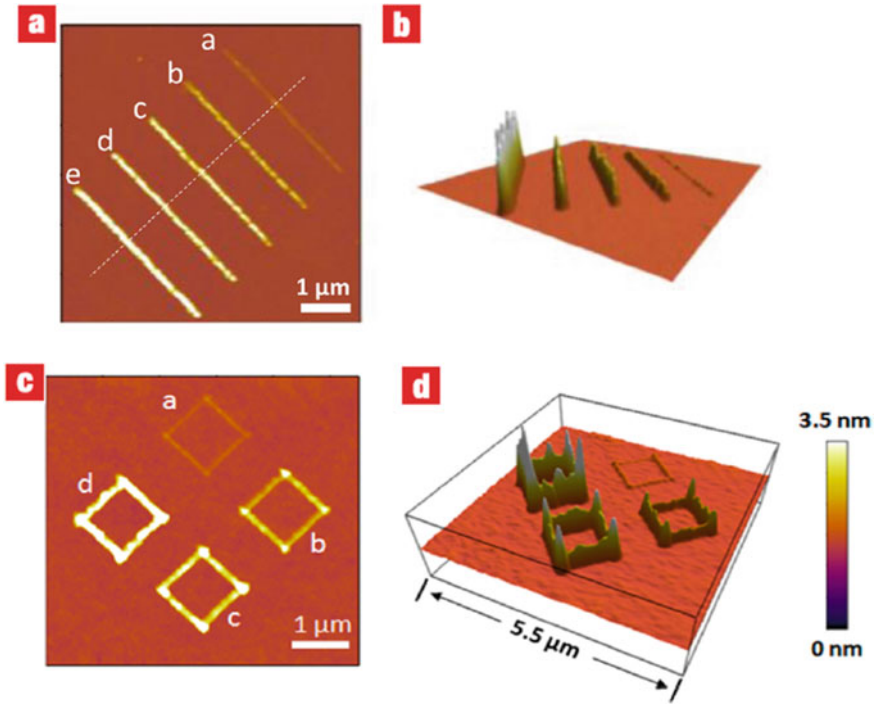

Fig. 3.31 **a** 3D nanoimprinted nanoline array imaged using AFM. **b** 3D view of **a**. **c** AFM images of four "nanocastle turrets" constructed via nanoprinting. Printing was performed at 20 nN delivery force **d** 3D view of **c** Reproduced with permission from [107]

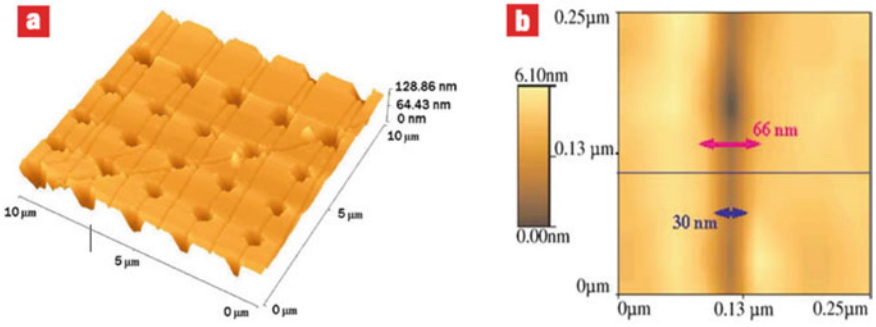

Fig. 3.32 **a** Subwavelength dot arrays at a laser input power coupled into the NSOM probe of 0.24 mW, an exposure time of 200 ms, and writing speed of 4 µm/s. **b** AFM images subwavelength patterns written on the photoresist film by the NSOM combined with the femtosecond laser at a laser input power coupled into the NSOM probe below 0.01 mW and at a writing speed of 6 µm/s

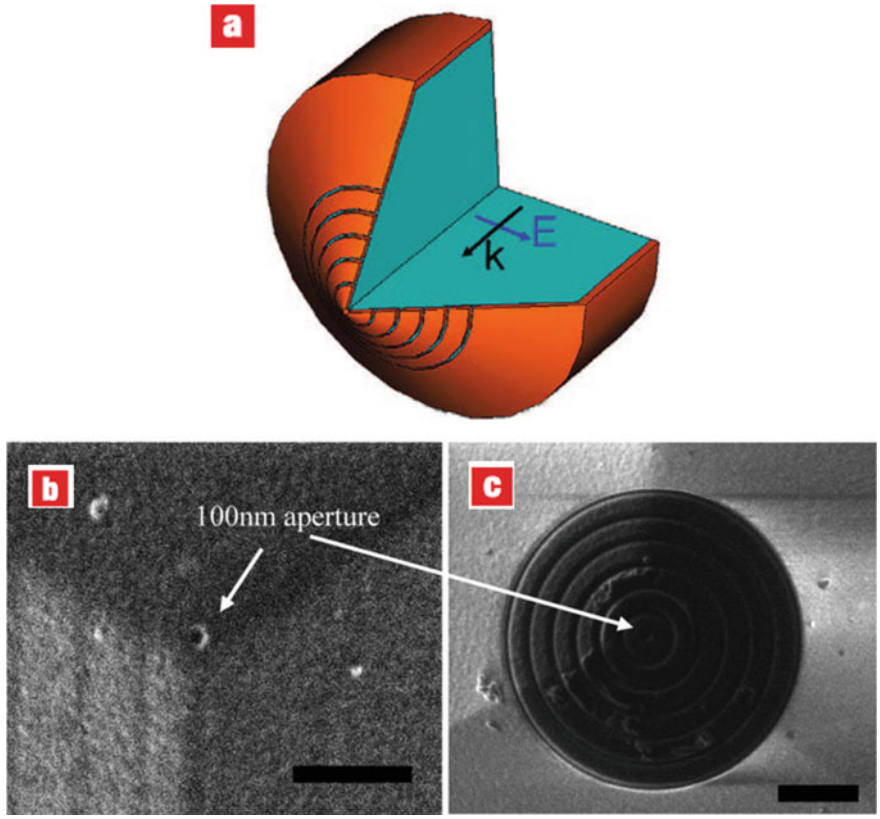

Fig. 3.33 **a** Schematic drawing of the conic plasmonic lens. NSOM probe consists of nanostructured plasmonic lens being fabricated on the end of an optical fiber. 100 nm aperture on the NSOM tip **b** before and **c** after the fabrication of the plasmonic lens. Scale bar is 1 μm

wavelength of operation. Classic NSOM measurements can therefore break the diffraction limit; however, aperture NSOM probes still suffer from low optical throughput, which ultimately limits the resolution due to a low signal-to-noise ratio [113]. Authors in [113] theoretically present a novel concept to design apertureless plasmonic probes for NSOM with enhanced optical power throughput and near-field enhancement. They have utilized the unidirectional surface plasmon polariton (SPP) generation with nanofocusing of SPPs through adiabatic propagation in order to enhance the near field of an apertureless tip. Further improvement in grating NSOM tip can be found in [114–122].

So far in this section, we have reviewed several methods that use SPL in order to fabricate sub-100-nm and plasmonic structures. Many SPM based lithography techniques are

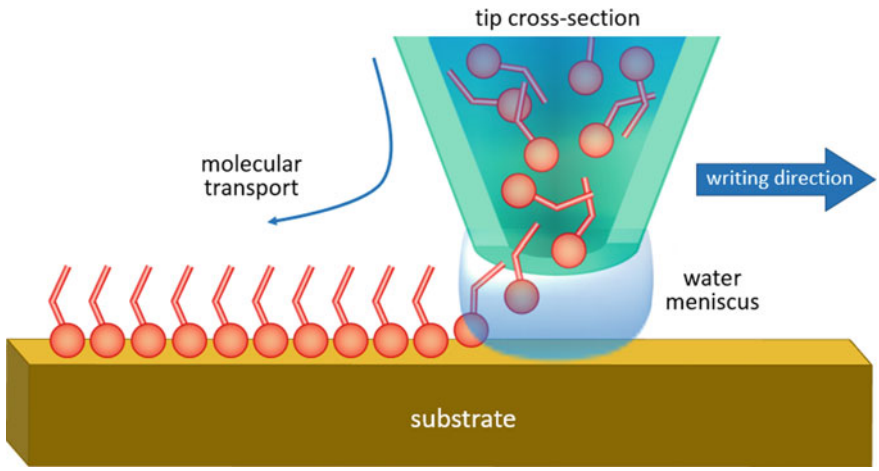

Fig. 3.34 Schematic representation of molecular deposition by DPN through a water meniscus formed between the scanning probe tip and the substrate surface

reported in the literature, including both top-down and bottom-up approaches, for example, scanning electron nanolithography, local anodic oxidation lithography mechanical nanolithography, and dip-pen nanolithography [123–125].

One of the most promising techniques as far as plasmonics is concerned, is the dip-pen nanolithography (DPN) which first was reported in 1999 (Fig. 3.34) [126].

DPN depends on an AFM tip which is coated with a thin film in order to transfer molecules from the tip to a solid substrate (such as gold) of interest through capillary transport. Writing with a fountain pen on paper is a familiar example of how ink is transported from the pen to a substrate. The advantage of DPN over other nanolithography techniques is the capability to selectively place different types of molecules to the same site of a nanostructure, allowing the selective modification of the chemical functionality of the surface in nanoscale. Accurate control of DPN parameters including, temperature, humidity, writing speed, and tip substrate allows one to obtain dots and lines small as 10–15 nm [126]. Parallel DPN has been demonstrated for increasing the speed of patterning [127, 128]. DPN has been recently used for various nanofabrication application [129, 130].

The fabrication of arrays of sub-50-nm gold dots and line structures with deliberately designed 12–100-nm gaps has been reported using DPN (Fig. 3.35) [131].

DPN is a versatile technique and can be applied to a wide range of molecular inks, including proteins [132], colloidal particles [133, 134], and DNA and Bacterial Cells [135, 136].

Integrated nanophotonic circuits made from wide-bandgap semiconductors offer exciting prospects for advanced sensing applications and broadband optical data processing.

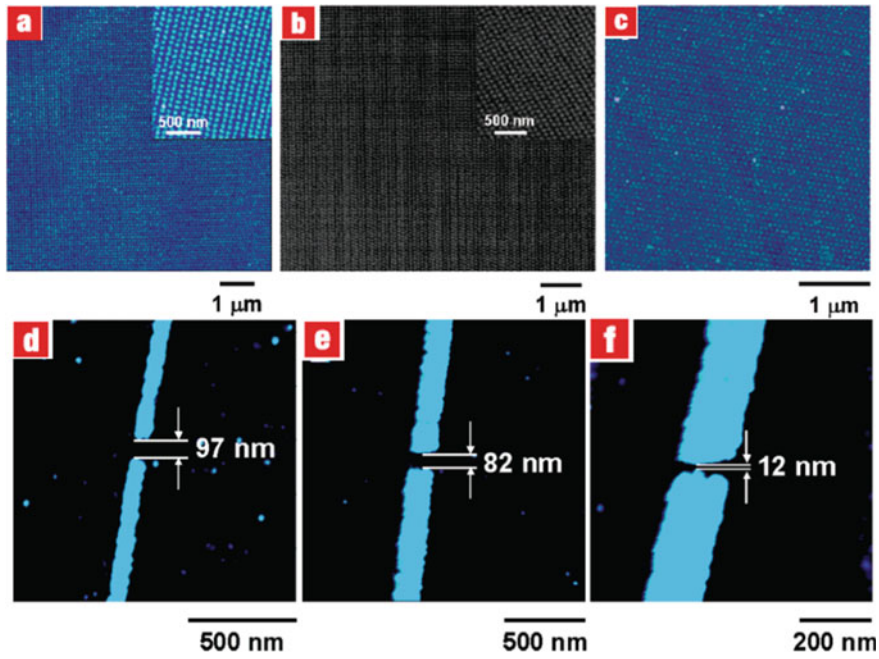

Fig. 3.35 TMAFM topographic images (**a**, **c**) and SEM image (**b**) of an etched MHA/Au/Ti/SiO_x/Si dot nanoarray. The insets are high resolution images. **d–f** TMAFM topographic images of etched MHA/Au/Ti/SiO_x/Si nanogaps

Among the available substrates, diamond is particularly appealing due to its long-term stability, bio-compatibility and chemical inertness [137]. Rath et al. in 2015 have used DPN in order to fabricate nanophotonic circuits based on polished diamond thin films (Fig. 3.36) [137].

Metallic nanoparticle (NP) inks offer a versatile, low-cost option to create conductive traces between two electrodes. In [138] authors used DPN to fabricate thin conductive traces (Ag) on electrode patterns and multiple substrates (SiO_2, Kapton, mica). This can lead to "nano-soldering" and can have many applications in photonic-electronic applications.

The fabrication of plasmonic nanoparticles and fishnet meta-structures have been reported using DPN in [139]. Au fishnet structures with 100-nm width were obtained through alkanethiol DPN printing ("bottom-up" approach) followed by Au wet etching ("top-down" approach) on a thin Au-film-coated silicon substrate. The fabricated fishnet structure is shown in the Fig. 3.37.

In summary, all the three SPMs have been explored for sub-100-nm nanopatterning and plasmonic applications, either by direct exposure of resists or modification of surface. They have the common features of high resolution capability and accurate alignment and

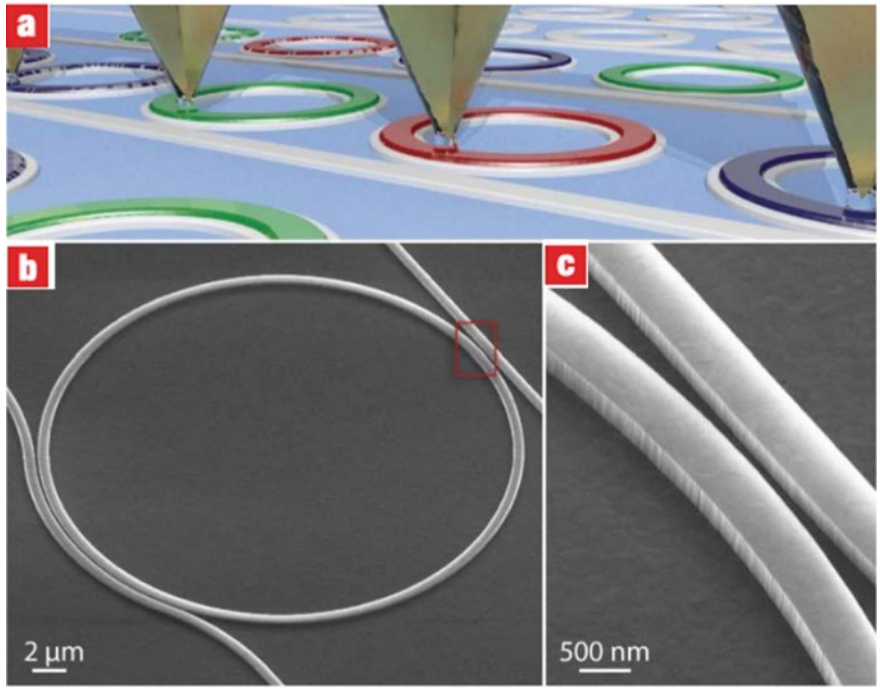

Fig. 3.36 Surface functionalization of diamond nanophotonic components. **a** Dip-pen nanolithography surface functionalization of diamond photonic components. **b** SEM image of fabricated diamond photonic waveguides coupled to a ring resonator. **c** SEM image showing the smooth top surface due to chemical–mechanical planarization and the straight sidewalls due to reactive ion etching

positioning. Conventional SPL suffers the same drawbacks as EBL and FIB, such as low throughput and limited pattern area. More recent techniques use multi-probe and parallel-probe techniques.

3.2 Emerging Techniques

Although costly nanofabrication tools such as e-beam lithography, focused ion beam, or EUV projection lithography can be successfully implemented for construction of plasmonic structures, they do not offer expedient, low cost fabrication methods viable for industrial-scale manufacturing. Alternative techniques to cost-intensive or limited-access fabrication methods with nanometer resolution have been under development for nearly three decades. This section will briefly review the most recent and state of the art sub-100 nm and plasmonic nanofabrication techniques.

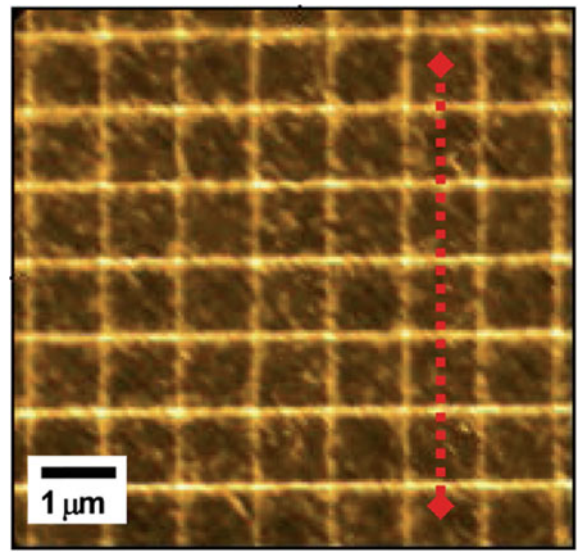

Fig. 3.37 AFM topographic image of the Au fishnet structure fabricated using DPN

3.2.1 Nanoimprint Lithography

Nanoimprint lithography (NIL) is one of the most promising low-cost, high-throughput technologies for nanostructure fabrication [140]. Its principle component is a patterned "mold" or "stamp" that is pressed onto the surface of a polymer, transferring its pattern. In 1995, NIL was proposed and demonstrated as a technology for sub-50 nm nanopatterning [141]. Depending on the type of polymer used, NIL can be done via a thermal or UV curing. Figure 3.38 shows the fabrication procedure of the nanoimprint technologies.

In thermal NIL, first a thermoplastic polymer (PMMA) is applied to a silicon substrate, then the complex is heated to above glass transition temperature (Tg), in which the polymer becomes viscous liquid. Next, the mold is pressed onto the surface with a high pressure. After the mold cavities are filled with molten PMMA, the complex is cooled below the glass transition temperature and the mold peeled off from the PMMA surface. Finally, the residue PMMA on the compressed areas is removed by anisotropic etching.

In order to overcome difficulties associated with thermal NIL, such as alignment errors and the time-consuming process of thermal transition, in 1999 Colburn et al. proposed another nanoimprint method based on the UV curing process [142]. A UV NIL mold must be transparent to UV light, and quartz is a popular choice. Initially, the UV curable polymer is dispensed onto the substrate. The quartz mold is pressed onto the polymer surface with low pressure, then the polymer is exposed to UV to cure and solidify. After curing, the mold is released from the substrate. More details of the physics and the choice of the material and resist can be found in [143–146].

There have been several key achievements in the development of NIL as a nanofabrication technique over the years. In 1997 feature sizes down to 6 nm in PMMA were

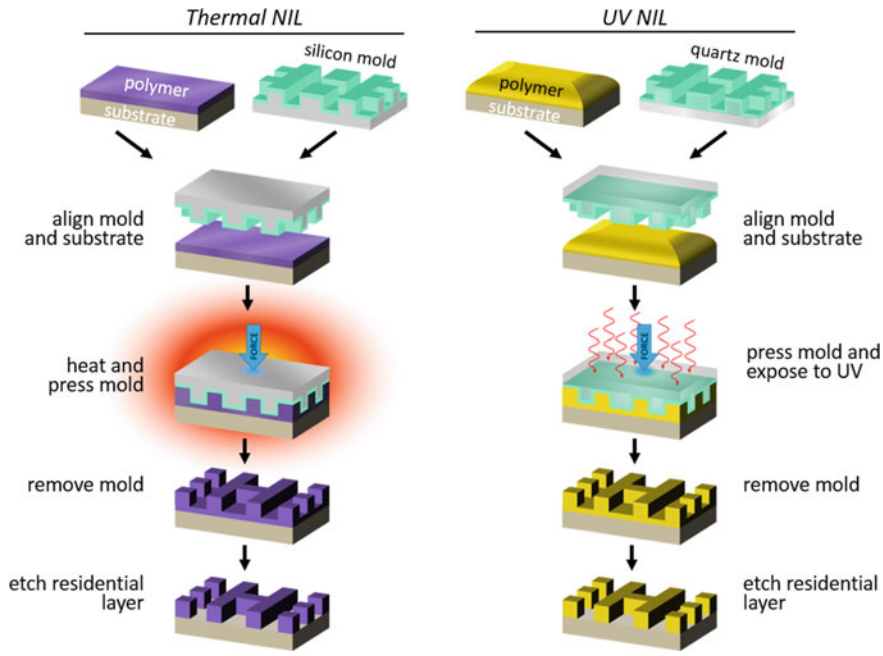

Fig. 3.38 Schematic illustration of thermal and UV NIL

achieved [147]. Sub-100 nm resolution on 6 in. Si substrates was attained in 2000 [148]. In the same year, a new class of polymers developed specifically for NIL triggered its commercial use [149–152]. NIL is capable of forming various geometries including lines, posts, holes, and 3-dimensional tiered structures. Figure 3.39 shows two examples of the plethora of structures that can be formed by NIL [153, 154].

NIL has also been used to fabricate metamaterials and photonic crystals [155–161]. For example, the authors in [155] designed a metamaterial structure with NIL consisting of an array of four metallic L-shaped components (Fig. 3.40).

Since its inception, the fishnet structure has been a staple of metamaterial research, particularly with regard to negative-index metamaterials. It comprises a pair of thin metallic layers, with periodically arrayed rectangular gaps or holes, separated by a thin dielectric filler layer. Recently, the ability to fabricate fishnets by nanoimprinting has been demonstrated in [162]. The structure is fabricated in a pre-deposited three-layer metal–dielectric–metal stack (Fig. 3.41).

NIL has been commonly used for the fabrication of nanoparticle arrays [163–168]. In [169] Skinner et al. explored the possibility of biosensors using silver and aluminum nanohole arrays. Both the arrays, with periodicity of 500 nm and nanohole diameters of 110 nm, were fabricated through NIL. Figure 3.42 shows arrays of gold nanocones

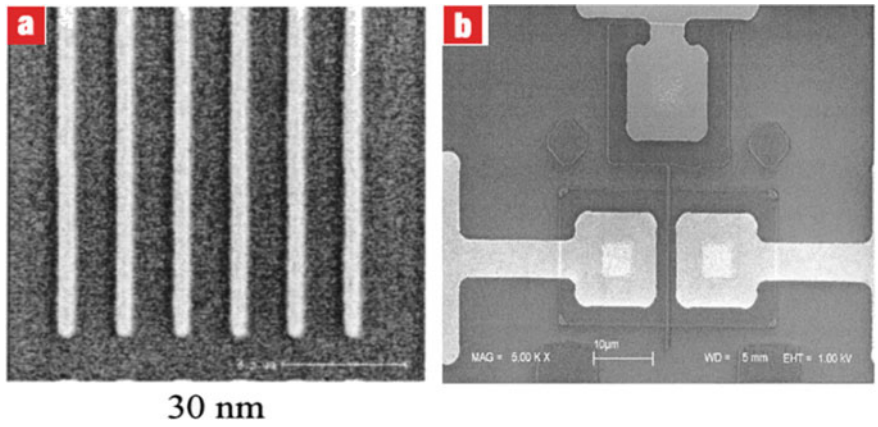

Fig. 3.39 **a** Printed features in the acrylate-based etch barrier [153]. **b** Dark-field optical image of a 1-mm-gate-length MOSFET. Reproduced with permission from [154]

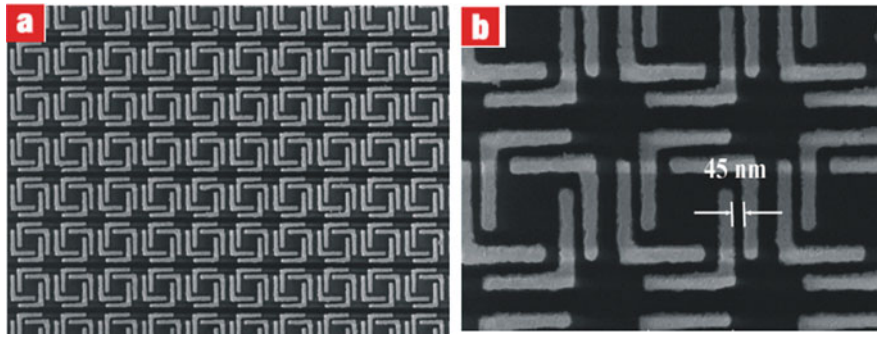

Fig. 3.40 **a** SEM image of a fragment of the final LSR metamaterial with the total size of about 1 mm * 100 μm. **b** SEM image of LSRs demonstrating the smallest feature size of about 45 nm

that have been fabricated using UV-NIL for plasmonic applications [170]. Nanocones are 130 nm in base diameter and are organized in a square grid with a 300 nm period.

Smaller Nanocavities ($\lambda^3/1000$) have been also realized for biosensing applications via UV-NIL [171].

Sharp V groove structures are of a great importance for plasmonic applications since they propagate channel plasmon-polariton modes. In [172, 173] authors have exploited UV-NIL for the fabrication of these structures.

The authors later designed a spectral plasmonic filter with Bragg gratings in plasmonic V-groove waveguides [174]. The structure is presented in Fig. 3.43c.

In [175], researchers fabricated a single device using NIL for the integration of delocalized surface plasmon resonances (SPRs) and localized surface plasmons (LSPs). They

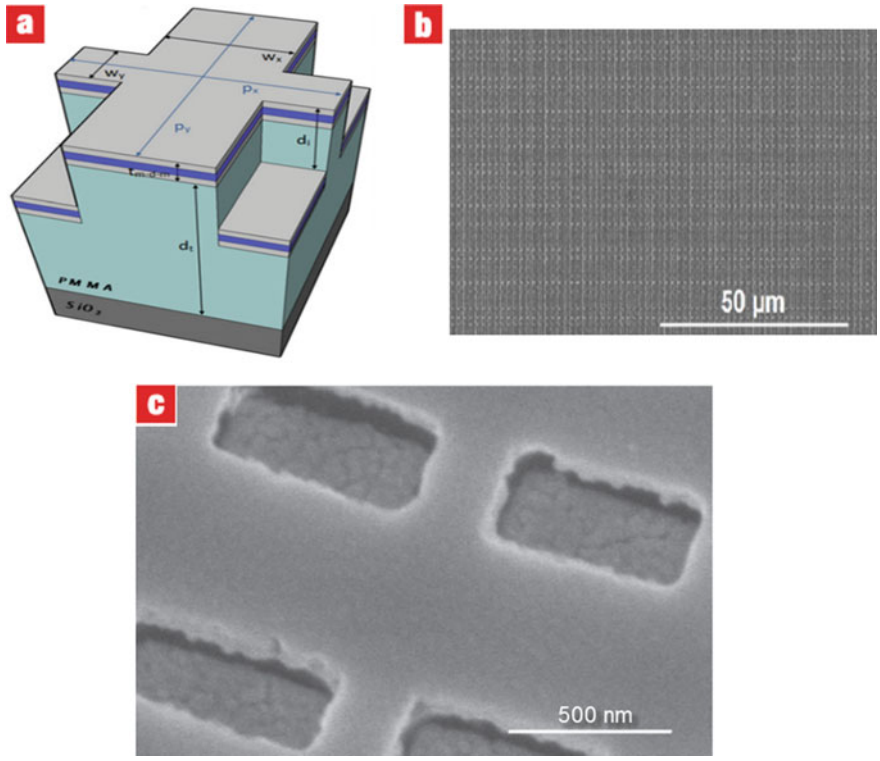

Fig. 3.41 **a** Model of an ideal single unit cell of the fishnet with pillars, the depth of the PMMA layer at its thickest, d_t, is 1000 nm. **b** A micrograph of the fishnet and pillar structure. **c** Angled SEM micrograph of structure. The dark region located between the fishnet and imprinted nano-pillars is PMMA

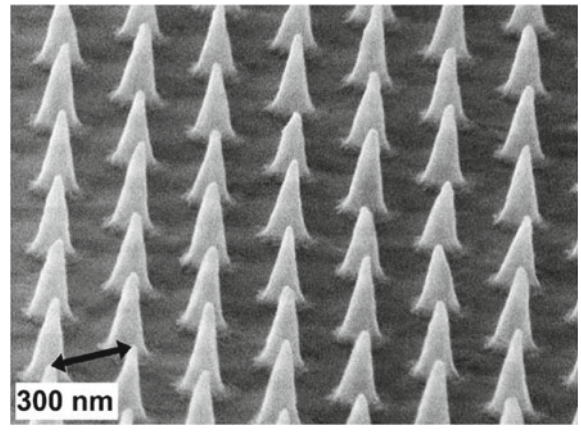

Fig. 3.42 An array of gold nanocones on a silicon substrate. The period is 300 nm, the cone bottom diameter is 130 nm, and the average height is 257 nm (Ti/Au 20/230 nm). The proposed method can be used to fabricate a variety of plasmonic metallic structures

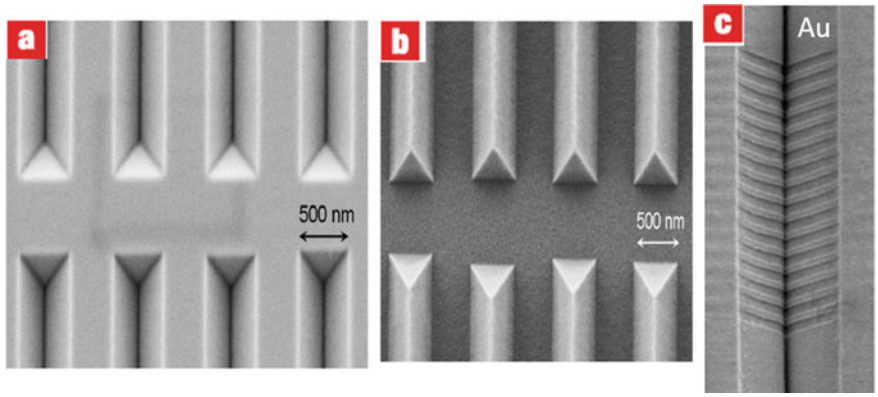

Fig. 3.43 **a**, **b** Silicon stamp, and its replication in PMMA. **c** Tilted SEM image of a V-groove containing a Bragg grating filter (BGF)

created gold nanoparticles from a diblock-copolymer NIL template in order to produce the LSPs.

Optical nanoantennas have generated increasing interest in the past ten years due to their unique abilities, such as breaking the diffraction limit of light, confining optical fields to very small dimensions, and localizing optical sources into the far field [176]. The ability to fabricate these structures is of utmost interest for plasmonic applications. In 2014, Wang et al. fabricated a thin plasmonic infrared absorber, termed "bar shaped disk-coupled dots-on-pillar antenna-array" (bar-D2PA) using NIL [177]. The plasmonic antenna is shown in Fig. 3.44.

The bar-D2PA comprises a dielectric (or semiconductor) bar-shaped pillar array of subwavelength dimensions, with each pillar topped with a metallic bar disk and sided with metallic nanodots (5–10 nm diameter). The nanobar pillars (700 nm long, 185 nm wide, and 70 nm high) are patterned on 1 in. square fused silica chips by NIL.

3.2.2 Soft Lithography

In the previous subsection we showed that molded polymer pattern structures can be transferred from a mold by pressing it into a substrate (NIL). In 1993, Kumar and Whitesides proposed another imprinting technique which uses a soft mold made of polydimethylsiloxane (PDMS) to transfer alkanethiol ink to a substrate coated with gold thin film [178]. The proposed method was later called soft lithography and it became an important replication technique parallel to the NIL. The process is schematically illustrated in Fig. 3.45.

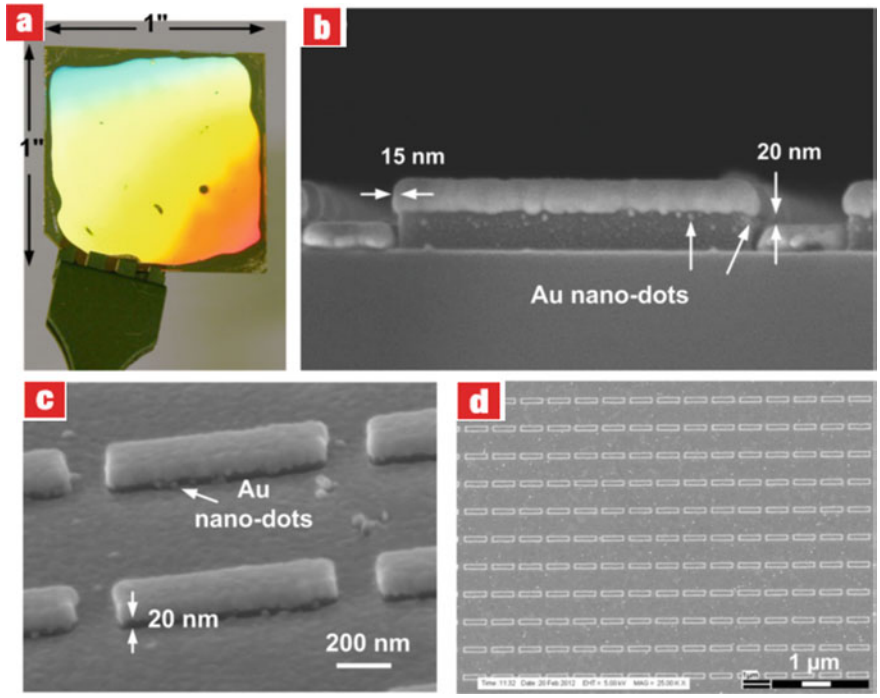

Fig. 3.44 Optical and SEM images of fabricated plasmonic bar-D2PA absorbers: **a** Optical image of 1 in. bar-D2PA absorber chip; **b** Cross-sectional view showing the vertical cavity, the overhang, and the self-assembled nanodots; **c** Side-view (30° titled). **d** Large-scale top-view SEM image. Images reprinted from [177]

First, the PDMS is patterned using conventional lithography techniques (usually photolithography or e-beam lithography) for use as a stamp. Then, the surface of the PDMS is coated with alkanethiol ink and pressed onto a thin gold layer atop a silicon substrate. Unlike NIL, here only the lip regions on the stamp interact with the gold surface while the ink is transferred from stamp to silicon substrate. Figure 3.46 shows a dot array pattern printed by hard PDMS stamp soft lithography [179].

The introduction of composite stamps in 2002 extended the capabilities of soft lithography to the generation of 50–100 nm features. George Whiteside's research group developed an improved two-layer stamp, fashioned of a stiff layer (30–40 μm h-PDMS) supported by a thick flexible layer (3 mm slab of 184 PDMS) [180]. Figure 3.47 shows lines with about 50 nm thickness fabricated using a composite stamp.

Although soft lithography can pattern metals over large areas, this technique has some drawbacks in producing the smooth patterned metals that are required for plasmonics. Besides, periodic elements less than about 80 nm thickness adhere to each other because of displacement during stamp alignment, and they cannot reform into the correct order

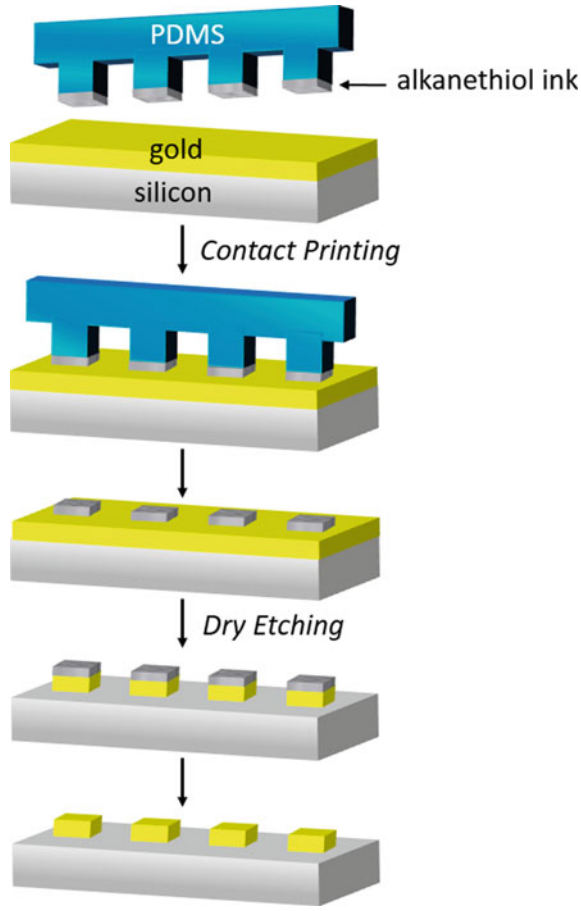

Fig. 3.45 Soft lithography process flow

because of adhesion forces. In 2007, Teri Odom's group developed soft interference lithography (SIL), a high-throughput nanofabrication technique based on soft lithography tailored for plasmonic applications [181]. SIL combines the wafer-scale nanopattern production capabilities of interference lithography with the versatility of soft lithography. SIL utilizes nanoscale patterns generated by interference lithography (IL) as high-quality masters for soft lithography (Fig. 3.48).

To transfer patterns from the master onto a photoresist, the SIL photomask is placed in contact with a positive-tone photoresist and then exposed to UV light. Developing the photoresist at this point produces posts with the same lateral dimensions as the IL master (that is, infinite arrays). If the photoresist is subjected again through a chromium mask patterned with microscale features and then developed, patches of post arrays (referred to as finite arrays) form. The photoresist patterns are mapped onto metal or dielectric

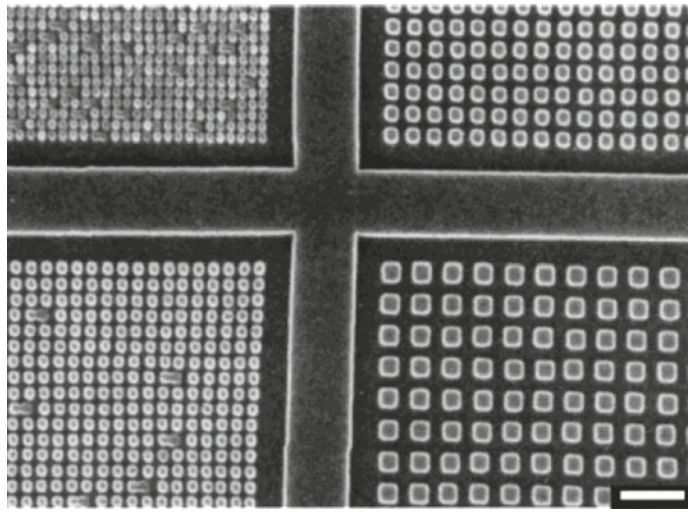

Fig. 3.46 Squares of 250 * 250 nm^2 (lower right quadrant) structures down to 80 nm (upper left quadrant). The height of the structures is 100 nm. Bar = 1 μm. Figure taken from [179]

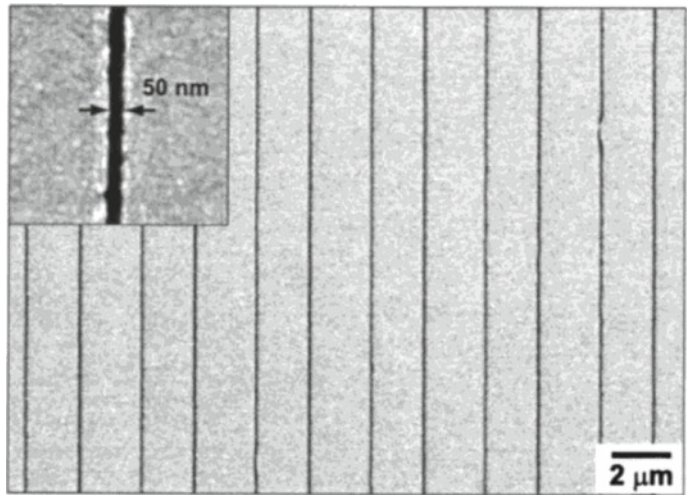

Fig. 3.47 Scanning electron micrograph of uniform, 50 nm lines produced from a composite soft lithography stamp. Figure taken from [180]

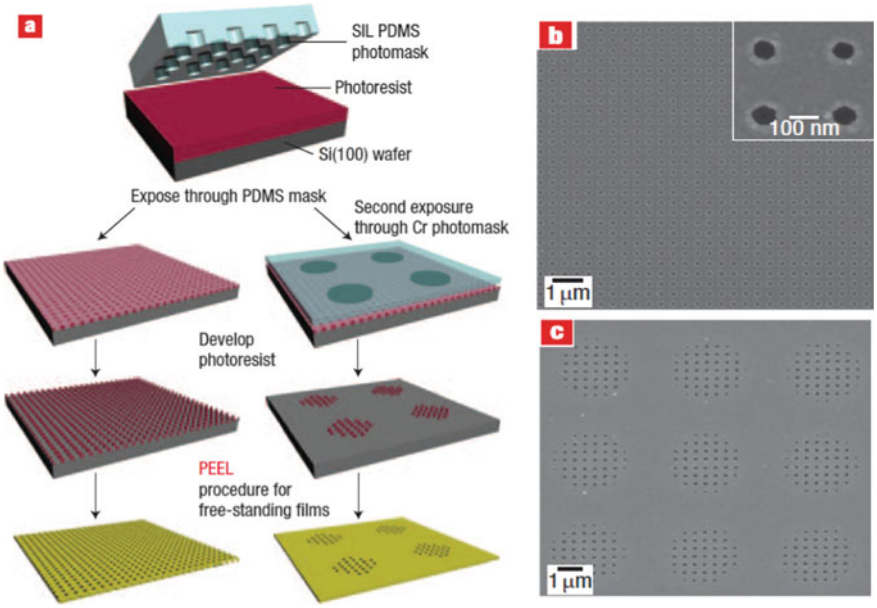

Fig. 3.48 **a** Illustrating the SIL fabrication process of infinite nanohole arrays and finite-sized patches of holes. **b** Infinite silicon nanohole arrays with 100-nm size holes. **c** Silicon patch nanohole array

films using a soft nanofabrication procedure called PEEL (Phase-shifting photolithography, Etching, Electron-beam deposition, and Lift-off) [181–183]. Figure 3.49 shows nanopyramidal gratings for screening plasmonic materials [184] fabricated via SIL. The structure has been used to generate plasmon dispersion diagrams for Al, Ag, Au, Cu, and Pd.

In [185] authors have utilized the angle-dependent optical properties of rhombic plasmonic crystals in order to tune resonances from SPPs propagating in different directions. The same concept has been applied to improve real-time biosensing [186]. Both structures were actuated with SIL.

3.2.3 Nanosphere Lithography

To enhance the consistency of particle size and arrangement, in 1995 Van Duyne and colleagues proposed a unique and simple fabrication method for metal nanoparticles called nanosphere lithography (NSL) [187]. NSL utilizes tightly packed polystyrene spheres on a substrate surface as a masking layer. The method is schematically shown in Fig. 3.50.

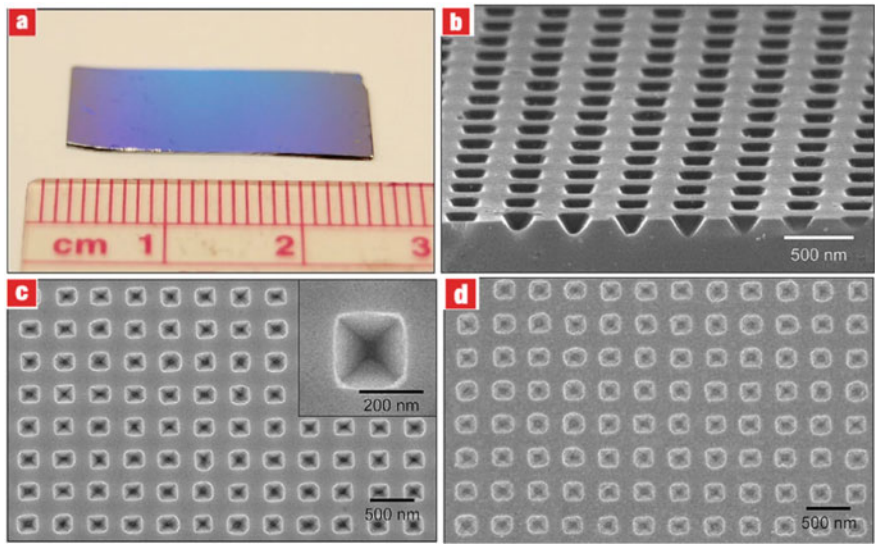

Fig. 3.49 Plasmonic materials on pyramidal nanograting. Optical micrograph **a** SEM **b**, **c** images of a large-area (0.9 cm × 2.3 cm) silicon pyramidal slit-grating. **d** SEM image of a 170-nm-thick Au film deposited on the silicon master. Reprinted from [184]

The first step in NSL is dropping polystyrene nanospheres on a pristine, pre-prepared glass substrate. The hexagonally close-packed (Fischer pattern) nanospheres create a crystal structure in which the gaps between the spheres form a regular array of dots. Next, the array is filled in with thermally evaporated silver. After the deposition, the polystyrene spheres are removed by agitating (sonicating) the entire substrate in either CH_2Cl_2 acid or absolute ethanol, and the product is an array of triangular dots (Fig. 3.50). As an example, Fig. 3.51 shows the triangular nanoparticle shape after deposition by NSL [188].

Nanosphere optical lithography (NSOL) utilizes polystyrene or silica nanospheres on a substrate surface as a lens array [189]. UV light is then used to pattern the photoresist using light spots under the nanospheres.

Figure 3.52a shows an SEM image of a typical monolayer of silica spheres with the diameter of about 90 nm formed on top of the photoresist. Figure 3.52b shows the top view of the SEM images of the developed samples. The minimum diameter of the hole is about 250 nm. The ratio of the feature size to the wavelength is about 0.625. The hole lattice has a periodicity of about 90 nm, almost identical to the diameter of the spheres. Figure 3.52c is the cross-sectional image of a hole in the AZ5214 photoresist. It shows a high aspect ratio, which can be utilized for demanding lift-off and deep dry etching processes. The process could be modified to produce holes with negative sidewall slopes for a more aggressive lift-off process [189].

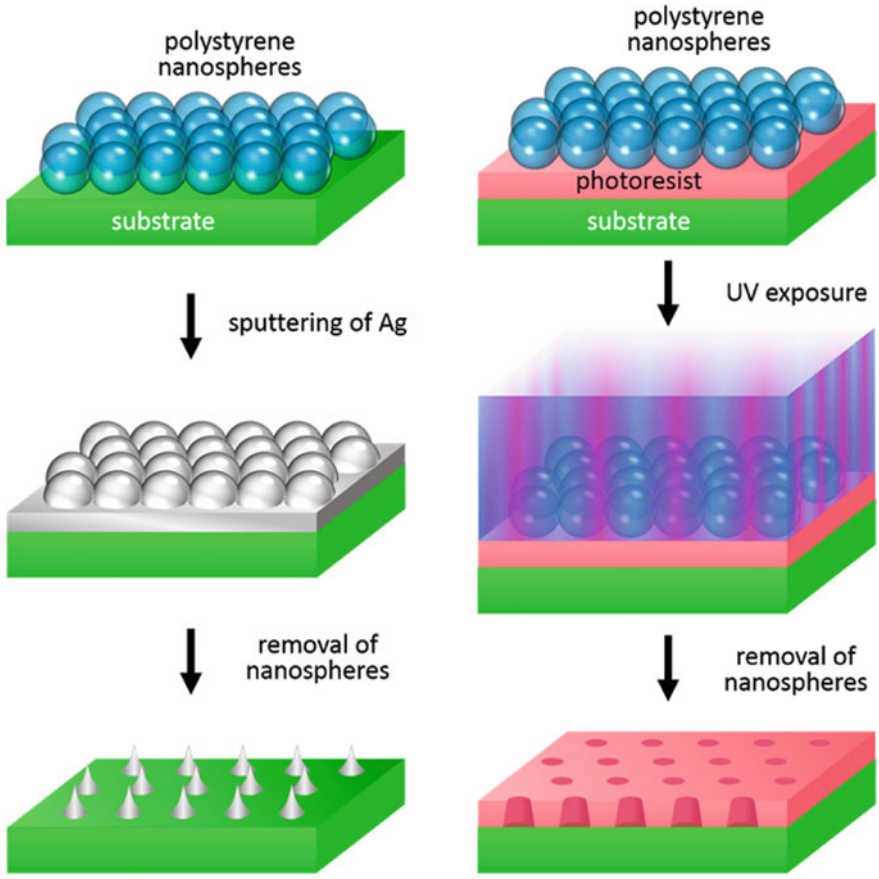

Fig. 3.50 (Left) Nanosphere lithography (NSL) process and (right) nanosphere optical lithography (NSOL)

More recently in 2015, feature sizes smaller than 100 nm have been achieved using NSL [190]. Figure 3.53 shows periodic unit cells produced by a single-exposure deep-UV projection lithography at 254 nm wavelength.

NSL has been widely used for the fabrication of plasmonic structures, nanowires, and arrays [167, 191–201]. Figure 3.54 shows an array of gold nanocones fabricated with NSL.

3.2.4 Nanofabrication by Self-assembly

Regardless of the maturity and flexibility of the lithographic techniques (all the aforementioned methods), difficulties remain in achieving the high-quality metal nanostructures that

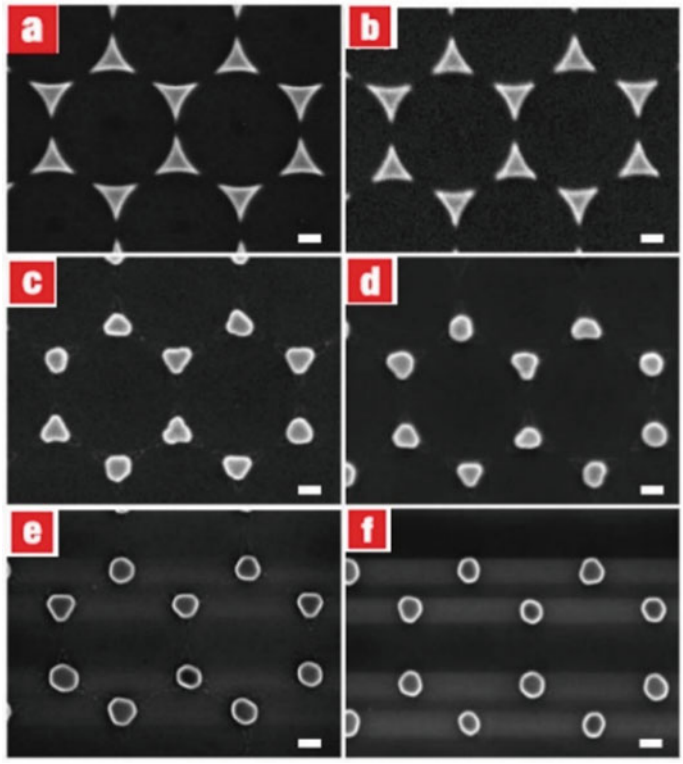

Fig. 3.51 SEM images of **a** deposited and **b**–**f** annealed Au nanoparticles. The pattern was annealed gradually with increasing temperatures at each phase, the images were taken after each annealing step. The corresponding annealing temperatures were **b** 205, **c** 325, **d** 451, **e** 700, and **f** 930 °C. Scale bars = 200 nm

are needed for the exploitation of plasmon effects. It is highly challenging to use EBL or FIB for the mass-production of features with dimensions below 4–10 nm. On the other hand, due to metal evaporation in which size, direction, and arrangement are not properly controlled, nanoparticles contain surface roughness which makes it challenging to obtain the sharp corners and nanometer scale interparticle gaps that are of absolute necessity in nanoparticle plasmonics.

To achieve greater control over the atomic-scale structure of metal nanoparticles, the complementary technique of self-assembly has been extensively pursued [202–204]. In this section, we will first introduce self-assembly and then review a few fabricated sub-100 nm and plasmonic structures and devices.

Self-assembly, a bottom-up approach, is defined as the spontaneous association of molecules into a defined three-dimensional geometry under a defined condition [195]. Self-assembly can be classified by the nature of building units as atomic, molecular, and

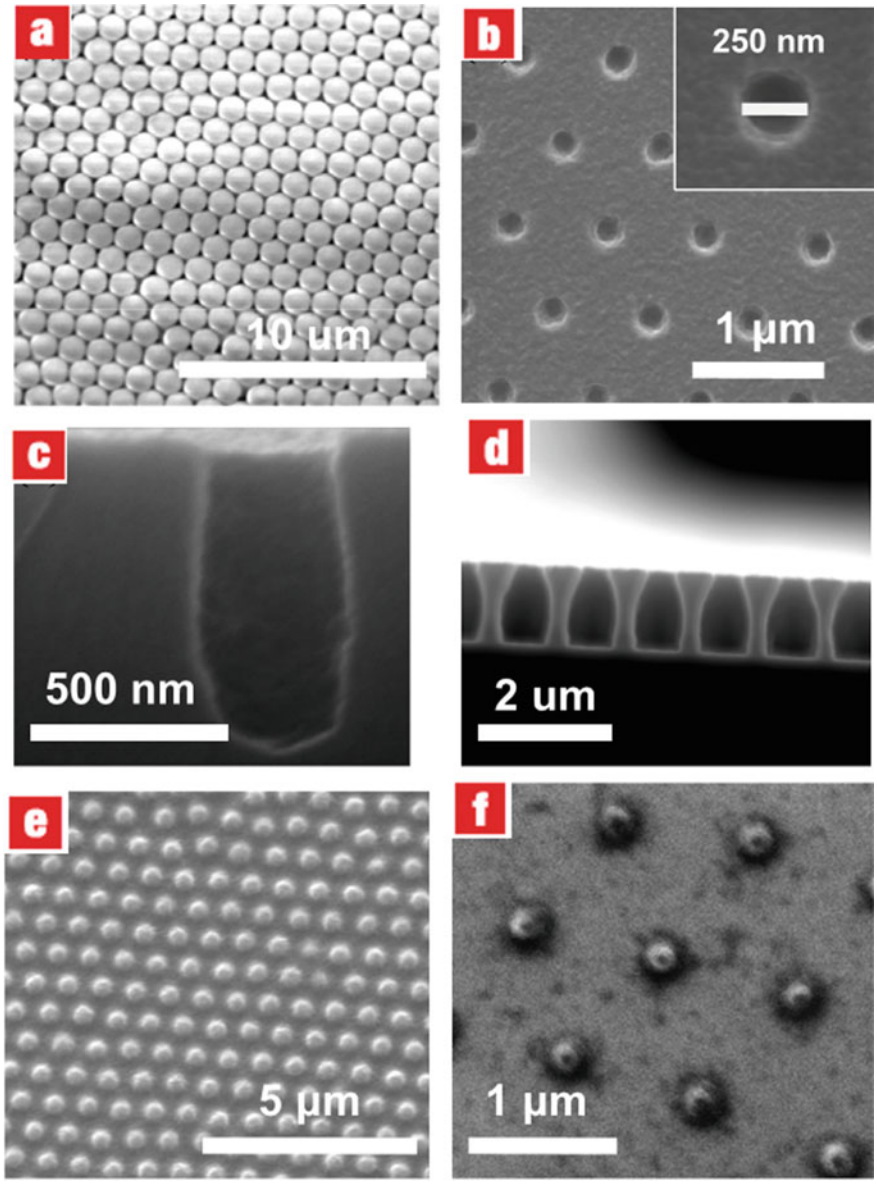

Fig. 3.52 SEM images of **a** a single layer of microspheres (0.97 µm diameter) deposited on top of the photoresist; **b** AZ5214 nanoholes (inset is a more enlarged image), after sphere removal and photoresist developing; **c** a cross section of nanopatterns formed by silica spheres and AZ5214 photoresist, **d** a cross section of nanopatterns formed by silica spheres and AZ5214 photoresist, **e** AZ5214 photoresist used as negative photoresist and formed nanopillars; **f** Shipley 1805 photoresist used as negative photoresist [189]

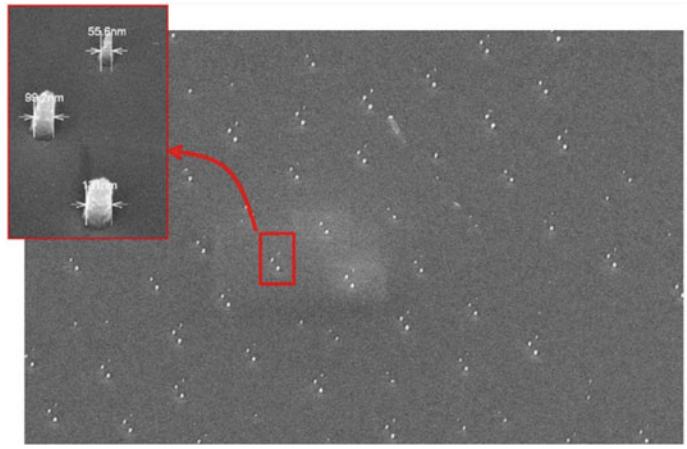

Fig. 3.53 SEM image of a periodic array of unit cells. Each unit cell consists of differently sized nanopillars, with a minimum size of about 55 nm (see inset). This pattern was produced with a single NSP exposure. Image from [190]

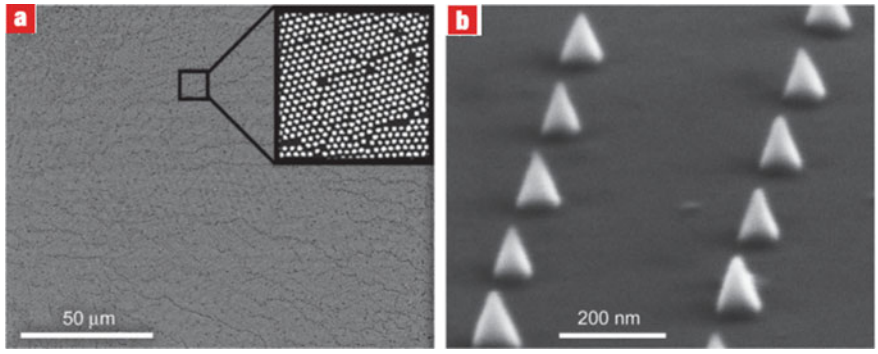

Fig. 3.54 **a** SEM image of gold nanocones fabricated over an area of larger than 100 μm^2. The enlarged image presents the homogeneous hexagonal pattern of cones with single grain boundaries. **b** Procedure (double layer and alumina mask) utilized to a silver film leads to sharp-tipped silver cones with a smaller tip aperture angle than for the gold cones

colloidal, or by the system where it occurs as biological or interfacial. Figure 3.55 shows its classification and the scale.

Self-assembly can be further classified, where single components work together to construct a larger structure without the aid of external forces, or templated, where single components cooperate with each other and with an external force to construct a larger structure [205]. In the rest of this section, we will briefly discuss the dominant self-assembly techniques for plasmonic fabrication.

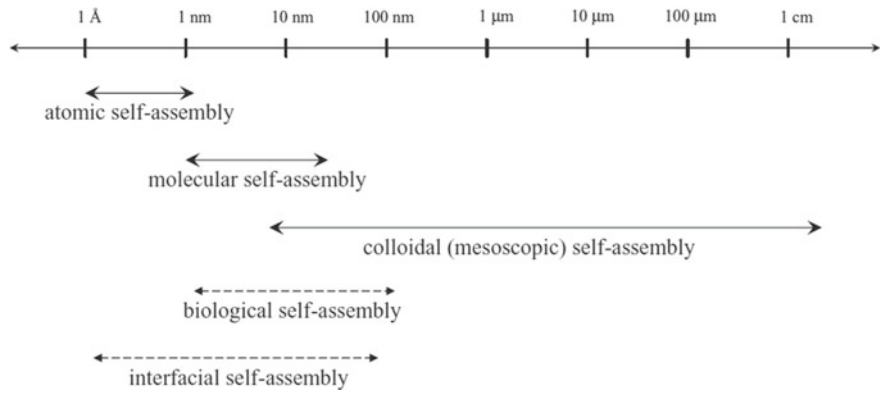

Fig. 3.55 Classification of self-assemblies based on the nature of building units and on the system where the self-assembly occurs

Self-assembled monolayers

Self-assembled monolayers (SAMs) are ordered molecular assemblies formed by the spontaneous adsorption of an active surfactant on a solid surface. SAMs are typically made by exposing the substrate to the vapor of the reactive species. The most renowned SAMs are n-alkanethiolates $CH_3(CH_2)_nS^-$ on Au(111) surfaces [206]. The first step in forming ordered SAMs is the absorption process, where sulfur atoms chemisorb to Au(111). This is feasible because of the strong affinity to transition metal surfaces that sulfur compounds exhibit, due to their ability to form multiple bonds with surface metal clusters. Sulfur atoms bonded to the gold surface bring the alkyl chains into close contact. These contacts freeze out configurational entropy and lead to an ordered structure (Fig. 3.56) [207].

In SAM contact printing (also called microcontact or nanotransfer printing), the transfer of thiol molecules onto a gold surface takes only a few seconds. Different SAM molecules have been used, depending on the metal. For example, alkanethiols have been used for gold and silver [208], alkanephosphonic acids for aluminum [209], and alkylphosphines for gold patterning [210].

Figure 3.57 illustrates the procedure for multilayer 3D SAM contact printing. In the first step, the stamp is coated with a thin layer of gold using physical vapor deposition. Then the pattern is transferred onto a layer of SAM which covers the substrate. The SAM layer provides exposed thiol groups that can bond to the Au layer.

SAMs have been commonly used in polymer-based soft lithography for the fabrication of sub-100 nm and plasmonic structures [211–214]. Figure 3.58 shows a printed pattern with high edge resolution (5–15 nm) in the geometry of a two-dimensional photonic crystal waveguide [214–216]. The pattern was transferred by a condensation reaction between surface silanols (Si–OH) on the PDMS and titanols (Ti–OH) on oxidized plasma.

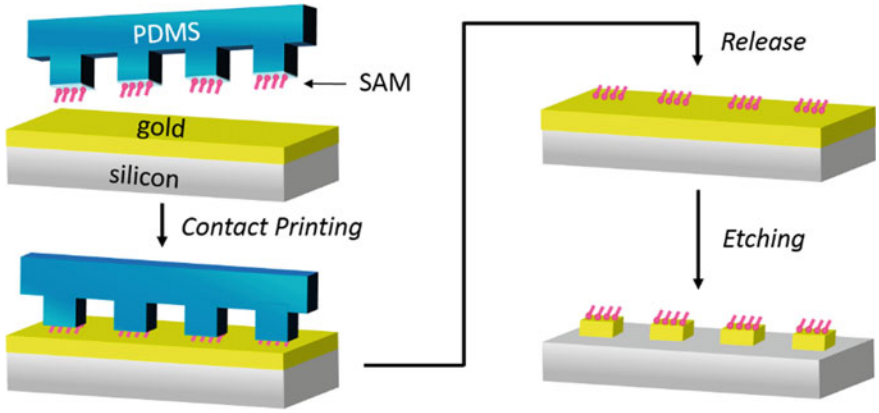

Fig. 3.56 A standard printing process based on SAM (contact printing). First, the PDMS mold is coated with SAMs and the substrate is covered with thin metal film. Contact printing then transfers the pattern onto the metal film

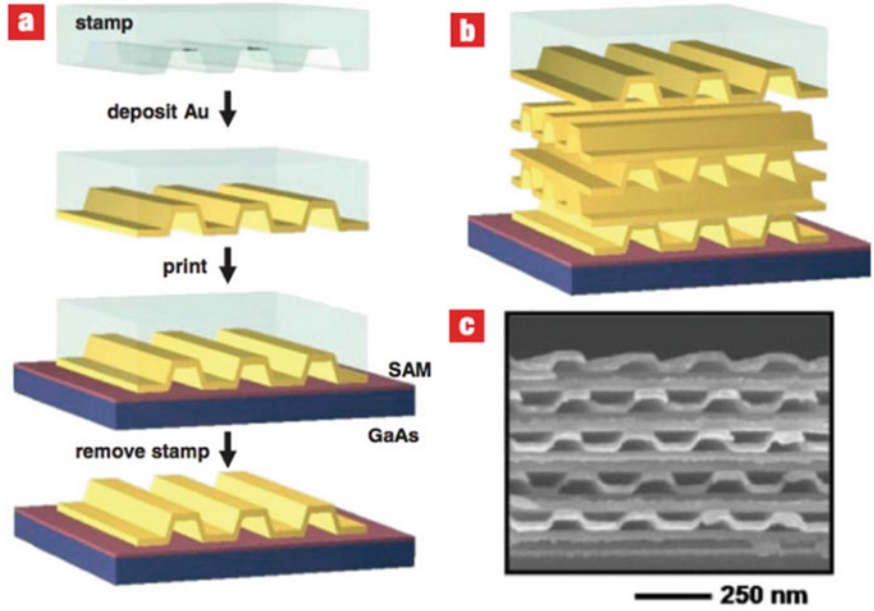

Fig. 3.57 Schematic illustration of SAM contact printing. A wide variety of patterned metal nanostructures and 3D stacks can be fabricated using pattern transfer of thin gold layers. (**a**) fabrication flow (**b**) 3-D visualization of fabricated structures (**c**) SEM of fabricated device. The 3D structure shown in figure c is difficult to fabricate by other techniques

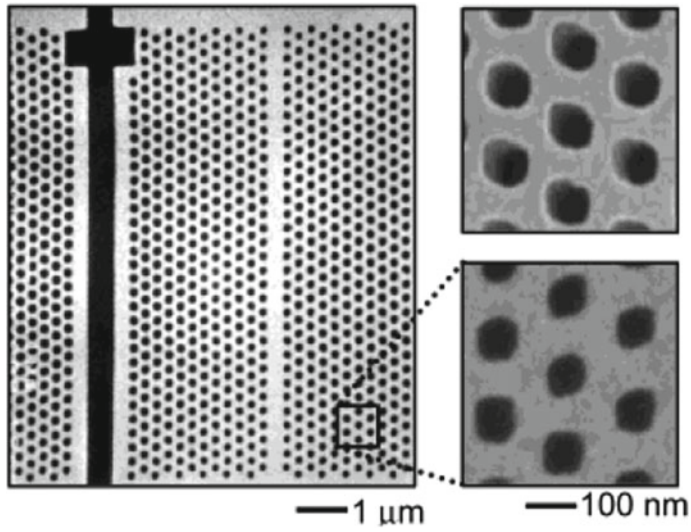

Fig. 3.58 SEM of a Ti–Au pattern in the geometry of a photonic crystal waveguide. Micrographs on the right display magnified views before transfer (top right frame) and the printed pattern (bottom right frame)

In this case, a condensation reaction produces bridging –Ti–O–Si– bonds that facilitate the transfer.

Using SAMs, gap sizes of less than 0.5 nm have been experimentally achieved [217]. Other applications of SAMs include bio-patterning [218–220], semiconductor electronics [221–224], organic Photovoltaic devices [225], and localized plasmon resonance (LSPR) spectroscopy [226–229].

Block Copolymer Self-assembly

The past decade has witnessed the development of new techniques to pattern polymers. Polymers have relatively low cost, good mechanical properties, and compatibility with most patterning techniques. Block copolymers represent a group of polymer materials which offer endless possibilities to assemble into different shapes and forms. A block copolymer molecule consists of two or more chemically different polymer chains joined by covalent bonds. A block copolymer can self-assemble to form a nanoscale structure with a domain spacing from 10 to 200 nm.

If let alone, they will shape some sort of unordered, "fingerprint" pattern microdomains (different spatial domains), a pattern which is composed of highly defective blocks, as shown in Fig. 3.59a [230].

To achieve long-range ordered microdomain separation, it is necessary to align nanostructures in block copolymer films. This can be performed by several methodologies, including solvent evaporation, electric fields, and chemical or mechanical patterning [230].

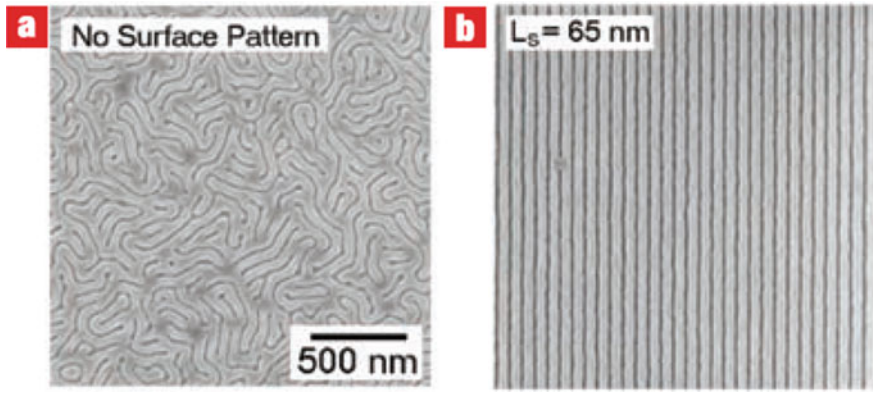

Fig. 3.59 **a** Top-down SEM image of the ternary PS-b-PMMA/PS/PMMA blend on an unpatterned neutral surface of PS-r-PMMA. **b** Ternary blend on linear surface patterns with LS of 60 nm, patterns over arbitrarily large areas in registry with lithographically defined chemical surface patterns [230]

Ordered, ultrahigh-density arrays of nanopores with high aspect ratios can be obtained from the copolymer film by chemical modification. The dimensions and lateral density of the array are determined by segmental interactions and the copolymer molecular weight [231]. The schematic representation of the process is presented in Fig. 3.60.

The fabricated nanohold and nanocavities via block copolymers have commonly been exploited for photonic crystal apllication [232, 233]. Core–shell nanostructures are attractive plasmonic structures due to thier versatile tunability of plasmonic properties along with the independent control of core size, shell thickness, and corresponding chemical composition, but they commonly suffer from difficult synthetic procedures [234]. Cha et al. in 2015, presented a reliable and controllable route to a highly ordered uniform Au@Ag core–shell nanoparticle array via block copolymer lithography. Figure 3.61 shows the fabricated nanoparticles. First, asymmetric polystyreneblock-poly(4-vinylpyridine) thin films were spin-cast onto a substrate. Solvent annealing afterwards induces vertically oriented hexagonal P4VP nanocylinder arrays enclosed by the PS matrix. The structure is immersed in $HAuCl_4$ acidic aqueous solution, then oxygen plasma etching is applied to remove polymer, leaving Au nanoparticles. Finally, deposition of Ag on the Au seeds generates Au@Ag core–shell structure.

More recent applications of block copolymer self-assemly are plasmonic gold nanoarrays [235], metalic nanowire arrays [236], plasmonic sensors [237], plasmonic vesicles [238, 239], and plasmonic nanoclusters for imaging [240].

Colloidal self-assembly

Colloidal self-assembly refers to self-assembly of particles or spheres with diameter from micrometers to nanometers in a liquid suspension. Colloidal self-assembly can be used in two forms for nanofabrication of sub-100 nm and plasmonic structures. The first way is

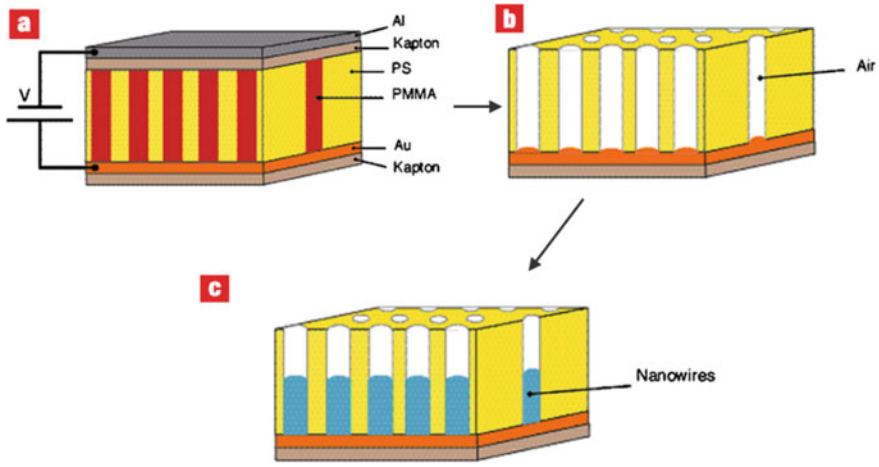

Fig. 3.60 A schematic representation of high density nanowire fabrication in a polymer matrix. **a** An asymmetric diblock copolymer annealed above the glass transition temperature of the copolymer between two electrodes under an applied electric field, forming a hexagonal array of cylinders oriented normal to the film surface. **b** After removal of the minor component, a nanoporous film is formed. **c** By electrodeposition, nanowires can be grown in the porous template, forming an array of nanowires in a polymer matrix [231]

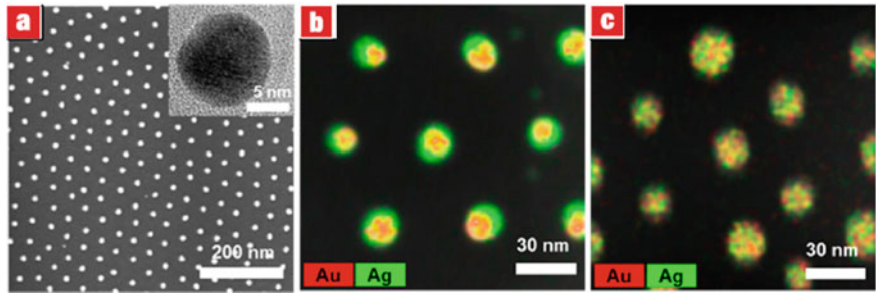

Fig. 3.61 **a** SEM image of Au NPs. Inset shows the HRTEM image of the Au NP. **b** EDS elemental mapping of the Au@Ag core–shell NP array. **c** EDS elemental mapping of the AuAg alloy NP array [234]

to fabricate the nanostructures inside the liquid, which we will refer to here as colloidal synthesis [241–243]. The second method, colloidal lithography [244], uses the fabricated nanostructures via colloidal synthesis as masks for other fabrication techniques, such as photolithography or nanoimprint lithography.

Triangular nanoprisms, are a class of nanostructures that have generated ardent interest within plasmonics due to their uncommon optical properties [245–248]. Both gold

and silver nanoprisms have been constructed using colloidal synthesis. In [249] authors used a three-step growth of seeds in an aqueous solution containing a capping agent (cetyltrimethylammonium bromide (CTAB)), gold ions ($HAuCl_4 \cdot 3H_2O$), reducing agent (ascorbic acid), and NaOH [249]. Other approaches such as dual-beam excitation have also exploited (Fig. 3.62) [250].

Colloidal synthesis has been widely used for the fabrication of plasmonic nanoparticles. Examples include nanospheres [251], nanostars [252, 253], nanorods [254], and nanoporous structures [2].

Colloidal lithography relies on colloidal crystals as masks for etching and deposition. In colloidal lithography, the feature size can easily shrink by decreasing the microsphere diameter in the colloidal mask. The feature shape can be diversified by varying the crystal structure of the colloidal mask, etching the mask, and altering the incidence angle of the vapor beam (Fig. 3.63) [244].

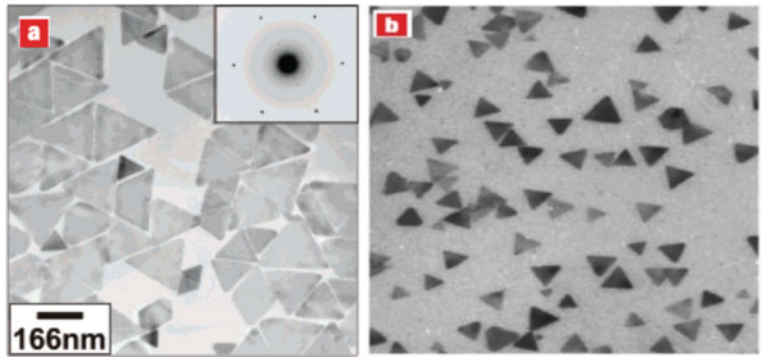

Fig. 3.62 **a**, **b** TEM image of Au triangular nanoparticles, inset shows the electron diffraction pattern of a single prism. growth of nanoprisms using dual-beam excitation, edge size is less than 100 nm

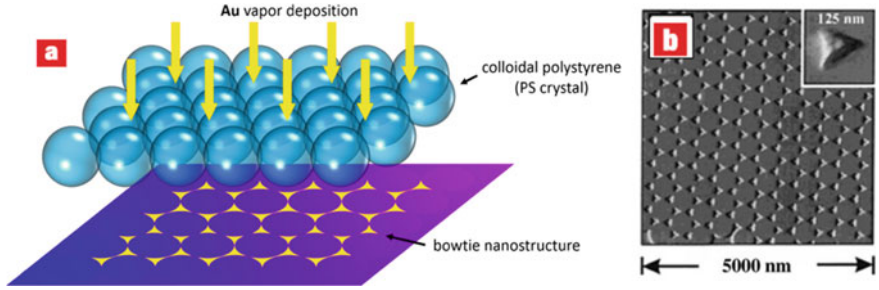

Fig. 3.63 **a** Schematic illustration of colloidal lithography. **b** AFM image of nanodots derived from Colloidal lithography using a hexagonal close-packing single layer as a mask for deposition

Figure 3.64 shows the process of using colloidal metal nanocrystals (NCs) as a mask for nanoimprint lithography [255].

Colloidal self-assembly has been exploited for increasing the efficiency of NSOM probe. In [256] gold nanoparticles with diameters of less than 100 nm were synthesized with colloidal synthesis, and then a single gold nanoparticle was mounted at the end of a NSOM tip (Fig. 3.65).

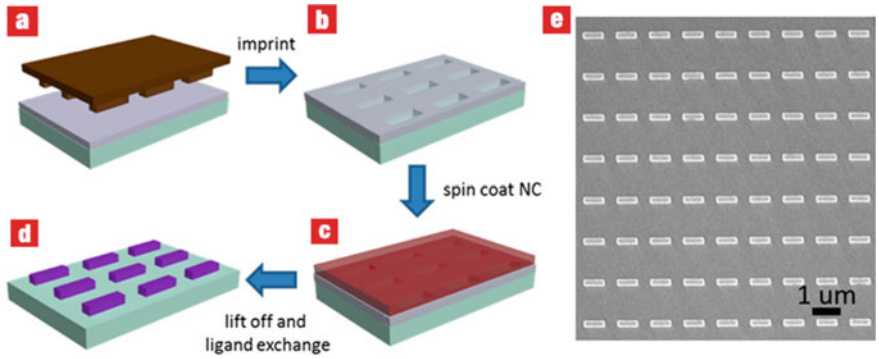

Fig. 3.64 Nanoantenna fabrication by **a** thermal nanoimprint lithography to **b** transfer the master pattern into the resist, followed by **c** spin coating of colloidal Au NCs and **d** ligand exchange and resist lift-off. **e** SEM image of a representative NC-based nanoantenna array fabricated by the nanoimprinting method

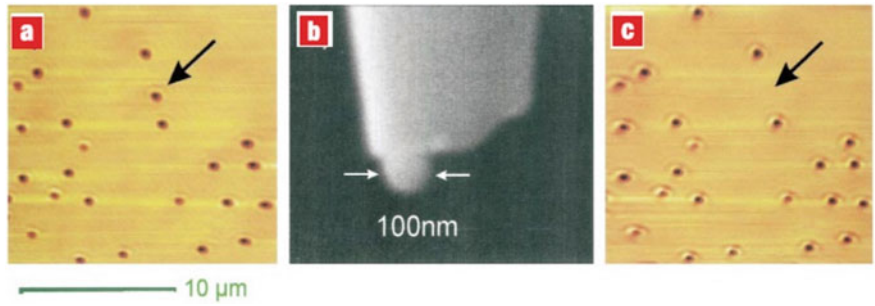

Fig. 3.65 **a** Confocal scan of individual gold spheres of 100 nm diameter spread on a glass substrate. A fiber tip has been approached to the particle indicated by the arrow using shear-force control. After establishing contact to the gold sphere, the particle has been fixed to the tip. **b** Scanning electron micrograph of the tip after the procedure described in **a**. **c** Confocal scan of the same area as in **a**, verifying that the chosen particle has left the substrate. Its former position is indicated by an arrow

References

1. C. Roman, T. Helbling, and C. Hierold, "Springer Handbook of Nanotechnology ed B Bhushan," ed: Berlin: Springer, 2010.
2. M. R. Jones, K. D. Osberg, R. J. Macfarlane, M. R. Langille, and C. A. Mirkin, "Templated Techniques for the Synthesis and Assembly of Plasmonic Nanostructures," *Chemical Reviews,* vol. 111, pp. 3736–3827, 2011/06/08 2011.
3. M. Stepanova and S. Dew, *Nanofabrication: techniques and principles*: Springer Science & Business Media, 2011.
4. A. A. Tseng, *Nanofabrication: fundamentals and applications*: World Scientific, 2008.
5. T. Ito and S. Okazaki, "Pushing the limits of lithography," *Nature,* vol. 406, pp. 1027–1031, 08/31/print 2000.
6. T. M. Bloomstein, M. W. Horn, M. Rothschild, R. R. Kunz, S. T. Palmacci, and R. B. Goodman, "Lithography with 157 nm lasers," *Journal of Vacuum Science & Technology B,* vol. 15, pp. 2112-2116, 1997.
7. J. White, P. Dunne, P. Hayden, F. O'Reilly, and G. O'Sullivan, "Optimizing 13.5nm laser-produced tin plasma emission as a function of laser wavelength," *Applied Physics Letters,* vol. 90, p. 181502, 2007.
8. N. Böwering, M. Martins, W. N. Partlo, and I. V. Fomenkov, "Extreme ultraviolet emission spectra of highly ionized xenon and their comparison with model calculations," *Journal of Applied Physics,* vol. 95, pp. 16-23, 2004.
9. T. Higashiguchi, K. Kawasaki, W. Sasaki, and S. Kubodera, "Enhancement of extreme ultraviolet emission from a lithium plasma by use of dual laser pulses," *Applied Physics Letters,* vol. 88, p. 161502, 2006.
10. R. W. Coons, D. Campos, M. Crank, S. S. Harilal, and A. Hassanein, "Comparison of EUV spectral and ion emission features from laser-produced Sn and Li plasmas," 2010, pp. 763636–763636–7.
11. R. M. Sankaran, *Plasma processing of nanomaterials*: CRC Press, 2011.
12. M. Cho, J.-H. Seo, J. Lee, D. Zhao, H. Mi, X. Yin*, et al.*, "Ultra-thin distributed Bragg reflectors via stacked single-crystal silicon nanomembranes," *Applied Physics Letters,* vol. 106, p. 181107, 2015.
13. G. Brummer, D. Nothern, A. Y. Nikiforov, and T. D. Moustakas, "Deep ultraviolet distributed Bragg reflectors based on graded composition AlGaN alloys," *Applied Physics Letters,* vol. 106, p. 221107, 2015.
14. Y. Yang, Q. Ji, H. Zong, T. Yan, J. Li, T. Wei*, et al.*, "Design of a tandem distributed Bragg reflectors specialized for enhancing the efficiency of GaN-based ultraviolet light-emitting diodes," *Optics Communications,* vol. 374, pp. 80–83, 9/1/ 2016.
15. T. Liang, P. Sanchez, G. Zhang, E. Shu, R. Nagpal, and A. Stivers, "Understanding and reduction of defects on finished EUV masks," 2005, pp. 654–662.
16. M. Waiblinger, K. Kornilov, T. Hofmann, and K. Edinger, "e-beam induced EUV photomask repair: a perfect match," 2010, pp. 75450P-75450P-8.
17. T. Liang, G. Zhang, P. Naulleau, A. Myers, S.-J. Park, A. Stivers*, et al.*, "EUV mask pattern defect printability," 2006, pp. 62830K-62830K-12.
18. T. Liang, A. R. Stivers, M. Penn, D. Bald, C. Sethi, V. Boegli*, et al.*, "Demonstration of damage-free mask repair using electron beam-induced processes," 2004, pp. 291–300.
19. K. Edinger, K. Wolff, H. Steigerwald, N. Auth, P. Spies, J. Oster*, et al.*, "Bringing mask repair to the next level," 2014, pp. 92350R-92350R-9.

20. D. Hay, I. Khaw, P. Bagge, L. Sun, O. Wood, Y. Chen*, et al.*, "Thin absorber EUV photomask based on mixed Ni and TaN material," 2016, pp. 99840G-99840G-6.
21. J. H. Noh, M. G. Stanford, B. B. Lewis, J. D. Fowlkes, H. Plank, and P. D. Rack, "Nanoscale electron beam-induced deposition and purification of ruthenium for extreme ultraviolet lithography mask repair," *Applied Physics A,* vol. 117, pp. 1705-1713, 2014.
22. P. P. Naulleau, C. N. Anderson, L.-M. Baclea-an, P. Denham, S. George, K. A. Goldberg*, et al.*, "Critical challenges for EUV resist materials," 2011, pp. 797202–797202–10.
23. Y. Ekinci, M. Vockenhuber, M. Hojeij, L. Wang, and N. M. Mojarad, "Evaluation of EUV resist performance with interference lithography towards 11 nm half-pitch and beyond," 2013, pp. 867910–867910–11.
24. M. Trikeriotis, W. J. Bae, E. Schwartz, M. Krysak, N. Lafferty, P. Xie*, et al.*, "Development of an inorganic photoresist for DUV, EUV, and electron beam imaging," 2010, pp. 76390E-76390E-10.
25. T. Minoru, S. Yuta, K. Masanori, S. Kazu, and I. Toshiro, "Metal resist for extreme ultraviolet lithography characterized by scanning transmission electron microscopy," *Applied Physics Express,* vol. 9, p. 031601, 2016.
26. J. Passarelli, M. Murphy, R. Del Re, M. Sortland, L. Dousharm, M. Vockenhuber*, et al.*, "High-sensitivity molecular organometallic resist for EUV (MORE)," 2015, pp. 94250T-94250T-13.
27. R. Del Re, J. Passarelli, M. Sortland, B. Cardineau, Y. Ekinci, E. Buitrago*, et al.*, "Low-line edge roughness extreme ultraviolet photoresists of organotin carboxylates," *Journal of Micro/Nanolithography, MEMS, and MOEMS,* vol. 14, pp. 043506-043506, 2015.
28. M. Sortland, J. Hotalen, R. D. Re, J. Passarelli, M. Murphy, T. S. Kulmala*, et al.*, "Platinum and palladium oxalates: positive-tone extreme ultraviolet resists," *Journal of Micro/Nanolithography, MEMS, and MOEMS,* vol. 14, pp. 043511-043511, 2015.
29. B. W. Smith and J. S. Cashmore, "Challenges in high NA, polarization, and photoresists," in *SPIE's 27th Annual International Symposium on Microlithography*, 2002, pp. 11–24.
30. B. Fay, "Advanced optical lithography development, from UV to EUV," *Microelectronic Engineering,* vol. 61–62, pp. 11–24, 7// 2002.
31. B. Wu and A. Kumar, *Extreme ultraviolet lithography*: McGraw-Hill, Inc., 2009.
32. V. Bakshi, *EUV lithography* vol. 178: Spie Press Bellingham, 2009.
33. X. Ma and G. R. Arce, *Computational lithography* vol. 77: John Wiley & Sons, 2011.
34. G. F. Cardinale, C. C. Henderson, J. E. M. Goldsmith, P. J. S. Mangat, J. Cobb, and S. D. Hector, "Demonstration of pattern transfer into sub-100 nm polysilicon line/space features patterned with extreme ultraviolet lithography," *Journal of Vacuum Science & Technology B,* vol. 17, pp. 2970-2974, 1999.
35. G. F. Cardinale, "Pattern transfer of sub-100-nm features in polysilicon using a single-layer photoresist and extreme ultraviolet lithography," 2000, pp. 413–422.
36. G. Simon, A. M. Haghiri-Gosnet, J. Bourneix, D. Decanini, Y. Chen, F. Rousseaux*, et al.*, "Sub-20 nm x-ray nanolithography using conventional mask technologies on monochromatized synchrotron radiation," *Journal of Vacuum Science & Technology B,* vol. 15, pp. 2489-2494, 1997.
37. C. Cuisin, A. Chelnokov, J.-M. Lourtioz, D. Decanini, and Y. Chen, "Fabrication of three-dimensional photonic structures with submicrometer resolution by x-ray lithography," *Journal of Vacuum Science & Technology B,* vol. 18, pp. 3505-3509, 2000.
38. E. Toyota, T. Hori, M. Khan, and F. Cerrina, "Technique for 25 nm x-ray nanolithography," *Journal of Vacuum Science & Technology B,* vol. 19, pp. 2428-2433, 2001.
39. S. Bollanti, P. D. Lazzaro, F. Flora, L. Mezi, D. Murra, and A. Torre, "First results of high-resolution patterning by the ENEA laboratory-scale extreme ultraviolet projection lithography system," *EPL (Europhysics Letters),* vol. 84, p. 58003, 2008.

40. A. Bartnik, H. Fiedorowicz, R. Jarocki, L. Pina, M. Szczurek, and P. Wachulak, "Short wavelength laboratory sources: Principles and practices," ed: Royal Society of Chemistry, London, 2015.
41. P. D. Ashby, D. L. Olynick, D. F. Ogletree, and P. P. Naulleau, "Resist Materials for Extreme Ultraviolet Lithography: Toward Low-Cost Single-Digit-Nanometer Patterning," *Advanced Materials,* vol. 27, pp. 5813-5819, 2015.
42. T. J. Yen, W. J. Padilla, N. Fang, D. C. Vier, D. R. Smith, J. B. Pendry, *et al.*, "Terahertz Magnetic Response from Artificial Materials," *Science,* vol. 303, pp. 1494-1496, 2004.
43. J. Lee, J. Song, G. Y. Sung, and J. H. Shin, "Plasmonic Waveguide Ring Resonators with 4 nm Air Gap and λ02/15 000 Mode-Area Fabricated Using Photolithography," *Nano Letters,* vol. 14, pp. 5533–5538, 2014/10/08 2014.
44. J. W. Chon and K. Iniewski, *Nanoplasmonics: Advanced Device Applications*: CRC Press, 2013.
45. T. Siegfried, Y. Ekinci, H. H. Solak, O. J. F. Martin, and H. Sigg, "Fabrication of sub-10 nm gap arrays over large areas for plasmonic sensors," *Applied Physics Letters,* vol. 99, p. 263302, 2011.
46. A. A. Tseng, C. Kuan, C. D. Chen, and K. J. Ma, "Electron beam lithography in nanoscale fabrication: recent development," *IEEE Transactions on Electronics Packaging Manufacturing,* vol. 26, pp. 141-149, 2003.
47. I. Utke, S. Moshkalev, and P. Russell, *Nanofabrication using focused ion and electron beams: principles and applications*: Oxford University Press, 2012.
48. M. Jérôme and P. Jérôme, "Fabrication of aluminium nanostructures for plasmonics," *Journal of Physics D: Applied Physics,* vol. 48, p. 184002, 2015.
49. C. P. Umbach, S. Washburn, R. B. Laibowitz, and R. A. Webb, "Magnetoresistance of small, quasi-one-dimensional, normal-metal rings and lines," *Physical Review B,* vol. 30, pp. 4048–4051, 10/01/ 1984.
50. N. L. (http://www.nanobeam.co.uk/). (2008).
51. A. Muray, M. Scheinfein, M. Isaacson, and I. Adesida, "Radiolysis and resolution limits of inorganic halide resists," *Journal of Vacuum Science & Technology B,* vol. 3, pp. 367-372, 1985.
52. W. Huang, W. Qian, P. K. Jain, and M. A. El-Sayed, "The Effect of Plasmon Field on the Coherent Lattice Phonon Oscillation in Electron-Beam Fabricated Gold Nanoparticle Pairs," *Nano Letters,* vol. 7, pp. 3227–3234, 2007/10/01 2007.
53. N. Liu, H. Liu, S. Zhu, and H. Giessen, "Stereometamaterials," *Nat Photon,* vol. 3, pp. 157–162, 03//print 2009.
54. Y. Wang, K. S. Kiang, M. Abb, O. L. Muskens, and C. H. de Groot, "Electron beam lithography tri-layer lift-off to create ultracompact metal/metal oxide 2D patterns on CaF2 substrate for surface-enhanced infrared spectroscopy," *Microelectronic Engineering,* vol. 141, pp. 87–91, 6/15/ 2015.
55. V. R. Manfrinato, L. Zhang, D. Su, H. Duan, R. G. Hobbs, E. A. Stach, *et al.*, "Resolution Limits of Electron-Beam Lithography toward the Atomic Scale," *Nano Letters,* vol. 13, pp. 1555–1558, 2013/04/10 2013.
56. W. F. van Dorp, B. van Someren, C. W. Hagen, P. Kruit, and P. A. Crozier, "Approaching the Resolution Limit of Nanometer-Scale Electron Beam-Induced Deposition," *Nano Letters,* vol. 5, pp. 1303–1307, 2005/07/01 2005.
57. Z. Tang and N. A. Kotov, "One-Dimensional Assemblies of Nanoparticles: Preparation, Properties, and Promise," *Advanced Materials,* vol. 17, pp. 951-962, 2005.

58. R. Abargues, J. Marqués-Hueso, J. Canet-Ferrer, E. Pedrueza, J. L. Valdés, E. Jiménez*, et al.*, "High-resolution electron-beam patternable nanocomposite containing metal nanoparticles for plasmonics," *Nanotechnology,* vol. 19, p. 355308, 2008.
59. N. J. Halas, S. Lal, W.-S. Chang, S. Link, and P. Nordlander, "Plasmons in Strongly Coupled Metallic Nanostructures," *Chemical Reviews,* vol. 111, pp. 3913–3961, 2011/06/08 2011.
60. G. Schider, J. R. Krenn, A. Hohenau, H. Ditlbacher, A. Leitner, F. R. Aussenegg*, et al.*, "Plasmon dispersion relation of Au and Ag nanowires," *Physical Review B,* vol. 68, p. 155427, 10/28/ 2003.
61. B. Lamprecht, J. R. Krenn, G. Schider, H. Ditlbacher, M. Salerno, N. Felidj*, et al.*, "Surface plasmon propagation in microscale metal stripes," *Applied Physics Letters,* vol. 79, pp. 51-53, 2001.
62. J. B. Lassiter, H. Sobhani, J. A. Fan, J. Kundu, F. Capasso, P. Nordlander*, et al.*, "Fano Resonances in Plasmonic Nanoclusters: Geometrical and Chemical Tunability," *Nano Letters,* vol. 10, pp. 3184–3189, 2010/08/11 2010.
63. N. A. Mirin, K. Bao, and P. Nordlander, "Fano Resonances in Plasmonic Nanoparticle Aggregates," *The Journal of Physical Chemistry A,* vol. 113, pp. 4028–4034, 2009/04/23 2009.
64. A. Pucci, F. Neubrech, D. Weber, S. Hong, T. Toury, and M. L. de la Chapelle, "Surface enhanced infrared spectroscopy using gold nanoantennas," *physica status solidi (b),* vol. 247, pp. 2071–2074, 2010.
65. M. W. Knight, N. S. King, L. Liu, H. O. Everitt, P. Nordlander, and N. J. Halas, "Aluminum for Plasmonics," *ACS Nano,* vol. 8, pp. 834–840, 2014/01/28 2014.
66. Y. Lee, K. Hoshino, A. Alù, and X. Zhang, "Tunable directive radiation of surface-plasmon diffraction gratings," *Optics Express,* vol. 21, pp. 2748–2756, 2013/02/11 2013.
67. Y. Lee, K. Hoshino, A. Alù, and X. Zhang, "Efficient directional beaming from small apertures using surface-plasmon diffraction gratings," *Applied Physics Letters,* vol. 101, p. 041102, 2012.
68. Q. Wang, J. Bu, and X. C. Yuan, "High-resolution 2D plasmonic fan-out realized by subwavelength slit arrays," *Optics Express,* vol. 18, pp. 2662–2667, 2010/02/01 2010.
69. G. Yuan, Q. Wang, and X. Yuan, "Dynamic generation of plasmonic Moiré fringes using phase-engineered optical vortex beam," *Optics Letters,* vol. 37, pp. 2715–2717, 2012/07/01 2012.
70. S. Zhu, H.-H. Cheng, I. Blakey, N. Stokes, K. Ostrikov, and M. Cortie, "Plasmonic 'top-hat' nano-star arrays by electron beam lithography," *Microelectronic Engineering,* vol. 139, pp. 13–18, 5/1/ 2015.
71. E. S. P. Leong, J. Deng, E. H. Khoo, S. Wu, W. K. Phua, and Y. J. Liu, "Fabrication of suspended, three-dimensional chiral plasmonic nanostructures with single-step electron-beam lithography," *RSC Advances,* vol. 5, pp. 96366-96371, 2015.
72. T. H. Taminiau, R. J. Moerland, F. B. Segerink, L. Kuipers, and N. F. van Hulst, "λ/4 Resonance of an Optical Monopole Antenna Probed by Single Molecule Fluorescence," *Nano Letters,* vol. 7, pp. 28–33, 2007/01/01 2007.
73. J. A. Veerman, A. M. Otter, L. Kuipers, and N. F. van Hulst, "High definition aperture probes for near-field optical microscopy fabricated by focused ion beam milling," *Applied Physics Letters,* vol. 72, pp. 3115-3117, 1998.
74. J. N. Farahani, D. W. Pohl, H. J. Eisler, and B. Hecht, "Single Quantum Dot Coupled to a Scanning Optical Antenna: A Tunable Superemitter," *Physical Review Letters,* vol. 95, p. 017402, 06/28/ 2005.
75. A. Dhawan, M. Gerhold, A. Madison, J. Fowlkes, P. E. Russell, T. Vo-Dinh*, et al.*, "Fabrication of nanodot plasmonic waveguide structures using FIB milling and electron beam-induced deposition," *Scanning,* vol. 31, pp. 139-146, 2009.

76. P. Nagpal, N. C. Lindquist, S.-H. Oh, and D. J. Norris, "Ultrasmooth Patterned Metals for Plasmonics and Metamaterials," *Science,* vol. 325, pp. 594–597, 2009–07–31 00:00:00 2009.
77. R. Zia, J. A. Schuller, A. Chandran, and M. L. Brongersma, "Plasmonics: the next chip-scale technology," *Materials Today,* vol. 9, pp. 20–27, 7// 2006.
78. C. Schafer, D. A. Gollmer, A. Horrer, J. Fulmes, A. Weber-Bargioni, S. Cabrini*, et al.*, "A single particle plasmon resonance study of 3D conical nanoantennas," *Nanoscale,* vol. 5, pp. 7861-7866, 2013.
79. H. Björn, V. Simon, C. Xue-Wen, G. Stephan, S. Vahid, and C. Silke, "Fabrication and characterization of plasmonic nanocone antennas for strong spontaneous emission enhancement," *Nanotechnology,* vol. 26, p. 404001, 2015.
80. S. Eishi, K. Jun-ichi, Y. Yutaka, O. Miyu, and F. Ryoshu, "Plasmonic trapping of sub-micro objects with metallic antenas," *Journal of Optics,* vol. 18, p. 075001, 2016.
81. K. Okuda, T. Okamoto, and M. Haraguchi, "Gap plasmon excitation into plasmonic waveguide using Si waveguide," in *2015 20th Microoptics Conference (MOC)*, 2015, pp. 1–2.
82. H. Goktas and V. J. Sorger, "Electroluminescence Enhancement via Grating on a Si-based Plasmonic Metal-Insulator-Semiconductor Tunnel Junction," *MRS Advances,* vol. FirstView, pp. 1–5, 2016.
83. T. Matsui, S. Tomita, M. Asai, Y. Tadokoro, K. Takano, M. Nakajima*, et al.*, "Terahertz wave emission from plasmonic chiral metasurfaces," *Applied Physics A,* vol. 122, pp. 1-5, 2016.
84. S. Yokogawa, S. P. Burgos, and H. A. Atwater, "Plasmonic Color Filters for CMOS Image Sensor Applications," *Nano Letters,* vol. 12, pp. 4349–4354, 2012/08/08 2012.
85. G. SI, Y. ZHAO, A. B. CHEW, and Y. J. LIU, "PLASMONIC COLOR FILTERS," *Journal of Molecular and Engineering Materials,* vol. 02, p. 1440009, 2014.
86. X. Jiang, E. S. P. Leong, Y. J. Liu, and G. Si, "Tuning plasmon resonance in depth-variant plasmonic nanostructures," *Materials & Design,* vol. 96, pp. 64–67, 4/15/ 2016.
87. H. T. Soh, K. W. Guarini, and C. F. Quate, *Scanning probe lithography* vol. 7: Springer Science & Business Media, 2013.
88. G. Binnig, H. Rohrer, C. Gerber, and E. Weibel, "Surface Studies by Scanning Tunneling Microscopy," *Physical Review Letters,* vol. 49, pp. 57–61, 07/05/ 1982.
89. P. Cubillas and M. W. Anderson, "Atomic Force Microscopy," in *Multi Length-Scale Characterisation*, ed: John Wiley & Sons, Ltd, 2014, pp. 121–193.
90. E. A. Ash and G. Nicholls, "Super-resolution Aperture Scanning Microscope," *Nature,* vol. 237, pp. 510–512, 06/30/print 1972.
91. V. Bouchiat, "Lithography Techniques Using Scanning Probe Microscopy," in *Nano-Lithography*, ed: John Wiley & Sons, Inc., 2013, pp. 169–206.
92. M. L. M. Balistreri, J. P. Korterik, L. Kuipers, and N. F. van Hulst, "Photon scanning tunneling optical microscopy with a three-dimensional multiheight imaging mode," *Applied Physics Letters,* vol. 77, pp. 4092-4094, 2000.
93. L. Novotny and S. J. Stranick, "NEAR-FIELD OPTICAL MICROSCOPY AND SPECTROSCOPY WITH POINTED PROBES," *Annual Review of Physical Chemistry,* vol. 57, pp. 303-331, 2006.
94. A. A. Tseng, A. Notargiacomo, and T. P. Chen, "Nanofabrication by scanning probe microscope lithography: A review," *Journal of Vacuum Science & Technology B,* vol. 23, pp. 877-894, 2005.
95. G. M. Shedd and P. Russell, "The scanning tunneling microscope as a tool for nanofabrication," *Nanotechnology,* vol. 1, p. 67, 1990.
96. M. A. McCord and R. F. W. Pease, "Lithography with the scanning tunneling microscope," *Journal of Vacuum Science & Technology B,* vol. 4, pp. 86-88, 1986.

97. M. A. McCord and R. F. W. Pease, "Lift-off metallization using poly(methyl methacrylate) exposed with a scanning tunneling microscope," *Journal of Vacuum Science & Technology B,* vol. 6, pp. 293-296, 1988.
98. D. P. Adams, T. M. Mayer, and B. S. Swartzentruber, "Nanometer-scale lithography on Si(001) using adsorbed H as an atomic layer resist," *Journal of Vacuum Science & Technology B,* vol. 14, pp. 1642-1649, 1996.
99. S. C. Minne, G. Yaralioglu, S. R. Manalis, J. D. Adams, J. Zesch, A. Atalar*, et al.*, "Automated parallel high-speed atomic force microscopy," *Applied Physics Letters,* vol. 72, pp. 2340-2342, 1998.
100. P. Vettiger, M. Despont, U. Drechsler, U. Durig, W. Haberle, M. I. Lutwyche*, et al.*, "The “Millipede”—More than thousand tips for future AFM storage," *IBM Journal of Research and Development,* vol. 44, pp. 323-340, 2000.
101. S. Devasia, E. Eleftheriou, and S. O. R. Moheimani, "A Survey of Control Issues in Nanopositioning," *IEEE Transactions on Control Systems Technology,* vol. 15, pp. 802-823, 2007.
102. R. Magno and B. R. Bennett, "Nanostructure patterns written in III–V semiconductors by an atomic force microscope," *Applied Physics Letters,* vol. 70, pp. 1855-1857, 1997.
103. M. Kaestner and I. W. Rangelow, "Scanning proximal probe lithography for sub-10 nm resolution on calix[4]resorcinarene," *Journal of Vacuum Science & Technology B,* vol. 29, p. 06FD02, 2011.
104. M. Kaestner, M. Hofer, and I. W. Rangelow, "Nanolithography by scanning probes on calixarene molecular glass resist using mix-and-match lithography," *Journal of Micro/Nanolithography, MEMS, and MOEMS,* vol. 12, pp. 031111-031111, 2013.
105. M. Lee and H.-Y. Kim, "Toward Nanoscale Three-Dimensional Printing: Nanowalls Built of Electrospun Nanofibers," *Langmuir,* vol. 30, pp. 1210–1214, 2014/02/11 2014.
106. J.-F. Xing, M.-L. Zheng, and X.-M. Duan, "Two-photon polymerization microfabrication of hydrogels: an advanced 3D printing technology for tissue engineering and drug delivery," *Chemical Society Reviews,* vol. 44, pp. 5031-5039, 2015.
107. J. Zhao, L. A. Swartz, W.-f. Lin, P. S. Schlenoff, J. Frommer, J. B. Schlenoff*, et al.*, "Three-Dimensional Nanoprinting via Scanning Probe Lithography-Delivered Layer-by-Layer Deposition," *ACS Nano,* 2016/05/20 2016.
108. V. F. Dryakhlushin, A. Y. Klimov, V. V. Rogov, and N. V. Vostokov, "Near-field optical lithography method for fabrication of the nanodimensional objects," *Applied Surface Science,* vol. 248, pp. 200–203, 7/30/ 2005.
109. F. Pan, X. Chen, I. Kubicova, J. Skriniarova, D. Pudis, L. Suslik*, et al.*, "The 18th International Vacuum Congress (IVC-18)Non-Contact NSOM Lithography for 2D Photonic Structure Fabrication," *Physics Procedia,* vol. 32, pp. 113–116, 2012/01/01 2012.
110. I. Kubicová, D. Pudiš, L. Šušlik, J. Škriniarová, S. Slabeyciusová, and I. Martinček, "Structures patterning by non-contact NSOM lithography," 2010, pp. 774616–774616–6.
111. Y. Lin, M. H. Hong, W. J. Wang, Y. Z. Law, and T. C. Chong, "Sub-30 nm lithography with near-field scanning optical microscope combined with femtosecond laser," *Applied Physics A,* vol. 80, pp. 461-465, 2005.
112. Y. Wang, W. Srituravanich, C. Sun, and X. Zhang, "Plasmonic Nearfield Scanning Probe with High Transmission," *Nano Letters,* vol. 8, pp. 3041–3045, 2008/09/10 2008.
113. Y. Lee, A. Alu, and J. X. J. Zhang, "Efficient apertureless scanning probes using patterned plasmonic surfaces," *Optics Express,* vol. 19, pp. 25990–25999, 2011/12/19 2011.
114. Q. Qian, H. Yu, P. Gou, J. Xu, and Z. An, "Plasmonic focusing of infrared SNOM tip patterned with asymmetric structures," *Optics Express,* vol. 23, pp. 12923–12934, 2015/05/18 2015.

115. N. C. Lindquist, J. Jose, S. Cherukulappurath, X. Chen, T. W. Johnson, and S.-H. Oh, "Tip-based plasmonics: squeezing light with metallic nanoprobes," *Laser & Photonics Reviews,* vol. 7, pp. 453-477, 2013.
116. W. Bao, M. Staffaroni, J. Bokor, M. B. Salmeron, E. Yablonovitch, S. Cabrini*, et al.*, "Plasmonic near-field probes: a comparison of the campanile geometry with other sharp tips," *Optics Express,* vol. 21, pp. 8166–8176, 2013/04/08 2013.
117. L. Neumann, J. van 't Oever, and N. F. van Hulst, "A Resonant Scanning Dipole-Antenna Probe for Enhanced Nanoscale Imaging," *Nano Letters,* vol. 13, pp. 5070–5074, 2013/11/13 2013.
118. S. S. Choi, M. J. Park, C. H. Han, S. J. Oh, S. H. Han, N. K. Park*, et al.*, "Fabrication of pyramidal probes with various periodic patterns and a single nanopore," *Journal of Vacuum Science & Technology B,* vol. 33, p. 06F203, 2015.
119. D. Chen, J. Miao, Y. Tian, J. Zhang, and Q. Liu, "Field Enhancement of Tip with Spiral Nanostructure," *Plasmonics,* vol. 9, pp. 1245-1249, 2014.
120. W. Zhu, T. Shi, G. Liao, and Z. Tang, "Antenna-Attached Parabolic Probe for Excitation and Collection Modes in SNOM," *Plasmonics,* pp. 1–6, 2016.
121. "Nanotechnology Reviews," 2012.
122. A. Grossmann and K. Sora, "Nanotechnology Reviews," in *Nanotechnology Reviews* vol. 1, ed, 2012, p. 299.
123. J. Červenka, R. Kalousek, M. Bartošík, D. Škoda, O. Tomanec, and T. Šikola, "Fabrication of nanostructures on Si(1 0 0) and GaAs(1 0 0) by local anodic oxidation," *Applied Surface Science,* vol. 253, pp. 2373–2378, 12/30/ 2006.
124. S. Masubuchi, M. Ono, K. Yoshida, K. Hirakawa, and T. Machida, "Fabrication of graphene nanoribbon by local anodic oxidation lithography using atomic force microscope," *Applied Physics Letters,* vol. 94, p. 082107, 2009.
125. Y. Yan, Z. Hu, X. Zhao, T. Sun, S. Dong, and X. Li, "Top-Down Nanomechanical Machining of Three-Dimensional Nanostructures by Atomic Force Microscopy," *Small,* vol. 6, pp. 724-728, 2010.
126. R. D. Piner, J. Zhu, F. Xu, S. Hong, and C. A. Mirkin, ""Dip-Pen" Nanolithography," *Science,* vol. 283, pp. 661–663, 1999–01–29 00:00:00 1999.
127. D. Bullen, S.-W. Chung, X. Wang, J. Zou, C. A. Mirkin, and C. Liu, "Parallel dip-pen nanolithography with arrays of individually addressable cantilevers," *Applied Physics Letters,* vol. 84, pp. 789-791, 2004.
128. K. Salaita, Y. Wang, J. Fragala, R. A. Vega, C. Liu, and C. A. Mirkin, "Massively Parallel Dip–Pen Nanolithography with 55 000-Pen Two-Dimensional Arrays," *Angewandte Chemie,* vol. 118, pp. 7378-7381, 2006.
129. D. S. Ginger, H. Zhang, and C. A. Mirkin, "The Evolution of Dip-Pen Nanolithography," *Angewandte Chemie International Edition,* vol. 43, pp. 30-45, 2004.
130. K. Ayse Cagil, E. Derya, M. Huan, R. Alain, and S. Ralph, "Polymer nanocomposite patterning by dip-pen nanolithography," *Nanotechnology,* vol. 27, p. 135303, 2016.
131. H. Zhang, S.-W. Chung, and C. A. Mirkin, "Fabrication of Sub-50-nm Solid-State Nanostructures on the Basis of Dip-Pen Nanolithography," *Nano Letters,* vol. 3, pp. 43–45, 2003/01/01 2003.
132. A. Noy, A. E. Miller, J. E. Klare, B. L. Weeks, B. W. Woods, and J. J. DeYoreo, "Fabrication of Luminescent Nanostructures and Polymer Nanowires Using Dip-Pen Nanolithography," *Nano Letters,* vol. 2, pp. 109–112, 2002/02/01 2002.
133. M. Ben Ali, T. Ondarçuhu, M. Brust, and C. Joachim, "Atomic Force Microscope Tip Nanoprinting of Gold Nanoclusters," *Langmuir,* vol. 18, pp. 872–876, 2002/02/01 2002.
134. C. D. O'Connell, M. J. Higgins, S. E. Moulton, and G. G. Wallace, "Nano-bioelectronics via dip-pen nanolithography," *Journal of Materials Chemistry C,* vol. 3, pp. 6431-6444, 2015.

135. L. M. Demers, D. S. Ginger, S.-J. Park, Z. Li, S.-W. Chung, and C. A. Mirkin, "Direct Patterning of Modified Oligonucleotides on Metals and Insulators by Dip-Pen Nanolithography," *Science,* vol. 296, pp. 1836–1838, 2002–06–07 00:00:00 2002.
136. J. Kim, Y.-H. Shin, S.-H. Yun, D.-S. Choi, J.-H. Nam, S. R. Kim*, et al.*, "Direct-Write Patterning of Bacterial Cells by Dip-Pen Nanolithography," *Journal of the American Chemical Society,* vol. 134, pp. 16500–16503, 2012/10/10 2012.
137. P. Rath, M. Hirtz, G. Lewes-Malandrakis, D. Brink, C. Nebel, and W. H. P. Pernice, "Diamond Nanophotonic Circuits Functionalized by Dip-pen Nanolithography," *Advanced Optical Materials,* vol. 3, pp. 328-335, 2015.
138. S.-C. Hung, O. A. Nafday, J. R. Haaheim, F. Ren, G. C. Chi, and S. J. Pearton, "Dip Pen Nanolithography of Conductive Silver Traces," *The Journal of Physical Chemistry C,* vol. 114, pp. 9672–9677, 2010/06/03 2010.
139. J.-W. Jang, B. Park, and S. Nettikadan, "Generation of plasmonic Au nanostructures in the visible wavelength using two-dimensional parallel dip-pen nanolithography," *Nanoscale,* vol. 6, pp. 7912-7916, 2014.
140. C. M. S. Torres, *Alternative lithography: unleashing the potentials of nanotechnology*: Springer Science & Business Media, 2012.
141. S. Y. Chou, P. R. Krauss, and P. J. Renstrom, "Imprint of sub-25 nm vias and trenches in polymers," *Applied Physics Letters,* vol. 67, pp. 3114-3116, 1995.
142. M. Colburn, S. C. Johnson, M. D. Stewart, S. Damle, T. C. Bailey, B. Choi*, et al.*, "Step and flash imprint lithography: a new approach to high-resolution patterning," 1999, pp. 379–389.
143. S. Zankovych, T. Hoffmann, J. Seekamp, J. U. Bruch, and C. M. S. Torres, "Nanoimprint lithography: challenges and prospects," *Nanotechnology,* vol. 12, p. 91, 2001.
144. H. Schift, "Nanoimprint lithography: An old story in modern times? A review," *Journal of Vacuum Science & Technology B,* vol. 26, pp. 458-480, 2008.
145. L. J. Guo, "Recent progress in nanoimprint technology and its applications," *Journal of Physics D: Applied Physics,* vol. 37, p. R123, 2004.
146. L. J. Guo, "Nanoimprint Lithography: Methods and Material Requirements," *Advanced Materials,* vol. 19, pp. 495-513, 2007.
147. S. Y. Chou, P. R. Krauss, W. Zhang, L. Guo, and L. Zhuang, "Sub-10 nm imprint lithography and applications," *Journal of Vacuum Science & Technology B,* vol. 15, pp. 2897-2904, 1997.
148. B. Heidari, I. Maximov, and L. Montelius, "Nanoimprint lithography at the 6 in. wafer scale," *Journal of Vacuum Science & Technology B,* vol. 18, pp. 3557-3560, 2000.
149. K. Pfeiffer, G. Bleidiessel, G. Gruetzner, H. Schulz, T. Hoffmann, H. C. Scheer*, et al.*, "International Conference on Micro- and NanofabricationSuitability of new polymer materials with adjustable glass temperature for nano-imprinting," *Microelectronic Engineering,* vol. 46, pp. 431–434, 1999/05/01 1999.
150. K. Pfeiffer, M. Fink, G. Bleidiessel, G. Gruetzner, H. Schulz, H. C. Scheer*, et al.*, "Novel linear and crosslinking polymers for nanoimprinting with high etch resistance," *Microelectronic Engineering,* vol. 53, pp. 411–414, 2000/06/01 2000.
151. F. Gaboriau, M. C. Peignon, A. Barreau, G. Turban, C. Cardinaud, K. Pfeiffer*, et al.*, "High density fluorocarbon plasma etching of new resists suitable for nano-imprint lithography," *Microelectronic Engineering,* vol. 53, pp. 501–505, 2000/06/01 2000.
152. L. J. Heyderman, H. Schift, C. David, J. Gobrecht, and T. Schweizer, "Flow behaviour of thin polymer films used for hot embossing lithography," *Microelectronic Engineering,* vol. 54, pp. 229–245, 12// 2000.
153. D. J. Resnick, W. J. Dauksher, D. Mancini, K. J. Nordquist, T. C. Bailey, S. Johnson*, et al.*, "Imprint lithography for integrated circuit fabrication," *Journal of Vacuum Science & Technology B,* vol. 21, pp. 2624-2631, 2003.

154. W. Zhang and S. Y. Chou, "Fabrication of 60-nm transistors on 4-in. wafer using nanoimprint at all lithography levels," *Applied Physics Letters,* vol. 83, pp. 1632-1634, 2003.
155. W. Wu, Z. Yu, S.-Y. Wang, R. S. Williams, Y. Liu, C. Sun*, et al.*, "Midinfrared metamaterials fabricated by nanoimprint lithography," *Applied Physics Letters,* vol. 90, p. 063107, 2007.
156. Y. Chen, J. Tao, X. Zhao, Z. Cui, A. S. Schwanecke, and N. I. Zheludev, "Nanoimprint lithography for planar chiral photonic meta-materials," *Microelectronic Engineering,* vol. 78–79, pp. 612–617, 3// 2005.
157. W. Wu, E. Kim, E. Ponizovskaya, Y. Liu, Z. Yu, N. Fang*, et al.*, "Optical metamaterials at near and mid-IR range fabricated by nanoimprint lithography," *Applied Physics A,* vol. 87, pp. 143-150, 2007.
158. A. Boltasseva and V. M. Shalaev, "Fabrication of optical negative-index metamaterials: Recent advances and outlook," *Metamaterials,* vol. 2, pp. 1–17, 5// 2008.
159. J. G. Ok, H. Seok Youn, M. Kyu Kwak, K.-T. Lee, Y. Jae Shin, L. Jay Guo*, et al.*, "Continuous and scalable fabrication of flexible metamaterial films via roll-to-roll nanoimprint process for broadband plasmonic infrared filters," *Applied Physics Letters,* vol. 101, p. 223102, 2012.
160. C. Zhang, H. Subbaraman, Q. Li, Z. Pan, J. G. Ok, T. Ling*, et al.*, "Printed photonic elements: nanoimprinting and beyond," *Journal of Materials Chemistry C,* vol. 4, pp. 5133-5153, 2016.
161. S. Sangkeun, K. Chul-Hyun, C. Dae-Geun, L. Jihye, C. Jun-Hyuk, and L. Eung-Sug, "Direct Nanoimprint of Metal Bilayer for Tunnable Metal Photonic Properties," *Japanese Journal of Applied Physics,* vol. 52, p. 10MC09, 2013.
162. J. S. Graham, I. K. Saima, Z. K. Ali, M. D. L. R. Richard, and P. J. Nigel, "Negative index fishnet with nanopillars formed by direct nano-imprint lithography," *Materials Research Express,* vol. 1, p. 045802, 2014.
163. B. D. Lucas, J.-S. Kim, C. Chin, and L. J. Guo, "Nanoimprint Lithography Based Approach for the Fabrication of Large-Area, Uniformly-Oriented Plasmonic Arrays," *Advanced Materials,* vol. 20, pp. 1129-1134, 2008.
164. R. M. Thantirige, J. John, N. R. Pradhan, K. R. Carter, and M. T. Tuominen, "Fabrication of flexible oriented magnetic thin films with large in-plane uniaxial anisotropy by roll-to-roll nanoimprint lithography," *Journal of Magnetism and Magnetic Materials,* vol. 407, pp. 273–278, 6/1/ 2016.
165. K. Nakamoto, R. Kurita, and O. Niwa, "Electrochemical Surface Plasmon Resonance Measurement Based on Gold Nanohole Array Fabricated by Nanoimprinting Technique," *Analytical Chemistry,* vol. 84, pp. 3187–3191, 2012/04/03 2012.
166. B. Alexandra, "Plasmonic components fabrication via nanoimprint," *Journal of Optics A: Pure and Applied Optics,* vol. 11, p. 114001, 2009.
167. J. K. K. Mona, G. Mickaël, W. Bernard, L. A. Dunbar, B. Jürgen, H. Harry*, et al.*, "Inexpensive and fast wafer-scale fabrication of nanohole arrays in thin gold films for plasmonics," *Nanotechnology,* vol. 21, p. 205301, 2010.
168. L. Duempelmann, B. Gallinet, and L. Novotny, "Nanoimprinted and Angular Evaporated Aluminum Plasmonic Nanoantennas Arrays," in *Advanced Photonics*, Barcelona, 2014, p. JTu2C.5.
169. J. L. Skinner, L. L. Hunter, A. A. Talin, J. Provine, and D. A. Horsley, "Large-Area Subwavelength Aperture Arrays Fabricated Using Nanoimprint Lithography," *IEEE Transactions on Nanotechnology,* vol. 7, pp. 527-531, 2008.
170. J. M. Kontio, J. Simonen, J. Tommila, and M. Pessa, "Arrays of metallic nanocones fabricated by UV-nanoimprint lithography," *Microelectronic Engineering,* vol. 87, pp. 1711–1715, 11// 2010.

171. A. Cattoni, P. Ghenuche, A.-M. Haghiri-Gosnet, D. Decanini, J. Chen, J.-L. Pelouard*, et al.*, "λ3/1000 Plasmonic Nanocavities for Biosensing Fabricated by Soft UV Nanoimprint Lithography," *Nano Letters,* vol. 11, pp. 3557–3563, 2011/09/14 2011.
172. I. Fernandez-Cuesta, R. B. Nielsen, A. Boltasseva, X. Borrisé, F. Pérez-Murano, and A. Kristensen, "V-groove plasmonic waveguides fabricated by nanoimprint lithography," *Journal of Vacuum Science & Technology B,* vol. 25, pp. 2649-2653, 2007.
173. R. B. Nielsen, I. Fernandez-Cuesta, A. Boltasseva, V. S. Volkov, S. I. Bozhevolnyi, A. Klukowska*, et al.*, "Channel plasmon polariton propagation in nanoimprinted V-groove waveguides," *Optics Letters,* vol. 33, pp. 2800–2802, 2008/12/01 2008.
174. C. L. C. Smith, B. Desiatov, I. Goykmann, I. Fernandez-Cuesta, U. Levy, and A. Kristensen, "Plasmonic V-groove waveguides with Bragg grating filters via nanoimprint lithography," *Optics Express,* vol. 20, pp. 5696–5706, 2012/02/27 2012.
175. C. Y. Peter Yang, E. L. Yang, C. A. Steinhaus, C.-C. Liu, P. F. Nealey, and J. L. Skinner, "Planar-localized surface plasmon resonance device by block-copolymer and nanoimprint lithography fabrication methods," *Journal of Vacuum Science & Technology B,* vol. 30, p. 026801, 2012.
176. H. T. Chorsi and S. D. Gedney, "Efficient high-order analysis of bowtie nanoantennas using the locally corrected Nystrom method," *Optics Express,* vol. 23, pp. 31452–31459, 2015/11/30 2015.
177. C. Wang, Q. Zhang, Y. Song, and S. Y. Chou, "Plasmonic Bar-Coupled Dots-on-Pillar Cavity Antenna with Dual Resonances for Infrared Absorption and Sensing: Performance and Nanoimprint Fabrication," *ACS Nano,* vol. 8, pp. 2618–2624, 2014/03/25 2014.
178. A. Kumar and G. M. Whitesides, "Features of gold having micrometer to centimeter dimensions can be formed through a combination of stamping with an elastomeric stamp and an alkanethiol "ink" followed by chemical etching," *Applied Physics Letters,* vol. 63, pp. 2002-2004, 1993.
179. H. Schmid and B. Michel, "Siloxane Polymers for High-Resolution, High-Accuracy Soft Lithography," *Macromolecules,* vol. 33, pp. 3042–3049, 2000/04/01 2000.
180. T. W. Odom, J. C. Love, D. B. Wolfe, K. E. Paul, and G. M. Whitesides, "Improved Pattern Transfer in Soft Lithography Using Composite Stamps," *Langmuir,* vol. 18, pp. 5314–5320, 2002/06/01 2002.
181. J. Henzie, M. H. Lee, and T. W. Odom, "Multiscale patterning of plasmonic metamaterials," *Nat Nano,* vol. 2, pp. 549–554, 09//print 2007.
182. J. Henzie, E.-S. Kwak, and T. W. Odom, "Mesoscale Metallic Pyramids with Nanoscale Tips," *Nano Letters,* vol. 5, pp. 1199–1202, 2005/07/01 2005.
183. H. Gao, J. Henzie, and T. W. Odom, "Direct Evidence for Surface Plasmon-Mediated Enhanced Light Transmission through Metallic Nanohole Arrays," *Nano Letters,* vol. 6, pp. 2104–2108, 2006/09/01 2006.
184. H. Gao, J. Henzie, M. H. Lee, and T. W. Odom, "Screening plasmonic materials using pyramidal gratings," *Proceedings of the National Academy of Sciences,* vol. 105, pp. 20146–20151, December 23, 2008 2008.
185. W. Zhou, H. Gao, and T. W. Odom, "Toward Broadband Plasmonics: Tuning Dispersion in Rhombic Plasmonic Crystals," *ACS Nano,* vol. 4, pp. 1241–1247, 2010/02/23 2010.
186. H. Gao, J.-C. Yang, J. Y. Lin, A. D. Stuparu, M. H. Lee, M. Mrksich*, et al.*, "Using the Angle-Dependent Resonances of Molded Plasmonic Crystals To Improve the Sensitivities of Biosensors," *Nano Letters,* vol. 10, pp. 2549–2554, 2010/07/14 2010.
187. J. C. Hulteen and R. P. Van Duyne, "Nanosphere lithography: A materials general fabrication process for periodic particle array surfaces," *Journal of Vacuum Science & Technology A,* vol. 13, pp. 1553-1558, 1995.

188. B. J. Y. Tan, C. H. Sow, T. S. Koh, K. C. Chin, A. T. S. Wee, and C. K. Ong, "Fabrication of Size-Tunable Gold Nanoparticles Array with Nanosphere Lithography, Reactive Ion Etching, and Thermal Annealing," *The Journal of Physical Chemistry B,* vol. 109, pp. 11100–11109, 2005/06/01 2005.
189. W. Wei, K. Alex, G. M. Omer, and M. Hooman, "A deep sub-wavelength process for the formation of highly uniform arrays of nanoholes and nanopillars," *Nanotechnology,* vol. 18, p. 485302, 2007.
190. A. Bonakdar, M. Rezaei, R. L. Brown, V. Fathipour, E. Dexheimer, S. J. Jang*, et al.*, "Deep-UV microsphere projection lithography," *Optics Letters,* vol. 40, pp. 2537–2540, 2015/06/01 2015.
191. P. Colson, C. Henrist, and R. Cloots, "Nanosphere Lithography: A Powerful Method for the Controlled Manufacturing of Nanomaterials," *Journal of Nanomaterials,* vol. 2013, p. 19, 2013.
192. X. Zhang, C. R. Yonzon, and R. P. Van Duyne, "Nanosphere lithography fabricated plasmonic materials and their applications," *Journal of Materials Research,* vol. 21, pp. 1083-1092, 2006.
193. K. Peng, M. Zhang, A. Lu, N.-B. Wong, R. Zhang, and S.-T. Lee, "Ordered silicon nanowire arrays via nanosphere lithography and metal-induced etching," *Applied Physics Letters,* vol. 90, p. 163123, 2007.
194. G. Jia, J. Westphalen, J. Drexler, J. Plentz, J. Dellith, A. Dellith*, et al.*, "Ordered silicon nanowire arrays prepared by an improved nanospheres self-assembly in combination with Ag-assisted wet chemical etching," *Photonics and Nanostructures - Fundamentals and Applications,* vol. 19, pp. 64–70, 4// 2016.
195. T. R. Jensen, M. D. Malinsky, C. L. Haynes, and R. P. Van Duyne, "Nanosphere Lithography: Tunable Localized Surface Plasmon Resonance Spectra of Silver Nanoparticles," *The Journal of Physical Chemistry B,* vol. 104, pp. 10549–10556, 2000/11/01 2000.
196. V. Lotito and T. Zambelli, "Self-assembly and nanosphere lithography for large-area plasmonic patterns on graphene," *Journal of Colloid and Interface Science,* vol. 447, pp. 202–210, 6/1/ 2015.
197. M. Swartz, M. Rodriguez, S. Blair, and J. S. Shumaker-Parry, "Nanosphere Template Lithography for the Fabrication of Aluminum Plasmonic Antenna," in *JSAP-OSA Joint Symposia 2015 Abstracts*, Nagoya, Aichi, 2015, p. 13p_2C_7.
198. C.-Y. Jao, B. A. Magill, K. Chen, E. M. See, and H. D. Robinson, "Enhanced Multiphoton-Induced Luminescence in Silver Nanoparticles Fabricated with Nanosphere Lithography," *Plasmonics,* vol. 10, pp. 87-98, 2015.
199. P. Zheng, S. K. Cushing, S. Suri, and N. Wu, "Tailoring plasmonic properties of gold nanohole arrays for surface-enhanced Raman scattering," *Physical Chemistry Chemical Physics,* vol. 17, pp. 21211-21219, 2015.
200. G. H. Chan, J. Zhao, E. M. Hicks, G. C. Schatz, and R. P. Van Duyne, "Plasmonic Properties of Copper Nanoparticles Fabricated by Nanosphere Lithography," *Nano Letters,* vol. 7, pp. 1947–1952, 2007/07/01 2007.
201. A. I. Kuznetsov, A. B. Evlyukhin, M. R. Gonçalves, C. Reinhardt, A. Koroleva, M. L. Arnedillo*, et al.*, "Laser Fabrication of Large-Scale Nanoparticle Arrays for Sensing Applications," *ACS Nano,* vol. 5, pp. 4843–4849, 2011/06/28 2011.
202. J. A. Pelesko, *Self assembly: the science of things that put themselves together*: CRC Press, 2007.
203. Y. S. Lee, *Self-assembly and nanotechnology: a force balance approach*: John Wiley & Sons, 2008.
204. Y. S. Lee, *Self-assembly and nanotechnology systems: design, characterization, and applications*: John Wiley & Sons, 2011.

205. K. J. M. Bishop, C. E. Wilmer, S. Soh, and B. A. Grzybowski, "Nanoscale Forces and Their Uses in Self-Assembly," *Small,* vol. 5, pp. 1600-1630, 2009.
206. Y. X. and and G. M. Whitesides, "SOFT LITHOGRAPHY," *Annual Review of Materials Science,* vol. 28, pp. 153–184, 1998.
207. L. Newton, T. Slater, N. Clark, and A. Vijayaraghavan, "Self assembled monolayers (SAMs) on metallic surfaces (gold and graphene) for electronic applications," *Journal of Materials Chemistry C,* vol. 1, pp. 376-393, 2013.
208. E. Delamarche, B. Michel, H. A. Biebuyck, and C. Gerber, "Golden interfaces: The Surface of Self-Assembled Monolayers," *Advanced Materials,* vol. 8, pp. 719-729, 1996.
209. L. B. Goetting, T. Deng, and G. M. Whitesides, "Microcontact Printing of Alkanephosphonic Acids on Aluminum: Pattern Transfer by Wet Chemical Etching," *Langmuir,* vol. 15, pp. 1182–1191, 1999/02/01 1999.
210. K. Uvdal, I. Persson, and B. Liedberg, "Tricyclohexylphosphine Adsorbed on Gold," *Langmuir,* vol. 11, pp. 1252–1256, 1995/04/01 1995.
211. K. H. Park, S. Lee, K. H. Koh, R. Lacerda, K. B. K. Teo, and W. I. Milne, "Advanced nanosphere lithography for the areal-density variation of periodic arrays of vertically aligned carbon nanofibers," *Journal of Applied Physics,* vol. 97, p. 024311, 2005.
212. A. Weddemann, I. Ennen, A. Regtmeier, C. Albon, A. Wolff, K. Eckstädt*, et al.*, "Review and outlook: from single nanoparticles to self-assembled monolayers and granular GMR sensors," *Beilstein journal of nanotechnology,* vol. 1, pp. 75-93, 2010.
213. R. K. Smith, P. A. Lewis, and P. S. Weiss, "Patterning self-assembled monolayers," *Progress in Surface Science,* vol. 75, pp. 1–68, 6// 2004.
214. J. A. Rogers and R. G. Nuzzo, "Recent progress in soft lithography," *Materials Today,* vol. 8, pp. 50–56, 2// 2005.
215. Y.-L. Loo, R. L. Willett, K. W. Baldwin, and J. A. Rogers, "Interfacial Chemistries for Nanoscale Transfer Printing," *Journal of the American Chemical Society,* vol. 124, pp. 7654–7655, 2002/07/01 2002.
216. I. B. Burgess, L. Mishchenko, B. D. Hatton, M. Kolle, M. Lončar, and J. Aizenberg, "Encoding Complex Wettability Patterns in Chemically Functionalized 3D Photonic Crystals," *Journal of the American Chemical Society,* vol. 133, pp. 12430–12432, 2011/08/17 2011.
217. C. Ciracì, R. T. Hill, J. J. Mock, Y. Urzhumov, A. I. Fernández-Domínguez, S. A. Maier*, et al.*, "Probing the Ultimate Limits of Plasmonic Enhancement," *Science,* vol. 337, pp. 1072–1074, 2012–08–31 00:00:00 2012.
218. S. K. Arya, P. R. Solanki, M. Datta, and B. D. Malhotra, "Recent advances in self-assembled monolayers based biomolecular electronic devices," *Biosensors and Bioelectronics,* vol. 24, pp. 2810–2817, 5/15/ 2009.
219. M. Xu, N. Lu, H. Xu, D. Qi, Y. Wang, S. Shi*, et al.*, "Fabrication of flexible superhydrophobic biomimic surfaces," *Soft Matter,* vol. 6, pp. 1438-1443, 2010.
220. P. Pallavicini, A. Dona, A. Taglietti, P. Minzioni, M. Patrini, G. Dacarro*, et al.*, "Self-assembled monolayers of gold nanostars: a convenient tool for near-IR photothermal biofilm eradication," *Chemical Communications,* vol. 50, pp. 1969-1971, 2014.
221. D. K. Aswal, S. Lenfant, D. Guerin, J. V. Yakhmi, and D. Vuillaume, "Self assembled monolayers on silicon for molecular electronics," *Analytica Chimica Acta,* vol. 568, pp. 84–108, 5/24/ 2006.
222. L. Wu, L. Cai, A. Liu, W. Wang, Y. Yuan, and Z. Li, "Self-assembled monolayers of perfluoroalkylsilane on plasma-hydroxylated silicon substrates," *Applied Surface Science,* vol. 349, pp. 683–694, 9/15/ 2015.

223. P. Song, C. S. S. Sangeeth, D. Thompson, W. Du, K. P. Loh, and C. A. Nijhuis, "Molecular Electronics: Noncovalent Self-Assembled Monolayers on Graphene as a Highly Stable Platform for Molecular Tunnel Junctions (Adv. Mater. 4/2016)," *Advanced Materials,* vol. 28, pp. 784-784, 2016.
224. A. Khassanov, H.-G. Steinrück, T. Schmaltz, A. Magerl, and M. Halik, "Structural Investigations of Self-Assembled Monolayers for Organic Electronics: Results from X-ray Reflectivity," *Accounts of Chemical Research,* vol. 48, pp. 1901–1908, 2015/07/21 2015.
225. M.-C. Chen, Y.-L. Yang, S.-W. Chen, J.-H. Li, M. Aklilu, and Y. Tai, "Self-Assembled Monolayer Immobilized Gold Nanoparticles for Plasmonic Effects in Small Molecule Organic Photovoltaic," *ACS Applied Materials & Interfaces,* vol. 5, pp. 511–517, 2013/02/13 2013.
226. M. Müller, U. Jung, V. Gusak, S. Ulrich, M. Holz, R. Herges*, et al.*, "Localized Surface Plasmon Resonance Investigations of Photoswitching in Azobenzene-Functionalized Self-Assembled Monolayers on Au," *Langmuir,* vol. 29, pp. 10693–10699, 2013/08/27 2013.
227. A. B. Dahlin, M. P. Jonsson, and F. Höök, "Specific Self-Assembly of Single Lipid Vesicles in Nanoplasmonic Apertures in Gold," *Advanced Materials,* vol. 20, pp. 1436-1442, 2008.
228. Y. Liu, J. Zhou, L. Zhou, E. Yue-Bun Pun, T. Jiang, L. Petti*, et al.*, "Self-assembled structures of polyhedral gold nanocrystals: shape-directive arrangement and structure-dependent plasmonic enhanced characteristics," *RSC Advances,* vol. 6, pp. 57320–57326, 2016.
229. P. R. Solanki, N. Prabhakar, M. K. Pandey, and B. D. Malhotra, "Self-assembled monolayer for toxicant detection using nucleic acid sensor based on surface plasmon resonance technique," *Biomedical Microdevices,* vol. 10, pp. 757-767, 2008.
230. M. P. Stoykovich, M. Müller, S. O. Kim, H. H. Solak, E. W. Edwards, J. J. de Pablo*, et al.*, "Directed Assembly of Block Copolymer Blends into Nonregular Device-Oriented Structures," *Science,* vol. 308, pp. 1442–1446, 2005–06–03 00:00:00 2005.
231. T. Thurn-Albrecht, J. Schotter, G. A. Kästle, N. Emley, T. Shibauchi, L. Krusin-Elbaum*, et al.*, "Ultrahigh-Density Nanowire Arrays Grown in Self-Assembled Diblock Copolymer Templates," *Science,* vol. 290, pp. 2126–2129, 2000–12–15 00:00:00 2000.
232. A. Gharbi, R. Tiron, M. Argoud, X. Chevalier, P. P. Barros, C. Nicolet*, et al.*, "Contact holes patterning by directed self-assembly of block copolymers: process window study," *Journal of Micro/Nanolithography, MEMS, and MOEMS,* vol. 14, pp. 023508-023508, 2015.
233. A. M. Wen, R. Podgornik, G. Strangi, and N. F. Steinmetz, "Photonics and plasmonics go viral: self-assembly of hierarchical metamaterials," *Rendiconti Lincei,* vol. 26, pp. 129-141, 2015.
234. S. K. Cha, J. H. Mun, T. Chang, S. Y. Kim, J. Y. Kim, H. M. Jin*, et al.*, "Au–Ag Core–Shell Nanoparticle Array by Block Copolymer Lithography for Synergistic Broadband Plasmonic Properties," *ACS Nano,* vol. 9, pp. 5536–5543, 2015/05/26 2015.
235. P. A. Mistark, S. Park, S. E. Yalcin, D. H. Lee, O. Yavuzcetin, M. T. Tuominen*, et al.*, "Block-Copolymer-Based Plasmonic Nanostructures," *ACS Nano,* vol. 3, pp. 3987–3992, 2009/12/22 2009.
236. Y. S. Jung, J. H. Lee, J. Y. Lee, and C. A. Ross, "Fabrication of Diverse Metallic Nanowire Arrays Based on Block Copolymer Self-Assembly," *Nano Letters,* vol. 10, pp. 3722–3726, 2010/09/08 2010.
237. W. Lee, S. Y. Lee, R. M. Briber, and O. Rabin, "Self-Assembled SERS Substrates with Tunable Surface Plasmon Resonances," *Advanced Functional Materials,* vol. 21, pp. 3424-3429, 2011.
238. J. Song, L. Cheng, A. Liu, J. Yin, M. Kuang, and H. Duan, "Plasmonic Vesicles of Amphiphilic Gold Nanocrystals: Self-Assembly and External-Stimuli-Triggered Destruction," *Journal of the American Chemical Society,* vol. 133, pp. 10760–10763, 2011/07/20 2011.
239. P. Huang, J. Lin, W. Li, P. Rong, Z. Wang, S. Wang*, et al.*, "Biodegradable Gold Nanovesicles with an Ultrastrong Plasmonic Coupling Effect for Photoacoustic Imaging and Photothermal Therapy," *Angewandte Chemie International Edition,* vol. 52, pp. 13958-13964, 2013.

240. J. M. Tam, J. O. Tam, A. Murthy, D. R. Ingram, L. L. Ma, K. Travis, *et al.*, "Controlled Assembly of Biodegradable Plasmonic Nanoclusters for Near-Infrared Imaging and Therapeutic Applications," *ACS Nano,* vol. 4, pp. 2178–2184, 2010/04/27 2010.
241. C. B. Murray, S. Sun, W. Gaschler, H. Doyle, T. A. Betley, and C. R. Kagan, "Colloidal synthesis of nanocrystals and nanocrystal superlattices," *IBM Journal of Research and Development,* vol. 45, pp. 47-56, 2001.
242. A. Sánchez-Iglesias, M. Grzelczak, J. Pérez-Juste, and L. M. Liz-Marzán, "Binary Self-Assembly of Gold Nanowires with Nanospheres and Nanorods," *Angewandte Chemie International Edition,* vol. 49, pp. 9985-9989, 2010.
243. B. Pietrobon, M. McEachran, and V. Kitaev, "Synthesis of Size-Controlled Faceted Pentagonal Silver Nanorods with Tunable Plasmonic Properties and Self-Assembly of These Nanorods," *ACS Nano,* vol. 3, pp. 21–26, 2009/01/27 2009.
244. G. Zhang and D. Wang, "Colloidal Lithography—The Art of Nanochemical Patterning," *Chemistry – An Asian Journal,* vol. 4, pp. 236–245, 2009.
245. K. Li, Q. Wu, Y. Shan, S. Qiu, F. Cui, Y. Lin, *et al.*, "Shape transformation of Ag nanospheres to triangular Ag nanoplates: Hydrogen peroxide is a magic reagent," *Integrated Ferroelectrics,* vol. 169, pp. 22–28, 2016/02/12 2016.
246. Z. Lou, M. Fujitsuka, and T. Majima, "Pt–Au Triangular Nanoprisms with Strong Dipole Plasmon Resonance for Hydrogen Generation Studied by Single-Particle Spectroscopy," *ACS Nano,* 2016/05/22 2016.
247. X. Geng, W. Leng, N. A. Carter, P. J. Vikesland, and T. Z. Grove, "Protein-aided formation of triangular silver nanoprisms with enhanced SERS performance," *Journal of Materials Chemistry B,* vol. 4, pp. 4182-4190, 2016.
248. K. L. Shuford, M. A. Ratner, and G. C. Schatz, "Multipolar excitation in triangular nanoprisms," *The Journal of Chemical Physics,* vol. 123, p. 114713, 2005.
249. J. E. Millstone, S. Park, K. L. Shuford, L. Qin, G. C. Schatz, and C. A. Mirkin, "Observation of a Quadrupole Plasmon Mode for a Colloidal Solution of Gold Nanoprisms," *Journal of the American Chemical Society,* vol. 127, pp. 5312–5313, 2005/04/01 2005.
250. J. E. Millstone, S. J. Hurst, G. S. Métraux, J. I. Cutler, and C. A. Mirkin, "Colloidal Gold and Silver Triangular Nanoprisms," *Small,* vol. 5, pp. 646-664, 2009.
251. Q. Zhang, Y. N. Tan, J. Xie, and J. Y. Lee, "Colloidal Synthesis of Plasmonic Metallic Nanoparticles," *Plasmonics,* vol. 4, pp. 9-22, 2009.
252. A. Guerrero-Martínez, S. Barbosa, I. Pastoriza-Santos, and L. M. Liz-Marzán, "Nanostars shine bright for you: Colloidal synthesis, properties and applications of branched metallic nanoparticles," *Current Opinion in Colloid & Interface Science,* vol. 16, pp. 118–127, 4// 2011.
253. V. Giannini, A. I. Fernández-Domínguez, S. C. Heck, and S. A. Maier, "Plasmonic Nanoantennas: Fundamentals and Their Use in Controlling the Radiative Properties of Nanoemitters," *Chemical Reviews,* vol. 111, pp. 3888–3912, 2011/06/08 2011.
254. P. Li, Y. Li, Z.-K. Zhou, S. Tang, X.-F. Yu, S. Xiao, *et al.*, "Evaporative Self-Assembly of Gold Nanorods into Macroscopic 3D Plasmonic Superlattice Arrays," *Advanced Materials,* vol. 28, pp. 2511-2517, 2016.
255. W. Chen, M. Tymchenko, P. Gopalan, X. Ye, Y. Wu, M. Zhang, *et al.*, "Large-Area Nanoimprinted Colloidal Au Nanocrystal-Based Nanoantennas for Ultrathin Polarizing Plasmonic Metasurfaces," *Nano Letters,* vol. 15, pp. 5254–5260, 2015/08/12 2015.
256. T. Kalkbrenner, M. Ramstein, J. Mlynek, and V. Sandoghdar, "A single gold particle as a probe for apertureless scanning near-field optical microscopy," *Journal of Microscopy,* vol. 202, pp. 72-76, 2001.

Plasmonics as a Fabrication Tool

4

In Chap. 3 we reviewed several nanofabrication techniques for the fabrication of sub-100 nm structures and plasmonic devices. All the stated techniques perform at the interface between Nano and Micro scale, hence the motivation of naming the previous chapter, "Nanopatterns on microscale structures". The physics of surface plasmons, mentioned in chapter one, is extremely interesting and heralds enchanting applications for nanofabrication. Recently, SPPs have been used to fabricate nanostructures, especially for patterning nanoscale structures. The main purpose in this part is to review recent advances in surface plasmon-based nanofabrication, a great phenomenon that happens at interface of plasmonic and micro structures. Plasmonic nanolithography can be classified into three categories: prism-coupled plasmonic nanolithography, grating-coupled plasmonic nanolithography, and direct writing plasmonic nanolithography.

4.1 Prism-Coupled Plasmonic Nanolithography

The idea of prism-coupled plasmonic nanolithography originated from the excitation of surface plasmons at the interface of a metal and dielectric via a prism. The main idea here is the use of evanescent waves (from the interaction of light with metal mask) to pattern photoresist. In 2006, Guo et al. proposed a large-area surface plasmon polariton interference lithography (LSPPIL) [1]. Figure 4.1a, which is characterized by the Kretschmann configuration, shows the physical arrangement.

An isosceles triangle is placed at the uppermost layer in order to excite the SPPs. The bottom surface of the prism is coated with a thin metal (silver) film and then brought into intimate contact with a thin photoresist coated on a substrate. When two mutually coherent TM (p-polarized) plane waves are incident on the base of the prism in the vicinity of the resonance angle, multiple counterparts of the SPPs arise everywhere on the interface. As

© The Author(s), under exclusive license to Springer Nature Switzerland AG 2023

J. X. J. Zhang, *Plasmonic MEMS*, Synthesis Lectures on Materials and Optics,
https://doi.org/10.1007/978-3-031-23137-7_4

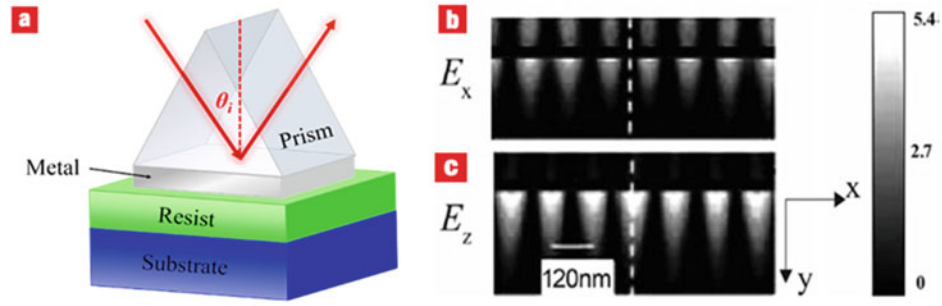

Fig. 4.1. **a** Schematic of the LSPPIL process, **b–c** Electric field distribution of the interference patterns with TM incident wave

a result, SPP interference fringes are formed in the photoresist. Figure 4.1b shows the electric field distributions of the interference pattern with an incidence angle of 59.9° at a wavelength of 441 nm. Line width less than 65 nm has been achieved using the same technique [2].

To extend and improve the performance and increase the flexibility of the prism-based SPPs interference, several implementation approaches have been demonstrated. Lim et al. proposed a thin-film patterning method based on the coupling between the surface plasmon mode and plasmon waveguide modes [3]. The crux of this method is resonance at three angles, 33.5, 56.3, and 90°, respectively. Different SPP interference patterns have been achieved using this method at different resonant angles.

Further improvement may be achieved by reducing the illumination wavelength. For reducing the feature size of a lithography pattern, authors in [4] have used 193 nm illumination wavelength in LSPPIL and replaced the silver coating by tungsten. Future sizes less than 32 nm will likely be attained using the proposed method.

In classical prism-coupled plasmonic nanolithography (contact based), the photoresist layer and the metallic thin film are placed in intimate contact; this may result in damage or pollution of surfaces. It is worth mentioning that He et al. in 2010 [5] proposed a backside exposure method to fabricate nanostructures that can prevent the drawbacks of the contact exposure scheme. Schematic of the backside-exposure SPPIL structure is shown in Fig. 4.2. The structure includes a prism, matching fluid layer and glass substrate, silver film, a resist layer, and an air layer.

In summary, prism-coupled plasmonic nanolithography has several advantages, including masklessness, high transmission, soft contact, and large-area fabrication capability.

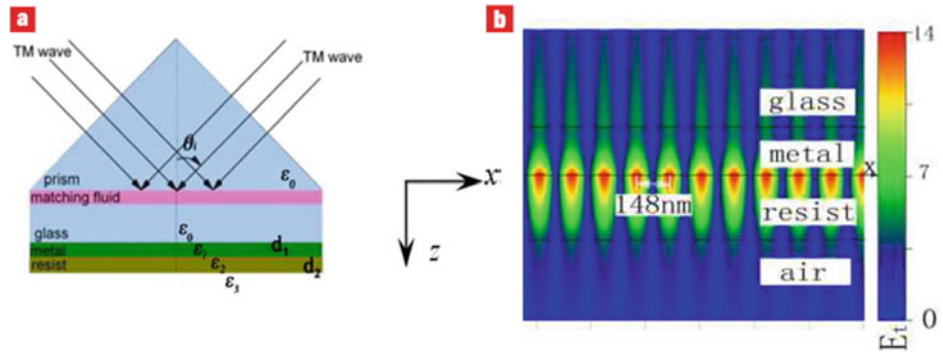

Fig. 4.2 **a** Backside-exposure SPPIL structure, **b** simulation result by FDTD, with incident wavelength 441.6 nm, thickness of silver film 40 nm, refractive index of resist 1.53 and thickness 50 nm. Electric field distribution when refractive index of the prism is 1.89

4.2 Grating-Coupled Plasmonic Nanolithography

Grating-coupled plasmonic nanolithography uses metallic grating masks along with appropriate structures to excite SPPs and pattern nanoscale features. As distinct from a Kretschmann scheme, the mask grating based scheme is much more compact. The schematic of plasmonic lithography configuration using metal mask is shown in Fig. 4.3a. It consists of a metal mask, which can be fabricated on a thin quartz glass by electron-beam lithography and lift off process. The mask is brought into intimate contact with a photoresist coated on a silica substrate. Normally incident light tunnels through the mask via SPPs and reradiates in to the photoresist.

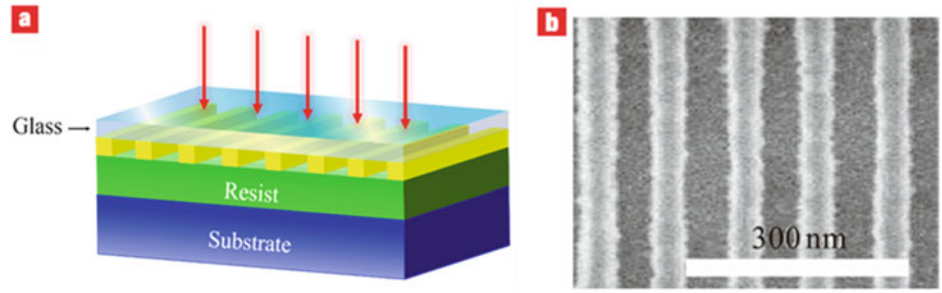

Fig. 4.3 **a** Schematic of a single metallic grating lithography. **b** SEM picture of the pattern using a single metallic grating lithography

In 2004, Luo et al. [6] performed analytical and numerical calculations to demonstrate this method. Figure 4.4 shows the considered nano-pattern. The proposed structure can be easily experimentally realized on a 2-mm thick quartz by electron beam lithography. To generate a high-contrast interference pattern, Doskolovich et al. optimized the diffraction grating for the substrate with a metal film at the interface of dielectric material. They have used a 3D metal–dielectric diffraction structure to generate the 2D surface plasmon interference patterns seen in Fig. 4.4 [7].

Figure 4.5 shows an interference pattern generated underneath the metal film in the case of TM wave incident with a wavelength of 550 nm. ψ is the polarization angle between the direction of the electric field vector E and the x-axis.

Patterns with even smaller sizes have been achieved using surface relief metal grating [8]. To further improve the intensity and quality of the interference fringes, surface plasmon interference lithography (SPIL) assisted by a Fabry–Perot (F-P) cavity was proposed by Liang et al. in 2015 [9]. The SPIL process is presented in Fig. 4.6.

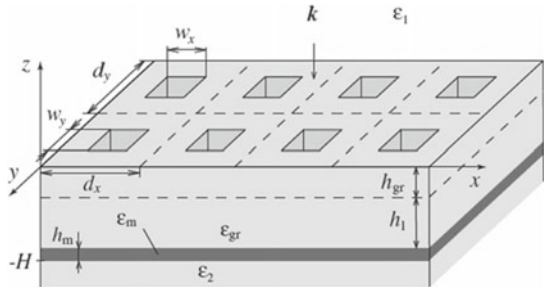

Fig. 4.4 Geometry of a 2D surface plasmon interference structure [7]

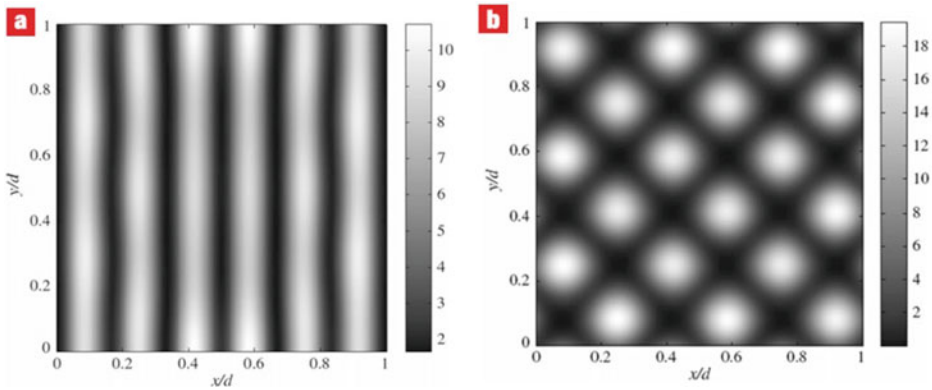

Fig. 4.5 **a** Electric field distribution underneath the metal film with TM wave incidence ($\psi = 0°$). **b** Electric field distribution in the case of linear polarization wave ($\psi = 45°$)

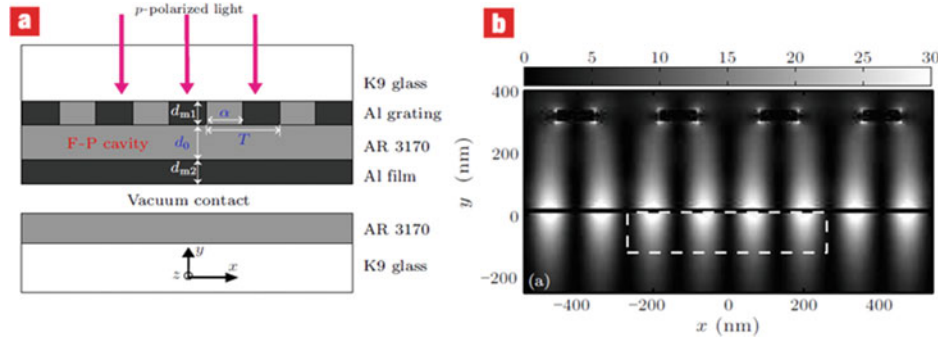

Fig. 4.6 **a** Fabry–Pérot cavity with the same photoresist material, this is useful to improve the intensity of interference fringes in the resist. Vacuum contact between two parts can be achieved with the assistance of a contact mask aligner

4.3 Focused Plasmonic Nanolithography

Focused plasmonic nanolithography, which is a promising technique due to its sub-diffraction resolution limit, can be described as an extension of scanning probe lithography (SPL). In this technique, resist is scanned and illuminated by a plasmonic lens-induced super-focused light spot.

In 2008, Wang et al. demonstrated a novel, practical plasmonic near-field scanning optical microscopy system (NSOM) experimentally for near-field lithography [10]. A subwavelength aperture is coated with thin Al and placed at the apex of the cone for the formation of a conic plasmonic lens. Subsequently, a high-speed maskless nanolithographic approach with a plasmonic lens was proposed by Srituravanich et al. [11] to improve efficiency. This idea combines the plasmonic lens with a flying head to focus the surface plasmon wave on a substrate rotating with a high speed. Its working principle is schematically shown in Fig. 4.7.

In this lithography experiment, a UV continuous-wave laser with 365 nm was focused down to a spot of several micrometers onto a plasmonic lens. It is further focused by the plasmonic lens to a spot of sub-100 nm to expose the spinning disk for writing arbitrary patterns on a thermal photoresist. The laser pulses were controlled by an electro-optic modulator according to the signals from a pattern generator. A "plasmonic flying head" with arrays of plasmonic lenses fabricated on its bottom surface was employed as the direct writing probe. Figure 4.7b shows the SEM image of the fabricated plasmonic lens, which has a 4 by 4 array of concentric ring gratings with a through hole perforated at the center.

Among all nanoparticles, the bowtie structure is attractive because of its triangular geometry, which leads to the "lightning-rod" effect at the gap apexes [12, 13]. In 2009,

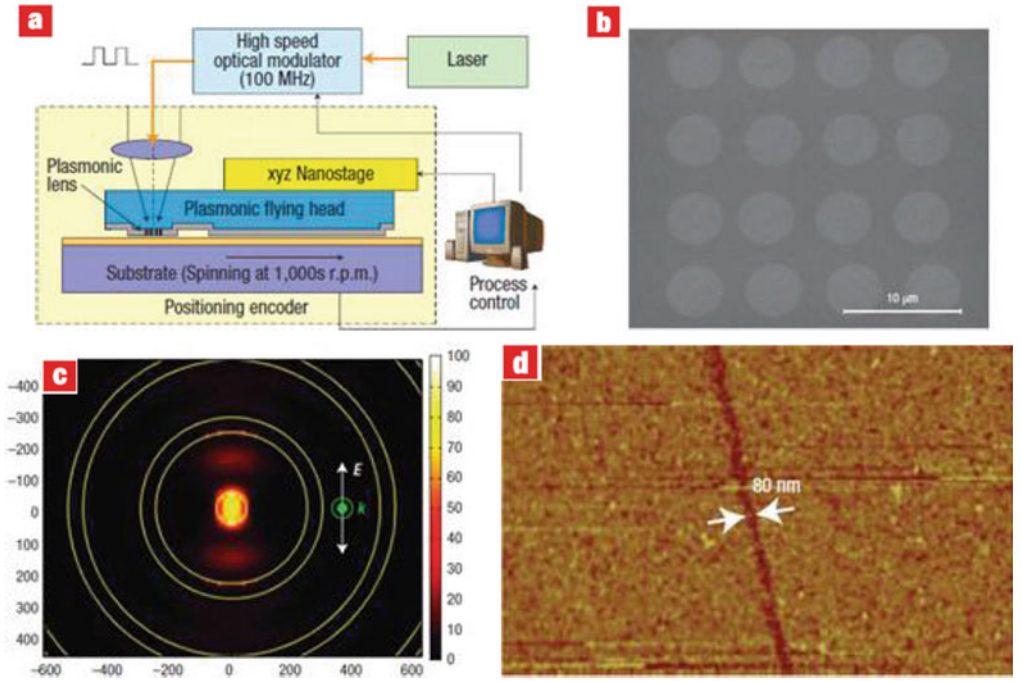

Fig. 4.7 **a** Maskless focused lens nanolithography with plasmonic lens array. **a** Schematic of the main process and the experimental setup. **b** SEM image of an array of plasmonic lenses fabricated on an air bearing surface. **c** FEM simulation of the focused spot using plasmonic lens. **d** AFM image of a resist pattern with 80 nm line width on a photoresist

Kim et al. reported a plasmonic lithography technique with bowtie-shaped contact probes [14].

As shown in Fig. 4.8, first an Al film of 120 nm thickness is coated on the flat surface of a conically shaped lens with a flat surface in 30 μm. In order to ensure the adhesion of the Al film and the glass substrate, a Cr layer of 2 nm thickness is added. Then, FIB is employed to fabricate bowtie apertures with about 140 nm dimension in order to achieve the highest transmission of the aperture. Finally, a single-atom self-assembled film was coated on the surface of silica film to reduce the friction between the probe and the photoresist during scanning. The experiment results are shown in Fig. 4.9; the smallest line width of 50 nm was realized when the polarized laser light had parameters of 405 nm wavelength and 0.5 mW power.

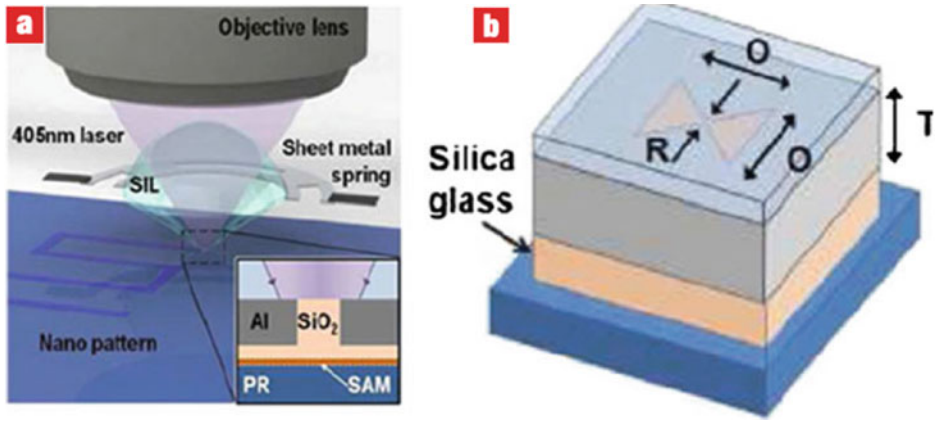

Fig. 4.8 **a** The structure of the bowtie-shaped probe. **b** Schematic of a bowtie aperture

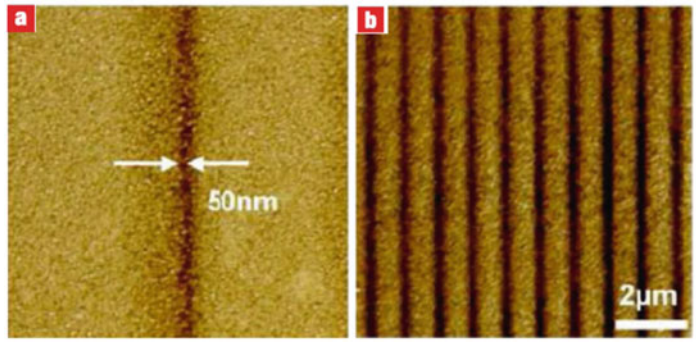

Fig. 4.9 **a** A single line of 50 nm width; **b** multiple line pattern of 150 nm width with 1 μm pitch

Recently, efforts have been redoubled to decrease the dimensions and increase the throughput of focused plasmonic nanolithography. Authors in [15] have utilized a bowtie aperture combined with a metal–insulator-metal (MIM) scheme to obtain sub-32 nm ($\lambda/12$) high-aspect plasmonic spots. In order to improve the throughput, a record number of near-field optical elements, an array of 1,024 bowtie antenna apertures, were simultaneously employed to generate a large number of patterns by carefully controlling their working distances over the entire array with an optical gap metrology system [16].

References

1. X. Guo, J. Du, Y. Guo, and J. Yao, "Large-area surface-plasmon polariton interference lithography," *Optics Letters,* vol. 31, pp. 2613–2615, 2006/09/01 2006.
2. X. Guo and Q. Dong, "Coupled surface plasmon interference lithography based on a metal-bounded dielectric structure," *Journal of Applied Physics,* vol. 108, p. 113108, 2010.
3. Y. Lim, S. Kim, H. Kim, J. Jung, and B. Lee, "Interference of Surface Plasmon Waves and Plasmon Coupled Waveguide Modes for the Patterning of Thin Film," *IEEE Journal of Quantum Electronics,* vol. 44, pp. 305-311, 2008.
4. W. Xiong, J. Du, L. Fang, X. Luo, Q. Deng, and C. Du, "193 nm interference nanolithography based on SPP," *Microelectronic Engineering,* vol. 85, pp. 754–757, 5// 2008.
5. M. He, Z. Zhang, S. Shi, J. Du, X. Li, S. Li*, et al.*, "A practical nanofabrication method: surface plasmon polaritons interference lithography based on backside-exposure technique," *Optics Express,* vol. 18, pp. 15975–15980, 2010/07/19 2010.
6. X. Luo and T. Ishihara, "Surface plasmon resonant interference nanolithography technique," *Applied Physics Letters,* vol. 84, pp. 4780-4782, 2004.
7. E. A. Bezus and L. L. Doskolovich, "Grating-assisted generation of 2D surface plasmon interference patterns for nanoscale photolithography," *Optics Communications,* vol. 283, pp. 2020–2025, 5/15/ 2010.
8. J. Dong, J. Liu, P. Liu, J. Liu, X. Zhao, G. Kang*, et al.*, "Surface plasmon interference lithography with a surface relief metal grating," *Optics Communications,* vol. 288, pp. 122–126, 2/1/ 2013.
9. H.-M. Liang, J.-Q. Wang, X. Wang, and G.-M. Wang, "Surface Plasmon Interference Lithography Assisted by a Fabry–Perot Cavity Composed of Subwavelength Metal Grating and Thin Metal Film," *Chinese Physics Letters,* vol. 32, p. 104206, 2015.
10. Y. Wang, W. Srituravanich, C. Sun, and X. Zhang, "Plasmonic Nearfield Scanning Probe with High Transmission," *Nano Letters,* vol. 8, pp. 3041–3045, 2008/09/10 2008.
11. W. Srituravanich, L. Pan, Y. Wang, C. Sun, D. B. Bogy, and X. Zhang, "Flying plasmonic lens in the near field for high-speed nanolithography," *Nat Nano,* vol. 3, pp. 733–737, 12//print 2008.
12. H. T. Chorsi and S. D. Gedney, "Efficient high-order analysis of bowtie nanoantennas using the locally corrected Nystrom method," *Optics Express,* vol. 23, pp. 31452–31459, 2015/11/30 2015.
13. B. J. Roxworthy, K. D. Ko, A. Kumar, K. H. Fung, E. K. C. Chow, G. L. Liu*, et al.*, "Application of Plasmonic Bowtie Nanoantenna Arrays for Optical Trapping, Stacking, and Sorting," *Nano Letters,* vol. 12, pp. 796–801, 2012/02/08 2012.
14. Y. Kim, S. Kim, H. Jung, E. Lee, and J. W. Hahn, "Plasmonic nano lithography with a high scan speed contact probe," *Optics Express,* vol. 17, pp. 19476–19485, 2009/10/26 2009.

15. Y. Wang, N. Yao, W. Zhang, J. He, C. Wang, Y. Wang, *et al.*, "Forming Sub-32-nm High-Aspect Plasmonic Spot via Bowtie Aperture Combined with Metal-Insulator-Metal Scheme," *Plasmonics,* vol. 10, pp. 1607-1613, 2015.
16. X. Wen, A. Datta, L. M. Traverso, L. Pan, X. Xu, and E. E. Moon, "High throughput optical lithography by scanning a massive array of bowtie aperture antennas at near-field," *Scientific Reports,* vol. 5, p. 16192, 11/03/online 2015.

Plasmonic MEMS in Biosensing and Imaging

5

Constructed on the theories discussed in "Chap. 2" and the versatile fabrication techniques described in "Chap. 3", the concept of plasmonic MEMS and micropatterning have been developed for various applications including compact chemical and biological sensors, optical data storage, micro/nano imaging, and ultrahigh resolution displayers and printers, to name a few. Subwavelength confinement and enhancement of light by surface plasmons make it possible to build ultra-sensitive biological imaging and sensing devices and integrate them in a wide range of different on-chip applications. In this chapter, we focus on the emerging field of bio-sensing and bio-imaging. This chapter is divided into four sections including refractive-index based label-free biosensing; plasmonic near-field scanning optical microscopy; plasmonic integrated lab-on-chip for point-of-care (POC) systems; and plasmonic on-chip cellular imaging.

5.1 Refractive-Index Based Label-Free Biosensing

Surface plasmons are extremely sensitive to their surrounding environment. This appealing feature has been exploited in a variety of designs and structures for refractive-index based label-free biosensing. The two main operation principles of the plasmonic based bio/gas sensing devices are the excitation of surface plasmon polaritons (SPPs) and the localized surface plasmons (LSPs). These two methods are schematically illustrated in Fig. 5.1.

Biosensors based on propagating SPPs in thin metallic films are the most well-explored and commercially available optical biosensors. Film-based SPP sensors have become the ideal technique for characterizing biomolecule interactions. Excitation of the SPR in thin films is usually carried out in the so-called Kretschmann configuration, in which light is

© The Author(s), under exclusive license to Springer Nature Switzerland AG 2023

J. X. J. Zhang, *Plasmonic MEMS*, Synthesis Lectures on Materials and Optics,
https://doi.org/10.1007/978-3-031-23137-7_5

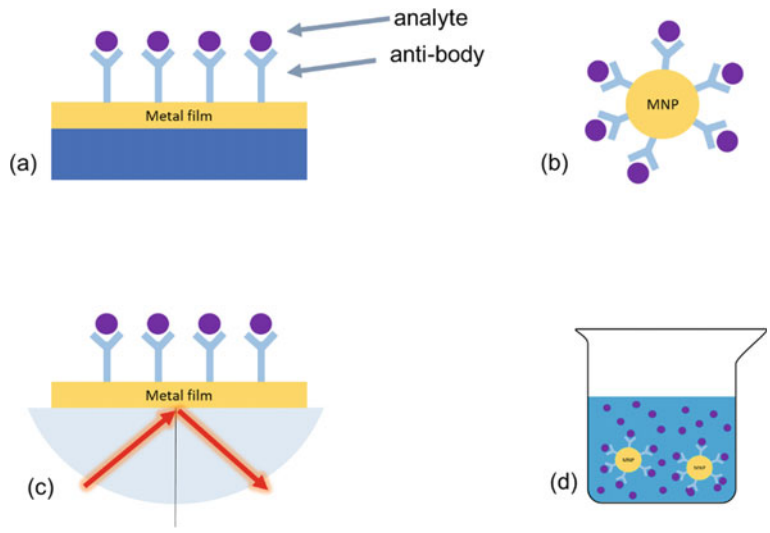

Fig. 5.1 Two main plasmonic detection and sensing methods. (**a**, **c**) Schematic of the surface plasmon polaritons (SPPs) based sensing and Kretschmann configuration. (**b**, **d**) Schematic of the localized surface plasmons (LSPs) based sensing

coupled into the gold film by a prism that facilitates total internal reflection. The structure is shown in Fig. 5.1c.

Surface plasmon based sensing experiment process can be divided into three main parts, first, a bioreceptor (antibody/antigen, enzymes/ligands, aptamer, DNA, etc.) is appended to the surface using either physisorption or covalent binding. Afterwards, a reference optical response of the instrument is obtained (transmission, reflection, or absorption). Finally, a target analyte is introduced to the surface, and the change in surface plasmon angle, phase or wavelength is recorded over time.

The development of surface plasmon based sensors in the past few decades, has led to the successful development of numerous sensing methods and methodologies with unique properties for a variety of application [1]. In this section we focus on two main topics, including plasmonic sensing for cancer therapy and neural sensing and imaging.

Exosomes are membranous nanovesicles (30–100 nm in size) secreted by most cell types including tumor cells. Exosomes have found potential applications in biotherapeutics and drug delivery and the current understanding of their operating mechanism is under intensive research.

Zhu et al. have recently demonstrated a real-time, label-free plasmonic biosensor combined with microfluidics for the detection of tumor-derived exosomes [2]. The structure of their setup is shown in Fig. 5.2.

The structure consists of thin gold film evaporated on a glass substrate and excited via a light source at a fixed incident angle. A 30 μL flow cell was mounted on top of

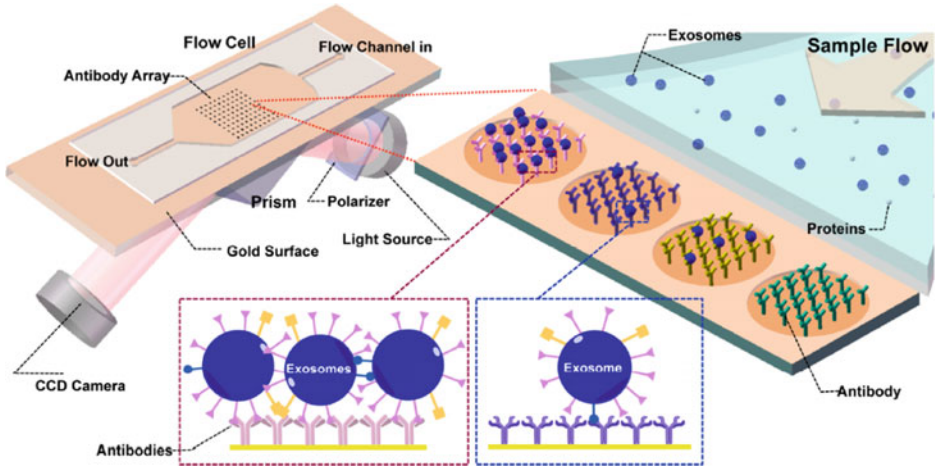

Fig. 5.2 Plasmonic-based microarray to capture and detect exosomes. Attachment of different exosomes to different functionalized surfaces induced a refractive index change which can be detected via shift in the reflection spectrum [2]

the plasmonic structure to allow the circulation of the sample. The reflectivity spectrum is obtain using a charge-coupled device (CCD) camera. Specific antibodies, including tetraspanins, glycoprotein CD41b, and tyrosine kinase receptor MET were used to capture cancer tumor secreted exosomes. The setup was able to identify exosomes in cell culture supernatant directly without enrichment or purification. The proposed design can be exploited toward monitoring the development and foreseeing the prognosis of cancer.

In a more recent work, authors in [3], have used surface-enhanced Raman scattering (SERS) to demonstrate a label-free and highly sensitive plasmonic biosensor for sensing exosomes. Instead of analyzing the reflectivity data, authors examined the SERS spectrum. The structure consists of plasmonic nanoparticles to enhance the Raman scattering. The schematic of the realized structure is shown in Fig. 5.3.

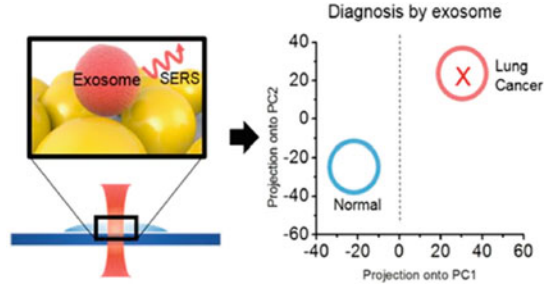

Fig. 5.3 Schematic of exosome detection and SERS enhancement. PCA method used for exosome classification

It has been shown that SERS based sensing can be more sensitive that thin film based plasmonic sensing and usually requires less biopsy samples. This apparent advantage makes SERS an appealing method to detect exosomes that are found in urine or saliva. Unfortunately, SERS-based methods require a very accurate analysis of the Raman scattering spectrum. To solve this problem, authors in [3], developed a principal component analysis (PCA) tool to reduce data by maximizing the covariance of the spectral data. Using the spectral variations in the SERS spectrum detection of the non-small-cell lung cancer (NSCLC) derived exosomes and alveolar cell derived exosomes were achieved.

Based on the above discussions, the combination of SERS and microfluidics can be considered as a powerful method for plasmonic sensing and detection of cancer cells and tumor-derived exosomes. Pallaoro, et al. from Martin Moskovits's group have exploited this combination for rapid identification cancer cells at low concentrations [4].

The designed chip-based device can be seen in Fig. 5.4. The device was used to detect cells labeled with mixtures of two spectroscopically distinguishable SERS biotags that target distinct cell epitopes. The designed geometrical shape of the microfluidic channel facilitates to focus the samples in a small region under the focused laser beam, which was used to excite the surface plasmons. Tagged silver nanoparticle monomers (with about 45 nm diameter) were encapsulated in polyvinylpyrrolidone for stability. Sensitivity down to one cancer cell was obtained with small batch-to-batch variability.

In a multi-laboratory collaboration, Cetin et al. present a handheld plasmonic biosensor capable of high-throughput, multiplexed detection of proteins without the need for resource- and labor-intensive lab equipment [5]. The device consists of a plasmonic sensor chip, integrated LED light source (683 nm peak) for plasmon excitation, an off-the-shelf CMOS imager chip, and a battery, all housed in a 7 cm tall portable case (Fig. 5.5). The plasmonic chip is a layered Au-Ti-SiN structure containing arrayed 100 μm^2 "pixels",

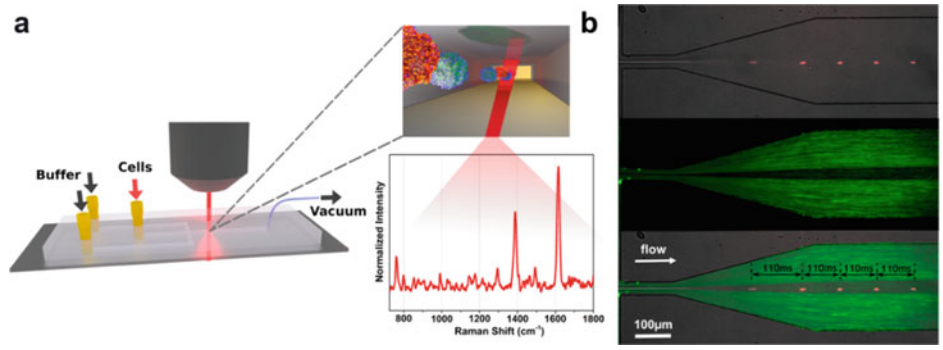

Fig. 5.4 Microfluidic device coupled to a microscope for cell imaging. **a** Graphical depiction of the microfluidic channel with cell transportation, optical detection and spectral data output. **b** bright-field and epifluorescence image of a single cell in the channel as a function of time [4]

each of which consists of 200 nm-wide nanoholes that form the sites of molecule interaction (Fig. 5.5c). Biosensing is achieved via imaging of the surface plasmon resonance diffraction patterns of the pixels upon administration of the biosample, with demonstrated sensitivity down to 3 nm-thick protein layers. Note that neither labels nor protein-specific antibodies are used. The result is a low-cost, 60 g portable diagnostic tool with potential point-of-care applications in resource-limited settings.

The multiplexing capabilities of the device arise from the differential intensities of plasmon diffraction patterns corresponding to binding of protein monolayers and bilayers, respectively as seen in Fig. 5.5c. The authors demonstrate simultaneous biosensing of protein BSA (monolayer) and protein IgG + A/G complex (bilayer) on adjacent sensor pixels.

The proteins cause a greater relative intensity difference compared to a bare pixel, as captured by the imager chip, and there is correlation between the on-chip measurement of plasmon diffraction intensity and the peak wavelength of transmission through the bound plasmon substrate in separate optical spectrum analyzer measurements.

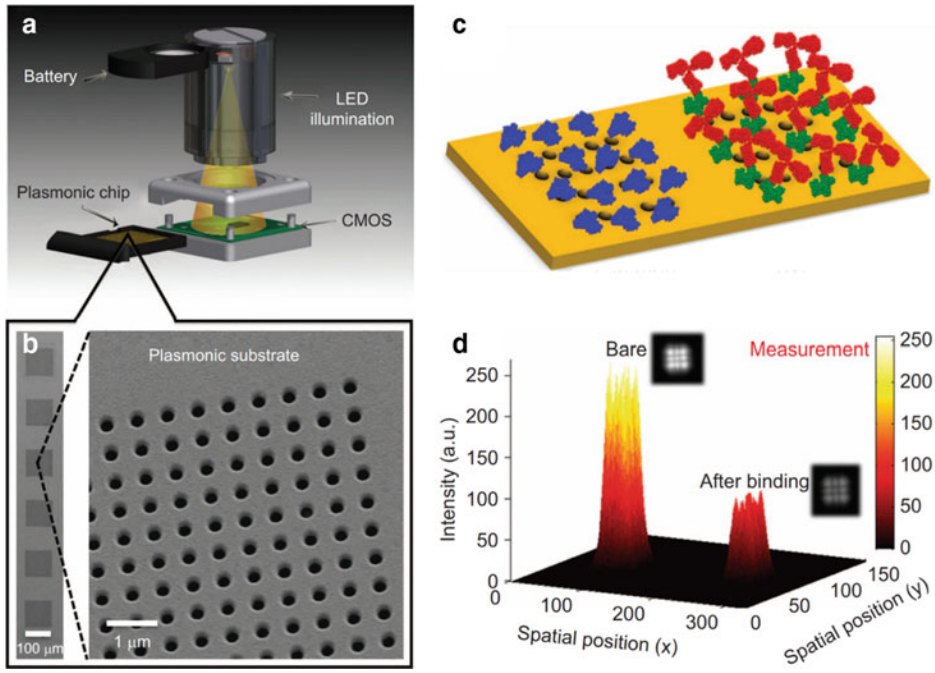

Fig. 5.5 Handheld plasmonic biosensor. **a** Plasmonic sensor chip integration along with its components. **b** SEM image of the device. **c**, **d** binding of protein monolayers and bilayers [5]

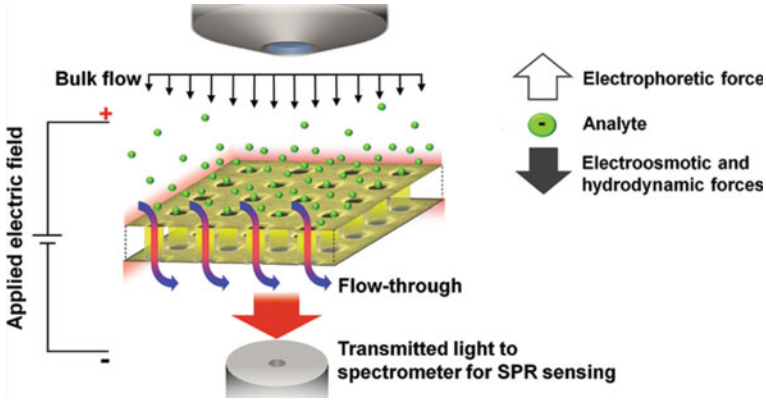

Fig. 5.6 Plasmonic optofluidic device and the accumulation of analyte inside plasmonic trenches [6]

The handheld device also performs a lens-free image reconstruction process to mitigate the diffraction pattern overlap which occurs as light travels from the densely arrayed plasmonic substrate to the CMOS imager chip 2 mm away. On the imager chip, raw incoming diffraction patterns are unsampled, from which field intensity information is computed and back-propagated to the chip aperture, and object support is then enforced at the aperture. Next, the modified field is back-propagated to the plasmonic sensor plane to create a complex two-dimensional phase function. The original intensity field and the new phase field are then fed into the start of the computational cycle; repetition of approximately 15 cycles gives a reconstructed image of the plasmonic microarrays recovered from a single original intensity image. The computational algorithm allows for high-throughput readout of the dense, multiplexed plasmonic microarrays, theoretically up to 170,000 plasmonic sensor pixels for a 5.7 mm by 4.3 mm CMOS chip (Fig. 5.6).

Escobedo et al. have created a plasmonic "optofluidic" device that utilizes the accumulation of analyte inside nanoscale flow-through channels for SPR-based detection at very low concentrations [6]. This technique of concentrating the analyte has potential applications for sensing sparse biomarkers at the early stages of disease in order to accelerate diagnosis and improve the chances of successful patient outcome.

The plasmonic structure consists of an array of flow-through nanoholes (300 nm in diameter with a 450 nm periodicity) in a layered substrate of Au-Si_3N_4 (each 100 nm thick). Electric field gradient focusing (EFGF) is achieved via an applied voltage to the optofluidic chip, which makes its surfaces act as cathode and anode. Along with bulk fluid flow, the EFGF results in the movement of buffer solution anions towards the anode. Due to the local depletion of anions that develops near the Au surface, the analyte tends to travel towards and concentrate in this region. A pressure bias then forces the concentrated analyte into the nanoholes, where it can be sensed via SPR.

The authors first demonstrate the principle of analyte concentration in the nanoholes by optical imaging of florescein, a florescent dye. With an applied voltage of 50 V and pressure of 4 kPa, saturation of florescein in the substrate occurs after approximately 2 min; the dye increases about 200-fold from its original concentration of 100 nM. For plasmonic-based sensing, the gold surface is functionalized with an amine monolayer and bovine serum albumin (BSA) is introduced as the analyte. An 8 nm shift in the wavelength of peak resonance of optical transmission is observed after a binding time of 120 s. This is a tenfold decrease in binding time and a fivefold increase in peak shift compared to controls (no voltage or pressure gradients). The results of optofluidic protein concentration are a 100-fold enrichment and simultaneous sensing of analyte in less than 1 min.

In addition to their work on low-cost and portable diagnostic devices, the Altug group has also made efforts to improve the sensitivity of plasmonic biosensors in infrared spectroscopy applications [7]. They present a graphene plasmonic device tuned to the mid-IR resonances of protein amide I and II bonds, and show that the extinction spectra of the graphene, with varying bias voltages, produces a biosensing signal that captures the dips corresponding to these molecular vibrational fingerprints in an A/G + IgG protein bilayer.

The device consists of a graphene layer etched into 20–60 nm wide ribbons on top of a 280-nm-thick silica oxide substrate connected to a variable voltage source. This configuration has an advantage over state-of-the art gold metallic LSPR biosensors due to its superior field confinement (29% vs. 4% overlap with the protein), enhanced biosensing signal modulation (27% vs. 11%), and magnified analyte-induced resonance shift (160 cm^{-1} vs 27 cm^{-1}) in the mid-IR. The authors also demonstrate that their graphene nanoribbon's peak resonance can be dynamically optimized to match the optical properties of the protein via sweeping the applied voltage between −20 V and −130 V to control the Fermi level, which tunability can only be achieved in a gold biosensor by fabricating gold dipoles of multiple lengths.

In contrast to the convention of SPR sensing based on resonance shift, Yesilkoy et al. have created the first plasmonic biosensor operating on the principle of optical phase shift [8]. Their system retains all the advantages of label-free biomarker sensing for point-of-care applications in resource-limited settings, but also integrates a high-throughput multiplexing platform free of the intensity-based noise of other plasmonic biosensors.

The sensor is constructed from multiple gold nanohole arrays, each functionalized to detect a different protein to give multiplexing capabilities, on top of a 4-inch glass wafer (fabricated using low-cost deep-ultraviolet lithography). This plasmonics chip is then integrated with a microfluidic device that passively drives the patient's blood sample over its surface (Fig. 5.7).

Haes et al. published one of the landmark papers in the progression of plasmonic biosensors, the first analysis of endogenous biological samples using LSPR detection [9]. They present an LSPR sensor to address the need for an Alzheimer's disease diagnostic device, specifically for the detection of amyloid-derived diffusible ligands (ADDLs) which are strongly implicated in the pathogenesis of neurodegeneration. The sensor is

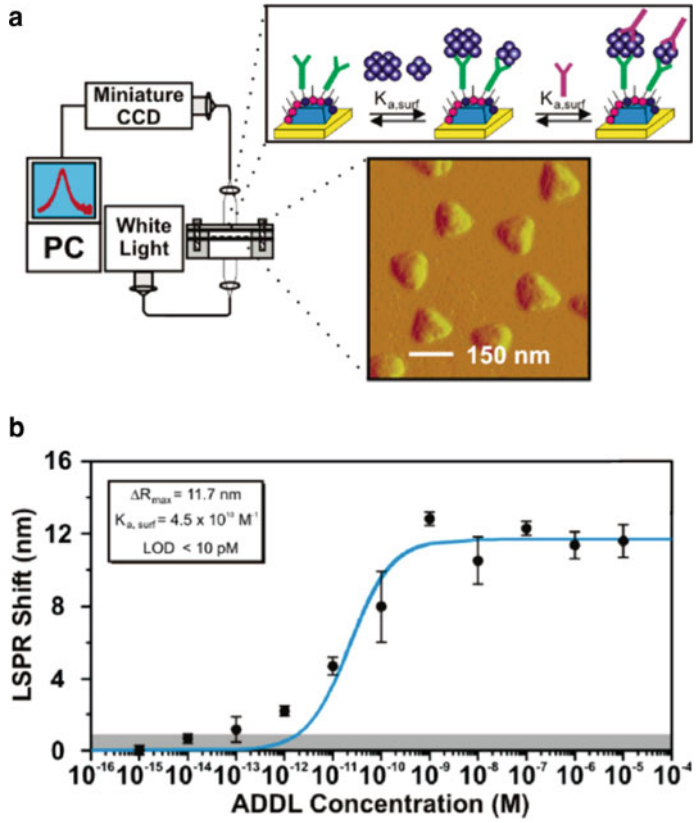

Fig. 5.7 Plasmonic sensor for the amyloid-derived diffusible ligands (ADDLs). **a** setup and surface functionalization methods. **b** plasmonic spectrum shift [9]

composed of gold nanoparticles functionalized with anti-ADDLS antibodies; association of the antigen and a secondary anti-ADDL antibody allows for an enzymatic sandwich assay in which the presence of the biomarker is revealed by extinction spectroscopy.

90 nm-wide triangular nanoparticles were first fabricated using nanosphere lithography on a gold substrate. The nanoparticles are functionalized with a self-assembled monolayer (SAM), which in turn is conjugated to anti-ADDL antibodies via covalent bonding. The electric field of the LSPR is confined to about 35 nm from the surface of the nanoparticles. To obtain the biomarker of interest, the authors collected cerebrospinal fluid and brain extract samples from both control and diseased patients, and also produced synthetic ADDLs in the laboratory.

During the detection process, the nanoparticles are incubated in solution with the ADDL antigen, then a second anti-ADDL antibody with a different epitope, each for 30 min. UV–Vis spectroscopy excites SPs and records the extinction profile of the sample.

The system displays a concentration-dependent LSPR shift upon binding of ADDL, from 718.5 nm to 722.7 nm. This shift can be used to quantify the amount of the biomarker present using an analytical model of the sample's refractive index and knowledge of the biomolecules' thermodynamic affinity constants; the model accurately predicts the binding responses for ADDL concentrations ranging from 1 fM (lower limit of detection) to 100 nM (upper limit of detection). Binding of the second antibody amplifies the peak resonance shift by an additional 7.6 nm wavelength and gives a greater signal-to-noise ratio.

This LSPR nanoparticle setup allows for detection of ADDL in human brain extract collected post-mortem, and more importantly in cerebrospinal fluid collected from living patients, at very low, biologically relevant concentrations that had previously precluded the possibility of Alzheimer's disease detection. The sensor displays virtually no non-specific binding. In addition to basic biomarker detection, the authors are also able to use their quantitative model to provide an estimate for the concentration of ADDL in brain diseased brain tissue (approximately 1 pM), and to hypothesize that there is a distinct oligomer conformation of ADDL in the spinal fluid compared to the brain.

Dipalo et al. have produced a plasmonic nanoantenna array capable of multiplexed and multifunctional recordings of neural activity in real time [10]. They combine surface-enhanced Raman spectroscopy (SERS) with multielectrode recordings on the same plasmonic substrate to achieve simultaneous sensing of cell-specific biomolecules and gross neural activity. Rat hippocampal neurons are cultured in vitro directly on the substrate so that the nanoantennas come into contact with the tissue.

The structure consists of FIB-milled plasmonic nanoantennas (cylinders) functionally connected to a gold multielectrode array (4 mm^2 with 25 electrodes) via a deposited gold layer as shown in Fig. 5.8. The authors investigate various ways of optimizing the fabrication process on bulk and pre-structured quartz wafers. The gold surface of the substrate supports surface plasmons and their analyte-induced resonance shifts, hence is suitable for SERS. Electric field enhancement by the nanoantennas is first validated with methylene blue dye on the bare substrate, then a $60\times$ immersion objective directly inserted in the cell culture media for the main experiment with live neurons.

For an excitation wavelength of 785 nm, the nanoantennas enhance the field by up to a factor of 30 compared to a rough gold surface. For neural recordings, spontaneous extracellular action potentials can be recorded between 14 to 24 days in vitro, from about 70% of the nanostructured electrodes. Detected spike amplitudes are in the range of 20–80 μV_{pp} with noise comparable to that of standard multielectrode arrays. SERs measurement on the living neurons displayed distinct vibrational fingerprints corresponding to amino acids; different spectra obtained by different nanoantennas for a single neuron opens the possibility of monitoring the subcellular molecular environment for various neural processes (e.g., gene expression) (Fig. 5.9).

Chanda et al. have developed a highly specific and sensitive plasmonic detector for dopamine in blood which has the unique advantage of not requiring sample preparation

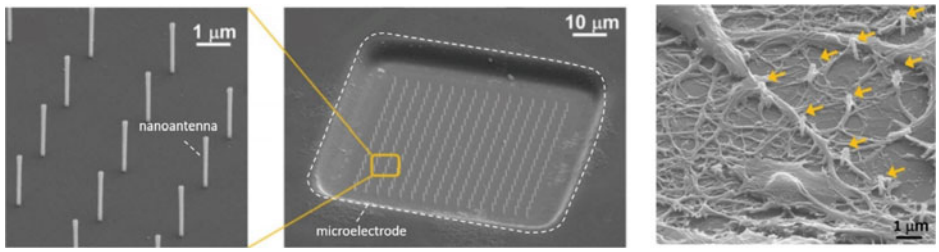

Fig. 5.8 Plasmonic nanoantenna array for recording neural activity. The gold surface of the substrate supports surface plasmons [10]

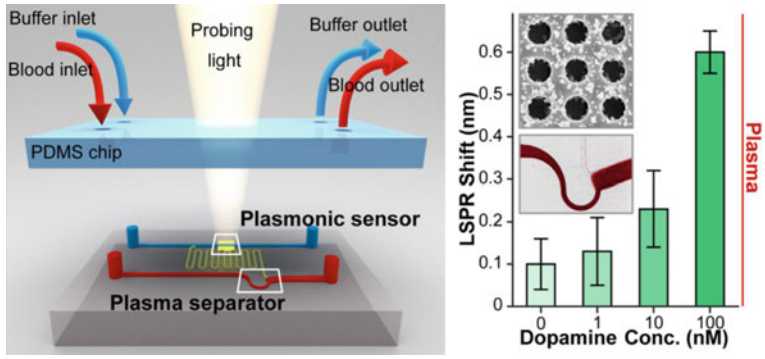

Fig. 5.9 Integrated microfluidic plasmonic detector for dopamine in blood and the corresponding plasmonic shift [11]

[11]. Dopamine in the bloodstream can serve as a biomarker for various forms of cancer, such as pheochromocytoma, neuroblastoma, or paraganglioma. Blood biomarker detection by traditional assays like ELISA and liquid chromatography have restricted applicability in resource-limited settings because of the extensive preparation procedures that must be run on the patient's sample. Thus, combining the sophisticated sensitivity of SPR-based sensing with a simple, low-tech sample preparation protocol opens a wide range of point-of-care applications.

The device is an integrated microfluidic chip for passive separation of plasma and a plasmonic substrate for SPR-based sensing of dopamine. The microfluidic system extracts a small amount of blood directly from the bloodstream and passes it through a bifurcation; differential flow rates between two channels causes the large blood cells to sift out of the rest of the plasma. Then, the pure plasma is shuttled towards the active plasmonic biosensing area. The plasmonic system consists of nanoholes (300 nm diameter) in a gold substrate on top of a PDMS layer.

In order to make the plasmon resonance shift sensitive to dopamine, the surface of the gold is functionalized with cerium oxide nanoparticles (CNP). The inorganic redox active CNPs act as a site for DA binding, causing a change in the refractive index of the gold substrate which can be measured via spectrophotometry. To optimize the sensitivity of the CNPs for dopamine and its selectivity (that is, its ability to distinguish dopamine from similarly electroactive compounds like ascorbic acid and epinephrine that are also found in blood), the authors engineered two CNPs with different ratios of Ce^{3+}/Ce^{4+} to control its redox activity. The more efficient of these two was taken as the enzyme-free dopamine ligand for the device, allowing for the dopamine-induced resonance shift to be 5.3- and 20-times that of ascorbic acid and epinephrine.

The final integrated microfluidic-plasmonic device can detect dopamine down to 100 fM concentration in laboratory-prepared solutions and 1 nM directly from untreated blood. Further work using this platform can help establish a generalized protocol for the detection of biomarkers directly from patient blood samples.

Boer et al. accomplish optical activation of neurons in vivo using second harmonic generation in gold nanoparticles (NPs) [12]. Their setup has advantages over other current photostimulation regimes, such as optogenetics, in that it does not require transgenic engineering or the use of intrusive pharmacological agents. The gold NPs are bound to the membrane of single cells and can be integrated with current electrophysiological recording techniques (Fig. 5.10).

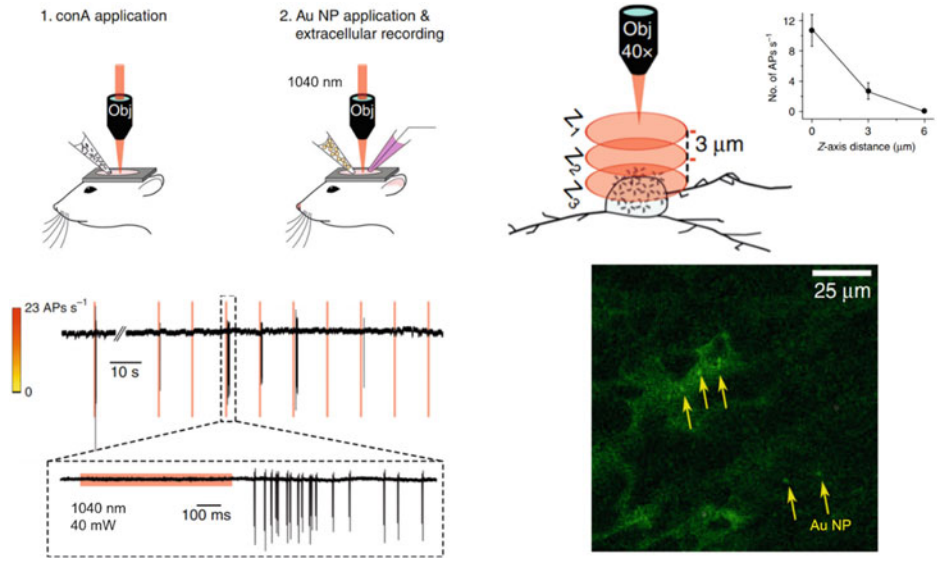

Fig. 5.10 Plasmonic activation of neurons in vivo using second harmonic generation in gold. Pulsed laser stimulation at 1040 nm [12]

First, to achieve photoactivation of mouse cortical slices in vitro, they coat neuronal membranes with either a concanavalin A-biotin (conA) complex or an NHS-biotin linker, each of which strongly binds streptavidin. Then, streptavidin-functionalized gold NPs are bathed over the neuron to create an immobilized NP layer. Photoactivation is performed by pulsed laser stimulation at 1040 nm (double the resonant wavelength of the gold NPs), for which the intensity neuronal action potentials can be reliably tuned by the power of the incident light. Activation is a nonlinear function of the depth of the focal plane with respect to the neuron, thereby achieving high spatial resolution. The authors are able to successfully evoke repeatable action potentials in 22 of 26 NHS-incubated cells, and all 8 of the conA cells. Interestingly, the control experiments also reveal that direct absorption of pulsed IR light can induce action potentials in the neuron, but only at a power 20–50 × higher than with gold NPs which results in cell damage in loss of precise control over neural activity.

Next, the authors demonstrate in vivo neuronal photostimulation in mice. Neurons in the visual cortex of anesthetized mice are treated with conA and fluorescent protein for visualization, then streptavidin- or neutravidin-functionalized gold NPs, also carrying a fluorescent protein, are applied to the cells. 40 mW laser excitation evokes either short bursts of action potentials directly following the stimulation or transient increases in the intrinsic firing rate. In 5 out of 6 neurons, this control was repeatable. For a final in vivo experiment, the authors use their gold NP scheme to control muscle contractions in the worm *Hydra vulgaris.*

An analytical study of the gold NPs reveals a strongly second-order energy absorption. Additionally, the authors calculate that the temperature increase accompanying NP excitation is safe for biological tissue within the confines of low-power laser stimulation. The NIR-excited gold NPs present a novel opportunity for precise optical control over neural activity in situations where prior genetic modification of the cell is prohibitive. The non-toxicity even at very high concentrations and the tunability of the optical properties of gold NPs makes them an attractive option for future development of human therapeutics.

5.2 Plasmonic Near-Field Scanning Optical Microscopy

As mentioned in Chaps. 1 and 2, the major roadblock in conventional optical systems, according to Abbe's diffraction theory, is that the wavelength of light (λ) has to be reduced to obtain a higher resolution. Unfortunately, conventional optical components such as bulk lenses and detectors are limited via this diffraction limit, and cannot provide high resolution imaging of micro/nanoscale components.

Near-field Scanning Optical Microscopy (NSOM) is a typical super-resolution optical microscopy that can beat the diffraction limit using near-filed evanescent waves and has been shown great promise in biological applications. NSOM converts the non-propagative

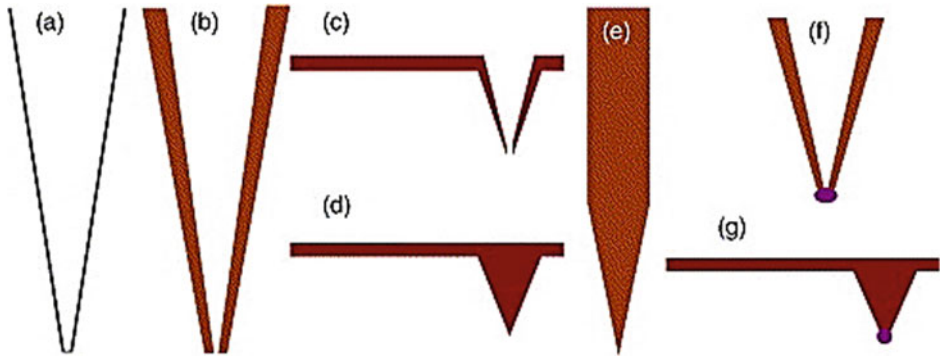

Fig. 5.11 Some types of NSOM tips. Uncoated fiber probe (**a**), metal-coated fiber probe (**b**), aperture cantilever probe (**c**), AFM cantilever probe (**d**), STM etched metal tip (**e**), metal-coated fiber probe with nanoparticle fixed tip (**f**), and AFM cantilever probe with nanoparticle at tip end (**g**) [15]

near-field signal into a measurable far-field contribution, so that nanoscale resolution can be achieved [13, 14] (Fig. 5.11).

Broadly speaking, NSOM techniques can be classified into "aperture" and "aperture-less" classes. Aperture NSOM uses a sub-wavelength metalized aperture along with an optical fiber; while apertureless NSOM exploits a plasmonic tip as a nanoantenna to provide higher spatial resolution.

In one of the early works, Zhang group demonstrated a high resolution near-field scanning "nanophotonic" microscopy [13]. The schematic of the operation principles of the device is shown in Fig. 5.12a.

The structure consists of a nanoscale light emitting diode (LED), attached to the apex of a metal-coated aperture cantilever probe. As can be seen in Fig. 5.12b ion milling was used to on an aperture at the apex of the probe. Next, electrical field was applied to trap the CdSe/ZnS core–shell nanoparticles. The probe was successfully exploited to measure the optical as well as topographical images of a chromium test sample with imaging resolutions of 400 and 50 nm, respectively. The proposed device is cost effective, mass-producible, light, and can be integrated for on-chip applications.

To enhance the imaging resolution, apertureless-type tip (also known as scattering-type tip) was employed [16, 17]. In a recent work, Jiang et al. have realized a plasmonic tip with subwavelength multiring to obtain super-focused plasmonic spot at the apex of a probe [17]. It has been shown that spot sizes with diameter as small as 8 nm can be achieved. Ultra-high signal to noise ratio of up to 18.2 was obtained. Near-field radial surface plasmons were excited via far-field radial illumination. Phase matching condition between the phase delay of the propagating surface plasmons and the phase delay of the excitation light was satisfied to ensure the constructive interference of plasmons at the apex of the probe (Fig. 5.13).

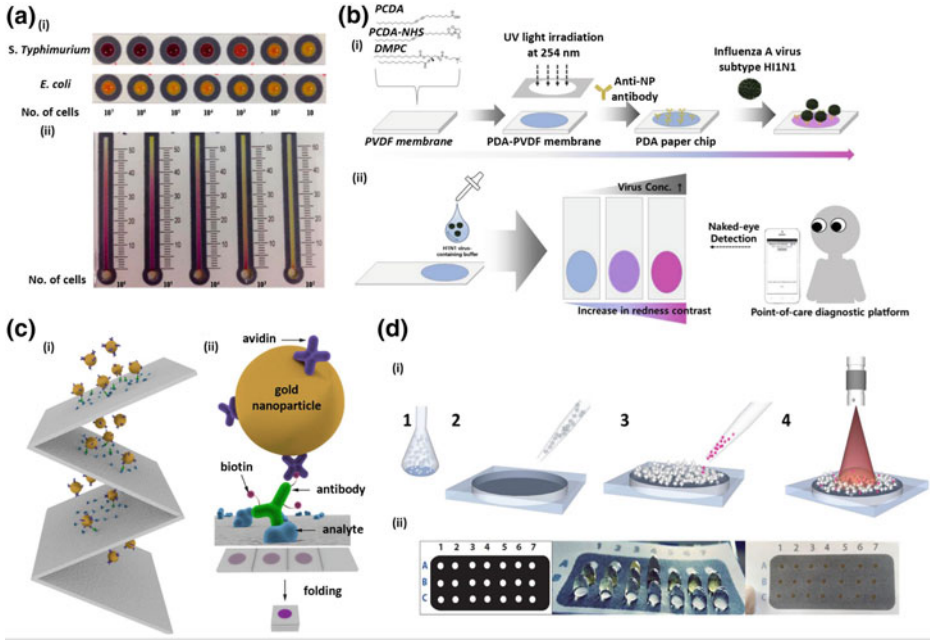

Fig. 5.12 **a** Concept of near-field scanning nanophotonic microscopy. **b** fabrication methods and tools. **c** Realized device. **d** Schematics of the experimental setup and the topographic images

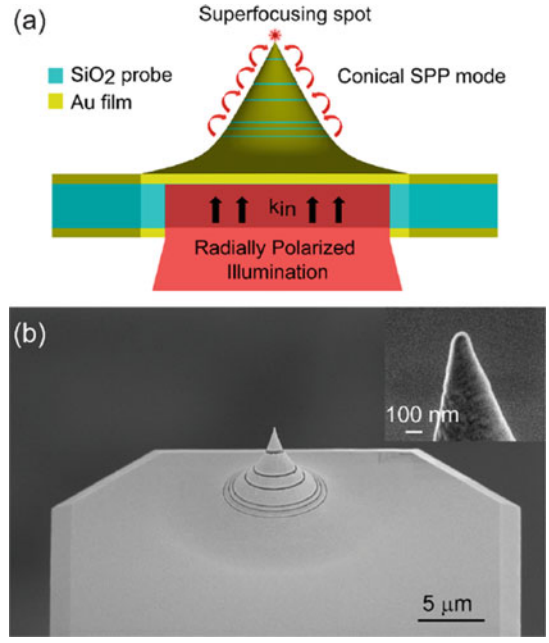

Fig. 5.13 **a** Plasmonic near-field scanning probe. Radial surface plasmons excited via radial illumination. **b** SEM image of the probe [17]

Müller et al. have reported the nonlinear emission of ultrashort electron wave packets from a plasmonic nanotip [18]. As shown in Fig. 5.14, nanograting was fabricated 20 μm away from the apex. This allows the generation and propagation of surface plasmons. Figure 5.14b shows the imaging setup along with the optical components. Sub-femtosecond electron pulses were generated from the apex of the gold nanotip. Generation of such ultra-short pulses can have interesting applications in biomedical imaging and cancer therapy.

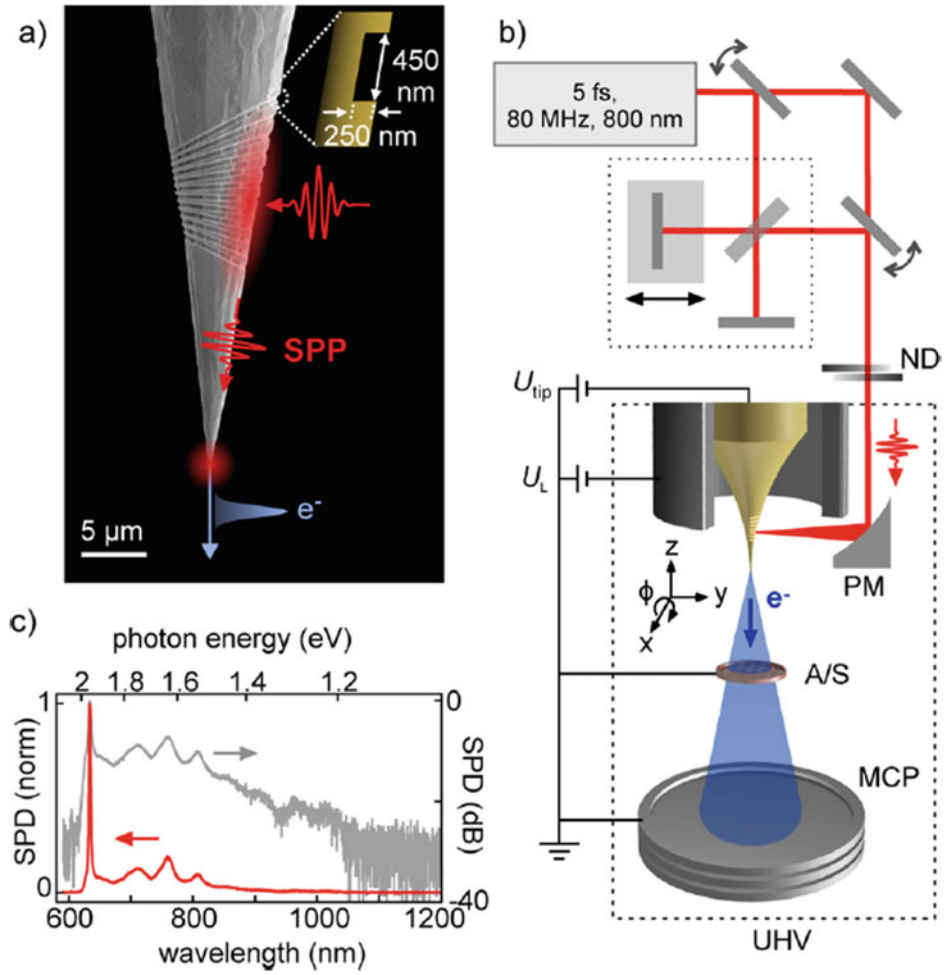

Fig. 5.14 **a** Plasmonic near-field probe. **b** optical imaging setup, PM: parabolic mirror, ND: neutral density filter, MCP: microchannel plate, UHV: ultrahigh vacuum, A/S: anode/sample. **c** The laser system spectral power density (SPD) [18]

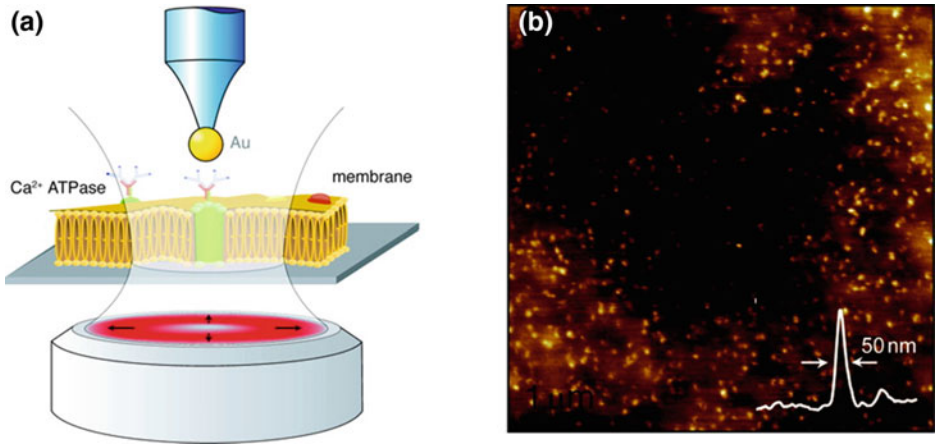

Fig. 5.15 **a** Localized surface plasmons at the apex of the tip excites fluorescently labeled erythrocyte plasma membrane. **b** Plasmon enhanced fluorescence image of individually resolved PMCA4 transporters [19]

NSOM as a powerful imaging technique has been used for ultra-high nano-spectroscopic imaging of single protein molecules. Ho1ppener et al. in a pioneering work have demonstrated the imaging of individual plasma-membrane-bound Ca^{2+} pumps (PMCA4) [19].

Figure 5.15a shows the operating principles of the realized antenna-based near field imaging. The sample is placed at the focal plane of the objective and excited via localized surface plasmons. Single membrane proteins in live cells with resolution down to 5 nm can be resolved using the proposed system. Besides detailed colocalization studies, this technique makes it possible to correlate topological and optical information. This technique opens up new possibilities for the identification of abnormalities in PMCA.

5.3 Plasmonic Nanosensors for Point-Of-Care (POC) Biomarker Screening

Here we extend the discussion from micro to nano, with focus on plasmonic nanomaterials and nanostructures. The rational design of plasmonic materials has the potential for profound implications within the field of biosensing, drastically increasing sensitivity and lowering limit-of-detection of assays that incorporate them. The materials and configurations though which this effect is employed has been rapidly expanding, leading to novel particle or structure geometries and/or configurations leading to greater levels of field enhancement. Plasmonic enhancement has been demonstrated to be a largely multifaceted parameter shown to be dependent upon numerous parameters of the overall

system, including particle or structure size, geometry, arrangement. morphology, material, areal density, among others [20, 21]. As such, there is significant interest in the optimization of these various parameters thereby allowing the rational design of the plasmonic nanomaterials with superior performance.

Of plasmonic nanomaterials, classifications can be developed that differentiate the two main systems reported in literature, namely particle-based systems and surface-based systems. The former class encapsulates efforts of engineering plasmonic nanoparticles based on material, geometry, morphology, size, and functional coatings [22–28]. Particles within these systems are typically fabricated using chemical synthesis methods, which provides significant levels of tunability and repeatability throughout batches. In these systems, the particles are often suspended and stabilized within solutions where the assays are completed. The latter class of surface-based systems consists of nanoparticles or structures upon a surface which can be tuned based on material, size, areal density, geometry, and periodicity [29]. Though this class may include singular particles aggregated upon the surface [21, 30], the mechanism and unique optical properties generated by this configuration merits differentiation from the former class. Fabrication methods can vary widely for such systems and prior reports have utilized simplistic processes such as chemical synthesis to advanced lithographic processes.

Currently within the field, there exists an emphasis on exploring various fabrication methodologies and techniques with the focus on the development of tunable plasmonic structures and systems. Though promising results have been shown with various system configurations, keeping scalability at the forefront of system development will enable future systems to be applicable in point-of-care (POC) settings. [31–33]. This application space requires a unique set of attributes not shared with use within clinical setting such as low-cost, scalable, and stable systems. By association, this provides unique challenges concerning fabrication methods employed or system configurations.

There are numerous unique considerations that must be considered concerning the design and implementation of plasmonic nanomaterials for POC biosensing applications. Namely, sensor type and structure (i.e., nanoparticle solution or substrate-based), reagent usage and sensor stability, as well as read-out method (i.e., colorimetric, fluorometric, etc.). Each of these factors have been explored in depth in literature thus they will be discussed in the following review. Recent developments aiding POC integration including automation of data analysis using machine learning techniques and integration of plasmonic materials with standard lateral flow assays will be reviewed and the future directions of the field will be elucidated. Lastly, current challenges of the field and where future developmental efforts need be focused will be discussed with an emphasis on current limitations concerning sensor fabrication, signal read-out, and scalability.

Demand for accessible, effective, and affordable management of infectious diseases in resource-limited settings is seeking for rapid, simple-to-use, inexpensive diagnostics for POC testing. Diagnostic criteria for POC testing in these settings are identified by the World Health Organization (WHO) to be ‘ASSURED’—affordable, sensitive,

specific, user-friendly, rapid, equipment free and delivered to the end-users [34]. Traditional diagnostic methods such as polymerase chain reaction (PCR) and enzyme linked immunosorbent assays (ELISA), although provide reliable diagnosis and post-treatment monitoring, they can hardly be applied in POC situations because they require a mass of manual preparation steps operated by well-trained technicians [35, 36]. As well-known POC solution, the lateral flow assays succeed in providing rapid, inexpensive, and semi-quantitative platforms for the detection of detection of various analytes but are held back by inadequate sensitivity and selectivity—especially the cross-reactivity problem [37]. Recently, plasmonic-based biosensors have emerged as a potential solution for disease diagnostics and treatment monitoring at POC [38–40]. They not only enhance the performance of existing platforms, but also provide new-emerging highly sensitive and label-free detection of biomarkers. Figure 5.16 provides an overview of typical biomarkers explored within point-of-care diagnostic technologies and those covered within this review. Disease types can vary greatly however biomarker type traditionally falls within four main classes, namely cells, viruses, bacteria, and/or other free-floating molecules. Within each biomarker class the components that aim to be detect can also vary, from the free-floating molecule itself, to nucleic acid cargo such as common within cells, viruses, and bacteria alike.

When light impinges from a dielectric medium onto a metallic surface, the electromagnetic (EM) field of the light excites the free electron of the metal to oscillate coherently

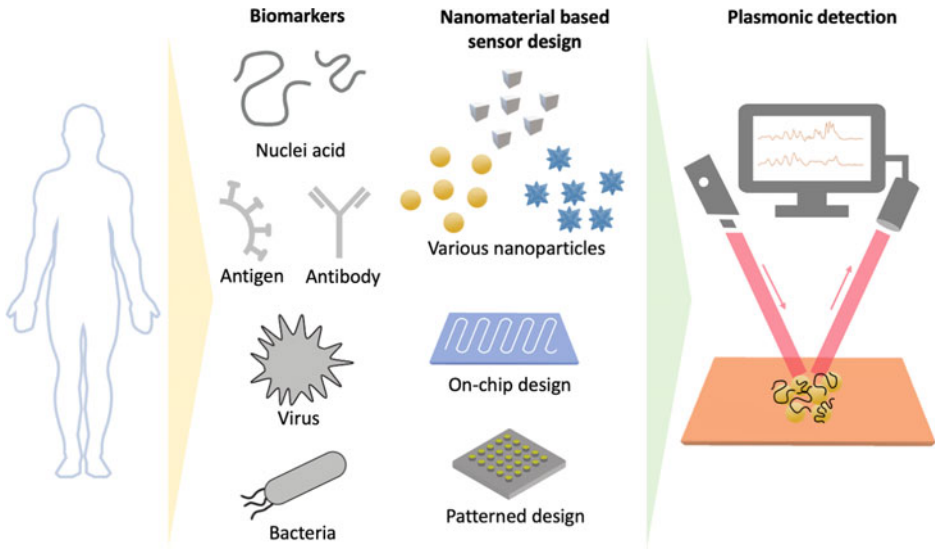

Fig. 5.16 Overview schematic showing typical biomarkers, the various shapes based sensor design and plasmonic detection that are explored within point-of-care diagnostic technologies reviewed in this work

and forms what is known as the surface plasmon [41]. Mainly two types of surface plasmons have been studied, namely the surface plasmon polariton and the localized surface plasmon (LSP) as shown in Fig. 5.16. A surface plasmon polariton is an EM surface wave that propagates along the planar dielectric-metal surface (Fig. 5.17a). A LSP is present when a surface plasmon is confined in a nanoparticle of size close or smaller than the wavelength of the excited light (Fig. 5.17b). For both the surface plasmon polariton and the localized surface plasmon, there exists a wavelength-specific resonant condition called the surface plasmon resonance (SPR), under which the surface plasmon is most efficiently excited. At the resonance wavelength, enhanced near-field amplitude is present. For localized surface plasmon, the highly localized field at the nanoparticle diminishes dramatically as it distances from the nanoparticle. The resonant interaction between the EM field and the surface plasmon at the SPR condition enables light to efficiently couple the plasmonic metal nanostructures. Such light coupling breaks the diffraction limit and creates an enhanced light-matter interaction at the subwavelength scale. A plasmonic metal nanostructure can have one or several SPR modes, each mode corresponds to a specific SPR wavelength. The SPR wavelength depends on the shape and material of the plasmonic nanostructure. It can also be tuned by nearby polarizable materials and optical cavities and is highly sensitive to the environmental refractive index changes.

The SPR enhanced light-matter interaction has benefited a wide range of biosensing applications. These applications are mainly of two categories. First, biosensors that interrogate the environmental changes through the change of the SPR signal, such as the SPR wavelength shift and SPR intensity changes. Second, biosensors based on a sensing mechanism that is not SPR itself but whose sensor responses are enhanced and augmented by the SPR, such as the SPR enhanced fluorescent imaging and the surface enhanced Raman spectroscopy (SERS) [42, 43].

The objective of this work is to provide a comprehensive review of the most recent progress on the design and assembly of plasmonic nanomaterials for POC biomarker detection. We will focus on, firstly, the design and assembly of the nanomaterials including nanoparticles and their shapes and configurations, patterned nanochips and

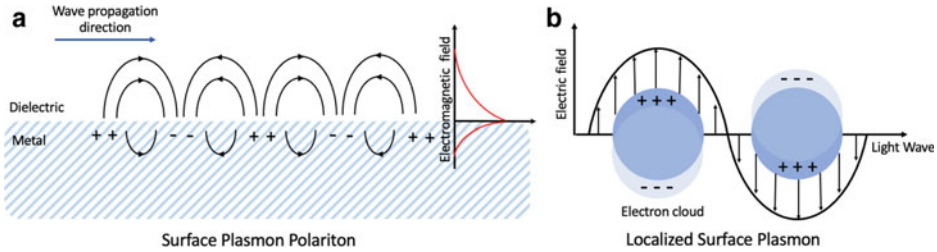

Fig. 5.17 The schematics of the mechanism of (**a**) a surface plasmon polariton and (**b**) a localized surface plasmon

nanomaterials embedded on paper, and, secondly, the large range of biomarker sensors particularly suitable for POC disease diagnosis. The rest of this work is arranged in the following section. In Sect. 5.4, optical signal read-out mechanisms will be reviewed, including colorimetric, Raman, fluorescence mechanisms and their corresponding instrumentations. The accessibility and size of these instrument are directly related to whether these techniques are suitable for POC applications or not. Section 5.5–5.7 categorize all plasmonic devices into three major groups in terms of their sensing platform structures. Section 5.5 focuses on reviewing nanoparticles that are used for fabrication of the biosensing platforms. Four different forms of nanoparticles including spheres, cubes, and spikes/stars will be presented. These nanoparticles are either placed in suspension and or on chip. Different nanoparticles shapes and chip platforms will be categorized and discussed. Next, Sect. 5.6 first reviews sandwich-, microfluidic-, chip-, and paper-based biosensors with plasmonic mechanism. Microfluidic system is an emerging tool to precisely control nanoparticles geometry and size by confining the chemical reaction in micro channels [43–45]. Paper-based devices are light weighted, small, easily portable, and are therefore extremely suitable for POC diagnosis. The following Sect. 5.6 reviews biomarker sensors with carefully patterned surface using different techniques such as sputtering, photolithography and chemical growth. Section 5.7 provides the author's perspectives on the challenges and opportunities in the field of plasmonic biosensors for biomarker detection. The example of such biosensor detection for the virus that caused the ongoing and biggest health crisis in human history which is the SARS coronavirus-2 virus is discussed. Lastly, this paper is concluded by a summary of the works reviewed.

5.4 Signal Read-Out Method

Due to the various manifestations of the plasmonic effect and inherent properties of materials demonstrating this effect, there exists numerous potential means to read out a signal from plasmonic nanomaterials. This section will cover main methods exploited including colorimetric, Raman, fluorescence, and handheld device assisted methods (Fig. 5.18).

5.4.1 Colorimetric

Colorimetric plasmonic sensing of target analytes has been a largely sought-after approach due to the simplistic nature and lack of dependency on complex instrumentation. Fundamentally, this process relies on the localized surface plasmon resonance (LSPR) of the underlying particle which, because of changes in the local refractive index, will shift the particles resonance wavelength. This shift is typically detected spectroscopically, and the position depends on several factors that will be discussed later in detail. For use within sensing, particles are often conjugated to target a specific analyte of interest, and the new

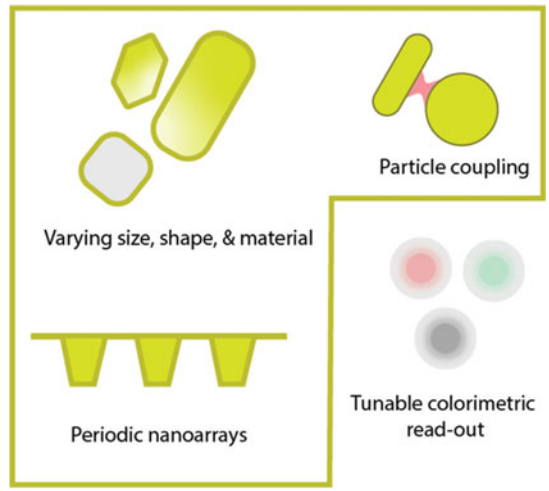

Fig. 5.18 Overview figure showing the various techniques used for colorimetric detection using plasmonic structures, namely varying shape, size and material, particle coupling, and periodic nanoarrays

complex is detected by shifting of this resonance wavelength, indicating presence, and by magnitude, concentration of the analyte of interest. Due to the ability to control a number of parameters surrounding the particles within the system, including material, shape, size, interparticle distance, and composition, there exists significant potential for tunability leading to varying levels of sensitivity. However, for specific materials and configurations it exists within the visible regime and in practice this shift within the visible regime can manifest into a characteristic color change, detectable using only a smartphone camera. In the simplest sensor embodiment, this method utilizes plasmonic nanoparticles within solution or within an array which results in a distinct and characteristic color upon analyte binding. Most commonly, such particles are fabricated through chemical synthesis, and tunability arises from changes in the chemical used or synthesis procedures. Due to the potential for scaling of such methods, there is significant potential for colorimetric read-out methods to be used within POC settings, thus a significant portion of work within this space targets this use-case and applications include medical diagnostics and agriculture.

Due to the amount of work completed within this field, there has been extensive efforts to characterize and optimize a number of different design parameters and their effect on the refractive index sensitivity and visible colors of the particles. Efforts have targeted both computational optimization and experimental investigation and have studied changes in particle shape, material formulation, size, and distance between particles. Shapes including nanospheres, nanorods, nanocubes, nanobipyramids, nanoflowers, nanostars, and nanoplates have been previously reported [46], whereas those with generally sharper geometries or edges have traditionally been show have higher enhancement levels [47, 48]. Of recent, particle size has been demonstrated to be a significant factor governing near-field enhancement thus regardless of shape, optimization of size, if possible, is

warranted when designing sensors [1]. Traditionally, particles are fabricated using chemical synthesis methods and most commonly are fabricated from gold, due to the LSPR falling within the visible regime. Once synthesized, particles can be functionalized and changes in the near-field such as that due to analyte binding detected using spectroscopy methods. An interesting alternative to this approach which enables the colorimetric detection of analytes is through post-synthesis etching or growth, enabling further tuning of particle morphology and thus properties [49]. In one such study using this approach, colorimetric detection of blood glucose was enabled by changing the morphology of the gold nanobipyramids within an assay through enzymatic etching resulting in a characteristic solution color change detectable by the naked eye [50] (Fig. 5.19a). Within the assay, glucose oxidase oxidizes glucose forming H_2O_2 which is subsequently broken down into hydroxyl radicals in the presence of horseradish peroxidase which accelerates initial nanobipyramid etching. Using this method, they showed a dynamic range of 0.05–90 μM, limit of detection of 0.02 μM, time to result of 30 min, and good correlation with traditional hospital detection methods. They lastly employed the sensor for glucose sensing within serum of a small cohort of healthy people and diabetic patients and enabled differentiation of the two groups through naked eye detection alone.

Though single particles within solution represent the predominate sensor configuration utilized, there has been intriguing recent advancements which utilize coupled particle systems as a means for detection. Such approaches make use of the plasmonic "hot-spot", or the highly enhanced EM field between nearby and interacting plasmonic nanoparticles. This phenomenon has been robustly investigated computationally and experimentally using nanofabricated samples which provides significant control over sample size, shape, spacing, and thus properties [53]. However, for use within POC settings there has been significant interest in finding alternative fabrication methods that are amendable to scaling. In one such study, Liang et al. [51] took advantage of the unique plasmonic properties of two morphologies of chemically synthesized plasmonic nanoparticles, a gold nanorod and gold nanosphere (Fig. 5.19b, left). Independently, the plasmonic properties of these two distinct particles have been well studied in literature, with robust links between varying size and shape of particles and characteristic resonance wavelengths. In this study, 50 nm AuNSs with a resonance peak of ~550 nm which scatters green light was coupled with 25 × 60 nm nanorods with a resonance peak of ~650 nm which scatters red lightClick or tap here to enter text. When these two particles were close enough to one another (<200 nm), the particles interact with another, leading to coupling and scattering of yellow light with a significantly higher intensity than either individual particle (Fig. 5.19b, middle). This was used as the basis for an assay by functionalizing both nanoparticles to bind to protein markers on the surface of extracellular vesicles (30–150 nm in diameter), CD63 and CD9. As a result, the binding of both particles to a singular extracellular vesicle would enable detection using dark-field microscopy. This method provided detection of circulating extracellular vesicles in as little as 1 μL of plasma and enabled differentiation between pancreatic cancer, pancreatitis, and normal controls based on area ratio, a

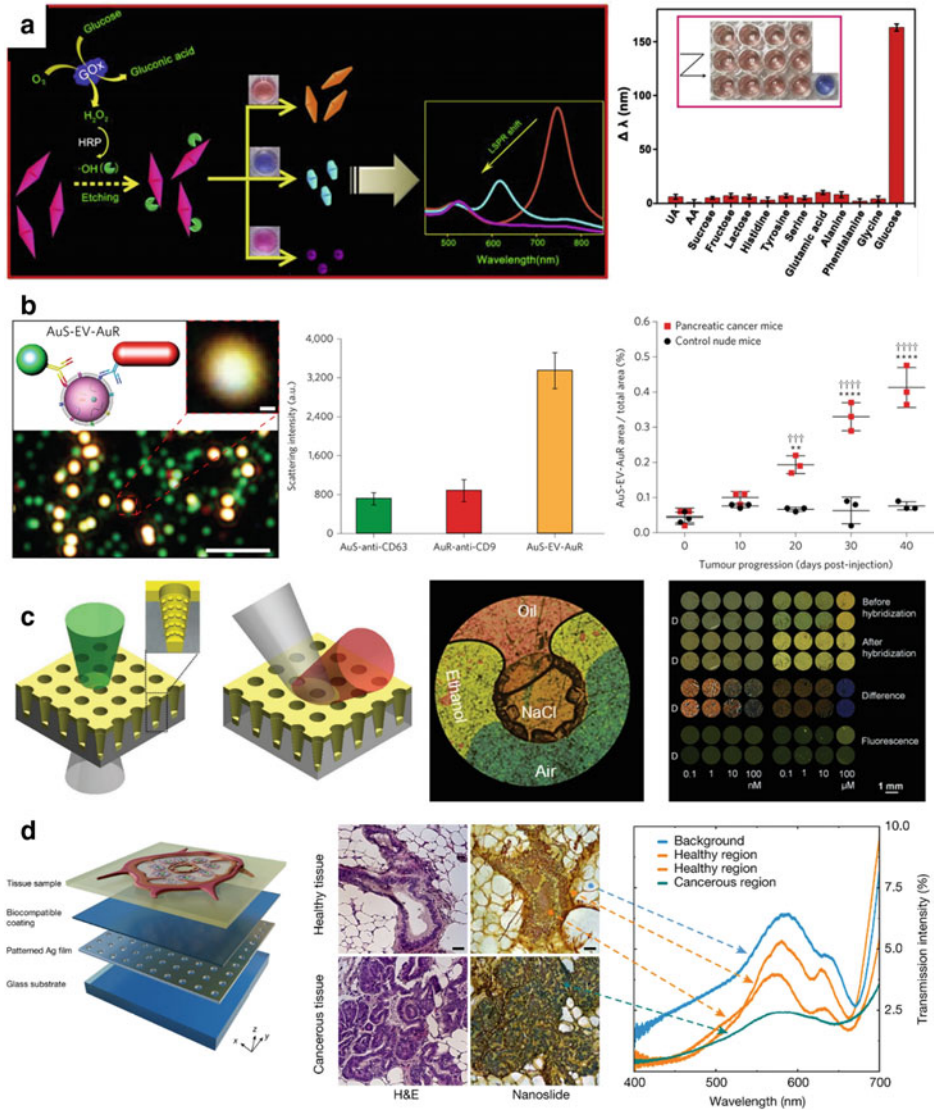

Fig. 5.19 Colorimetric plasmonic sensing. **a** Method of colorimetric detection enabled by etching of gold nanobipyramids within an assay, resulting in characteristic solution color changes. This was utilized within for the specific detection of glucose within a patient cohort and enabled the discrimination of healthy and diabetic patients. Replicated with permission from [50]. **b** Method for the detection of tumor-derived extracellular via coupling of plasmonic particle which demonstrates enhanced scattering. Replicated with permission from [51]. **c** A nano Lycurgus Cup array which demonstrates high refractive index sensitivity (46,000 nm/RIU) and enables colorimetric detection of varying refractive index environments, such as that within DNA solutions of varying concentrations. Replicated with permission from [10]. **d** Method for colorimetric histology using patterned silver films, enabling the detection of tissues by subtle changes in the dielectric constant of various tissues. Replicated with permission from [52]

metric that considers the signal area versus background as a proxy for concentration [51] (Fig. 5.19b, right).

The ability to detect multiple analytes within a single test, multiplexed detection, lowers cost and simplifies the diagnostic workflow significantly. As such, there has been significant interest in combining plasmonic nanoparticles within single assays to allow for the differentiation and detection of multiple analytes simultaneously. The significant levels of tunability within system design and configuration when to comes to particle-based systems makes them an ideal candidate for such assays. A straightforward approach to achieve multiplexing is by changing the shape between multiple underlying particles within the system, however this increases complexity when to comes to chemical synthesis as each particle need by synthesized independently. A simpler alternative approach which has been investigated is multiplexing spatially, by patterning specific areas within the assay with unique particles or structures. In this manner, theoretically the same particles can be used in multiple areas of the assay, as long as it is spatially accounted for, both reducing assay complexity and increasing repeatability. In a recent study in this field, Pinheiro et al. [54] utilized configurable gold nanoparticles for colorimetric multiplex detection of glucose, uric acid, and free cholesterol in a single paper-based microfluidic assay. This work made use of in situ gold nanoparticle synthesis for the detection of glucose and demonstrated detection at physiologically relevant ranges with a limit of detection of 1.25 mM. For the other two analytes, tailored gold nanoparticles were used to functionalize paper and the optical properties altered by changing degree of aggregationClick or tap here to enter text. Due to the addition of multiple techniques leading to colorimetric detection, the development and optimization of such an assay is quite involved, however preliminary results are encouraging. Another example to achieve multiple readouts is provided by Wang et al. [55] by utilizing the catalytic-regulated gold nanoparticle etching process. Aggregation behavior, catalytic activity and etching level are used in the system as triple sensing channels for protein discrimination, which can be well reflected by the color change of solution. The differentiation of pure protein and protein mixtures is validated through urine sample.

Plasmonic particle-based systems, mainly those for solution-based sensing, represent a significant portion of the colorimetric sensors reported thus far in literature, however of recent there has been advances that utilize periodic nanoarrays that enable colorimetric sensing. Although fabrication of these systems is more complex, requiring specialized equipment and lengthy processing stages, the ability to pattern these upon surfaces provides unique potential and integrates well with standard clinical sample processing. This field is still early in its development, however if methods are developed that reach scalability of particle-based system then there exists significant potential or POC assay development. Gartia and coworkers [10, 56–58] developed a periodic nanolycurgus cup array and demonstrated its potential for colorimetric detection of refractive index environment changes such as in the presence of air, oil, ethanol, and NaCl solution (Fig. 5.19c).

In this study, due to the high sensitivity (~46,000 nm/RIU) they further showed colorimetric sensing directly upon the fabricated surface via changes of DNA concentration within solution [10]. Though the fabrication of such a sensor requires specialized equipment and nanofabrication techniques, it provides an intriguing proof-of-concept platform that would be largely applicable in biosensing if scalability was achieved. In another example, Balaur et al. [52] developed a plasmonic microscope slide that allows colorimetric histology of tissues without the use of staining by transducing minute changes in the dielectric constant of various tissue types into visibly detectable color changes (Fig. 5.19d). In this paper, they showed the feasibility to differentiate between normal epithelium, usual ductal hyperplasia, and early-stage breast cancer within a diagnostic cohort. Such a system in its current embodiment has little to no POC relevance, but it's likely that such a configuration would also allow for robust surface-based colorimetric sensing. Intriguing results have been presented within literature, however, there still exists high dependence on nanofabricated sample and lithographic methods to enable colorimetric sensing. Considering the ideal use-case for this detection method, POC applications, therefore needs to be further progression into similarly sensitive, yet scalable fabrication methods within this field.

5.4.2 Fluorescence, Raman, and Handheld-Format Systems

Fluorescence is a photoluminescence process where a fluorophore molecule absorbs a photon and then emits a photon of lower energy (longer wavelength). Roughly, the fluorescence process can be separated into three steps. First, the fluorophore molecule absorbs the photon and was put into an excited state. Then, the excited fluorophore molecule converts to a lower energy without emitting any photons. Finally, the excited fluorophore radiatively decay to a lower energy and emit a photon. In these three steps, while the second step is independent of the excitation light intensity, the efficiency of the first and third steps can be enhanced by a higher excitation light intensity.

Raman spectroscopy is a technique used to identify molecules by providing a molecular fingerprint. Its working mechanism relies on inelastic scattering of light, or specifically, photons, which is also called Raman scattering. When an incident light or a group of photons pass the sample with a photon frequency ν_{i}, some will leave the sample in a path along the direction of the incident light, which is called transmitted light, while others will leave the sample in all other directions, which is called light scattering. For the scattered photons, when their frequency (ν_{s}) equals the frequency of incident light (ν_{i}), or $\upsilon_i = \upsilon_s$, Raleigh scattering, occurs. When they are not equal, or $\upsilon_i \neq \upsilon_s$, Stoke scattering occurs. Raleigh scattering is elastic scattering while Stoke scattering is inelastic scattering. There are two energy scenarios when $\upsilon_i \neq \upsilon_s$. . As the incident photon interact with the electron cloud of the sample, the vibrational energy of the electron cloud either gains energy (goes to a higher energy level) or lose it (goes to a lower energy level) after the photo

is emitted out (Fig. 5.20a). Correspondingly, to maintain the total energy in the system, the emitted photon will either have a lower energy (lower frequency) when the electron adsorbs energy or a higher energy (higher frequency) when the electron lose energy. If the emitted photon's energy (or frequency) is smaller than that of incident photon, or $v_s < v_s$, Stokes scattering will be observed. On the other hand, if the emitted photon's energy (or frequency) is larger than that of incident photon, or $v_s > v_s$, Anti-stokes scattering will be observed (Fig. 5.20b). These shifts in energy, also called Raman shift, provide information about the vibrational mode in the sample molecules. Hence, Raman can be used to reveal the identity of the sample molecule by comparing the observed shifts in frequencies to those known substances. In addition, the intensity of those peaks represents the number of photons received by the detector. The higher the intensity, the more photons are detected. By this means, Raman can quantitatively measure the concentration of the sample molecules Raman spectroscopy. As shown in Fig. 5.20c Conventional Raman spectroscopy has a big and bulky machine body that include all the optical components in it such as a microscope, lens, lasers, filters, etc., which can be hardly adapted to POC applications due to their bulky size. However, more recently, handheld Raman spectrometer (Fig. 5.20d) emerges in the market that make Raman detection and analysis easily and conveniently accessible, opening a new revenue for its applications in the realm of POC medical diagnostics.

While many portable diagnosis platforms emphasize convenient detection through bare eyes, it is notable that detection error from bare eyes can sometimes lead to significantly inaccurate diagnosis results. Thanks to the rapid development of computing techniques and miniaturized chips, smartphones have become a highly integrated sensing and computing system, thus playing a vital role in the portable diagnosis platform for fast and accurate detection for POC applications.

The sensing capability of smart phones that has been predominantly utilized in the mobile diagnosis platform is their imaging camera. In typical colorimetric assays, the biochemical reaction takes place to introduce a distinguishable color change in the solution or chip to enable detection of analyte. With the use of smart phones, the color transition or color intensity is captured through the cameras and followed with image processing techniques and a variety of computations to quantify the concentration of detected analyte. Examples of smartphone readers for colorimetric sensing includes the detection of ascorbic acid in tear fluid by Misra et al. [59] detection of human C-reactive protein with graphene-based microliter plate in diluted human whole blood by Vashist et al. [60] detection of cancer antigen 125 (CA125) through functionalized Au–Ag NPs by Hosu et al. [61] and detection of bacteria by Zheng et al. [62] In other studies, researchers develop smartphone-based imaging platforms to serve as a household instrument for plasmonic detection and analysis software. For instance, Lee et al. [63] combined a highly sensitive SPR biochip and a simple portable imaging setup for label-free detection of imidacloprid pesticides. Their plasmonic chip showed spot shift in response to changes of pesticide concentration, which can be accurately detected through imaging of smart phone and do

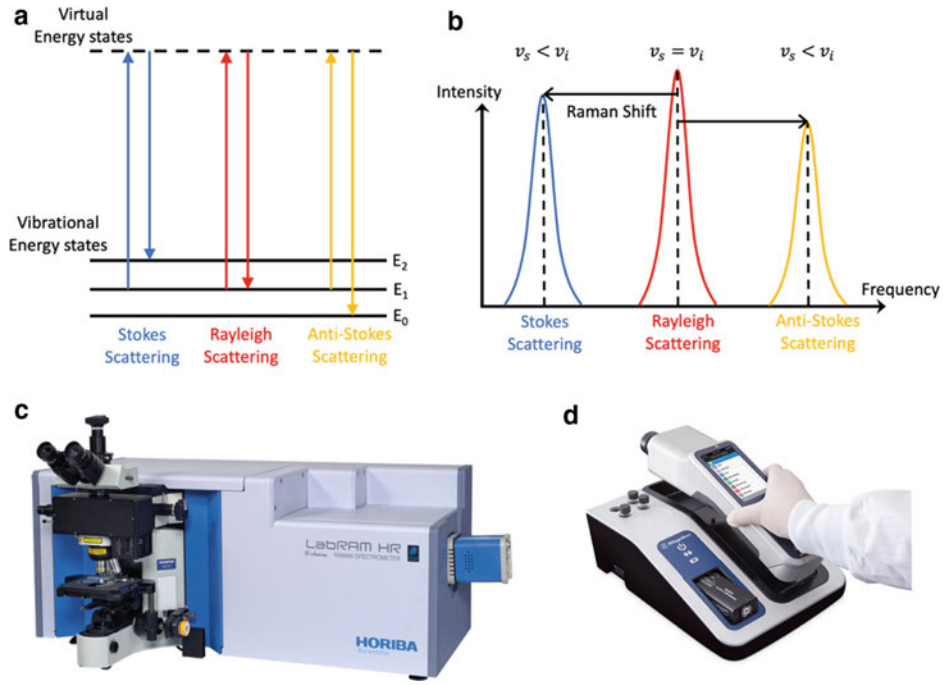

Fig. 5.20 Raman Spectroscopy. **a** The change of vibrational energy states in the process of a photon interacting with sample molecule. **b** A Raman spectrum showing three different energy shift scenarios. **c** A Raman spectroscopy machine. Photo credit by Horiba, Ltd. **d** A handheld Raman spectrometer. Photo courtesy of Rigaku Analytical Devices

quantitative analysis. Another hand-held SPR imaging platform was developed by Guner et al. [64] which is composed of SPR sensor chips and a smartphone-based compact optical system (Fig. 5.21a). The silver/gold (Ag/Au) bilayer structure coated Blu-ray disc sensor chips were capable to perform plasmon resonance imaging at the central region of visible spectrum, and the image intensity was captured through the smartphone to estimate the analyte concentration. Smartphone is also reported to be applied for fluorescence imaging by Lee et al. [65], as shown in Fig. 5.21b. In this study, Lee et al. performed a smartphone-based fluorescence microscopy to do dual-wavelength fluorescent detection of 17-β-estradiol in water. The smartphone's camera is connected to a microscope with a band-pass filter to display the two channels fluorescent images of the sensing array with high resolution. More recently, Bian et al. [66] proposed a metasurface-inspired biosensor, patterned plasmonic gradient, together with a smartphone for high precision sensing. The patterned plasmonic gradient transduced local index information into 2D patterns by forming visible resonance contour lines for easy readout. The smartphone was connected

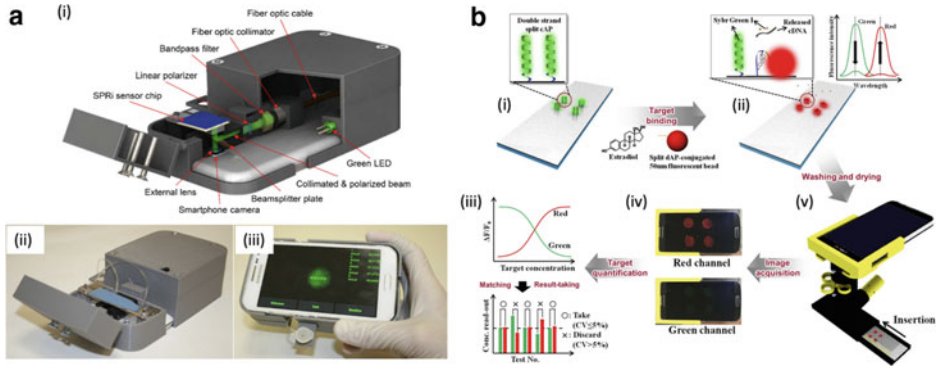

Fig. 5.21 Hand-held Devices and systems. **a** SPR imaging platform integrated with a smartphone. Replicated with permission from [64]. **b** A schematic illustration of the overall work design for the dual wavelength fluorescent detection. Replicated with permission from [65]

to a microscope to directly read the 2D patterns with high sensitivity and do the real-time analysis with a homemade program.

5.5 Nanoparticle Based Designs

Most plasmonic biosensor utilize plasmonic nanoparticles to induce or enhance surface plasmon effect. In designing these nanoparticles-based sensors, different particle forms, shapes, fabrication methods and working mechanisms are employed to produce devices that detect different biomarkers and diseases such as hepatitis B virus (HBV), human immunodeficiency virus (HIV) and tuberculosis (TB) with various limit of detection. Table 5.1 summarizes these characteristics of some the most representative devices developed recently that are based on nanoparticles. In addition, the potential of these devices' POC applicability is evaluated. In the following sub-sections, we categorize the plasmonic nanoparticles into three major forms including sphere, cubic, and spike/star structures and reviewed and discussed their role in biosensors.

5.5.1 Sphere

As early as the late nineteenth century, the topic of interaction between light and small particles, especially colloidal particles of gold and silver, has been attractive [96, 97]. It is widely known that the EM fields around the surfaces of the nanoparticles exhibit strong resonant and oscillating behavior—which is called plasmon resonance if light with

Table 5.1 Summary of representative nanoparticle based plasmonic biosensors developed recently

Particle form	Synthesis method	System/Method	Disease detected	Biomarker	POC ability	Limit of detection	References
Spheres	Hydroxylamine hydrochloride reduction (Ag)	SERS	HBV	L-arginine, nucleic acid	Low	N/A	[67]
	Citrate Reduction (Au)	Colorimetric sensing	HBV	Hepatitis B surface antigen (HBsAg)	High	1 pg/mL	[68]
	Seed-mediated growth (Au)	Colorimetric sensing	HIV	HIV template DNA	High	0.01 zeptomoles	[69]
	Citrate reduction (Au)	SERS	HIV	HIV-1 DNA	High	0.24 pg/mL	[70]
	Citrate reduction (Au)	Colorimetric sensing	TB	TB DNA	High	19.5 pg/mL	[71]
	Commercial product (Au)	SERS	TB	ManLAM	Low	NA	[72]
	Commercial product (Au)	Toroidal electrodynamics	COVID-19	SARS-CoV-2 spike protein	Medium	4.2 fmol	[73]
	Citrate Reduction (Au)	Colorimetric sensing	Epithelial ovarian cancer	Cancer antigen 125	High	30 U/mL	[61]
	Citrate reduction (Au)	Colorimetric sensing	COVID-19	SARS-CoV-2 RNA	High	0.18 ng/μL	[74]
Cube	Seed-mediated growth (Au)	LSPR	Lung cancer	MiR-205	Medium	5 pM	[75]

(continued)

Table 5.1 (continued)

Particle form	Synthesis method	System/Method	Disease detected	Biomarker	POC ability	Limit of detection	References
	Chemical reduction (Au) Seed-mediated growth (Ag)	LSPR	Hypo/ hyperkalemia	Potassium	Low	1 nM	[76]
	Seed-mediated growth (Ag)	SERS	Mycotoxin	Ochratoxin A	Medium	0.01 nM	[77]
	Sulfide-mediated method (Ag)	SPR	N/A	Immunoglobulin G (igG)	Medium	0.6 μg/mL	[78]
	Chemical reduction (Ag)	SERS	Toxicity	Dithiocarbamate (DTC)	Low	44 nM	[79]
Spike/star	Seed-mediated growth (Au)	SPR	N/A	Genomic DNA	Medium	6.9 fM	[80]
	One-pot seedless protocol	SERS	Hand, food and mouth disease	Enterovirus 71	High	107 pfu/mL	[81]
	Ascorbic acid reduction (Au)	SPR	Influenza A	H5N1, H4N6	Low	0.0268 HAU/50 μL	[82]
	Chemical reduction (Au)	SERS	Mosquito-borne diseases	Nonstructural protein	Medium	55.3 ng/mL	[83]
	Chemical reduction (Au)	SERS	Oxidative stress and related diseases	Hypochlorite (ClO^-) and glutathione (GSH)	Medium	0.40 μM	[84]
	Sputtering (Au)	SERS	Influenza	Influenza antibody	Medium	10 pM	[85]

(continued)

Table 5.1 (continued)

Particle form	Synthesis method	System/Method	Disease detected	Biomarker	POC ability	Limit of detection	References
Other nanostructures	Seed-mediated Growth (Au)	LSPR	TB	CFP-10 ESAT6 antibody	High	N/A	[86]
	Seed-mediated Growth (Au)	LSPR	Tumor	ctDNA	Medium	2 ng/mL	[87]
	NIL and thin-film (Au)	Plasmonic fluorescence	Ebola	EBOV antigens	Medium	220 fg/mL	[88]
	Simulation	SPR	COVID-19	SARS-CoV-2 spike protein	Low	111.11 deg/RIU	[89]
	Commercial product (Au)	LSPR	HIV	HIV-1 p24 antigen	Low	10^{-5} pg/mL	[90]
	seed-mediated growth (Au)	LSPR	HBV	Hepatitis B surface antigen (HBsAg)	Medium	100 fg/mL	[91]
	Electrodeposition (Au)	LSPR	COVID-19	SARS-CoV-2 spike protein	High	0.08 ng/mL	[92]
	Boiling reduction (Au) on magnetic NP	SPR	TB	Anti-CFP-10	Low	0.1 ng/mL	[93]
	DNA template (Ag/Pt)	Colorimetric	Cancer	miRNA-21	High	0.6 pM	[94]
	Dipping (Au)	Plasmonic fluorescence	Malaria	PfLDH	Low	11111 pg/mL	[95]

appropriate wavelength is incident. Various nanostructures have been fabricated, characterized, and applied in applications through decades of development on nanomaterial fabrication techniques, such as self-assembly, chemical growth and lithography. However, nanospheres are still primarily used in plasmonic sensors due to their easy fabrication process and low-cost. In addition, significant enhancement of light occurs in the narrow gap regions when plasmonic nanospheres are closely coupling [98].

Chemical growth is the most popular method to synthesize Au and Ag nanospheres of different sizes. Turkevich et al. first developed the single-phase-based reduction of gold or silver salt by citrate to fabricate size tunable nanospheres [99]. 40 years later, Brust introduced a two-phase (water-toluene) reduction of $AuCl_4^-$ to prepare 1–3 nm gold nanospheres (AuNSs) bearing a surface coating of thiol [100]. For the synthesis of plasmonic AuNSs, gold chloride trihydrate ($HAuCl_4$) is the most commonly used precursor, which requires reducing agent such as trisodium citrate or sodium citrate to initiate the reaction [69–71, 101]. Seeding-mediated fabrication based on the separation of nucleation and growth is also used to synthesize citrate-stabilized AuNSs with the diameter up to ~200 nm [102, 103]. Silver nanospheres (AgNSs) can be fabricated in a similar way. For example, by reduction of silver nitrate ($AgNO_3$) with hydroxylamine hydrochloride at alkaline pH, highly SERS-active AgNSs with diameters between 23 and 67 nm are produced [67, 104].

Pure nanospheres without further functionalization can be feasible for label-free disease detection. For instance, Yudong et al. directly mixed blood serum from patients confirmed with HBV and healthy volunteers with AgNSs solution at 1:1 ratio for SERS measurement [67]. By comparing Raman bands and first order derivative SERS data in the serum SERS spectrum between HBV patients and healthy volunteers, especially the peak position of biomolecules (like L-arginine and saccharide) that are relevant to HBV transformation and infection, they achieved a non-invasive and accurate diagnostic of HBV detection in 10 min. Another way to utilize pure plasmonic nanospheres for biosensing is through seed-mediated growth. The mechanism is to take advantage of reducing agent produced in physiological processes or reactions in the sample, such as NADH, to reduce $HAuCl_4$, which results in the enlargement of AuNSs. The color change caused by the enlarged AuNSs is a convenient and robust signal for colorimetric assay. For example, Peng et al. developed a colorimetric sensing method based on alcohol dehydrogenase catalyzed AuNSs growth for the detection of the hepatitis B surface antigen (HBsAg) [68]. In the plasmonic ELISA design, they attached streptavidin-alcohol dehydrogenase (ADH) to biotinylated secondary antibodies, so that biocatalytic cycle can be catalyzed between NAD^+ and ethanol to generate NADH (Fig. 5.22a). Therefore, in the presence of antigen (HBsAg), the size of AuNSs enlarged and the solution color changed from yellow to purple. Comparing to other sophisticated methods, it provides POC ability to detect any disease biomarkers as long as appropriate antibodies exist.

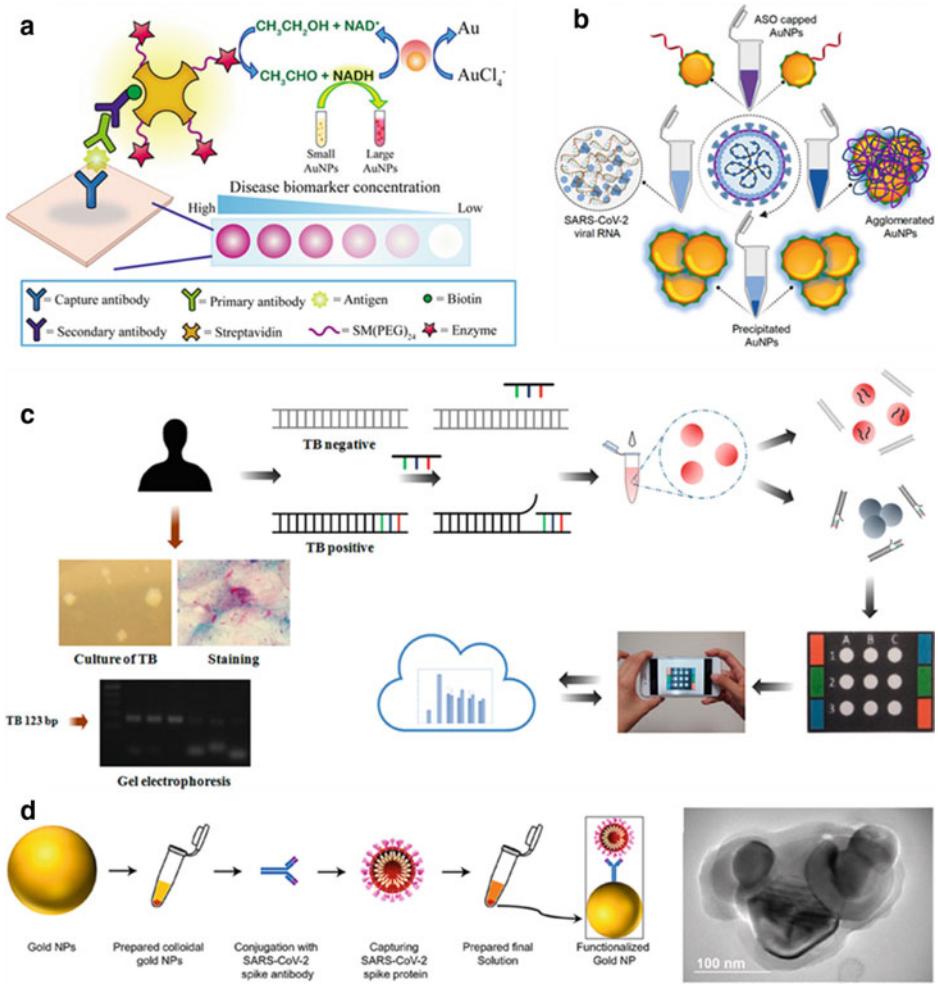

Fig. 5.22 Nanospheres-enabled biosensors for diseases detection. **a** Schematic diagram of plasmonic ELISA using AuNSs seed-mediated growth principle. Replicated with permission from [68]. **b** Schematic representation for the detection of SARS-cov-2 RNA mediated by the antisense oligonucleotides (ASOs)-capped AuNSs. Replicated with permission from [101]. **c** Schematic Illustration of the tuberculosis diagnostic method. Replicated with permission from [71]. **d** Schematic for the workflow of the SARS-cov-2 spike proteins-AuNSs conjugate and TEM image of conjugated structure. Replicated with permission from [73]

Functionalized nanospheres provide even more possibilities. Since Mirkin modified AgNSs with polynucleotides to achieve colorimetric detection based on the concentration of target molecule [105], enormous effects have been made for the development of nanospheres surface functionalization with different probes to provide highly sensitive and specific detection of a wide range of markers. Detection of DNA, RNA and oligonucleotide has received the greatest attention. Capping rationally designed thiol-modified antisense oligonucleotides onto AuNSs is a simple and straightforward approach for diagnosing. For example, Moitra et al. developed a colorimetric assay based on oligonucleotides capped AuNSs specific for N-gene of SARS-CoV-2, which diagnosed positive COVID-19 cases within 10 min [101]. Such modified AuNSs bunch up only in the presence of target RNA sequence, and lead to a change in SPR with a redshift of ~40 nm in absorbance spectra (Fig. 5.22b). More importantly, the colorimetric detection can even be recognized by naked eye without complicated instrument, which complies with the ASSURED criteria for POC testing. Tsai et al. shows that when ssDNA modified AuNSs is combined with target dsDNA, the DNA hybridization affects the zeta potential of the AuNSs, resulting in aggregation of the colloid and thus a colorimetric change [71], as shown in Fig. 5.22c. They extended the sensor to a paper-based system so that the colorimetric results can be rapidly analyzed by smartphone instead of sophisticated equipment. In addition to nucleic acids, antibody or antigen are frequently used in nanospheres surface modification since they have similar complementary counter parts. For instance, Ahmadivand et al. conjugated AuNSs with the monoclonal antibody targeting at spike protein (S1) of SARS-CoV-2 virus and measured the toroidal dipole-resonant shift with different spike protein concentrations (Fig. 5.22d) [73]. The authors demonstrated that dispersing antibody capped AuNSs to toroidal metasurfaces promoted the binding strength of biomolecules, and they achieved a limit-of-detection (LoD) down to ~4.2 fM. Recently, an entropy-driven DNA amplification networks have been achieved using photostable Au−Ag hollow porous nanospheres [106]. Rather than amplify the DNA hairpins, this platform increases double-stranded assembly structures. Au−Ag nanospheres are engineered to be hollow and porous excellent photothermal conversion efficiency. Apart from nucleic acids, functionalized Au nanospheres also show promising applications in various protein detection. For instance, Jiang et al. [107] developed a sensor platform consisting of gold nanoparticles (AuNPs) complexed with aptamers to detect exosomal proteins. The present exosomes bind to the aptamers, resulting in the aggregation of AuNPs and a visible color change that can be detect by naked eyes.

Although broadly used as plasmonic materials, metal nanoparticles alone are limited by their low tunability and short lifetime. Surface plasmon hybridization of metal nanoparticles and other nanostructures can enhance the plasmonic properties and provide better sensing performance. For example, Rostami et al. [108] developed a sensing platform by integrating graphene nanoribbons and sliver nanoparticles. The presented hybrid sensor is capable of detecting dopamine and glutathione in sequence by showing a color change from green to red (dopamine) and to grey (glutathione) in human serum samples. DA

and GSH were successfully detected in low concentrations of 0.04 μM and 0.23 μM, respectively.

5.5.2 Cube

Nanocubes have also drawn great attention in plasmonic sensing for their numerous advantages. Nanocubes have large and uniform faces that can be readily attached to peptidoglycan layer and stay that way, offering antibacterial effect via enzyme-like activities [109]. Jeon and co-workers [110] fabricated and compared Au nanospheres and nanocubes with vertices. The shape effect on the refractive index sensitivity is compared for their LSPR performance. They found that single Au nanocubes with vertices are more sensitive in refractive index than single Au nanospheres of similar size. Nanocubes also provide high electrocatalytic activities than their spherical catalysts counterparts as result of their abundant (100) faces [111, 112]. For instance, Au coated Pd nanocubes were placed on networks of single-walled carbon nanotubes (SWCNTs) for building a highly sensitive electrochemical biosensing platform [113]. Platinum (Pt) nanocubes were used to build an amperometric glucose biosensor to increase the activity of the oxidation and reduction of H_2O_2 [114]. In another work, a non-enzymatic glucose sensor was developed by Yang et al. [115] using electrospun Au nanocubes decorated on vertically aligned multi-walled carbon nanotube (MWCNTs) arrays. Further, many research indicate that polyhedral nanoparticles such as nanocubes which have many edges and vertices tend to have stronger localized surfaces plasmon resonance than rounder particles such as nanospheres [76, 116, 117].

Au and Ag are the two most used materials for fabricating nanocubes for plasmon enhancement. Dr. Xia is one of pioneers of synthesizing high quality, uniform Ag nanocubes [118–120], and many later works that use Ag nanocubes for plasmon biosensing either directly employed his protocol or with slight modification. In Xia's method [118], Ag nanocubes are fabricated using polyol synthesis method where ethylene glycol is used as the reducing agent and the solvent. Na_2S is then added to the system. Ag_2S nanocrystallites, which can reduce $AgNO_3$, are generated after $AgNO_3$ is added to the solution. This rapid reduction process helps shape the formation of Ag cube. Poly(vinyl pyrrolidone) (PVP), which selectively binds to Ag's {100} facets, also contribute to the formation of Ag cubes. For the fabrication of Au nanocubes, a two-step seed-mediated growth method is usually employed [75]. In the first step, the Au seed is prepared by quick addition and mixing of ice-cold $NaBH_4$ solution into a mixture solution of $HAuCl_4$ and cetrimonium bromide (CTAB). In the second step, the growth solution is made by mixing water, $HAuCl_4$, CTAB and ascorbic acid which the seeds solution is added to. The mixture solution stays at room temperature overnight followed by wash and centrifugation process to obtain the Au nanocubes.

Before researchers utilized the plasmonic effect to enhance the signal of silver nanocubes for biosensors, they simply use Ag nanocubes for its electrochemical properties such as the electron transfer effect with H_2O_2. For example, Yang et al. [112] designed an amperometric bienzyme biosensor for glucose detection using Ag nanocubes and Au electrode. The substrate for the Ag nanocubes is horseradish peroxidase (HRP)-chitosan (CS)-glucose oxidase (GOx) bienzymatic film. The working mechanism for this biosensor involves reduction of H_2O_2 which is produced in the enzyme reaction. The chemical reaction can be expressed with Eqs. 5.1–5.3 [112]. Similarly, Yang et al. [115] built a non-enzymatic glucose sensor based on Cu nanocubes electrodeposited on vertically aligned multi-walled carbon nanotubes (MWCNTs). It is demonstrated that this sensor showed enhanced electrocatalytic activity to glucose oxidation in NaOH solution. Ren et al. [114] promote the electrocatalytic activity of the oxidation and reduction of H_2O_2 by fabricating an amperometric glucose biosensor. In this design, Pt nanocubes are used to facilitate the electron transfer activity which significantly increase by H_2O_2 which is produced in the glucose oxidization process by GOx.

$$Glucose + O_2 \rightarrow Gluconic\,acid + H_2O_2 \tag{5.1}$$

$$H_2O_2 + 2H^+ + Ag \rightarrow 2H_2O_2 + Ag^+ \tag{5.2}$$

$$Ag^+ + e^- \rightarrow Ag \tag{5.3}$$

Zhang et al. [75] designed a cancer biomarker detector based on plasmonic effect using Au nanocubes. The mechanism of the sensor is based on the increase in reflective index induced by hybridization on the surface of Au nanocubes which are modified by thiolated single strand DNA (ssDNS) (Fig. 5.23a). The device's sensing capability is demonstrated by detecting microRNA205 (miR-205) which is an important tumor biomarker. It is shown in the experiment that the limit of detection reaches as low as 5 pM in serum samples. A recent work also reported that Au nanocubes with flat surfaces exhibited better performance than nanospheres for highly sensitive DNA detection assay because of the faster DNA binding kinetics, sharper DNA melting transition and wider hot spot regions [121]. Another example to detect cancer biomarker is presented by Li et al. [122] using the gold-silver alloy nanoboxes. With the strong Raman signal enhancement capability, the reported alloy nanoboxes combined with nanoyeast single-chain variable fragments show high sensitivity and specific capture performance. The researchers successfully detect three different soluble cancer protein biomarkers (sPD-1, sPD-L1, sEGFR) with a limit of detection of 6.17 pg/mL, 0.68 pg/mL, and 69.86 pg/mL, respectively. The detection of the three cancer protein biomarkers is also validated in human serum samples and achieved high recovery rates.

Tian et al. [76] fabricated a simple and sensitive plasmonic aptamer sensor on a single Au coated Ag nanocube and used its LSPR effect to analyze K^+ ions and monitor the

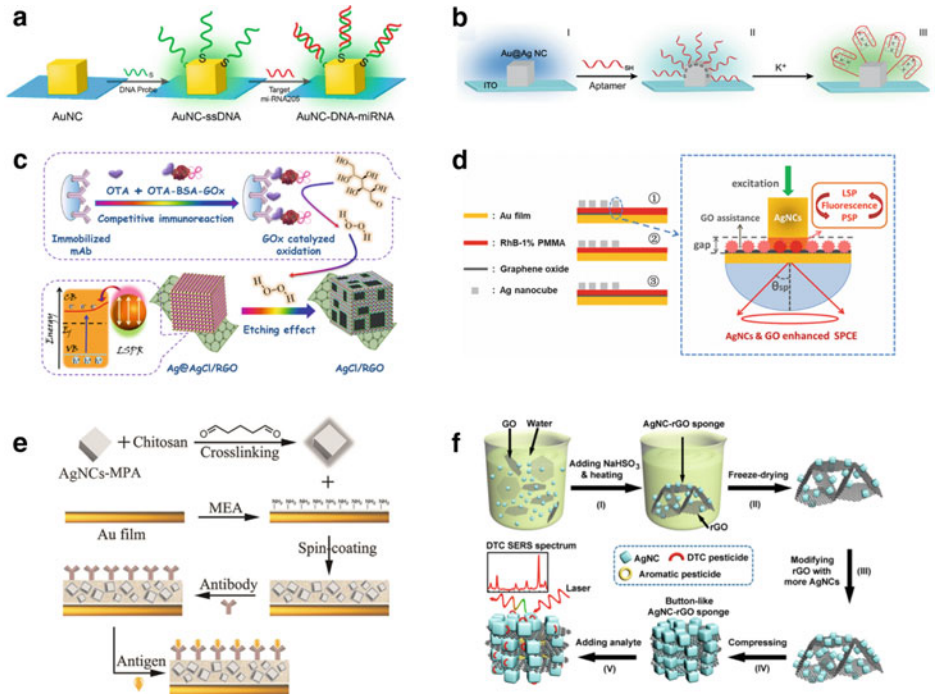

Fig. 5.23 Biosensors with plasmon assisted metal nanocubes. **a** Au nanocubes which are modified by thiolated ssDNA. Replicated with permission from [75]. **b** Plasmonic aptamer sensor on a single Au coated Ag nanocube. Replicated with permission from [76]. **c** A plasmon enabled ochratoxin A (OTA) biosensor. Replicated with permission from [77]. **d** A plasmonic sensor where Ag nanocubes are loaded on GO on Au films. Replicated with permission from [123]. **e** A novel biosensor based on SPR with enhanced sensitivity using Ag nanocubes/chitosan composite. Replicated with permission from [78]. **f** A SERS based sensor to detect dithiocarbanmate (DTC). Replicated with permission from [79]

formation of G-quadruplex structure in real time. In this design, a single strand DNA (ssDNA) with G-rich specific sequency providing K^+ bonding site is bonded to the surface of the Au@Ag nanocubes as shown in Fig. 5.23b. This work showed that LSPR can provide an efficient tool for monitoring the interaction of K^+ ions with a range of 1×10^{-9}–1×10^{-2} M and a limit of detection of 1×10^{-9}. M. Tang et al. [77] constructed a photoelectrochemical immunosensing platform using Ag@AgCl nanocubes decorated on reduced graphene oxide (RGO) heterostructure. RGO nanosheets serves as the substrate for Ag@AgCl nanoparticle are used for their improved charge separation and transportation. The device is fabricated by a sacrificial salt-crystal-template procedure followed by an ethylene glycol assisted reduction reaction. In their study, Tang and coworkers observed that glucose oxidase oxidation generates H_2O_2 which have etching effect on Ag nanocubes. The etching of the Ag material can be quantified via measuring

the photocurrent. Therefore, they use this phenomenon as a new mode of signal detection and designed the plasmon enabled ochratoxin A (OTA) biosensor with the structure aforementioned which showed high sensitivity, low limit of detection and good reproducibility which can be ascribed to the role of LSPR (Fig. 5.23c). Xie et al. [123] investigated the plasmonic enhancement of the sensor based on Ag nanocubes loaded graphene oxide (GO) (Fig. 5.23d). In their study, they fabricated a plasmonic sensor where Ag nanocubes are loaded on GO on Au films. The enhancement is studied and via modeling the EM field patterns using FDTD solutions software (Lumerical Solutions). The found that the high EM field of Ag nanocubes, the localized surface plasmons (LSP) and the propagating surface plasmons (PSP) are responsible for the over 30 enhancement factors. Zhang et al. [78] fabricated a novel biosensor based on SPR with enhanced sensitivity using Ag nanocubes/chitosan composite. They synthesized Ag nanocubes using sulfide-mediated method. Au film is used as the substrate for the spin-coated Ag nanocubes/chitosan composite. The schematic of the device is shown in Fig. 5.23e. They attribute the enhancement in SPR response to the electronic coupling of the Ag nanocubes and the plasmonic surface waves. The biosensor demonstrated by detecting the IgG of mouse. In the experiment, the device showed a large detection range from 0.6 to 40 $\mu g\ ml^{-1}$. Zhang and coworkers reported an electrochemiluminescence sensor enabled by surface plasmon coupling effect on Au nanocubes. The found this effect is particularly strong on the apexes and edges of the Au nanocubes. Graphite phase carbon nitride quantum dots are used to further enhance the surface plasmon coupling effect, and as a result, the signal has been increased three times. In addition, toehold-mediated strand displacement, a simple and enzyme-free strategy, is employed to amplify the nucleic acid. The biosensor can detect rapidly accelerated fibrosarcoma B-type (BRAF) gene with a range of 1 pM to 1 nM and a limit of detection of 3.06×10^{-5} nM. Zhu et al. [79] developed a SERS based sensor to detect dithiocarbanmate (DTC), a pesticide, using sponge like RGO wrapped Ag nanocubes. As shown in Fig. 5.23f, layers of porous RGO sheets form a scaffold structure to hold Ag nanocubes. Adjacent Ag nanocubes contribute to the "hotspot" for the amplification of SERS signal. The sensor's selectivity of DTC is owing to the pesticide's preferential adsorption on the Ag surface and aromatic pesticides on the RGO surface. The detecting concentration ranges from 50 nM to 2 μM, and the limit of detection are 10–16 ppb.

Nanocubes can be applied to directly capture virus. A team has been working on the detection of norovirus using molybdenum and silver nanotubes by SERS. These nanocubes were functionalized with norovirus-specific antibody so that a core-satellite immunocomplex can be formed through antigen–antibody immunoreaction [124], 125. This detection sensor was characterized with a broad linear range from 10 fg/mL to 100 ng/mL and a limit of detection of ~0.1 fg/mL.

5.5.3 Spike/Star

In addition to spherical and cubic shapes, Au nanoparticles (AuNPs) can be synthesis into star or spike shapes or similar shapes with sharp vertices [126]. For the first time, Au nanostars (Fig. 5.24a) were used in an assay for DNA detection based on selective capturing of DNA targets [80]. It is found that the electrical field enhancement at the nanostar tips contribute to the coupling of the LSP and surface plasmons. This bioprobe can detect unamplified human genomic DNA extracted from lymphocytes with a sensitivity down to 10 aM. Chatterjee and co-workers [127] developed a high-yield synthesis for fabricating Au nanostars with just one step. These nanostars have longer and sharper spikes which contribute to stronger "hot spot" at the spike tips. They also employed numerical tools to quantify the local electric field enhancement and LSPR. The single molecule SERS enhancement factor was found to be 10^{10} to 10^{13} in the calculation of optical simulation. Reyes et al. [81] developed a SERS based label-free method that utilize protein-induced aggregation of colloidal Au nanostars for rapid detection of enterovirus 71 (EV71) without substrate and laborious sample handling (Fig. 5.24b). Ahmed et al. reported a self-assembled Au nanostar based chiroimmunosensor for virus detection, specifically, avian influenza A (H4N6) [82]. They synthesized AuNPs with four different morphologies, namely, prolate-shaped, dendritic-shaped, flower-shaped and spiky-like. The detection performance of these AuNPs is compared in the test of detecting influenza A virus (Fig. 5.24c). It is shown that the detection ranges are heavily dependent on the shapes of the AuNPs. Dr. Hamad-Schifferli and her research group developed a SERS based multiplexed assay that can distinguish between Zika and dengue, mosquito-borne diseases which have similar symptoms but may result in greatly different health outcomes [83]. This assay is designed to be a POC biosensor in which Au nanostars are conjugated to specific antibodies for Zika and dengue and employed in a dipstick-format immunoassay. The viral nonstructural proteins (NS1) from dengue and Zika are used as biomarkers. The immunoassay consists of a nitrocellulose strip on which NS1 antibodies are immobilized on the test line and a control antibody at the control line. Figure 5.24d shows the immunoassay's schematic. To reduce time-to-result on a single platform without additional labeling and immobilization, a team reported an Au nanospike biosensor composed of DNA to achieve three functions at one time—target recognition, signal amplification, and connection to substrate [128]. They introduced DNA 3-way junction on the surface of Au nanospikes for protein recognition aptamer, FAM dye and immobilization thiol-group, respectively. A SERS based bioprobe was reported by Wang et al. that can image and biosense hypochlorite (ClO^-) and glutathione (GSC) [84]. 4-mercaptophenol (4-MP)-functionalized Au nanoflowers are fabricated and used to provide a large amount of "hot spots" to increase the SERS signals. The biosensor's working mechanism is shown in Fig. 5.24e. As a result, the limit of detection of the biosensor can achieve 0.38 and 0.4 μM for GSH and ClO^-, respectively. More recently, a new method is proposed to fabricate scaled-up, reproducible plasmonic biosensor which include a large number of

"hotspots" for greatly enhanced detection capabilities [85]. In this design as shown in Fig. 5.24f, Au are made into nanopillars arrays by depositing AuNPs on a plasma-etched PET substrate via a vacuum process. The enhancement was found to be over 8.3×10^8-fold for SERS and 270-fold for plasmon enhanced fluorescence due to the high density of plasmonic coupling and quantity of "hotspot" in this design. The biosensor is able to detect influenza related antibodies with high sensitivity. This fabrication technique, which is simple and highly scalable, provide new avenues to facilitate mass production for POC plasmonic biosensors.

5.6 Sandwich-, Chip-, and Paper-Based Designs

Immobilizing nanoparticles onto solid substrates provides higher flexibility, robustness, and easy application to plasmonic sensing, especially when applying non-water-soluble molecules [129]. This section reviews three major sensing platform structures, namely, sandwich-, chip-, and paper-based designs for plasmonic biosensing. Silicon has been used as a traditional substrate for nanoparticles immobilization for years due to the well-developed nanofabrication methods, such as e-beam lithography [130, 131], charged particle beams [132] and thermal evaporation [133], to precisely control the size, shape and density of deposited nanoparticles. For instance, Bibikova presented a straightforward method to produce SEIRA- and SERS-active substrates based on the plasmonic properties of wet-chemically synthesized AuNSts, which were subsequently immobilized at silicon chips mediated by a gold layer and α-ω-dimercapto polyethylene glycol [134]. The advantage of nanoparticle deposition at the silicon surface is their strong adhesion at the gold-coated silicon interference. This property significantly improves the stability of the obtained AuNP modified Si substrates, which allows reusability after cleaning.

5.6.1 Sandwich Structure

Immunoassays typically include two modes: competitive assays and noncompetitive assays. In competitive assays, unlabeled antigen in the test samples competes with prelabeled antigen to bind the antibody. When the amount of antigen in the test sample increases, the detected signal measured from the labeled antigen typically decreases. As a result, competitive assays need to have a strong detected signal for the labeled antigen. [135, 136] Another mode is the noncompetitive immunoassays, which typically combine a primary antibody for immobilization and a secondary antibody for signaling. Since analyte is bond between two antibodies, this type of assay is also known as the sandwich-type assays. The measured signal is directly proportional to the concentration of analyte, thus this type of assay has very high sensitivity.

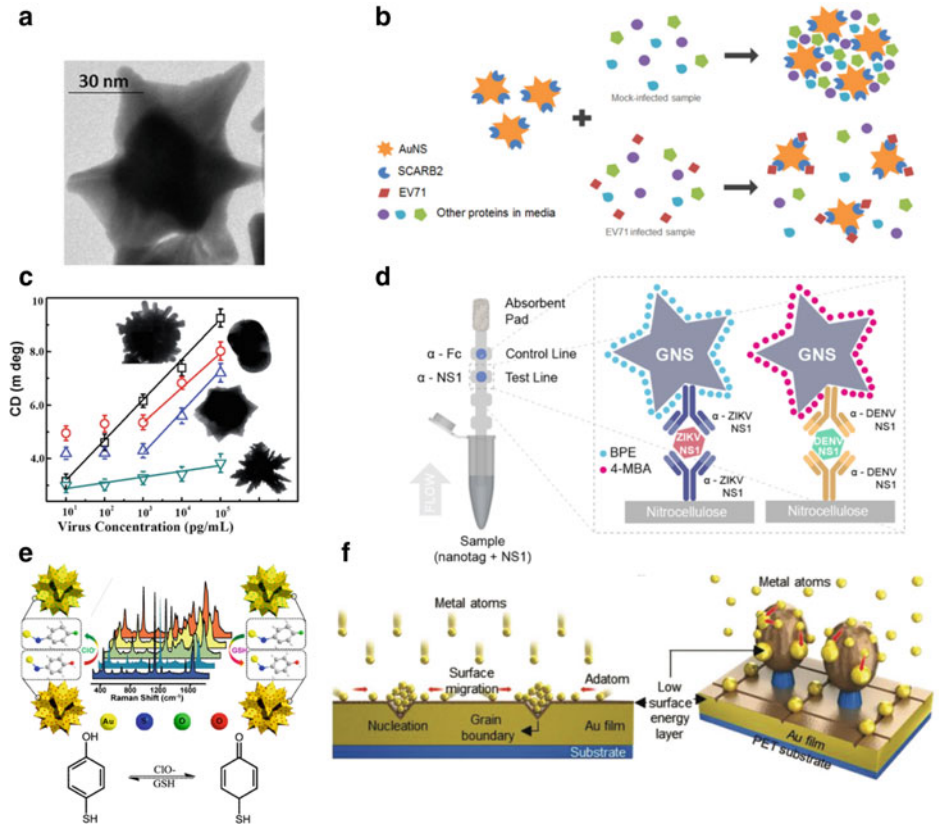

Fig. 5.24 Spike/star shaped AuNPs based plasmonic biosensor. **a** DNA detection using Au nanostars. Replicated with permission from [114]. **b** A SERS based label-free method that utilize protein-induced aggregation of colloidal Au nanostars for rapid detection of EV71. Replicated with permission from [116]. **c** a self-assembled Au nanostar based chiroimmunosensor for virus detection. Replicated with permission from [117]. **d** A SERS based multiplexed assay that can distinguish between Zika and dengue. Replicated with permission from [118]. **e** A SERS based bioprobe that can image and biosense hypochlorite (ClO^-) and glutathione (GSC). Replicated with permission from [119]. **f** A scaled-up, reproducible plasmonic biosensor that include many "hotspots" for detection enhancement. Replicated with permission from [120]

For decades, sandwich-structured biosensors have been intensively developed for disease diagnosis. The most commonly used sandwich immunosensor is the AuNPs/antigen/AuNPs where AuNPs are conjugated with different antibodies for different detection purpose. For example, Kim et al. [102] developed a heteroassembled AuNPs sandwich-immunoassay LSPR chip for detection of hepatitis B surface antigen, which is shown in Fig. 5.25a. The HBsAg were captured on AuNPs arrayed on glass substrate, and

the captured HBsAg were further conjugated with a layer of AuNPs for signal amplification. The gold nanoparticles were fabricated through a classic seed growing method. This platform is able to detect HBV with a LOD of 100 fg/mL in 10–15 min, which satisfies the rapid and sensitive requirements of POC diagnosis. These results were validated in spiked human serum samples. Similar AuNPs/antigen/AuNps sandwich-structured immunosensors include the detection of ManLAM (Tuberculosis biomarker) with SERS by Crawford et al. [72], detection of SARS-Cov-2 Virus (COVID 19 protein) with SPR by Das et al. (Fig. 5.25b) [137] and the detection of thrombin by Lee [138].

In immunoassays, one of the challenges is to enhance the plasmonic signal. For this purpose, different signaling markers have been employed in the sandwich immunoassays. For example, Zou et al. [139] developed a sandwich-structured immunosensor to detect Tuberculosis with magneto-plasmonic nanoparticles (MPN) (Fig. 5.25c). In this platform, antigen was captured on a gold chip and conjugated with Fe3O4@Au nanoparticles for enhanced signaling. Zou et al., fabricated Fe3O4@Au core–shell nanoparticles in three different morphologies (sphere, short spiky and long spiky) to amplify the SPR signals and found spherical MPN can enhance the electronic coupling effect significantly, showing the

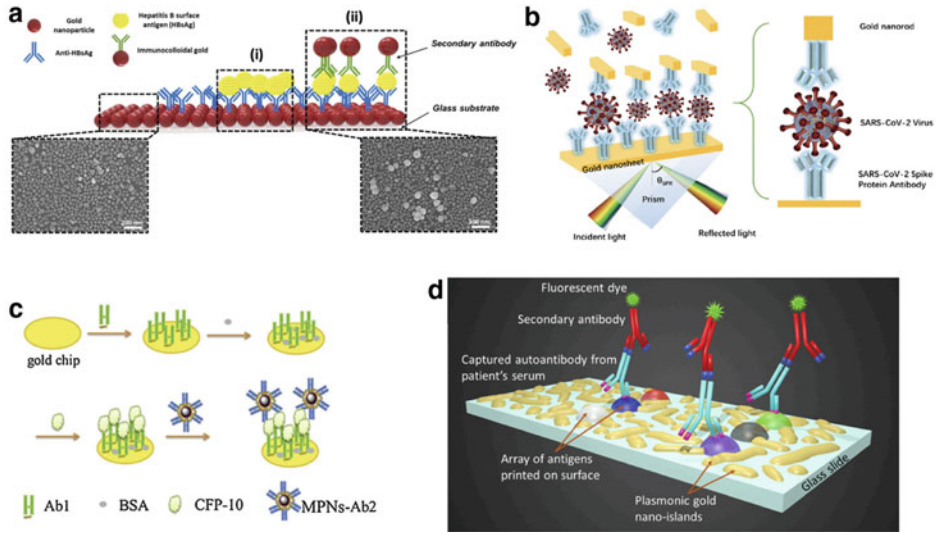

Fig. 5.25 Scheme of sandwich-structured biosensors for diagnosis. **a** The heteroassembled AuNPs sandwich immunoassay LSPR chip to detect HBV. Replicated with permission from [122]. **b** Structure of the gold nanorod assisted plasmonic immunoassay for detection of COVID-19 SARS-CoV-2 Spike Protein. Replicated with permission from [124]. **c** The magneto-plasmonic nanoparticles enhanced SPR chip to detect Tuberculosis. Replicated with permission from [125]. **d** Plasmonic sandwich microarray structure to detect cardiovascular diseases. Replicated with permission from [127]

best detection sensitivity. Their system was able to detect CFP-10, which is an early secretary antigen of Tuberculosis, with a LOD of 0.1 ng/mL. The developed immunosensor was evaluated in artificially CFP-10-containing urine which are easy to collect. In another study from Zhang et al. [140] they form the sandwich sensor by using IRDye800 fluorophore to label the captured antigen on the plasmonic Au substrate for the detection of type 1 diabetes. Li et al. [141] also employed IRDye800 fluorophore in their sandwich sensor for labeling (Fig. 5.25d). However, Li et al. developed this platform not to detect an already-known disease biomarker, but to profile the autoantibodies that are related to hypertensive heart disease. Through evaluating the detected cardiovascular autoantibodies, autoantibodies to troponin I, annexin-A5, and ADRBK1 emerged as the most strongly associated with LV remodeling and dysfunction in patients with hypertension.

5.6.2 Microfluidic Chip

Being the technique to precisely manipulate fluids at the microscale, microfluidic technology is capable of implementing bioreaction with minimized reagent and shortened span, thus can significantly reduce the cost and time of detection [43–45]. Compared with traditional platforms, integrating microfluidic systems with plasmonic microsensors offer a bunch of advantages in cost, sensitivity, and adaptability. Microfluidic chips are typically fabricated in a simple and reproducible approach with low cost, which are suitable for batch-fabrication to the clinic. In the meantime, microfluidic reactors enable homogeneous and thorough reaction with reduced specimen, thus increase the sensitivity and accuracy of detection. Further, microfluidic chips are versatile and can be easily adapted for various purposes, such as automated measurements, connection to other instruments, and label-free sensing. Low cost, portable device, high throughput, high sensitivity, rapid reaction, simplified steps, all these characters indicate that microfluidic-based plasmonic sensing platforms are ideal for POC disease diagnosis [142, 143].

Thanks to the high throughput, microfluidic chips can generate a well-defined detection environment for plasmonic sensing systems. Mühlig et al. [144] set up a droplet-based lab-on-a-chip device to detect mycobacteria using the surface-enhanced Raman spectroscopy. In this platform, bacteria were disrupted and pumped into the microfluidic channel together with the fabricated Ag nanoparticles to record the LOC-SERS spectra. The droplet-based microfluidic device can analyze a large number of independent samples rapidly with low sample volume, thus can conveniently generate a statistical valid data set for detection. However, this system still requires a Raman microscope device to do the measurement, which limits the application scenario. Other researchers incorporate microfluidic devices with plasmonic sensors to introduce a fast and portable detection method [145–148]. For example, Yap et al. [145] presented a novel bifunctional microfluidic SERS immunoassay with plasmonic-magnetic nanoparticles. In the immunoassay, plasmonic nanoparticles act as soluble SERS immunosubstrates and magnetic particles

promote micromixing, together yielding a rapid detection in a simple device. Zhou et al. [146] built up a cost-effective plasmonic immunochip for the detection of carcinoembryonic antigen (CEA) by integrating plasmonic sensing with microfluidics and nanoimprint lithography (Fig. 5.26a). Plasmonic nanocave array with excellent bulk refractive index sensitivity is implemented in the platform to provide stable functionality and simple measuring configuration. This chip achieves detection capability for the CEA concentration of less than 5 ng/ml within 30 min, which is much lower than the CEA cancer diagnosis threshold of 20 ng/ml. Vazquez-Guardado et al. [147] developed a plasmonic sensing system to directly detect neurotransmitter dopamine from whole blood (Fig. 5.26b). The microfluidic separator enables in-line separation of plasma directly from the bloodstream and channels it to the detection area coated with inorganic cerium oxide nanoparticles for rapid detection. The platform achieves detection of dopamine at 100 fM concentration in simulated body fluid and 1 nM directly from blood. In the following year, Inci et al. [148] reported a disposable hand-held microfluidic plasmonic platform to detect hemoglobin protein. With the capability to finish the typical assess in 15–30 min for end-users, this cost-effective miniaturized chip shows great potential in POC applications. At the meantime, microfluidic devices are easily to be designed with parallel microchannels, which allows for parallel detection of multiple antigens [149, 150] An example was presented by Geng et al. [149] with an optofluidic-portable platform to integrate LSPR spectroscopy and microfluidic technology to deliver a low-cost, ultra-sensitive detection system for liver cancer antigen (Fig. 5.26c). The vacuum evaporation followed by thermal annealing method was used to fabricate the AuNPs on microfluidic chip. This chip contains 9 cells and is connected to optical probe and data handling system to allow for parallel in-situ test and real-time measurement. Soler et al. [150] also reported a nanoplasmonic microfluidic biosensing system that can do simultaneous detection of two bacterial infections: Chlamydia trachomatis and Neisseria gonorrhoeae. This system introduces precise immobilization of specific antibodies on the individual sensor arrays for selective detection and real-time quantification with a limit of detection of 300 CFU/mL and 1500 CFU/mL for the o bacteria respectively. Peláez et al. [151] combined the SPR gold chip with microfluidics to realize POC for tuberculosis diagnosis. The presented biosensor is functionalized with highly specific monoclonal antibodies, allowing for detection and quantification of the heat shock protein X (HspX) directly in pretreated sputum samples. Microfluidic plasmonic sensing system offers new solutions for the current COVID-19 pandemic. Funari et al. [152] developed an opto-microfluidic chip for the detection of antibodies against SARS-CoV-2 spike protein by gold nanospikes. The microfluidic chip is covered with functionalized Au nanospike and combined with a homemade reflection probe to collect the reflective light to the detector to record and process the absorbance spectrum. Funari et al. showed that this opto-microfluidic platform can detect the target protein in diluted human plasma within 30 min and achieves an LOD of ∼0.08 ng/mL.

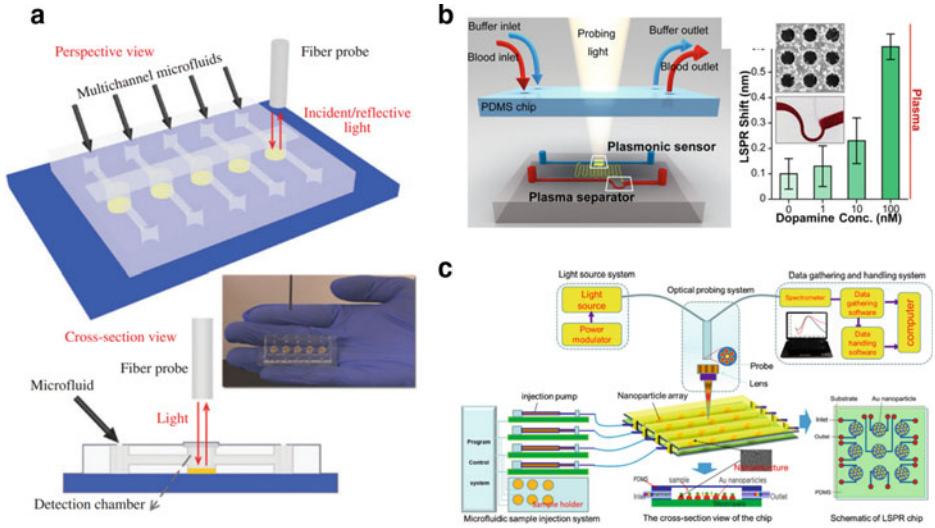

Fig. 5.26 Microfluidic plasmonic sensing platforms. **a** Microfluidic immunochip with plasmonic gold nanocave array and a fiber probe for tumor detection. Replicated with permission from [72]. **b** Microfluidic separator embedded with plasmonic sensor to directly detect neurotransmitter dopamine from whole blood. Replicated with permission from [137]. **c** Optofluidic biosensor platform integrated microfluidics and LSPR sensing chip. Replicated with permission from [139]

5.6.3 Paper Based Design

Paper-based sensing platforms have attracted increasing interest and obtained rapid development in the past few years since Whitesides et al. first introduced the potential of microfluidic paper-based analytical devices (μPADs) in 2007 [153]. With the properties of low-cost, widespread availability of material, facile manufacture, high biocompatibility and ease of use, paper-based devices have becoming ideal platforms for POC diagnosis applications. Paper-based devices are typically composed of hydrophilic or hydrophobic microstructures patterned on the paper substrate to allow for capillary-driven flow. These paper-based devices are usually fabricated through wax printing [154], inkjet printing [155], screen printing [156], photolithography [157] and plasma treatment [158].

Paper-based devices are easy to combine with the colorimetric detection method to serve fast and cheap diagnosis through visual readout without handling other tools or apparatus. In colorimetric assays, the reagents are first loaded to the paper substrate and will be later interact with the analyte solution to create a visible color change in the paper. For example, Fakhri et al. [159] developed a novel paper-based biosensor to detect concentrations of miRNA-21 in human urine sample. This biosensor is incorporated with DNA-templated Ag/Pt nanoclusters to catalyze the reaction of hydrogen peroxide and 3,30,5,50 tetramethylbenzidine (TMB) to produce a blue color. This biosensor is able to

reach a detection limit of 0.6PM with a large linear detection range. Another example is presented by Srisa-Art et al. [160] to detect Salmonella typhimurium using paper-based device (Fig. 5.27a). IMS anti-Salmonella coated magnetic beads are applied to capture and separate the bacteria from sample, followed by the implementation of a sandwich immunoassay for the detection. The concentration of Salmonella typhimurium can be read as the length of colored band and reach a detection limit of 10^2 CFU mL^{-1}. Instead of using simple piece of paper, Son et al. [161] show the potential of PDA-paper in the immunoassays to detect the high infectious pH1N1 virus among influenza A viruses (Fig. 5.27b). Their colorimetric sensor employs PDA-paper chip as the substrate, which exhibits blue-to-red colorimetric transitions upon environmental change. Conjugated with antibody, the PDA-paper chip is able to detect pH1N1 virus with visible color change. Other researchers also use paper-based colorimetric immunosensors to detect different irons which are toxic to human beings, including lead ions [162] and mercury ions [163].

It is worth noting that paper-based colorimetric immunosensors usually have low sensing signal, which often limits their application in the disease diagnosis. To amplify the

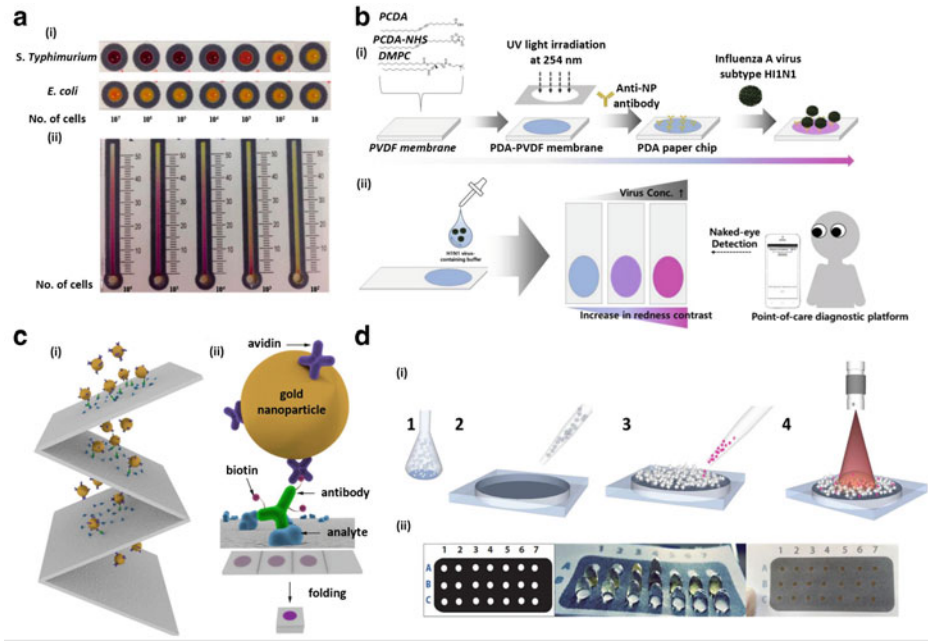

Fig. 5.27 Examples of paper-based immunosensors. **a** The readout results from colorimetric paper-based sensor to detect Salmonella typhimurium. Replicated with permission from [149]. **b** Preparation of PDA-paper chips and their application for the colorimetric detection of influenza A (pH1N1) virus. Replicated with permission from [150]. **c** Schematic representation of the origami paper-based biosensor. Replicated with permission from [153]. **d** The fabrication process and pattern design of the office paper based plasmonic SERS substrates. Replicated with permission from [155]

sensing signal of paper-based sensors, Alba-Patino et al. [164] developed an origami paper-based colorimetric biosensor with decreased detection limit. By simply folding a piece of paper as substrate and loaded with conjugated gold nanoparticles, the immunosensor can generate simultaneous visualization of colorimetric signals in each layer of paper (Fig. 5.27c). Due to the semitransparent nature of wet paper, signals are added layer upon layer to form higher optical density. It is showed that the limit of detection is decreased 10 times in a model immunosensor for the detection of immunoglobulins.

Paper-based devices also show great potential in SERS. Traditional SERS immunosensors are fabricated by generating metal nanostructures on the substrate, which is typically done by sophisticated and expensive deposition technology. Compared with traditional substrate material such as silicon wafer or glass, paper has cellulose structure to directly absorb the reagent via spotting and can even form a higher Raman enhancement factor [129]. The theme of flexibility, low cost and high sensitivity can be reflected in many recent studies. For example, Oliveira et al. [165] decorated office paper with silver nanostars to obtain increased SERS sensibility, high uniformity and reproducibility (Fig. 5.27d). Moram et al. [166] fabricated a SERS platform by employing filter paper embedded with salt-induced aggregated Ag/Au nanoparticles and validate their application to detect multiple explosive molecules. Hu et al. [167] constructed a uniform paper-based SERS test strip via in situ synthesis of Au NPs on paper fibers for the detection of Mucin-1 in whole blood. Lee et al. [168] reported a filter paper based SERS sensor which is hydrophobic modified by alkyl ketene dimer for the detection of pesticide with sub-nanomolar sensitivity. In addition to paper-based devices, we have summarized a list of other non-metal based plasmonic devices in Table 5.2. A commonly used materials is graphene that is proven to increase the sensitivity of plasmonic detections [169]. These nonmetal based devices' synthesis and working method, target disease and biomarkers, their potential POC feasibility, and limit of detection are also summarized and evaluated.

5.7 Meta-Surface Patterned Design

This section of the review will review and discuss efforts towards the patterning of surfaces with plasmonic structures to enable large-scale surface-based sensors [173]. Table 5.3 summarized some recently developed, representative examples of plasmonic biosensors based on patterned meta-surface and nanoarray structures that enhance the plasmonic effect. Their synthesis and working method, target disease and biomarkers, their potential POC feasibility, and limit of detection are also summarized and evaluated. This section will cover four main classes within this field, discussed in increasing levels of scalability, namely lithographic patterning, nanoisland films, nanoparticle deposition upon surfaces, and finally chemical growth (Fig. 5.28).

Table 5.2 Summary of examples of nonmetal based plasmonic biosensors

Materials	Synthesis method	System/Method	Disease detected	Biomarker	POC ability	Limit of detection	References
RGO	Sputter coating (Au) incubated with RGO	SPR	Dengue	DENV 2 E-proteins	High	0.08 pM	[170]
Paper	Commercial product (Dynabeads, streptavidin—β-galactosidase conjugate)	Colorimetric sensing	Salmonellosis	Salmonella typhimurium	High	100 CFU/mL	[160]
	Photo irridation (PDA)	Colorimetric sensing	Influenza A	pH1N1	High	$10^3 \sim 5 \times 10^3$ $TCID_{50}$	[171]
Polymer	Polymerization	SPR	HBV	Anti-HBs	High	N/A	[172]
Graphene	Commercial product (Graphene)	Colorimetric	Inflammation	C-reactive protein	High	0.07 ng/mL	[60]

Table 5.3 Summary of examples of meta-surface and nanoarray based plasmonic biosensors

Surface form	Synthesis method	System/Method	Disease detected	Biomarker	POC ability	Limit of detection	References
Meta-substrate	Commercial product (Au), magnetic sputtering method	Plasmonic fluorescence	Cardiac disease	Cardiac troponin I	High	0.01 ng/mL	[174]
	Commercial product (Au)	SPR	TB	DIG	High	63 pg/mL	[175]
Meta-coated slides	Sputtering (Au)	SPR	Dengue	DENV-2 E-proteins	Low	0.08 pM	[176]
	Seed-mediated growth on glass slide (Au)	Plasmonic fluorescence	Diabetes	Islet cell–targeting autoantibodies	High	N/A	[140]
	Commercial product (Au)	SPR	Cardiac disease	Cardiovascular autoantibodies	Medium	N/A	[177]
	Thermal annealing (Ag)	LSPR	Dengue	Dengue NS1 antigen	High	9 nm/(μg/mL)	[178]
	Evaporation (Au)	SPR	Cancer	Carcinoembryonic antigen	High	5 ng/ml	[146]
	Electron beam evaporation, thermal annealing	LSPR	Liver cancer	Liver antigen, liver antibody	High	Antigen 45.24 ng/ml Antibody 25 ng/ml	[179]
	Coating Au on butterfly wings	SERS	Malaria	Malarial hemozoin	Low	N/A	[180]

(continued)

Table 5.3 (continued)

Surface form	Synthesis method	System/Method	Disease detected	Biomarker	POC ability	Limit of detection	References
Nanoarray	Tetrahedron DNA monomers	SPR	HIV	HIV-related DNA	High	48 fM	[181]
	Commercial product (Spreeta 2000 chip)	SPR	TB	Ag85	High	10 ng/mL	[182]
	Commercial product (Au)	SPR	Ebola	mAb1, mAb2, mAb3	Medium	0.5 pg/mL	[183]
	Seed-mediated growth on glass slide (Au)	SPR	Diabetes	ZnT8A	Low	N/A	[184]

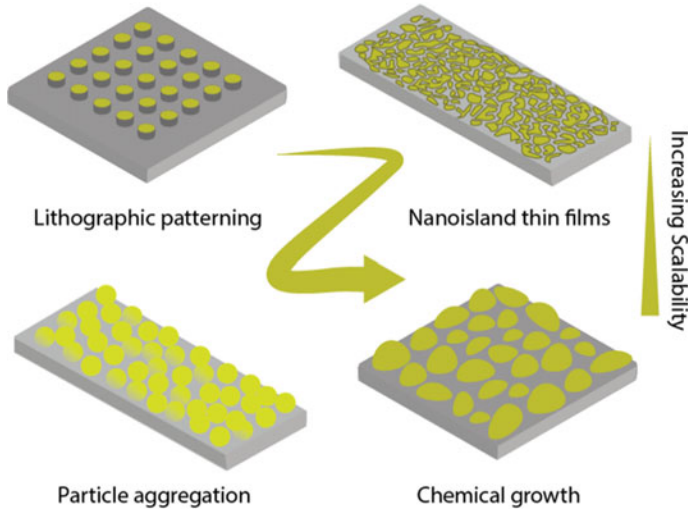

Fig. 5.28 Overview figure showing the various techniques used for patterning of surfaces, namely lithographic patterning, nanoisland thin films, particle aggregation, and chemical growth

5.7.1 Lithographic Patterning

Lithographic patterning of metallic films for the creation of plasmonic nanostructures is a commonly utilized approach that allows for unparalleled levels of tunability and control. By virtue, such systems often achieve the highest levels of enhancement of the techniques that will be discussed herein, however due to lack of scalability of many of the techniques used these configurations have not found significant translation to POC applications. Due to the size of the desired structures, electron-beam lithography is often required for their fabrication, creating further limitations in terms of scalability and time of processing. In its most basic form, this technique requires the spin coating and patterning of a photoresist film via electron-beam writing. Following pattering, the photoresist can be developed removing the unwanted areas after which metallic thin films can be deposited and the remaining resist removed via a lift-off process. Due to the use of an electron-beam, the resolution of this technique allows for the writing of nanoscale features and highly controlled geometries benefiting performance. Using this approach, an early demonstration of plasmon-enhanced fluorescence was demonstrated, with fluorescence enhancement of up to 1000-fold demonstrated experimentally [53]. Alternative, more scalable and wafer-scale lithographic processes have been developed using variations of more standard traditional ultraviolet lithography. In one example, a modified deep UV lithographic process was used to create wafer scale plasmonic nanohole array geometries [185] (Fig. 5.29a). This system was coupled with gold nanoparticles which when bound to the nanohole array

reduces the transmission of the normally extraordinary optical transmission at the resonance wavelength of the nanohole array. The developed system was coupled with a portable optical reader which enables POC potential and results from the system could be ascertained within 15 min. As a use-case for the developed system, the group explored the detection of sepsis using two sepsis-related biomarkers, procalcitonin (PCL) and C-reactive protein (CRP), and showed limit of detection of 21 and 36 pg/mL, for each, respectively. Within a clinical cohort they demonstrated the ability to distinguish between sepsis, noninfectious sepsis, and healthy individuals (Fig. 5.29a). Though these results are promising and performance impressive, for use within the POC, scalability is a crucial concern and a shortcoming of lithographic methods.

5.7.2 Nanoisland Films

The nanoisland film morphology has been a widely utilized configuration due to advantageous optical properties including enhanced field intensities resulting from closely packed yet isolated clusters of particles. This general morphology has been fabricated using two main methods, both involving first the deposition of metallic thin films. In the standard configuration of this morphology, highly controlled deposition of metallic film films prior to film percolation is completed (often <10 nm for gold thin films) [186–188]. High percolation thresholds due to atom mobility and surface tension results in gold thin films forming in a non-continuous sheet of closely packed though distinct island-like clusters [189]. Due to the close-packed, yet distinct islands there exists significant interaction between adjacent "hot-spots" leading to significant field enhancement [190]. As the film thickness grows, the film will become continuous and the advantageous optical properties diminish [191]. An alternative method in the fabrication of nanoisland-like geometry is thermal dewetting of gold thin films. In this case, the metallic thin film layers are heated to high temperatures and rearrangement of the gold particles occurs as the sheets undergo a deposition process, resulting in the formation of nanoislands [190]. By altering numerous parameters within the process including the temperature, metallic thin film thickness, time of heating, among others, the level of rearrangement can be altered leaving to various characteristic morphologies [192–196]. One intriguing study within this field utilized repeated deposition and dewetting to increase the number of plasmonic "hot-spots" and as a result the extinction intensity (Fig. 5.29b). This substrate was tested for surface-enhanced Raman scattering (SERS) of octopamine molecules with a limit of detection of 10 μM for multi-step dewetting, compared to 100 μm for single-step detwetting [190]. Both pre-percolation films and thin film detwetting techniques introduced first require the step of metal deposition, however due to the thickness of the desired films and possibility for large-scale patterning, there is potential for such techniques to be useful for POC applications.

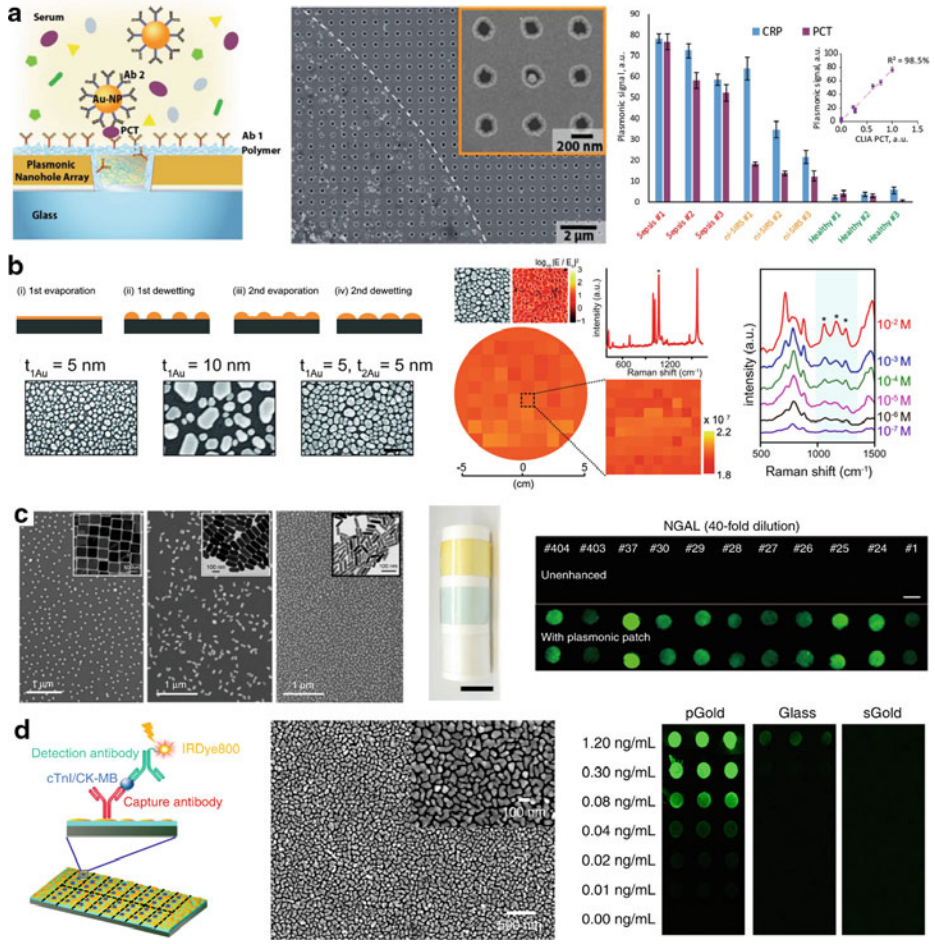

Fig. 5.29 Overview of patterned plasmonic surfaces. **a** Shows nanoplasmonic array fabricated using lithographic methods, which utilizes extraordinary transmission demonstrated by the structure for the sensing of captured analytes then applies this for sepsis diagnosis using two widely accepted sepsis-related biomarkers, CRP and PCT. Replicated with permission from [176]. **b** Shows a repeated thin film dewetting process to form densely packed particle arrays which exhibit significant Raman enhancement and was used in the detection of octopamine molecules. Replicated with permission from [181]. **c** Shows nanoparticle deposition/aggregation using three different nanoparticle morphologies, their large-scale patterning potential using a polymeric surface, and their application within plasmon enhanced fluorescence applications. Replicated with permission from [2]. **d** Shows a solution-based synthesized microchip containing densely packed films and its application within plasmon-enhanced fluorescence application for the diagnosis of myocardial infarction. Replicated with permission from [186]

5.7.3 Chemical Growth

Chemical growth is another means for the development of patterned plasmonic surfaces and has the highest potential for scalability to meet demands of POC assays. To promote the use for POC applications which necessitate scalability there has been a continual push in the field for simplistic fabrication mechanisms which omit the use of specialized equipment and processing such as that in lithographic processing and traditional nanoisland films. Arising from this work there has been a host of papers utilizing a simple yet highly effective technique in which chemically synthesized nanoparticles are bound onto a substrate forming a plasmonic surface which can be used directly within fluorescent assays, surface-enhanced RAMAN, LSPR, and the like [1, 2, 4, 11]. In contrast to lithographic methods which allow for highly controlled patterning, within nanoparticle deposition/aggregation there exists no means to control where particles are patterned and particles are often suspended within a solution where incubation enables particle binding. By the nature of this process and the need for particle adsorption to the surface, this process is slow, yet due to the solution-based nature, can be highly scalable. A unique attribute of these systems is the ability to finely control the chemically synthesized particles prior to deposition thereby drastically altering the resulting films optical and plasmonic properties [1, 2]. In one example of this system confirmation, three different particle geometries were explored, namely gold core-silver shell nanocubes with an LSPR peak of 490 nm, and two gold nanorods with LSPR peaks of 670 and 760 nm, respectively, for sure within plasmon-enhanced fluorescence applications (Fig. 5.29c). Particle aggregation was completed using a simple incubation process resulting in positively changed plasmonic particles absorbing to a negatively charged polydimethylsiloxane layer. Since spacing between fluorophore and plasmonic particles is critical to overall enhancement, following deposition, a polymer spacer was added via solution processing to enable a spacer layer between the plasmonic particles and nearby fluorophores [2]. As a use case, they tested this substrate for the detection of early-stage biomarkers or acute kidney injury, namely kidney injury molecule-1 and neutrophil gelatinase-associated lipocalin and showed 100-fold fluorescence enhancement over non-treated substrates (Fig. 5.29c).

In chemical growth, techniques common for solution-based synthesis of gold nanoparticles are modified and in turn can allow for the growth of particles upon a substrate. As is commonly within chemically synthesized particles, protocols of this nature typically include a seeding step followed by a growth step where the particle size can be tuned. Though as of yet, this technique hasn't been able to show the breadth of morphologies and geometries that are able to be formed using standard solution-based chemical synthesis leading to lower levels of tunability, the application of these techniques to substrates has led to the creation of unique morphologies similar to the nanoisland-like films. Considering that fabrication occurs directly upon the desired substrate and that no specialized equipment is needed, fabrication can be highly scalable and rapid [191, 197–200]. Many

of these structures have found use within plasmon-enhanced fluorescence and surface-enhanced RAMAN spectroscopy. Another unique attribute of chemical methods, is the ability to pattern alternative substrates, including polymeric surfaces. The earliest demonstration of this fabrication method was presented by Tabakman et al. [191], where full substrate synthesis could be completed in ~ 30 min of solution time, which included a three step process. Firstly, seeding of gold was completed upon the substrate by adding ammonium hydroxide into a chloroauric acid solution resulting in the precipitation of Au seeds upon the substrate of choice. Following seeding, reduction of the gold seeds was completed using sodium borohydride leading to the formation of Au^0. Lastly, selective growth of seeds via hydroxylamine reduction in a chloroauric acid solution enabled reduction of Au^{3+} onto the seeds, forming nanoislands [191]. This initial paper further showed the feasibility for tuning structure by changing parameters including seed density and concentration of Au^{3+} during growth phase, altering optical properties. This substrate was later optimized and utilized for the diagnosis of myocardial infarction using the plasmonic nano-islands as a means for plasmon-enhanced fluorescence [197] (Fig. 5.29d), where it showed a diagnostic sensitivity of 100% and specificity of 95.54%. This study utilized cardiac troponin I, and showed dynamic range of 0.01–1.20 ng/mL and limit-of-detection as low as 0.0100 ng/mL, an 130-fold improvement over a substrate without nanoislands.

The four methods discussed herein describe the main methods presented thus far in literature for the patterning of substrates with plasmonic materials. Future efforts of this field should focus on the development of alternative fabrication mechanisms that emphasize scalability and portability to promote use within POC settings.

5.8 Challenges and Perspectives

Despite the booming of development of nanomaterial based plasmonic sensors for POC applications in recent years, there remain many challenges at present and ahead. Among many challenges the technologies are facing, we selectively discuss the ones that are most urgent. The first one is the Covid-19 global pandemic which requires rapid, POC diagnostic tool to quickly identify contraction of the virus. To develop reliable, accurate plasmonic sensing tools, machine learning assisted algorithms can serve as a fast and predictive tool to model the optical properties of nanoparticles. Miniaturization of sensing devices is also critical in facilitating the process of converting the current lab-based detection method to POC tools. Lastly, in disease detection, there exist many gold standards in clinical settings, to which many other innovative detection tools are compared including plasmonic sensing tools. In this section, we provide discussions and unique perspectives on these areas and hold a general belief that plasmonic diagnostic devices are able to cope with those challenges with future works.

5.8.1 Covid-19 Testing

As of November 2021, there are approximately 250 million people worldwide contracted Covid-19, a severe acute respiratory disease caused by coronavirus SARS-CoV-2, and 5.05 million people dies associated with it, according to The New York Times and Johns Hopkins University. Regardless of the stages of this pandemic, the ability to access Covid-19 test is extremely important. The tests have to be timely, easy, quick and accurate in order for more people to get tested, which provide important information to governments and health agencies to contain the virus and drive the world to "new normal". During the pandemic, governments in many countries offer test sites where people can go and get tested. However, problems like complicated registering process, long waiting time and travelling to these sites remain hurtles that prevent some people getting tested. Therefore, to solve this problem, scientists and engineers developed various types of POC biosensors that aim to provide rapid testing of coronavirus at one's own location, saving the time-consuming trip to go to a test site and providing an important tool to governments and health agencies to monitor the spread and progress of the highly contagious disease [201–203]. Plasmon enabled Covid-19 biosensors are one of the most promising tools to provide a POC solutions to Covid testing [204]. Djaileb et al. [205] developed a portable SPR based sensor for Covid-19 detection. In the design, the sensing chip's gold surface is modified with a monolayer of 3-MPA-LHDLHD-COOH which bond with the SARS-CoV-2 nucleocapsid protein (rN). SPR shift is then observed and calculated as indicator for the existence of anti-rN antibody release by immune system in response to the SARS-CoV-2 virus. Qiu et al. [206] designed a biosensor that combines the plasmonic photothermal effect and LSPR mechanism. Au nanoislands are fabricated and functionalized with complementary DNA receptors. Selected sequences from of the SARS-CoV-2 virus can be detected through nucleic acid hybridization on the DNA receptors with a low limit of detection of 0.22 pM concentration. In addition to developing the above-mentioned Covid-19 sensor prototypes, researcher also investigated the sensor using theoretical analysis and computational simulations in an effort to design an ideal Covid-19 sensor. Masterson et al. [207] reported a label-free plamonic nanosensor that can quantitatively detect 10 different biomarkers within one platform. The developed biosensor platform shows the capability to quantify IgG and IgM directly from COVID-19-positive patient plasma samples at the same time. Peng et al. [208] and Manas Das et al. [89] constructed models of near infrared SPR biosensor and plasmonic immunoassay, respectively, to explore the theoretical potentials of these sensors in POC coronavirus diagnoses. Moreover, rapid onsite detection is crucial to realize POC diagnosis. Li et al. [209] developed a plasmonic biosensor based on surface-enhanced infrared absorption that can deliver results in real time and on-site. A genetic algorithm intelligent program was employed to facilitate automation of the design process with optimal sensing performance. Most diagnostic tools need advanced laboratory instrument to read the result which prevent many portable sensors from becoming true POC devices. To solve this, Moitra et al. [101] developed a colorimetric assay with

AuNPs with which the result can be observed by naked eye without the need for any laboratory signal reading system.

5.8.2 Machine Learning

Despite of the advances in development of nanostructures for various detection purposes, the design of plasmonic sensors remain an iterative process and calls for experience from researchers. Traditional design strategy starts from computational modeling of plasmonic nanoparticles to predict their optical properties. However, these modeling tools to solve EM equations are typically time consuming and not accurate. More importantly, there's no way for the forward simulations to solve the inverse problem, that is to find the required nanostructure for the target optical property. Thanks to the fast development of artificial intelligence algorithm during recent years, there exist new chances in efficient design of plasmonic nanostructures.

Machine-learning based method serves as a fast and predictive tool to model the optical properties of nanoparticles. Traditional modeling methods do the prediction via numerically solving the Maxwell equation, whose predicting results are usually limited by the resolution and observational error. Differently, neural network (NN) can discover the intrinsic correlation between the nanostructure and their optical properties from a real dataset, even though their underlying physics are unknown. As a result, NN can provide more accurate predictions than conventional modeling methods. Besides, once a neural network is trained well, it can predict the optical properties of numerous designs within a few seconds [210–212]. NN is also able to solve the inverse design problems by directly providing the required design parameters for target sensing properties [213, 214]. Once a NN is trained well from the provided dataset, the mapping from design parameters to their resulting optical characteristics are established. The advanced NN tools can automatically optimizing the design parameters to achieve the target optical properties, therefore automating the entire design process. In addition to the plasmonic design, machine-learning algorithms also facilitate the characterization of plasmonic sensing. Conventional neural network (CNN) has the outstanding capability to recognize and extract the features in images, thus becoming a powerful tool in image classification. In recent years, CNN has been extensively employed in various plasmonic image analysis, including the colorimetric detection [215] and SERS detection [216, 217].

5.8.3 Miniaturization

The main challenges in optical biosensors are the light source and the optical readout equipment. Conventional optical biosensors have taken advantage of two "equipment"

from nature, the broadband daylight as the light source and the human eyes as the photodetector in the visible wavelength. One example of such a sensor is the colorimetric pregnancy test strip, in which the LSPR by the aggregated gold nanoparticles induces significant light absorption change that can be detected by human eyes. However, moving forward, improving the sensitivity and resolution of optical biosensors requires better controlled light sources and more accurate photodetectors. In recent years, thanks to the fast-growing semiconductor technologies, cellphones are packed with more and more powerful computing power and advanced cameras. This brings a unique opportunity in tackling the aforementioned challenges in the POC optical biosensors. The light emitted diode (LED) on the cell phone can act as a light source with well-controlled wavelength and intensity while the high-resolution camera can act as a sensitive photodetector for the sensing. Furthermore, the computing power on the cell phone enables the acquired optical signal to be analyzed with a complex algorithm and provides real-time diagnosis results.

5.8.4 Gold Standard

Compared to the gold standard methods, such as diagnostics for HIV/HBV by enzyme immunoassay, detection for Dengue, Malaria and COVID-19 by PCR, and judgement for TB by growth of colony-forming units of mycobacterium tuberculosis on culture of sputum [218, 219], the POC testing enabled by plasmonic nanosensors has shown high sensitivity, low cost, easy operation and good correlation to those gold standards [220]. There is growing consensus that these screening tools can play important role in disease or biomarker detection along with existing clinical settings, instead of being used as independent technologies. For instance, reverse transcriptase PCR (RT-PCR) is currently considered to be the gold standard for the early detection of COVID-19 pioneered by the U.S. Centers for Disease Control and Prevention [221]. However, the clinical manifestation of COVID-19 can be significantly divergent from individual to individual, some patients are even asymptomatic. Therefore, physicians need choose suitable techniques, such as chest computed tomography (CT), ELISA and lateral flow immunoassay for COVID-19 early diagnosis and clinical management [222]. RT-PCR offers the most sensitive detection, but this test takes several hours to complete and requires extensive human labor and consumable materials. Plasmonic nanosensors can reduce the time-to-result down to less than 15 min with high portability, although their limit of detection is still not competitive against the gold standard test. Advancement of nanomaterials facilitate the progress in medicine ranging from implantable biomedical devices [223–228] to disease biosensors as illustrated in this review. We believe advanced healthcare technologies enabled by plasmonic nanosensors are still in development and validation, and they can serve as an alternative detection procedure for the screening of infectious diseases soon.

References

1. C. Liang, J. Luan, Z. Wang, Q. Jiang, R. Gupta, S. Cao, K.-K. Liu, J.J. Morrissey, E.D. Kharasch, R.R. Naik, S. Singamaneni, Gold Nanorod Size-Dependent Fluorescence Enhancement for Ultrasensitive Fluoroimmunoassays, ACS Applied Materials & Interfaces. 13 (2021) 11414–11423. https://doi.org/https://doi.org/10.1021/acsami.0c20303.
2. J. Luan, J.J. Morrissey, Z. Wang, H.G. Derami, K.K. Liu, S. Cao, Q. Jiang, C. Wang, E.D. Kharasch, R.R. Naik, S. Singamaneni, Add-on plasmonic patch as a universal fluorescence enhancer, Light: Science and Applications. 7 (2018) 2047–7538. https://doi.org/10.1038/s41377-018-0027-8.
3. L. Scarabelli, L.M. Liz-Marzán, An Extended Protocol for the Synthesis of Monodisperse Gold Nanotriangles, ACS Nano. (2021) acsnano.1c10538. https://doi.org/10.1021/acsnano.1c10538.
4. J. Luan, A. Seth, R. Gupta, Z. Wang, P. Rathi, S. Cao, H. Gholami Derami, R. Tang, B. Xu, S. Achilefu, J.J. Morrissey, S. Singamaneni, Ultrabright fluorescent nanoscale labels for the femtomolar detection of analytes with standard bioassays, Nature Biomedical Engineering. 4 (2020) 518–530. https://doi.org/10.1038/s41551-020-0547-4.
5. M.L. Personick, M.R. Langille, J. Wu, C.A. Mirkin, Synthesis of Gold Hexagonal Bipyramids Directed by Planar-Twinned Silver Triangular Nanoprisms, J Am Chem Soc. 135 (2013) 3800–3803. https://doi.org/https://doi.org/10.1021/ja400794q.
6. H. Yoo, M.H. Jang, Size-controlled synthesis of gold bipyramids using an aqueous mixture of CTAC and salicylate anions as the soft template, Nanoscale. 5 (2013) 6708. https://doi.org/https://doi.org/10.1039/c3nr01553j.
7. Y.-C. Yeh, B. Creran, V.M. Rotello, Gold nanoparticles: preparation, properties, and applications in bionanotechnology., Nanoscale. 4 (2012) 1871–80. https://doi.org/https://doi.org/10.1039/c1nr11188d.
8. J. Piella, N.G. Bastús, V. Puntes, Size-Controlled Synthesis of Sub-10-nanometer Citrate-Stabilized Gold Nanoparticles and Related Optical Properties., Chemistry of Materials. 28 (2016) 1066–1075. https://doi.org/https://doi.org/10.1021/acs.chemmater.5b04406.
9. A. Tadimety, Z. Wu, J.H. Molinski, R. Beckerman, C. Jin, L. Zhang, T.J. Palinski, J.X.J. Zhang, Shape Effects of Plasmonic Gold Nanoparticles for Circulating Tumor DNA Screening, in: Proceedings of IEEE Sensors, 2020: pp. 16–19. https://doi.org/10.1109/SENSORS47125.2020.9278614.
10. M.R. Gartia, A. Hsiao, A. Pokhriyal, S. Seo, G. Kulsharova, B.T. Cunningham, T.C. Bond, G.L. Liu, Colorimetric Plasmon Resonance Imaging Using Nano Lycurgus Cup Arrays, Advanced Optical Materials. 1 (2013) 68–76. https://doi.org/https://doi.org/10.1002/adom.201200040.
11. P. Gupta, J. Luan, Z. Wang, S. Cao, S.H. Bae, R.R. Naik, S. Singamaneni, On-Demand Electromagnetic Hotspot Generation in Surface-Enhanced Raman Scattering Substrates via "Add-On" Plasmonic Patch, ACS Applied Materials & Interfaces. 11 (2019) 37939–37946. https://doi.org/https://doi.org/10.1021/acsami.9b12402.
12. L. Tang, J. Li, Plasmon-Based Colorimetric Nanosensors for Ultrasensitive Molecular Diagnostics, ACS Sensors. 2 (2017) 857–875. https://doi.org/https://doi.org/10.1021/acssensors.7b00282.
13. Z. Li, L. Leustean, F. Inci, M. Zheng, U. Demirci, S. Wang, Plasmonic-based platforms for diagnosis of infectious diseases at the point-of-care, Biotechnology Advances. 37 (2019) 107440. https://doi.org/https://doi.org/10.1016/j.biotechadv.2019.107440.

14. A. Tadimety, Z. Wu, J.H. Molinski, R. Beckerman, C. Jin, L. Zhang, T.J. Palinski, J.X.J. Zhang, Rational design of on-chip gold plasmonic nanoparticles towards ctDNA screening, Scientific Reports. 11 (2021). https://doi.org/10.1038/s41598-021-93207-7.
15. D. Mabey, R.W. Peeling, A. Ustianowski, M.D. Perkins, Diagnostics for the developing world, Nature Reviews Microbiology. 2 (2004) 231–240. https://doi.org/https://doi.org/10.1038/nrmicro841.
16. O. Tokel, F. Inci, U. Demirci, Advances in plasmonic technologies for point of care applications, Chemical Reviews. 114 (2014) 5728–5752. https://doi.org/https://doi.org/10.1021/cr4000623.
17. T. Mahmoudi, M. de la Guardia, B. Baradaran, Lateral flow assays towards point-of-care cancer detection: A review of current progress and future trends, TrAC - Trends in Analytical Chemistry. 125 (2020) 115842. https://doi.org/https://doi.org/10.1016/j.trac.2020.115842.
18. A. Prasad, J. Choi, Z. Jia, S. Park, M.R. Gartia, Nanohole array plasmonic biosensors: Emerging point-of-care applications, Biosensors and Bioelectronics. 130 (2019) 185–203. https://doi.org/https://doi.org/10.1016/j.bios.2019.01.037.
19. Y. Wang, J. Zhou, J. Li, Construction of Plasmonic Nano-Biosensor-Based Devices for Point-of-Care Testing, Small Methods. 1 (2017) 1–13. https://doi.org/https://doi.org/10.1002/smtd.201700197.
20. R. T. Hill, "Plasmonic biosensors," *Wiley interdisciplinary reviews. Nanomedicine and nanobiotechnology,* vol. 7, pp. 152-168, 2015.
21. L. Zhu, K. Wang, J. Cui, H. Liu, X. Bu, H. Ma, *et al.*, "Label-Free Quantitative Detection of Tumor-Derived Exosomes through Surface Plasmon Resonance Imaging," *Analytical Chemistry,* vol. 86, pp. 8857–8864, 2014/09/02 2014.
22. J. Park, M. Hwang, B. Choi, H. Jeong, J.-h. Jung, H. K. Kim, *et al.*, "Exosome Classification by Pattern Analysis of Surface-Enhanced Raman Spectroscopy Data for Lung Cancer Diagnosis," *Analytical Chemistry,* vol. 89, pp. 6695–6701, 2017/06/20 2017.
23. A. Pallaoro, M. R. Hoonejani, G. B. Braun, C. D. Meinhart, and M. Moskovits, "Rapid Identification by Surface-Enhanced Raman Spectroscopy of Cancer Cells at Low Concentrations Flowing in a Microfluidic Channel," *ACS Nano,* vol. 9, pp. 4328–4336, 2015/04/28 2015.
24. A. E. Cetin, A. F. Coskun, B. C. Galarreta, M. Huang, D. Herman, A. Ozcan, *et al.*, "Handheld high-throughput plasmonic biosensor using computational on-chip imaging," *Light: Science &Amp; Applications,* vol. 3, p. e122, 01/03/online 2014.
25. C. Escobedo, A. G. Brolo, R. Gordon, and D. Sinton, "Optofluidic Concentration: Plasmonic Nanostructure as Concentrator and Sensor," *Nano Letters,* vol. 12, pp. 1592–1596, 2012/03/14 2012.
26. D. Rodrigo, O. Limaj, D. Janner, D. Etezadi, F. J. García de Abajo, V. Pruneri, *et al.*, "Mid-infrared plasmonic biosensing with graphene," *Science,* vol. 349, pp. 165-168, 2015.
27. F. Yesilkoy, R. A. Terborg, J. Pello, A. A. Belushkin, Y. Jahani, V. Pruneri, *et al.*, "Phase-sensitive plasmonic biosensor using a portable and large field-of-view interferometric microarray imager," *Light: Science &Amp; Applications,* vol. 7, p. 17152, 02/23/online 2018.
28. A. J. Haes, L. Chang, W. L. Klein, and R. P. Van Duyne, "Detection of a Biomarker for Alzheimer's Disease from Synthetic and Clinical Samples Using a Nanoscale Optical Biosensor," *Journal of the American Chemical Society,* vol. 127, pp. 2264–2271, 2005/02/01 2005.
29. M. Dipalo, G. C. Messina, H. Amin, R. La Rocca, V. Shalabaeva, A. Simi, *et al.*, "3D plasmonic nanoantennas integrated with MEA biosensors," *Nanoscale,* vol. 7, pp. 3703-3711, 2015.
30. A. Vázquez-Guardado, S. Barkam, M. Peppler, A. Biswas, W. Dennis, S. Das, *et al.*, "Enzyme-Free Plasmonic Biosensor for Direct Detection of Neurotransmitter Dopamine from Whole Blood," *Nano Letters,* vol. 19, pp. 449–454, 2019/01/09 2019.

31. W. D. A. M. de Boer, J. J. Hirtz, A. Capretti, T. Gregorkiewicz, M. Izquierdo-Serra, S. Han, *et al.*, "Neuronal photoactivation through second-harmonic near-infrared absorption by gold nanoparticles," *Light: Science & Applications,* vol. 7, p. 100, 2018/12/05 2018.
32. H. T. Chorsi, Y. Zhu, and J. X. J. Zhang, "Patterned Plasmonic Surfaces—Theory, Fabrication, and Applications in Biosensing," *Journal of Microelectromechanical Systems,* vol. 26, pp. 718-739, 2017.
33. H. T. Chorsi and J. X. J. Zhang, "Apertureless Near-Field Scanning Probes Based on Graphene Plasmonics," *IEEE Photonics Journal,* vol. 9, pp. 1-7, 2017.
34. J. Kim and K.-B. Song, "Recent progress of nano-technology with NSOM," *Micron,* vol. 38, pp. 409–426, 2007/06/01/2007.
35. K. Hoshino, A. Gopal, and X. Zhang, "Near-Field Scanning Nanophotonic Microscopy—Breaking the Diffraction Limit Using Integrated Nano Light-Emitting Probe Tip," *IEEE Journal of Selected Topics in Quantum Electronics,* vol. 15, pp. 1393-1399, 2009.
36. S. Berweger, J. M. Atkin, R. L. Olmon, and M. B. Raschke, "Adiabatic Tip-Plasmon Focusing for Nano-Raman Spectroscopy," *The Journal of Physical Chemistry Letters,* vol. 1, pp. 3427–3432, 2010/12/16 2010.
37. R.-H. Jiang, C. Chen, D.-Z. Lin, H.-C. Chou, J.-Y. Chu, and T.-J. Yen, "Near-Field Plasmonic Probe with Super Resolution and High Throughput and Signal-to-Noise Ratio," *Nano Letters,* vol. 18, pp. 881–885, 2018/02/14 2018.
38. S.D. Bindesri, D.S. Alhatab, C.L. Brosseau, Development of an electrochemical surface-enhanced Raman spectroscopy (EC-SERS) fabric-based plasmonic sensor for point-of-care diagnostics, Analyst. 143 (2018) 4128–4135. https://doi.org/https://doi.org/10.1039/c8an01117f.
39. M. Müller, V. Kravtsov, A. Paarmann, M. B. Raschke, and R. Ernstorfer, "Nanofocused Plasmon-Driven Sub-10 fs Electron Point Source," *ACS Photonics,* vol. 3, pp. 611–619, 2016/04/20 2016.
40. C. Höppener and L. Novotny, "Antenna-Based Optical Imaging of Single Ca2+ Transmembrane Proteins in Liquids," *Nano Letters,* vol. 8, pp. 642–646, 2008/02/01 2008.
41. D.K. Gramotnev, S.I. Bozhevolnyi, Plasmonics beyond the diffraction limit, Nature Photonics. 4 (2010) 83–91. https://doi.org/https://doi.org/10.1038/nphoton.2009.282.
42. M. Zhang, C. Jin, Y. Nie, Y. Ren, N. Hao, Z. Xu, L. Dong, J.X.J. Zhang, Silver nanoparticle on zinc oxide array for label-free detection of opioids through surface-enhanced raman spectroscopy, RSC Advances. 11 (2021) 11329–11337. https://doi.org/https://doi.org/10.1039/d1ra00760b.
43. N. Hao, Z. Xu, Y. Nie, C. Jin, A.B. Closson, M. Zhang, J.X.J. Zhang, Microfluidics-enabled rational design of ZnO micro-/nanoparticles with enhanced photocatalysis, cytotoxicity, and piezoelectric properties, Chemical Engineering Journal. 378 (2019) 122222. https://doi.org/https://doi.org/10.1016/j.cej.2019.122222.
44. N. Hao, Y. Nie, Z. Xu, C. Jin, T.J. Fyda, J.X.J. Zhang, Microfluidics-enabled acceleration of Fenton oxidation for degradation of organic dyes with rod-like zero-valent iron nanoassemblies, Journal of Colloid and Interface Science. 559 (2020) 254–262. https://doi.org/https://doi.org/10.1016/j.jcis.2019.10.042.
45. Y. Nie, C. Jin, J.X.J. Zhang, Microfluidic in Situ Patterning of Silver Nanoparticles for Surface-Enhanced Raman Spectroscopic Sensing of Biomolecules, ACS Sensors. 6 (2021) 2584–2592. https://doi.org/https://doi.org/10.1021/acssensors.1c00117.
46. J. Zeng, Y. Zhang, T. Zeng, R. Aleisa, Z. Qiu, Y. Chen, J. Huang, D. Wang, Z. Yan, Y. Yin, Anisotropic plasmonic nanostructures for colorimetric sensing, Nano Today. 32 (2020) 100855. https://doi.org/https://doi.org/10.1016/j.nantod.2020.100855.

47. A. Sousa-Castillo, M. Comesaña-Hermo, B. Rodríguez-González, M. Pérez-Lorenzo, Z. Wang, X.-T. Kong, A.O. Govorov, M.A. Correa-Duarte, Boosting Hot Electron-Driven Photocatalysis through Anisotropic Plasmonic Nanoparticles with Hot Spots in Au–TiO 2 Nanoarchitectures, The Journal of Physical Chemistry C. 120 (2016) 11690–11699. https://doi.org/https://doi.org/10.1021/acs.jpcc.6b02370.
48. C.S. Kumarasinghe, M. Premaratne, Q. Bao, G.P. Agrawal, Theoretical analysis of hot electron dynamics in nanorods, Scientific Reports. 5 (2015) 12140. https://doi.org/https://doi.org/10.1038/srep12140.
49. Z. Zhang, H. Wang, Z. Chen, X. Wang, J. Choo, L. Chen, Plasmonic colorimetric sensors based on etching and growth of noble metal nanoparticles: Strategies and applications, Biosensors and Bioelectronics. 114 (2018) 52–65. https://doi.org/https://doi.org/10.1016/J.BIOS.2018.05.015.
50. S. Xu, L. Jiang, Y. Liu, P. Liu, W. Wang, X. Luo, A morphology-based ultrasensitive multicolor colorimetric assay for detection of blood glucose by enzymatic etching of plasmonic gold nanobipyramids, Analytica Chimica Acta. 1071 (2019) 53–58. https://doi.org/https://doi.org/10.1016/J.ACA.2019.04.053.
51. K. Liang, F. Liu, J. Fan, D. Sun, C. Liu, C.J. Lyon, D.W. Bernard, Y. Li, K. Yokoi, M.H. Katz, E.J. Koay, Z. Zhao, Y. Hu, Nanoplasmonic quantification of tumour-derived extracellular vesicles in plasma microsamples for diagnosis and treatment monitoring, Nature Biomedical Engineering. 1 (2017) 0021. https://doi.org/https://doi.org/10.1038/s41551-016-0021.
52. E. Balaur, S. O' Toole, A.J. Spurling, G.B. Mann, B. Yeo, K. Harvey, C. Sadatnajafi, E. Hanssen, J. Orian, K.A. Nugent, B.S. Parker, B. Abbey, Colorimetric histology using plasmonically active microscope slides, Nature. 598 (2021) 65–71. https://doi.org/10.1038/s41586-021-03835-2.
53. A. Kinkhabwala, Z. Yu, S. Fan, Y. Avlasevich, K. Müllen, W.E. Moerner, Large single-molecule fluorescence enhancements produced by a bowtie nanoantenna, Nature Photonics. 3 (2009) 654–657. https://doi.org/https://doi.org/10.1038/nphoton.2009.187.
54. T. Pinheiro, A.C. Marques, P. Carvalho, R. Martins, E. Fortunato, Paper Microfluidics and Tailored Gold Nanoparticles for Nonenzymatic, Colorimetric Multiplex Biomarker Detection, ACS Applied Materials & Interfaces. 13 (2021) 3576–3590. https://doi.org/https://doi.org/10.1021/ACSAMI.0C19089.
55. F. Wang, N. Na, J. Ouyang, A catalytic—regulated gold nanorods etching process as a receptor with multiple readouts for protein detection, Sensors and Actuators B: Chemical. 318 (2020) 128215. https://doi.org/https://doi.org/10.1016/j.snb.2020.128215.
56. A. Ameen, L.P. Hackett, S. Seo, F.K. Dar, M.R. Gartia, L.L. Goddard, G.L. Liu, Plasmonic Sensing of Oncoproteins without Resonance Shift Using 3D Periodic Nanocavity in Nanocup Arrays, Advanced Optical Materials. 5 (2017) 1601051. https://doi.org/https://doi.org/10.1002/adom.201601051.
57. A. Ameen, M.R. Gartia, A. Hsiao, T.-W. Chang, Z. Xu, G.L. Liu, Ultra-Sensitive Colorimetric Plasmonic Sensing and Microfluidics for Biofluid Diagnostics Using Nanohole Array, Journal of Nanomaterials. 2015 (2015) 1–21. https://doi.org/https://doi.org/10.1155/2015/460895.
58. T.-W. Chang, X. Wang, A. Hsiao, Z. Xu, G. Lin, R. Gartia, X. Liu, L. Liu, Bifunctional Nano Lycurgus Cup Array Plasmonic Sensor for Colorimetric Sensing and Surface-Enhanced Raman Spectroscopy, (2015). https://doi.org/https://doi.org/10.1002/adom.201500092.
59. S.K. Misra, K. Dighe, A.S. Schwartz-Duval, Z. Shang, L.T. Labriola, D. Pan, In situ plasmonic generation in functional ionic-gold-nanogel scaffold for rapid quantitative bio-sensing, Biosensors and Bioelectronics. 120 (2018) 77–84. https://doi.org/https://doi.org/10.1016/j.bios.2018.08.019.

60. S.K. Vashist, E. Marion Schneider, R. Zengerle, F. von Stetten, J.H.T. Luong, Graphene-based rapid and highly-sensitive immunoassay for C-reactive protein using a smartphone-based colorimetric reader, Biosensors and Bioelectronics. 66 (2015) 169–176. https://doi.org/10.1016/j.bios.2014.11.017.
61. O. Hosu, A. Ravalli, G.M. lo Piccolo, C. Cristea, R. Sandulescu, G. Marrazza, Smartphone-based immunosensor for CA125 detection, Talanta. 166 (2017) 234–240. https://doi.org/10.1016/j.talanta.2017.01.073.
62. L. Zheng, P. Qi, D. Zhang, A simple, rapid and cost-effective colorimetric assay based on the 4-mercaptophenylboronic acid functionalized silver nanoparticles for bacteria monitoring, Sensors and Actuators, B: Chemical. 260 (2018) 983–989. https://doi.org/https://doi.org/10.1016/j.snb.2018.01.115.
63. K.L. Lee, M.L. You, C.H. Tsai, E.H. Lin, S.Y. Hsieh, M.H. Ho, J.C. Hsu, P.K. Wei, Nanoplasmonic biochips for rapid label-free detection of imidacloprid pesticides with a smartphone, Biosensors and Bioelectronics. 75 (2016) 88–95. https://doi.org/https://doi.org/10.1016/j.bios.2015.08.010.
64. H. Guner, E. Ozgur, G. Kokturk, M. Celik, E. Esen, A.E. Topal, S. Ayas, Y. Uludag, C. Elbuken, A. Dana, A smartphone based surface plasmon resonance imaging (SPRi) platform for on-site biodetection, Sensors and Actuators, B: Chemical. 239 (2017) 571–577. https://doi.org/https://doi.org/10.1016/j.snb.2016.08.061.
65. W. il Lee, S. Shrivastava, L.T. Duy, B. Yeong Kim, Y.M. Son, N.E. Lee, A smartphone imaging-based label-free and dual-wavelength fluorescent biosensor with high sensitivity and accuracy, Biosensors and Bioelectronics. 94 (2017) 643–650. https://doi.org/10.1016/j.bios.2017.03.061.
66. J. Bian, X. Xing, S. Zhou, Z. Man, Z. Lu, W. Zhang, Patterned plasmonic gradient for high-precision biosensing using a smartphone reader, Nanoscale. 11 (2019) 12471–12476. https://doi.org/https://doi.org/10.1039/c9nr00455f.
67. Y. Lu, Y. Lin, Z. Zheng, X. Tang, J. Lin, X. Liu, M. Liu, G. Chen, S. Qiu, T. Zhou, Y. Lin, S. Feng, Label free hepatitis B detection based on serum derivative surface enhanced Raman spectroscopy combined with multivariate analysis, Biomedical Optics Express. 9 (2018) 4755. https://doi.org/https://doi.org/10.1364/BOE.9.004755.
68. M.P. Peng, W. Ma, Y.T. Long, Alcohol Dehydrogenase-Catalyzed Gold Nanoparticle Seed-Mediated Growth Allows Reliable Detection of Disease Biomarkers with the Naked Eye, Analytical Chemistry. 87 (2015) 5891–5896. https://doi.org/https://doi.org/10.1021/acs.analchem.5b00287.
69. P. Valentini, P.P. Pompa, A universal polymerase chain reaction developer, Angewandte Chemie - International Edition. 55 (2016) 2157–2160. https://doi.org/https://doi.org/10.1002/anie.201511010.
70. X. Fu, Z. Cheng, J. Yu, P. Choo, L. Chen, J. Choo, A SERS-based lateral flow assay biosensor for highly sensitive detection of HIV-1 DNA, Biosensors and Bioelectronics. 78 (2016) 530–537. https://doi.org/https://doi.org/10.1016/j.bios.2015.11.099.
71. T.T. Tsai, C.Y. Huang, C.A. Chen, S.W. Shen, M.C. Wang, C.M. Cheng, C.F. Chen, Diagnosis of Tuberculosis Using Colorimetric Gold Nanoparticles on a Paper-Based Analytical Device, ACS Sensors. 2 (2017) 1345–1354. https://doi.org/https://doi.org/10.1021/acssensors.7b00450.
72. A.C. Crawford, L.B. Laurentius, T.S. Mulvihill, J.H. Granger, J.S. Spencer, D. Chatterjee, K.E. Hanson, M.D. Porter, Detection of the tuberculosis antigenic marker mannose-capped lipoarabinomannan in pretreated serum by surface-enhanced Raman scattering, Analyst. 142 (2017) 186–196. https://doi.org/https://doi.org/10.1039/C6AN02110G.

73. A. Ahmadivand, B. Gerislioglu, Z. Ramezani, A. Kaushik, P. Manickam, S.A. Ghoreishi, Functionalized terahertz plasmonic metasensors: Femtomolar-level detection of SARS-CoV-2 spike proteins, Biosensors and Bioelectronics. 177 (2021) 112971. https://doi.org/https://doi.org/10.1016/j.bios.2021.112971.
74. P. Moitra, M. Alafeef, K. Dighe, M.B. Frieman, D. Pan, Selective Naked-Eye Detection of SARS-CoV-2 Mediated by N Gene Targeted Antisense Oligonucleotide Capped Plasmonic Nanoparticles, ACS Nano. 14 (2020) 7617–7627. https://doi.org/https://doi.org/10.1021/acsnano.0c03822.
75. L. Zhang, J. Wang, J. Zhang, Y. Liu, L. Wu, J. Shen, Y. Zhang, Y. Hu, Q. Fan, W. Huang, L. Wang, Individual Au-Nanocube Based Plasmonic Nanoprobe for Cancer Relevant MicroRNA Biomarker Detection, ACS Sensors. 2 (2017) 1435–1440. https://doi.org/https://doi.org/10.1021/acssensors.7b00322.
76. Y. Tian, L. Zhang, J. Shen, L. Wu, H. He, D.-L. Ma, C.-H. Leung, W. Wu, Q. Fan, W. Huang, L. Wang, An Individual Nanocube-Based Plasmonic Biosensor for Real-Time Monitoring the Structural Switch of the Telomeric G-Quadruplex, Small. 12 (2016) 2913–2920. https://doi.org/https://doi.org/10.1002/smll.201600041.
77. J. Tang, P. Xiong, Y. Cheng, Y. Chen, S. Peng, Z.-Q. Zhu, Enzymatic oxydate-triggered AgNPs etching: A novel signal-on photoelectrochemical immunosensing platform based on Ag@AgCl nanocubes loaded RGO plasmonic heterostructure, Biosensors and Bioelectronics. 130 (2019) 125–131. https://doi.org/https://doi.org/10.1016/j.bios.2019.01.014.
78. D. Zhang, Y. Sun, Q. Wu, P. Ma, H. Zhang, Y. Wang, D. Song, Enhancing sensitivity of surface plasmon resonance biosensor by Ag nanocubes/chitosan composite for the detection of mouse IgG, Talanta. 146 (2016) 364–368. https://doi.org/https://doi.org/10.1016/j.talanta.2015.08.050.
79. C. Zhu, X. Wang, X. Shi, F. Yang, G. Meng, Q. Xiong, Y. Ke, H. Wang, Y. Lu, N. Wu, Detection of Dithiocarbamate Pesticides with a Spongelike Surface-Enhanced Raman Scattering Substrate Made of Reduced Graphene Oxide-Wrapped Silver Nanocubes, ACS Applied Materials & Interfaces. 9 (2017) 39618–39625. https://doi.org/https://doi.org/10.1021/acsami.7b13479.
80. S. Mariani, S. Scarano, J. Spadavecchia, M. Minunni, A reusable optical biosensor for the ultrasensitive and selective detection of unamplified human genomic DNA with gold nanostars, Biosensors and Bioelectronics. 74 (2015) 981–988. https://doi.org/https://doi.org/10.1016/j.bios.2015.07.071.
81. M. Reyes, M. Piotrowski, S.K. Ang, J. Chan, S. He, J.J.H. Chu, J.C.Y. Kah, Exploiting the Anti-Aggregation of Gold Nanostars for Rapid Detection of Hand, Foot, and Mouth Disease Causing Enterovirus 71 Using Surface-Enhanced Raman Spectroscopy, Analytical Chemistry. 89 (2017) 5373–5381. https://doi.org/https://doi.org/10.1021/acs.analchem.7b00066.
82. S.R. Ahmed, É. Nagy, S. Neethirajan, Self-assembled star-shaped chiroplasmonic gold nanoparticles for an ultrasensitive chiro-immunosensor for viruses, RSC Advances. 7 (2017) 40849–40857. https://doi.org/https://doi.org/10.1039/C7RA07175B.
83. M. Sánchez-Purrà, M. Carré-Camps, H. de Puig, I. Bosch, L. Gehrke, K. Hamad-Schifferli, Surface-Enhanced Raman Spectroscopy-Based Sandwich Immunoassays for Multiplexed Detection of Zika and Dengue Viral Biomarkers, ACS Infectious Diseases. 3 (2017) 767–776. https://doi.org/https://doi.org/10.1021/acsinfecdis.7b00110.
84. W. Wang, L. Zhang, L. Li, Y. Tian, A Single Nanoprobe for Ratiometric Imaging and Biosensing of Hypochlorite and Glutathione in Live Cells Using Surface-Enhanced Raman Scattering, Analytical Chemistry. 88 (2016) 9518–9523. https://doi.org/https://doi.org/10.1021/acs.analchem.6b02081.

85. S. Park, X. Xiao, J. Min, C. Mun, H.S. Jung, V. Giannini, R. Weissleder, S.A. Maier, H. Im, D. Kim, Self-Assembly of Nanoparticle-Spiked Pillar Arrays for Plasmonic Biosensing, Advanced Functional Materials. 29 (2019) 1904257. https://doi.org/https://doi.org/10.1002/adfm.201904257.
86. W. Sun, S. Yuan, H. Huang, N. Liu, Y. Tan, A label-free biosensor based on localized surface plasmon resonance for diagnosis of tuberculosis, Journal of Microbiological Methods. 142 (2017) 41–45. https://doi.org/https://doi.org/10.1016/j.mimet.2017.09.007.
87. A. Tadimety, Y. Zhang, K.M. Kready, T.J. Palinski, G.J. Tsongalis, J.X.J. Zhang, Design of peptide nucleic acid probes on plasmonic gold nanorods for detection of circulating tumor DNA point mutations, Biosensors and Bioelectronics. 130 (2019) 236–244. https://doi.org/https://doi.org/10.1016/j.bios.2019.01.045.
88. F. Zang, Z. Su, L. Zhou, K. Konduru, G. Kaplan, S.Y. Chou, Ultrasensitive Ebola Virus Antigen Sensing via 3D Nanoantenna Arrays, Advanced Materials. 31 (2019) 1902331. https://doi.org/https://doi.org/10.1002/adma.201902331.
89. C.M. Das, Y. Guo, G. Yang, L. Kang, G. Xu, H.P. Ho, K.T. Yong, Gold Nanorod Assisted Enhanced Plasmonic Detection Scheme of COVID-19 SARS-CoV-2 Spike Protein, Advanced Theory and Simulations. 3 (2020) 1–8. https://doi.org/https://doi.org/10.1002/adts.202000185.
90. P.M. Kosaka, V. Pini, M. Calleja, J. Tamayo, Ultrasensitive detection of HIV-1 p24 antigen by a hybrid nanomechanical-optoplasmonic platform with potential for detecting HIV-1 at first week after infection, PLOS ONE. 12 (2017) e0171899. https://doi.org/https://doi.org/10.1371/journal.pone.0171899.
91. J. Kim, S.Y. Oh, S. Shukla, S.B. Hong, N.S. Heo, Vivek.K. Bajpai, H.S. Chun, C.-H. Jo, B.G. Choi, Y.S. Huh, Y.-K. Han, Heteroassembled gold nanoparticles with sandwich-immunoassay LSPR chip format for rapid and sensitive detection of hepatitis B virus surface antigen (HBsAg), Biosensors and Bioelectronics. 107 (2018) 118–122. https://doi.org/10.1016/j.bios.2018.02.019.
92. R. Funari, K.-Y. Chu, A.Q. Shen, Detection of antibodies against SARS-CoV-2 spike protein by gold nanospikes in an opto-microfluidic chip, Biosensors and Bioelectronics. 169 (2020) 112578. https://doi.org/https://doi.org/10.1016/j.bios.2020.112578.
93. F. Zou, X. Wang, F. Qi, K. Koh, J. Lee, H. Zhou, H. Chen, Magneto-plamonic nanoparticles enhanced surface plasmon resonance TB sensor based on recombinant gold binding antibody, Sensors and Actuators B: Chemical. 250 (2017) 356–363. https://doi.org/https://doi.org/10.1016/j.snb.2017.04.162.
94. N. Fakhri, S. Abarghoei, M. Dadmehr, M. Hosseini, H. Sabahi, M.R. Ganjali, Paper based colorimetric detection of miRNA-21 using Ag/Pt nanoclusters, Spectrochimica Acta Part A: Molecular and Biomolecular Spectroscopy. 227 (2020) 117529. https://doi.org/https://doi.org/10.1016/j.saa.2019.117529.
95. A. Minopoli, B. della Ventura, B. Lenyk, F. Gentile, J.A. Tanner, A. Offenhäusser, D. Mayer, R. Velotta, Ultrasensitive antibody-aptamer plasmonic biosensor for malaria biomarker detection in whole blood, Nature Communications. 11 (2020) 6134. https://doi.org/10.1038/s41467-020-19755-0.
96. M.R. Gonçalves, Plasmonic nanoparticles: Fabrication, simulation and experiments, Journal of Physics D: Applied Physics. 47 (2014). https://doi.org/10.1088/0022-3727/47/21/213001.
97. M. Faraday, LIX. Experimental relations of gold (and other metals) to light.—The bakerian lecture , The London, Edinburgh, and Dublin Philosophical Magazine and Journal of Science. 14 (1857) 512–539. https://doi.org/10.1080/14786445708642424.
98. S. Yu, H. Ammari, Plasmonic interaction between nanospheres, SIAM Review. 60 (2018) 356–385. https://doi.org/https://doi.org/10.1137/17M1115319.

99. J. Turkevich, P.C. Stevenson, J. Hillier, A study of the nucleation and growth processes in the synthesis of colloidal gold, Discuss Faraday Soc. 11 (1951) 55–75. https://doi.org/https://doi.org/10.1039/DF9511100055.
100. M. Brust, M. Walker, D. Bethell, D.J. Schiffrin, R. Whyman, Synthesis of thiol-derivatised gold nanoparticles in a two-phase Liquid–Liquid system, J. Chem. Soc., Chem. Commun. (1994) 801–802. https://doi.org/10.1039/C39940000801.
101. P. Moitra, M. Alafeef, M. Alafeef, M. Alafeef, K. Dighe, M.B. Frieman, D. Pan, D. Pan, D. Pan, Selective Naked-Eye Detection of SARS-CoV-2 Mediated by N Gene Targeted Antisense Oligonucleotide Capped Plasmonic Nanoparticles, ACS Nano. 14 (2020) 7617–7627. https://doi.org/https://doi.org/10.1021/acsnano.0c03822.
102. J. Kim, S.Y. Oh, S. Shukla, S.B. Hong, N.S. Heo, V.K. Bajpai, H.S. Chun, C.H. Jo, B.G. Choi, Y.S. Huh, Y.K. Han, Heteroassembled gold nanoparticles with sandwich-immunoassay LSPR chip format for rapid and sensitive detection of hepatitis B virus surface antigen (HBsAg), Biosensors and Bioelectronics. 107 (2018) 118–122. https://doi.org/https://doi.org/10.1016/j.bios.2018.02.019.
103. N.G. Bastús, J. Comenge, V. Puntes, Kinetically controlled seeded growth synthesis of citrate-stabilized gold nanoparticles of up to 200 nm: Size focusing versus ostwald ripening, Langmuir. 27 (2011) 11098–11105. https://doi.org/https://doi.org/10.1021/la201938u.
104. N. Leopold, B. Lendl, A new method for fast preparation of highly surface-enhanced raman scattering (SERS) active silver colloids at room temperature by reduction of silver nitrate with hydroxylamine hydrochloride, Journal of Physical Chemistry B. 107 (2003) 5723–5727. https://doi.org/https://doi.org/10.1021/jp027460u.
105. R. Elghanian, J.J. Storhoff, R.C. Mucic, R.L. Letsinger, C.A. Mirkin, Selective colorimetric detection of polynucleotides based on the distance-dependent optical properties of gold nanoparticles, Science (1979). 277 (1997) 1078–1081. https://doi.org/https://doi.org/10.1126/science.277.5329.1078.
106. T. Wu, Y. Cao, Y. Zhang, Z. Zheng, J. Li, H. Li, Entropy-Driven DNA Amplification Networks Coupled with Hollow Porous Au–Ag Nanospheres for Split-Type Plasmonic Photothermal Biosensing, ACS Applied Nano Materials. 5 (2022) 537–545. https://doi.org/https://doi.org/10.1021/acsanm.1c03365.
107. Y. Jiang, M. Shi, Y. Liu, S. Wan, C. Cui, L. Zhang, W. Tan, Aptamer/AuNP Biosensor for Colorimetric Profiling of Exosomal Proteins, Angewandte Chemie. 129 (2017) 12078–12082. https://doi.org/https://doi.org/10.1002/ange.201703807.
108. S. Rostami, A. Mehdinia, R. Niroumand, A. Jabbari, Enhanced LSPR performance of graphene nanoribbons-silver nanoparticles hybrid as a colorimetric sensor for sequential detection of dopamine and glutathione, Analytica Chimica Acta. 1120 (2020) 11–23. https://doi.org/https://doi.org/10.1016/j.aca.2020.04.060.
109. D. Han, Y. Yan, X. Bian, J. Wang, M. Zhao, X. Duan, L. Kong, W. Cheng, S. Ding, A novel electrochemical biosensor based on peptidoglycan and platinum-nickel-copper nano-cube for rapid detection of Gram-positive bacteria, Microchimica Acta. 187 (2020) 607. https://doi.org/https://doi.org/10.1007/s00604-020-04581-4.
110. H. bin Jeon, P.V. Tsalu, J.W. Ha, Shape Effect on the Refractive Index Sensitivity at Localized Surface Plasmon Resonance Inflection Points of Single Gold Nanocubes with Vertices, Scientific Reports. 9 (2019) 13635. https://doi.org/10.1038/s41598-019-50032-3.
111. J.-S. Ye, C.-W. Chen, C.-L. Lee, Pd nanocube as non-enzymatic glucose sensor, Sensors and Actuators B: Chemical. 208 (2015) 569–574. https://doi.org/https://doi.org/10.1016/j.snb.2014.11.091.
112. P. Yang, L. Wang, Q. Wu, Z. Chen, X. Lin, A method for determination of glucose by an amperometric bienzyme biosensor based on silver nanocubes modified Au electrode, Sensors and

Actuators B: Chemical. 194 (2014) 71–78. https://doi.org/https://doi.org/10.1016/j.snb.2013.12.074.
113. J.C. Claussen, A.D. Franklin, A. ul Haque, D.M. Porterfield, T.S. Fisher, Electrochemical Biosensor of Nanocube-Augmented Carbon Nanotube Networks, ACS Nano. 3 (2009) 37–44. https://doi.org/10.1021/nn800682m.
114. J. Ren, W. Shi, K. Li, Z. Ma, Ultrasensitive platinum nanocubes enhanced amperometric glucose biosensor based on chitosan and nafion film, Sensors and Actuators B: Chemical. 163 (2012) 115–120. https://doi.org/https://doi.org/10.1016/j.snb.2012.01.017.
115. J. Yang, W.-D. Zhang, S. Gunasekaran, An amperometric non-enzymatic glucose sensor by electrodepositing copper nanocubes onto vertically well-aligned multi-walled carbon nanotube arrays, Biosensors and Bioelectronics. 26 (2010) 279–284. https://doi.org/https://doi.org/10.1016/j.bios.2010.06.014.
116. A.W. Powell, D.M. Coles, R.A. Taylor, A.A.R. Watt, H.E. Assender, J.M. Smith, Plasmonic Gas Sensing Using Nanocube Patch Antennas, Advanced Optical Materials. 4 (2016) 634–642. https://doi.org/https://doi.org/10.1002/adom.201500602.
117. C. Noguez, Surface Plasmons on Metal Nanoparticles: The Influence of Shape and Physical Environment, The Journal of Physical Chemistry C. 111 (2007) 3806–3819. https://doi.org/https://doi.org/10.1021/jp066539m.
118. S.E. Skrabalak, L. Au, X. Li, Y. Xia, Facile synthesis of Ag nanocubes and Au nanocages, Nature Protocols. 2 (2007) 2182–2190. https://doi.org/https://doi.org/10.1038/nprot.2007.326.
119. A.R. Siekkinen, J.M. McLellan, J. Chen, Y. Xia, Rapid synthesis of small silver nanocubes by mediating polyol reduction with a trace amount of sodium sulfide or sodium hydrosulfide, Chemical Physics Letters. 432 (2006) 491–496. https://doi.org/https://doi.org/10.1016/j.cplett.2006.10.095.
120. Y. Sun, Y. Xia, Shape-Controlled Synthesis of Gold and Silver Nanoparticles., ChemInform. 34 (2003) 2176–2180. https://doi.org/https://doi.org/10.1002/chin.200310226.
121. M. Kim, S.M. Ko, C. Lee, J. Son, J. Kim, J.-M. Kim, J.-M. Nam, Hierarchic Interfacial Nanocube Assembly for Sensitive, Selective, and Quantitative DNA Detection with Surface-Enhanced Raman Scattering, Analytical Chemistry. 91 (2019) 10467–10476. https://doi.org/https://doi.org/10.1021/acs.analchem.9b01272.
122. J. Li, J. Wang, Y.S. Grewal, C.B. Howard, L.J. Raftery, S. Mahler, Y. Wang, M. Trau, Multiplexed SERS Detection of Soluble Cancer Protein Biomarkers with Gold–Silver Alloy Nanoboxes and Nanoyeast Single-Chain Variable Fragments, Analytical Chemistry. 90 (2018) 10377–10384. https://doi.org/https://doi.org/10.1021/acs.analchem.8b02216.
123. K.-X. Xie, L.-T. Xu, Y.-Y. Zhai, Z.-C. Wang, M. Chen, X.-H. Pan, S.-H. Cao, Y.-Q. Li, The synergistic enhancement of silver nanocubes and graphene oxide on surface plasmon-coupled emission, Talanta. 195 (2019) 752–756. https://doi.org/https://doi.org/10.1016/j.talanta.2018.11.112.
124. O.J. Achadu, F. Abe, T. Suzuki, E.Y. Park, Molybdenum Trioxide Nanocubes Aligned on a Graphene Oxide Substrate for the Detection of Norovirus by Surface-Enhanced Raman Scattering, ACS Applied Materials & Interfaces. 12 (2020) 43522–43534. https://doi.org/https://doi.org/10.1021/acsami.0c14729.
125. O.J. Achadu, F. Abe, F. Hossain, F. Nasrin, M. Yamazaki, T. Suzuki, E.Y. Park, Sulfur-doped carbon dots@polydopamine-functionalized magnetic silver nanocubes for dual-modality detection of norovirus, Biosensors and Bioelectronics. 193 (2021) 113540. https://doi.org/https://doi.org/10.1016/j.bios.2021.113540.
126. Y. Liu, N. Lyu, V.K. Rajendran, J. Piper, A. Rodger, Y. Wang, Sensitive and Direct DNA Mutation Detection by Surface-Enhanced Raman Spectroscopy Using Rational Designed and

Tunable Plasmonic Nanostructures, Analytical Chemistry. 92 (2020) 5708–5716. https://doi.org/https://doi.org/10.1021/acs.analchem.9b04183.
127. S. Chatterjee, A.B. Ringane, A. Arya, G.M. Das, V.R. Dantham, R. Laha, S. Hussian, A high-yield, one-step synthesis of surfactant-free gold nanostars and numerical study for single-molecule SERS application, Journal of Nanoparticle Research. 18 (2016) 242. https://doi.org/https://doi.org/10.1007/s11051-016-3557-0.
128. T. Lee, G.H. Kim, S.M. Kim, K. Hong, Y. Kim, C. Park, H. Sohn, J. Min, Label-free localized surface plasmon resonance biosensor composed of multi-functional DNA 3 way junction on hollow Au spike-like nanoparticles (HAuSN) for avian influenza virus detection, Colloids and Surfaces B: Biointerfaces. 182 (2019) 110341. https://doi.org/https://doi.org/10.1016/j.colsurfb.2019.06.070.
129. Y.H. Ngo, D. Li, G.P. Simon, G. Garnier, Gold nanoparticle-paper as a three-dimensional surface enhanced raman scattering substrate, Langmuir. 28 (2012) 8782–8790. https://doi.org/https://doi.org/10.1021/la3012734.
130. P.M. Mendes, S. Jacke, K. Critchley, J. Plaza, Y. Chen, K. Nikitin, R.E. Palmer, J.A. Preece, S.D. Evans, D. Fitzmaurice, Gold nanoparticle patterning of silicon wafers using chemical e-beam lithography, Langmuir. 20 (2004) 3766–3768. https://doi.org/https://doi.org/10.1021/la049803g.
131. M.K. Corbierre, J. Beerens, R.B. Lennox, Gold nanoparticles generated by electron beam lithography of gold(I)-thiolate thin films, Chemistry of Materials. 17 (2005) 5774–5779. https://doi.org/https://doi.org/10.1021/cm051085b.
132. M. Kolíbal, M. Konečný, F. Ligmajer, D. Škoda, T. Vystavěl, J. Zlámal, P. Varga, T. Šikola, Guided assembly of gold colloidal nanoparticles on silicon substrates prepatterned by charged particle beams, ACS Nano. 6 (2012) 10098–10106. https://doi.org/https://doi.org/10.1021/nn3038226.
133. J. Spadavecchia, P. Prete, N. Lovergine, L. Tapfer, R. Rella, Au nanoparticles prepared by physical method on Si and sapphire substrates for biosensor applications, Journal of Physical Chemistry B. 109 (2005) 17347–17349. https://doi.org/https://doi.org/10.1021/jp053194j.
134. O. Bibikova, J. Haas, A.I. López-Lorente, A. Popov, M. Kinnunen, I. Meglinski, B. Mizaikoff, Towards enhanced optical sensor performance: SEIRA and SERS with plasmonic nanostars, Analyst. 142 (2017) 951–958. https://doi.org/https://doi.org/10.1039/c6an02596j.
135. J. Shen, Y. Li, H. Gu, F. Xia, X. Zuo, Recent development of sandwich assay based on the nanobiotechnologies for proteins, nucleic acids, small molecules, and ions, Chemical Reviews. 114 (2014) 7631–7677. https://doi.org/https://doi.org/10.1021/cr300248x.
136. X. Pei, B. Zhang, J. Tang, B. Liu, W. Lai, D. Tang, Sandwich-type immunosensors and immunoassays exploiting nanostructure labels: A review, Analytica Chimica Acta. 758 (2013) 1–18. https://doi.org/https://doi.org/10.1016/j.aca.2012.10.060.
137. C.M. Das, Y. Guo, G. Yang, L. Kang, G. Xu, H.P. Ho, K.T. Yong, Gold Nanorod Assisted Enhanced Plasmonic Detection Scheme of COVID-19 SARS-CoV-2 Spike Protein, Advanced Theory and Simulations. 3 (2020). https://doi.org/10.1002/adts.202000185.
138. W. Lee, S.M. Shaban, D.G. Pyun, D.-H. Kim, Solid-phase colorimetric apta-biosensor for thrombin detection, Thin Solid Films. 686 (2019) 137428. https://doi.org/https://doi.org/10.1016/j.tsf.2019.137428.
139. F. Zou, X. Wang, F. Qi, K. Koh, J. Lee, H. Zhou, H. Chen, Magneto-plamonic nanoparticles enhanced surface plasmon resonance TB sensor based on recombinant gold binding antibody, Sensors and Actuators, B: Chemical. 250 (2017) 356–363. https://doi.org/https://doi.org/10.1016/j.snb.2017.04.162.

140. B. Zhang, R.B. Kumar, H. Dai, B.J. Feldman, A plasmonic chip for biomarker discovery and diagnosis of type 1 diabetes, Nature Medicine. 20 (2014) 948–953. https://doi.org/https://doi.org/10.1038/nm.3619.
141. X. Li, T. Kuznetsova, N. Cauwenberghs, M. Wheeler, H. Maecker, J.C. Wu, F. Haddad, H. Dai, Autoantibody profiling on a plasmonic nano-gold chip for the early detection of hypertensive, Proc Natl Acad Sci U S A. 114 (2017) 7089–7094. https://doi.org/https://doi.org/10.1073/pnas.1621457114.
142. J.R. Mejía-Salazar, O.N. Oliveira, Plasmonic Biosensing, Chemical Reviews. 118 (2018) 10617–10625. https://doi.org/https://doi.org/10.1021/acs.chemrev.8b00359.
143. B. Špačková, P. Wrobel, M. Bocková, J. Homola, Optical Biosensors Based on Plasmonic Nanostructures: A Review, Proceedings of the IEEE. 104 (2016) 2380–2408. https://doi.org/https://doi.org/10.1109/JPROC.2016.2624340.
144. A. Mühlig, T. Bocklitz, I. Labugger, S. Dees, S. Henk, E. Richter, S. Andres, M. Merker, S. Stöckel, K. Weber, D. Cialla-May, J. Popp, LOC-SERS: A promising closed system for the identification of mycobacteria, Analytical Chemistry. 88 (2016) 7998–8004. https://doi.org/https://doi.org/10.1021/acs.analchem.6b01152.
145. L.W. Yap, H. Chen, Y. Gao, K. Petkovic, Y. Liang, K.J. Si, H. Wang, Z. Tang, Y. Zhu, W. Cheng, Bifunctional plasmonic-magnetic particles for an enhanced microfluidic SERS immunoassay, Nanoscale. 9 (2017) 7822–7829. https://doi.org/https://doi.org/10.1039/c7nr01511a.
146. J. Zhou, F. Tao, J. Zhu, S. Lin, Z. Wang, X. Wang, J.Y. Ou, Y. Li, Q.H. Liu, Portable tumor biosensing of serum by plasmonic biochips in combination with nanoimprint and microfluidics, Nanophotonics. 8 (2019) 307–316. https://doi.org/https://doi.org/10.1515/nanoph-2018-0173.
147. A. Vázquez-Guardado, S. Barkam, M. Peppler, A. Biswas, W. Dennis, S. Das, S. Seal, D. Chanda, Enzyme-Free Plasmonic Biosensor for Direct Detection of Neurotransmitter Dopamine from Whole Blood, Nano Letters. 19 (2019) 449–454. https://doi.org/https://doi.org/10.1021/acs.nanolett.8b04253.
148. F. Inci, Y. Saylan, A.M. Kojouri, M.G. Ogut, A. Denizli, U. Demirci, A disposable microfluidic-integrated hand-held plasmonic platform for protein detection, Applied Materials Today. 18 (2020). https://doi.org/10.1016/j.apmt.2019.100478.
149. Z. Geng, Q. Kan, J. Yuan, H. Chen, A route to low-cost nanoplasmonic biosensor integrated with optofluidic-portable platform, Sensors and Actuators, B: Chemical. 195 (2014) 682–691. https://doi.org/https://doi.org/10.1016/j.snb.2014.01.110.
150. M. Soler, A. Belushkin, A. Cavallini, C. Kebbi-Beghdadi, G. Greub, H. Altug, Multiplexed nanoplasmonic biosensor for one-step simultaneous detection of Chlamydia trachomatis and Neisseria gonorrhoeae in urine, Biosensors and Bioelectronics. 94 (2017) 560–567. https://doi.org/https://doi.org/10.1016/j.bios.2017.03.047.
151. E.C. Peláez, M.C. Estevez, A. Mongui, M.-C. Menéndez, C. Toro, O.L. Herrera-Sandoval, J. Robledo, M.J. García, P. del Portillo, L.M. Lechuga, Detection and Quantification of HspX Antigen in Sputum Samples Using Plasmonic Biosensing: Toward a Real Point-of-Care (POC) for Tuberculosis Diagnosis, ACS Infectious Diseases. 6 (2020) 1110–1120. https://doi.org/https://doi.org/10.1021/acsinfecdis.9b00502.
152. R. Funari, K.Y. Chu, A.Q. Shen, Detection of antibodies against SARS-CoV-2 spike protein by gold nanospikes in an opto-microfluidic chip, Biosensors and Bioelectronics. 169 (2020). https://doi.org/10.1016/j.bios.2020.112578.
153. A.W. Martinez, S.T. Phillips, M.J. Butte, G.M. Whitesides, Patterned Paper as a Platform for Inexpensive, Low-Volume, Portable Bioassays, Angewandte Chemie. 119 (2007) 1340–1342. https://doi.org/https://doi.org/10.1002/ange.200603817.

154. E. Carrilho, A.W. Martinez, G.M. Whitesides, Understanding wax printing: A simple micropatterning process for paper-based microfluidics, Analytical Chemistry. 81 (2009) 7091–7095. https://doi.org/https://doi.org/10.1021/ac901071p.
155. K. Abe, K. Kotera, K. Suzuki, D. Citterio, Inkjet-printed paperfluidic immuno-chemical sensing device, Analytical and Bioanalytical Chemistry. 398 (2010) 885–893. https://doi.org/https://doi.org/10.1007/s00216-010-4011-2.
156. A. Savolainen, Y. Zhang, D. Rochefort, U. Holopainen, T. Erho, J. Virtanen, M. Smolander, Printing of polymer microcapsules for enzyme immobilization on paper substrate, Biomacromolecules. 12 (2011) 2008–2015. https://doi.org/https://doi.org/10.1021/bm2003434.
157. L. Ouyang, C. Wang, F. Du, T. Zheng, H. Liang, Electrochromatographic separations of multi-component metal complexes on a microfluidic paper-based device with a simplified photolithography, RSC Advances. 4 (2014) 1093–1101. https://doi.org/https://doi.org/10.1039/c3ra43625j.
158. C.L. Sones, I.N. Katis, P.J.W. He, B. Mills, M.F. Namiq, P. Shardlow, M. Ibsen, R.W. Eason, Laser-induced photo-polymerisation for creation of paper-based fluidic devices, Lab on a Chip. 14 (2014) 4567–4574. https://doi.org/https://doi.org/10.1039/c4lc00850b.
159. N. Fakhri, S. Abarghoei, M. Dadmehr, M. Hosseini, H. Sabahi, M.R. Ganjali, Paper based colorimetric detection of miRNA-21 using Ag/Pt nanoclusters, Spectrochimica Acta - Part A: Molecular and Biomolecular Spectroscopy. 227 (2020). https://doi.org/10.1016/j.saa.2019.117529.
160. M. Srisa-Art, K.E. Boehle, B.J. Geiss, C.S. Henry, Highly Sensitive Detection of Salmonella typhimurium Using a Colorimetric Paper-Based Analytical Device Coupled with Immunomagnetic Separation, Analytical Chemistry. 90 (2018) 1035–1043. https://doi.org/https://doi.org/10.1021/acs.analchem.7b04628.
161. S.U. Son, S.B. Seo, S. Jang, J. Choi, J. woo Lim, D.K. Lee, H. Kim, S. Seo, T. Kang, J. Jung, E.K. Lim, Naked-eye detection of pandemic influenza a (pH1N1) virus by polydiacetylene (PDA)-based paper sensor as a point-of-care diagnostic platform, Sensors and Actuators, B: Chemical. 291 (2019) 257–265. https://doi.org/10.1016/j.snb.2019.04.081.
162. H. Wang, L. Yang, S. Chu, B. Liu, Q. Zhang, L. Zou, S. Yu, C. Jiang, Semiquantitative Visual Detection of Lead Ions with a Smartphone via a Colorimetric Paper-Based Analytical Device, Analytical Chemistry. 91 (2019) 9292–9299. https://doi.org/https://doi.org/10.1021/acs.analchem.9b02297.
163. K.N. Han, J.S. Choi, J. Kwon, Gold nanozyme-based paper chip for colorimetric detection of mercury ions, Scientific Reports. 7 (2017). https://doi.org/10.1038/s41598-017-02948-x.
164. A. Alba-Patiño, S.M. Russell, R. de la Rica, Origami-enabled signal amplification for paper-based colorimetric biosensors, Sensors and Actuators, B: Chemical. 273 (2018) 951–954. https://doi.org/https://doi.org/10.1016/j.snb.2018.07.019.
165. M.J. Oliveira, P. Quaresma, M.P. de Almeida, A. Araújo, E. Pereira, E. Fortunato, R. Martins, R. Franco, H. Águas, Office paper decorated with silver nanostars-an alternative cost effective platform for trace analyte detection by SERS, Scientific Reports. 7 (2017). https://doi.org/10.1038/s41598-017-02484-8.
166. S.S.B. Moram, C. Byram, S.N. Shibu, B.M. Chilukamarri, V.R. Soma, Ag/Au Nanoparticle-Loaded Paper-Based Versatile Surface-Enhanced Raman Spectroscopy Substrates for Multiple Explosives Detection, ACS Omega. 3 (2018) 8190–8201. https://doi.org/https://doi.org/10.1021/acsomega.8b01318.
167. S.W. Hu, S. Qiao, J. bin Pan, B. Kang, J.J. Xu, H.Y. Chen, A paper-based SERS test strip for quantitative detection of Mucin-1 in whole blood, Talanta. 179 (2018) 9–14. https://doi.org/10.1016/j.talanta.2017.10.038.

168. M. Lee, K. Oh, H.K. Choi, S.G. Lee, H.J. Youn, H.L. Lee, D.H. Jeong, Subnanomolar Sensitivity of Filter Paper-Based SERS Sensor for Pesticide Detection by Hydrophobicity Change of Paper Surface, ACS Sensors. 3 (2018) 151–159. https://doi.org/https://doi.org/10.1021/acssensors.7b00782.
169. H.T. Chorsi, H.T. Chorsi, J.X.J. Zhang, Using graphene plasmonics to boost biosensor sensitivity, SPIE Newsroom. (2016). https://doi.org/https://doi.org/10.1117/2.1201610.006712.
170. N.A.S. Omar, Y.W. Fen, J. Abdullah, A.R. Sadrolhosseini, Y. Mustapha Kamil, N.I.M. Fauzi, H.S. Hashim, M.A. Mahdi, Quantitative and Selective Surface Plasmon Resonance Response Based on a Reduced Graphene Oxide–Polyamidoamine Nanocomposite for Detection of Dengue Virus E-Proteins, Nanomaterials. 10 (2020) 569. https://doi.org/10.3390/nano10030569.
171. S.U. Son, S.B. Seo, S. Jang, J. Choi, J. Lim, D.K. Lee, H. Kim, S. Seo, T. Kang, J. Jung, E.-K. Lim, Naked-eye detection of pandemic influenza a (pH1N1) virus by polydiacetylene (PDA)-based paper sensor as a point-of-care diagnostic platform, Sensors and Actuators B: Chemical. 291 (2019) 257–265. https://doi.org/https://doi.org/10.1016/j.snb.2019.04.081.
172. T. Riedel, F. Surman, S. Hageneder, O. Pop-Georgievski, C. Noehammer, M. Hofner, E. Brynda, C. Rodriguez-Emmenegger, J. Dostálek, Hepatitis B plasmonic biosensor for the analysis of clinical serum samples, Biosensors and Bioelectronics. 85 (2016) 272–279. https://doi.org/https://doi.org/10.1016/j.bios.2016.05.014.
173. H. T. Chorsi, Y. Zhu, J.X.J. Zhang, Patterned Plasmonic Surfaces—Theory, Fabrication, and Applications in Biosensing, Journal of Microelectromechanical Systems. 26 (2017) 718–739. https://doi.org/https://doi.org/10.1109/JMEMS.2017.2699864.
174. W. Xu, L. Wang, R. Zhang, X. Sun, L. Huang, H. Su, X. Wei, C.-C. Chen, J. Lou, H. Dai, K. Qian, Diagnosis and prognosis of myocardial infarction on a plasmonic chip, Nature Communications. 11 (2020) 1654. https://doi.org/https://doi.org/10.1038/s41467-020-15487-3.
175. B.A. Prabowo, Y.-F. Chang, H.-C. Lai, A. Alom, P. Pal, Y.-Y. Lee, N.-F. Chiu, K. Hatanaka, L.-C. Su, K.-C. Liu, Rapid screening of Mycobacterium tuberculosis complex (MTBC) in clinical samples by a modular portable biosensor, Sensors and Actuators B: Chemical. 254 (2018) 742–748. https://doi.org/https://doi.org/10.1016/j.snb.2017.07.102.
176. N.A.S. Omar, Y.W. Fen, J. Abdullah, Y. Mustapha Kamil, W.M.E.M.M. Daniyal, A.R. Sadrolhosseini, M.A. Mahdi, Sensitive Detection of Dengue Virus Type 2 E-Proteins Signals Using Self-Assembled Monolayers/Reduced Graphene Oxide-PAMAM Dendrimer Thin Film-SPR Optical Sensor, Scientific Reports. 10 (2020) 2374. https://doi.org/10.1038/s41598-020-59388-3.
177. X. Li, T. Kuznetsova, N. Cauwenberghs, M. Wheeler, H. Maecker, J.C. Wu, F. Haddad, H. Dai, Autoantibody profiling on a plasmonic nano-gold chip for the early detection of hypertensive heart disease, Proceedings of the National Academy of Sciences. 114 (2017) 7089–7094. https://doi.org/https://doi.org/10.1073/pnas.1621457114.
178. P.P. Austin Suthanthiraraj, A.K. Sen, Localized surface plasmon resonance (LSPR) biosensor based on thermally annealed silver nanostructures with on-chip blood-plasma separation for the detection of dengue non-structural protein NS1 antigen, Biosensors and Bioelectronics. 132 (2019) 38–46. https://doi.org/10.1016/j.bios.2019.02.036.
179. Z. Geng, Q. Kan, J. Yuan, H. Chen, A route to low-cost nanoplasmonic biosensor integrated with optofluidic-portable platform, Sensors and Actuators B: Chemical. 195 (2014) 682–691. https://doi.org/https://doi.org/10.1016/j.snb.2014.01.110.
180. N.L. Garrett, R. Sekine, M.W.A. Dixon, L. Tilley, K.R. Bambery, B.R. Wood, Bio-sensing with butterfly wings: Naturally occurring nano-structures for SERS-based malaria parasite detection, Physical Chemistry Chemical Physics. 17 (2014) 21164–21168. https://doi.org/https://doi.org/10.1039/c4cp04930f.

181. W. Diao, M. Tang, S. Ding, X. Li, W. Cheng, F. Mo, X. Yan, H. Ma, Y. Yan, Highly sensitive surface plasmon resonance biosensor for the detection of HIV-related DNA based on dynamic and structural DNA nanodevices, Biosensors and Bioelectronics. 100 (2018) 228–234. https://doi.org/https://doi.org/10.1016/j.bios.2017.08.042.
182. M. Trzaskowski, A. Napiórkowska, E. Augustynowicz-Kopeć, T. Ciach, Detection of tuberculosis in patients with the use of portable SPR device, Sensors and Actuators B: Chemical. 260 (2018) 786–792. https://doi.org/https://doi.org/10.1016/j.snb.2017.12.183.
183. P.K. Sharma, J.S. Kumar, V. v. Singh, U. Biswas, S.S. Sarkar, S.I. Alam, P.K. Dash, M. Boopathi, K. Ganesan, R. Jain, Surface plasmon resonance sensing of Ebola virus: a biological threat, Analytical and Bioanalytical Chemistry. 412 (2020) 4101–4112. https://doi.org/10.1007/s00216-020-02641-5.
184. H. Wan, C. Merriman, M.A. Atkinson, C.H. Wasserfall, K.M. Mcgrail, Y. Liang, D. Fu, H. Dai, Proteoliposome-based full-length ZnT8 self-antigen for type 1 diabetes diagnosis on a plasmonic platform, Proceedings of the National Academy of Sciences. 114 (2017) 10196–10201. https://doi.org/https://doi.org/10.1073/pnas.1711169114.
185. A. Belushkin, F. Yesilkoy, J.J. González-López, J.C. Ruiz-Rodríguez, R. Ferrer, A. Fàbrega, H. Altug, Rapid and Digital Detection of Inflammatory Biomarkers Enabled by a Novel Portable Nanoplasmonic Imager, Small. 16 (2020) 1906108. https://doi.org/https://doi.org/10.1002/smll.201906108.
186. K. Leosson, A.S. Ingason, B. Agnarsson, A. Kossoy, S. Olafsson, M.C. Gather, Ultra-thin gold films on transparent polymers, Nanophotonics. 2 (2013) 3–11. https://doi.org/https://doi.org/10.1515/nanoph-2012-0030.
187. T.J. Palinski, A. Tadimety, I. Trase, B.E. Vyhnalek, G.W. Hunter, E. Garmire, J.X.J. Zhang, Vibrant reflective sensors with percolation film Fabry-Pérot nanocavities, Optics Express. 29 (2021) 25000. https://doi.org/https://doi.org/10.1364/oe.432097.
188. V. Krachmalnicoff, E. Castanié, Y. de Wilde, R. Carminati, Fluctuations of the Local Density of States Probe Localized Surface Plasmons on Disordered Metal Films, (2010) 183901–183902. https://doi.org/10.1103/PhysRevLett.105.183901.
189. R. Malureanu, A. Lavrinenko, Ultra-thin films for plasmonics: a technology overview, Nanotechnology Reviews. 4 (2015) 259–275. https://doi.org/10.1515/ntrev-2015-0021.
190. M. Kang, S.G. Park, K.H. Jeong, Repeated Solid-state Dewetting of Thin Gold Films for Nanogap-rich Plasmonic Nanoislands, Scientific Reports. 5 (2015) 1–7. https://doi.org/10.1038/srep14790.
191. S.M. Tabakman, Z. Chen, H.S. Casalongue, H. Wang, H. Dai, A New Approach to Solution-Phase Gold Seeding for SERS Substrates, Small. 7 (2011) 499–505. https://doi.org/10.1002/smll.201001836.
192. X. Sun, H. Li, Gold nanoisland arrays by repeated deposition and post-deposition annealing for surface-enhanced Raman spectroscopy, Nanotechnology. 24 (2013) 355706. https://doi.org/10.1088/0957-4484/24/35/355706.
193. A. Bonyár, I. Csarnovics, M. Veres, L. Himics, A. Csik, J. Kámán, L. Balázs, S. Kökényesi, Investigation of the performance of thermally generated gold nanoislands for LSPR and SERS applications, Sensors and Actuators B: Chemical. 255 (2018) 433–439. https://doi.org/10.1016/J.SNB.2017.08.063.
194. B. Miranda, K.-Y. Chu, P.L. Maffettone, A.Q. Shen, R. Funari, Metal-Enhanced Fluorescence Immunosensor Based on Plasmonic Arrays of Gold Nanoislands on an Etched Glass Substrate, ACS Applied Nano Materials. 3 (2020) 10470–10478. https://doi.org/10.1021/acsanm.0c02388.

195. D. Wang, R. Ji, P. Schaaf, Formation of precise 2D Au particle arrays via thermally induced dewetting on pre-patterned substrates, Beilstein Journal of Nanotechnology. 2 (2011) 318–326. https://doi.org/10.3762/bjnano.2.37.
196. H.T.H. Lin, C.K. Yang, C.C. Lin, A.M.H. Wu, L.A. Wang, N.T. Huang, A large-area nanoplasmonic sensor fabricated by rapid thermal annealing treatment for label-free and multi-point immunoglobulin sensing, Nanomaterials. 7 (2017). https://doi.org/10.3390/nano7050100.
197. W. Xu, L. Wang, R. Zhang, X. Sun, L. Huang, H. Su, X. Wei, C.C. Chen, J. Lou, H. Dai, K. Qian, Diagnosis and prognosis of myocardial infarction on a plasmonic chip, Nat Commun. 11 (2020) 1654. https://doi.org/10.1038/s41467-020-15487-3.
198. R. Zhang, B. Le, W. Xu, K. Guo, X. Sun, H. Su, L. Huang, J. Huang, T. Shen, T. Liao, Y. Liang, J.X.J. Zhang, H. Dai, K. Qian, Magnetic "Squashing" of Circulating Tumor Cells on Plasmonic Substrates for Ultrasensitive NIR Fluorescence Detection, Small Methods. 3 (2019) 1800474. https://doi.org/10.1002/smtd.201800474.
199. S.M. Tabakman, L. Lau, J.T. Robinson, J. Price, S.P. Sherlock, H. Wang, B. Zhang, Z. Chen, S. Tangsombatvisit, J.A. Jarrell, P.J. Utz, H. Dai, Plasmonic substrates for multiplexed protein microarrays with femtomolar sensitivity and broad dynamic range, Nature Communications. 2 (2011) 466. https://doi.org/10.1038/ncomms1477.
200. B. Liu, Y. Li, H. Wan, L. Wang, W. Xu, S. Zhu, Y. Liang, B. Zhang, J. Lou, H. Dai, K. Qian, High Performance, Multiplexed Lung Cancer Biomarker Detection on a Plasmonic Gold Chip, Advanced Functional Materials. 26 (2016) 7994–8002. https://doi.org/10.1002/adfm.201603547.
201. J.R. Choi, Development of Point-of-Care Biosensors for COVID-19, Frontiers in Chemistry. 8 (2020). https://doi.org/10.3389/fchem.2020.00517.
202. A. Parihar, P. Ranjan, S.K. Sanghi, A.K. Srivastava, R. Khan, Point-of-Care Biosensor-Based Diagnosis of COVID-19 Holds Promise to Combat Current and Future Pandemics, ACS Applied Bio Materials. 3 (2020) 7326–7343. https://doi.org/10.1021/acsabm.0c01083.
203. Y. Rasmi, X. Li, J. Khan, T. Ozer, J.R. Choi, Emerging point-of-care biosensors for rapid diagnosis of COVID-19: current progress, challenges, and future prospects, Analytical and Bioanalytical Chemistry. 413 (2021) 4137–4159. https://doi.org/10.1007/s00216-021-03377-6.
204. A.M. Shrivastav, U. Cvelbar, I. Abdulhalim, A comprehensive review on plasmonic-based biosensors used in viral diagnostics, Communications Biology. 4 (2021) 1–12. https://doi.org/10.1038/s42003-020-01615-8.
205. A. Djaileb, B. Charron, M.H. Jodaylami, V. Thibault, J. Coutu, K. Stevenson, S. Forest, L.S. Live, D. Boudreau, J.N. Pelletier, J.F. Masson, A rapid and quantitative serum test for SARS-CoV-2 antibodies with portable surface plasmon resonance sensing, ChemRxiv. (2020) 1–12. https://doi.org/10.26434/chemrxiv.12118914.
206. G. Qiu, Z. Gai, Y. Tao, J. Schmitt, G.A. Kullak-Ublick, J. Wang, Dual-Functional Plasmonic Photothermal Biosensors for Highly Accurate Severe Acute Respiratory Syndrome Coronavirus 2 Detection, ACS Nano. 14 (2020) 5268–5277. https://doi.org/10.1021/acsnano.0c02439.
207. A.N. Masterson, B.B. Muhoberac, A. Gopinadhan, D.J. Wilde, F.T. Deiss, C.C. John, R. Sardar, Multiplexed and High-Throughput Label-Free Detection of RNA/Spike Protein/IgG/IgM Biomarkers of SARS-CoV-2 Infection Utilizing Nanoplasmonic Biosensors, Analytical Chemistry. 93 (2021) 8754–8763. https://doi.org/10.1021/acs.analchem.0c05300.
208. X. Peng, Y. Zhou, K. Nie, F. Zhou, Y. Yuan, J. Song, J. Qu, Promising near-infrared plasmonic biosensor employed for specific detection of SARS-CoV-2 and its spike glycoprotein, New Journal of Physics. 22 (2020). https://doi.org/10.1088/1367-2630/abbe53.

209. D. Li, H. Zhou, X. Hui, X. He, X. Mu, Plasmonic Biosensor Augmented by a Genetic Algorithm for Ultra-Rapid, Label-Free, and Multi-Functional Detection of COVID-19, Analytical Chemistry. 93 (2021) 9437–9444. https://doi.org/10.1021/acs.analchem.1c01078.
210. X. Li, J. Shu, W. Gu, L. Gao, Deep neural network for plasmonic sensor modeling, Optical Materials Express. 9 (2019) 3857. https://doi.org/10.1364/ome.9.003857.
211. Z.S. Ballard, D. Shir, A. Bhardwaj, S. Bazargan, S. Sathianathan, A. Ozcan, Computational Sensing Using Low-Cost and Mobile Plasmonic Readers Designed by Machine Learning, ACS Nano. 11 (2017) 2266–2274. https://doi.org/10.1021/acsnano.7b00105.
212. G. Moon, J. ryul Choi, C. Lee, Y. Oh, K.H. Kim, D. Kim, Machine learning-based design of meta-plasmonic biosensors with negative index metamaterials, Biosensors and Bioelectronics. 164 (2020). https://doi.org/10.1016/j.bios.2020.112335.
213. J. He, C. He, C. Zheng, Q. Wang, J. Ye, Plasmonic nanoparticle simulations and inverse design using machine learning, Nanoscale. 11 (2019) 17444–17459. https://doi.org/10.1039/c9nr03450a.
214. I. Malkiel, M. Mrejen, A. Nagler, U. Arieli, L. Wolf, H. Suchowski, Plasmonic nanostructure design and characterization via Deep Learning, Light: Science and Applications. 7 (2018). https://doi.org/10.1038/s41377-018-0060-7.
215. Institute of Electrical and Electronics Engineers, 2019 13th International Conference on Software, Knowledge, Information Management and Applications (SKIMA)., n.d.
216. M.K. Song, S.X. Chen, P.P. Hu, C.Z. Huang, J. Zhou, Automated Plasmonic Resonance Scattering Imaging Analysis via Deep Learning, Analytical Chemistry. 93 (2021) 2619–2626. https://doi.org/10.1021/acs.analchem.0c04763.
217. M. Erzina, A. Trelin, O. Guselnikova, B. Dvorankova, K. Strnadova, A. Perminova, P. Ulbrich, D. Mares, V. Jerabek, R. Elashnikov, V. Svorcik, O. Lyutakov, Precise cancer detection via the combination of functionalized SERS surfaces and convolutional neural network with independent inputs, Sensors and Actuators, B: Chemical. 308 (2020). https://doi.org/10.1016/j.snb.2020.127660.
218. K.M. Hanafiah, M. Garcia, D. Anderson, Point-of-care testing and the control of infectious diseases, Biomarkers in Medicine. 7 (2013) 333–347. https://doi.org/10.2217/bmm.13.57.
219. C. Tymm, J. Zhou, A. Tadimety, A. Burklund, J.X.J. Zhang, Scalable COVID-19 Detection Enabled by Lab-on-Chip Biosensors, Cellular and Molecular Bioengineering. 13 (2020) 313–329. https://doi.org/10.1007/s12195-020-00642-z.
220. R. Lei, R. Huo, C. Mohan, Current and emerging trends in point-of-care urinalysis tests, Expert Review of Molecular Diagnostics. 20 (2020) 69–84. https://doi.org/10.1080/14737159.2020.1699063.
221. M.N. Esbin, O.N. Whitney, S. Chong, A. Maurer, X. Darzacq, R. Tjian, Overcoming the bottleneck to widespread testing: a rapid review of nucleic acid testing approaches for COVID-19 detection, RNA. 26 (2020) 771–783. https://doi.org/10.1261/rna.076232.120.
222. P. Rai, B.K. Kumar, V.K. Deekshit, I. Karunasagar, I. Karunasagar, Detection technologies and recent developments in the diagnosis of COVID-19 infection, Applied Microbiology and Biotechnology. 105 (2021) 441–455. https://doi.org/10.1007/s00253-020-11061-5.
223. L. Dong, C. Jin, A.B. Closson, I. Trase, H.R. Richards, Z. Chen, J.X.J. Zhang, Cardiac energy harvesting and sensing based on piezoelectric and triboelectric designs, Nano Energy. 76 (2020) 105076. https://doi.org/10.1016/j.nanoen.2020.105076.
224. C. Jin, N. Hao, Z. Xu, I. Trase, Y. Nie, L. Dong, A. Closson, Z. Chen, J.X.J. Zhang, Flexible piezoelectric nanogenerators using metal-doped ZnO-PVDF films, Sensors and Actuators, A: Physical. 305 (2020) 111912. https://doi.org/10.1016/j.sna.2020.111912.
225. Z. Xu, C. Jin, A. Cabe, D. Escobedo, N. Hao, I. Trase, A.B. Closson, L. Dong, Y. Nie, J. Elliott, M.D. Feldman, Z. Chen, J.X.J. Zhang, Flexible Energy Harvester on a Pacemaker Lead

Using Multibeam Piezoelectric Composite Thin Films, ACS Applied Materials & Interfaces. 12 (2020) 34170–34179. https://doi.org/10.1021/acsami.0c07969.

226. L. Dong, A.B. Closson, C. Jin, Y. Nie, A. Cabe, D. Escobedo, S. Huang, I. Trase, Z. Xu, Z. Chen, M.D. Feldman, J.X.J. Zhang, Multifunctional Pacemaker Lead for Cardiac Energy Harvesting and Pressure Sensing, Advanced Healthcare Materials. 9 (2020). https://doi.org/10.1002/adhm.202000053.
227. C. Jin, L. Dong, Z. Xu, A. Closson, A. Cabe, A. Gruslova, S. Jenney, D. Escobedo, J. Elliott, M. Zhang, N. Hao, Z. Chen, M.D. Feldman, J.X.J. Zhang, Skin-like Elastomer Embedded Zinc Oxide Nanoarrays for Biomechanical Energy Harvesting, Advanced Materials Interfaces. 2100094 (2021) 1–10. https://doi.org/10.1002/admi.202100094.
228. Z. Xu, C. Jin, A. Cabe, D. Escobedo, A. Gruslova, S. Jenney, A.B. Closson, L. Dong, Z. Chen, M.D. Feldman, J.X.J. Zhang, Implantable Cardiac Kirigami-Inspired Lead-Based Energy Harvester Fabricated by Enhanced Piezoelectric Composite Film, Advanced Healthcare Materials. 10 (2021) 1–9. https://doi.org/10.1002/adhm.202002100.

Summary and Future Perspectives

Advancement of photonic materials and structures along with their fascinating properties play increasingly important role facilitating the rapid progress in medicine. An excellent example is the recent development of biosensors based on plasmonic MEMS and nanostructures that induces surface plasmon effect for screening biomarkers of various diseases ranging from cancer to Covid-19. The recent global pandemics re-confirmed a trend of real-time diagnosis in public health to be in point-of-care (POC) settings that can screen interested biomarkers at home, or literally anywhere else, at any time. Plasmonic MEMS, thanks to its versatile designs and extraordinary sensitivities, can be scaled into small and portable device for POC diagnostic tools. In the meantime, efforts are being made to speed up, simplify and lower the cost of the signal readout process including converting the conventional heavy laboratory instruments into handheld devices. This book reviews the theory, fabrication and application on the design of plasmonic nanomaterial and structures-based devices in biomedical engineering applications.

Cutting-edge works in the field focusing on the technology's design, especially including photonic designs, nanomaterials development, structure assembly, and target applications are examined. There are emerging devices beyond this review with innovative nanomaterial and structural design that enhance the sensitivity, limit of detection and reliability of the sensor. Although many technologies are still in the laboratory research and development phase, some of them already have already met the basic requirements to be a commercial product, while others have shown promising potential to become one. Challenges remain in plasmonic MEMS and biosensor for biomarker detection, such as using the technology to rapid and accurate test of SARS-Cov-2 and further enhancing the sensor's accuracy and limit of detection, while the future of the plasmonic biosensing technology is full of opportunities such as miniaturization of both the sensor and the read-out machines and incorporation of machine learning.

© The Editor(s) (if applicable) and The Author(s), under exclusive license to Springer Nature Switzerland AG 2023

J. X. J. Zhang, *Plasmonic MEMS*, Synthesis Lectures on Materials and Optics,
https://doi.org/10.1007/978-3-031-23137-7

Appendix 1

© The Editor(s) (if applicable) and The Author(s), under exclusive license to Springer Nature Switzerland AG 2023

J. X. J. Zhang, *Plasmonic MEMS*, Synthesis Lectures on Materials and Optics,
https://doi.org/10.1007/978-3-031-23137-7

Device	Control mechanism	Applications	Material	Fabrication method	Journal's title	year
Optical Nanoantenna	Electromechanically	Optomechani, sensing, and active plasmonics	single-crystal gold flakes	focused-ion beam (FIB) milling	Electromechanically Tunable Suspended Optical Nanoantenna	2016
Plasmonic Nanowires	Electromechanically	controlled plasmonic resonators in visible wavelengths	500-nm-wide and 150-nm-thick gold NW suspended over an aluminum oxide-coated (20 nm thick) gold film (80 nm thick)	probe-based pick and-place method	Electromechanically Tunable Plasmonic Nanowires Operating in Visible Wavelengths	2016
Actuators	Electromechanically	MEMS based THz filter	double split-ring resonator (DSRR), 20-nm-thick Al2O3 and 500-nm-thick Al, respectively	a surface micromachining process is developed	Development of stress-induced curved actuators for a tunable THz filter based on double split-ring resonators	2013
Metasurface lens	Electromechanically	Tunable flat lens, LIDAR scanners, laser printing	Au, SiO2, Si	Photolithography, focused ion beam (FIB)	Dynamic metasurface lens based on MEMS technology	2018
Modulator	opto-mechanical	Modulating light with light	asymmetrically spaced gold resonators on silicon nitride strips	focused ion beam milling	Modulating light with light via giant nano-opto-mechanical nonlinearity of plasmonic metamaterial	2015
MIM Fabry–Perot resonator	Electromechanically	plasmonic color or sky radiator from visible to infrared range	500-nm-wide and 150-nm-thick gold NW suspended over Al2O3 coated (20 nm thick) Au film (80 nm thick) with an initial air gap of ~ 250 nm	probe-based pick-and-place method	Passive and active metasurface based on metal–insulator-metal structures	2016

Device	Control mechanism	Applications	Material	Fabrication method	Journal's title	year
Plasmonic Switch	mechanical	active plasmonic switching	Au-Air-Au gap	Theory	Nanomechanical Plasmonic Switch Based on Multimode Interference	2016
Resonators Based on Dimer Nanoantennas	Plasmomechanical	sensors of minute forces, displacements, or masses	gold plasmonic dipole – dipole-coupled dimer antenna integrated with silicon nitride nanobeams	Electron-beam lithography	Plasmomechanical Resonators Based on Dimer Nanoantennas	2015
Stretchable nanorod Substrate	mechanical	reconfigurable flat optics, chromatic and spherical aberrations of the optical lens	Au nanorod array fabricated on a stretchable polydimethylsiloxane substrate	electron beam lithography	Tunable Metasurface and Flat Optical Zoom Lens on a Stretchable Substrate	2016
Plasmonic Spectrometer	Electromechanically	Mid-Infrared Plasmonic Spectrometer, Fabry-Pérot interferometer	An array of subwavelength holes in a gold film is suspended above a gold reflector, A polysilicon frame supports a suspended gold film, in which an array of holes is fabricated	focused ion beam (FIB)	MEMS Tunable Mid-Infrared Plasmonic Spectrometer	2015

Device	Control mechanism	Applications	Material	Fabrication method	Journal's title	year
Programmable Plasmonic Metamaterial	Thermo-mechanical	SPP logic gate, SPP digital phase Shifter, controllable slow-wave generations, programmable plasmonic integrated circuits at microwave and terahertz frequencies	metallic strip, tunable capacitance a varactor diode MA46H120, low-noise HEMT EHX77Z1BTs, and a home-made microsystem (see Supporting Information) are chosen as the tunable capacitor, isolator, and core control modules, respectively	printed circuit board (PCB)	Real-Time Controls of Designer Surface Plasmon Polaritons Using Programmable Plasmonic Metamaterial	2017
Metasurface lens	electromechanical	Tunable flat lens, LIDAR	α-Si, silica, SiN	electron beam lithography	MEMS-tunable dielectric metasurface lens	2018
Flexible Plasmonics	mechanical	flexible, stretchable, nonplanar electronic and photonic systems	PDMS substrate, gold nanorod, gold particles	nanostencil lithography (NSL)	Flexible Plasmonics on Unconventional and Nonplanar Substrates	2011
nanomechanical plasmonic phase modulators	electromechanical	ultracompact-footprint π rad phase modulator, applications in optical switch fabrics and reconfigurable plasmonic optics	gold–air–gold waveguide fabricated from a gold–SiO_2–gold MIM stack	electron-beam lithography, focused ion beam (FIB)	Compact nanomechanical plasmonic phase modulators	2015

Device	Control mechanism	Applications	Material	Fabrication method	Journal's title	year
electro-optical modulator	electromechanical	extremely subwavelength broadband modulation of optical signals	Graphene, hexagonal boron nitride (hBN), gold	electron beam lithography and electron beam evaporation techniques, micromechanical exfoliation	Nanomechanical electro-optical modulator based on atomic heterostructures	2016
phase shifter	opto-electromechanical	opto-electromechanical tuning of the effective refractive index	SiNx/Ti/Au microbridge	electron-beam lithography	Broadband opto-electro-mechanical effective refractive index tuning on a chip	2016
motion transduction	opto-electromechanical	Subdiffraction optical motion transduction, highly sensitive motion measurements	silicon nitride, gold	electron beam lithography	Nanomechanical motion transduction with a scalable localized gap plasmon architecture	2016
plasmonic light amplitude and phase modulator	Thermo-mechanical	modulate light amplitude, plasmonic switch	Silicon, silver	Theory	Double bi-material cantilever structures for complex surface plasmon modulation	2015
Reconfigurable nanoantennas	Mechanical + electromagnetic	reconfigurable nanoantennas that can inform exciting photonic applications, near-field optical forces and high refractive index sensitivity	Gold pillar-bowtie nanoantenna (p-BNA) array on an indium-tin-oxide (ITO)-coated SiO_2 substrate	a combination of EBL, electron-beam evaporation and reactive-ion etching (RIE) processes	Reconfigurable nanoantennas using electron-beam manipulation	2014

Device	Control mechanism	Applications	Material	Fabrication method	Journal's title	year
piezoelectric plasmonic metasurface	thermomechanical	nanomechanical resonator, fast, high-resolution, uncooled infrared detector	an aluminum nitride (AlN) piezoelectric nanoplate (500-nm-thick) sandwiched between the two metal layers, platinum (Pt), gold	a combination of photolithography (four masks) and electron-beam lithography (one step)	Plasmonic piezoelectric nanomechanical resonator for spectrally selective infrared sensing	2016
Stretchable split-ring resonator	high-strain mechanical deformation	Stretchable electronics	Au SRRs to a 1 mm thick PDMS substrate	electron beam lithography	Highly Strained Compliant Optical Metamaterials with Large Frequency Tunability	2010
mechanically reconfigurable metamaterials	thermomechanical	metamaterial devices with reversible and large-range tunable characteristics	100 nm thick silicon nitride membrane covered by 50 nm thick thermally evaporated gold layers on both sides	focused ion beam milling	Reconfigurable Photonic Metamaterials	2011
chiroptical nanocomposites	mechanical stretching	new operational principles for optical and optoelectronic devices from nanoparticles, carbon nanotubes and other nanoscale components	poly(dimethylsiloxane) (PDMS) substrates, AuNPs	Films made by layer-by-layer (LBL) assembly	Reconfigurable chiroptical nanocomposites with chirality transfer from the macro- to the nanoscale	2016
reconfigurable metamaterials	electromechanical	tunable spectral filters, switches, modulators and adaptable transformation optics devices. protective optical circuitry and reconfigurable optical networks	silicon nitride, gold	focused ion beam	An electromechanically reconfigurable plasmonic metamaterial operating in the near-infrared	2013

Device	Control mechanism	Applications	Material	Fabrication method	Journal's title	year
NANOMECHANICAL TRANSDUCTION	thermomechanical	plasmonic mechanical actuation	Gold, silicon nitride	focused ion beam	Parallel Transduction of Nanomechanical Motion Using Plasmonic Resonators	2014
nanoelectromechanical cantilever	mechanical	Biosensors based on nanoelectromechanical systems (NEMS)	Gold, silicon nitride (SiN)	Theory	All-nanophotonic NEMS biosensor on a chip	2015
Programmable plasmon modes	mechanical stretching	amplify localized optical fields and support ultranarrow resonances	aluminum nanoparticle arrays embedded in an elastomeric slab (PDMS)	template stripping aluminum deposited on photoresist posts, Aluminum nanoparticle arrays on glass were fabricated by depositing aluminum through a gold nanohole-array mask, which was created by a process combining photolithography, etching, electron-beam deposition, and lift-off (PEEL)	Programmable and reversible plasmon mode engineering	2016